Three-dimensional wake development and structural loading on dual step cylinders in cross-flow

by

Christopher R. Morton

A thesis
presented to the University of Waterloo
in fulfillment of the
thesis requirement for the degree of
Doctor of Philosophy
in
Mechanical Engineering

Waterloo, Ontario, Canada, 2014

AUTHOR'S DECLARATION

I hereby declare that I am the sole author of this thesis. This is a true copy of the thesis, including any required final revisions, as accepted by my examiners.

I understand that my thesis may be made electronically available to the public.

Abstract

Many cylindrical structures in engineering applications undergo flow-induced periodic loading due to the vortex shedding phenomenon. This can lead to early fatigue failure and be a source of unwanted noise. To mitigate or reduce the mean and fluctuating loading, the flow development can be altered by adding geometrical modifications to the structure. This thesis is focused on the dual step cylinder geometry, which consists of a finite-span circular cylinder (the large cylinder) attached co-axially to the mid-span of a uniform circular cylinder of smaller diameter (the small cylinder). The dual step cylinder is a geometrical modification to a uniform cylinder that is ubiquitous in engineering applications, but has not been investigated extensively for its potential use in flow control. Accordingly, there is a need for developing an understanding of the flow development and structural loading on dual step cylinders in cross-flow.

This thesis provides a comprehensive characterization of the effects of dual step cylinder geometry and Reynolds number on wake development and structural loading in the turbulent vortex shedding regime. Experiments were carried out in the Water Flume Facility at the University of Waterloo and an open jet wind tunnel at TU Delft. Experimental measurements included flow and surface visualizations, wake velocity measurements with Tomographic Particle Image Velocimetry (PIV), planar PIV, and Laser Doppler Velocimetry (LDV), and lift and drag force measurements. Through an analysis of the qualitative and quantitative results, six distinct flow regimes have been identified based on observed changes in the flow development downstream of the large cylinder. The results are summarized in a two-dimensional map which has both practical and fundamental importance. Specifically, the map can be used to select dual step cylinder geometries which produce desirable flow and loading characteristics, and the map provides detailed insight into the turbulent wake development of dual step cylinders and other similar complex cylindrical geometries including cantilevered cylinders, single step cylinders, coin-like cylinders, and cylinders with two free ends.

For complex bluff body geometries, such as that of a dual step cylinder, the flow development is highly three-dimensional. In order to investigate such flows experimentally, quantitative measurements of the three-dimensional flow field are required. The presently available techniques of three-dimensional velocity field measurement, e.g., Tomographic PIV, Particle Tracking Velocimetry, and Holography, are expensive to implement and are not yet commonplace in experimental facilities world-wide. The present study employs multi-plane PIV measurements in order to investigate the three-dimensional wake development of a dual step cylinder. Two techniques of multi-plane PIV data

analysis are proposed in order to reconstruct the dominant vortical structures and vortex interactions in the wake: (i) a Proper Orthogonal Decomposition (POD) based phase-averaging approach, and (ii) a pattern recognition based conditional averaging approach. Through a comparison with Tomographic PIV results, both techniques are shown to successfully reconstruct the wake vortex shedding and vortex interactions downstream of a dual step cylinder. The techniques developed can be applied to complex bluff body flows and can accommodate the presence of more than one dominant frequency.

Acknowledgements

I would like to thank my advisor, Dr. Serhiy Yarusevych. Your guidance, expertise, and advice have been invaluable. I also am grateful for the support of my fellow graduate students, specifically, Manpreet Bansal, Holly Neatby, Jeff McClure, Tom Kirk, Sahil Mahey, Andrew Lambert, and Eugene Zikov. Thank you for always being available to lend a helping hand. In addition, I would like to thank my examination committee: Dr. Sean Peterson, Dr. Cecile Devaud, Dr. Bruce Macvicar, and Dr. Gregory Kopp.

Finally, I would like to thank the Natural Sciences and Engineering Research Council of Canada (NSERC) and the University of Waterloo for their financial support.

For my family

Table of Contents

List of Figures

List of Tables

List of Abbreviations

AIS	Asymmetric Irregular vortex Shedding
BL	boundary layer
CFL	Courant Friedrichs Lewy number
CS	Cellular vortex Shedding
DAQ	Data Acquisition System
DHT	Discrete Hilbert Transform
HFS	High Frequency vortex Shedding
K-H	Kelvin-Helmholtz
IS	Irregular vortex Shedding
LDV	Laser Doppler Velocimetry
LES	Large Eddy Simulation
LFS	Low Frequency vortex Shedding
MART	Multiplicative Algebraic Reconstruction Technique
NS	No vortex Shedding
PPP	particles per pixel
PIV	Particle Image Velocimetry
PTV	Particle Tracking Velocimetry
POD	Proper Orthogonal Decomposition
PRA	Pattern Recognition Analysis
RMS	Root Mean Square
SG	Specific Gravity
VIV	Vortex Induced Vibrations
VODIM	Volume Deformation Iterative Multigrid
WIDIM	Window Deformation Iterative Multigrid

List of Symbols

a_i	temporal coefficient *i*, obtained from the POD of PIV data
A	planform area of model
C_D	drag coefficient, $F_D / \left(\frac{1}{2}\rho U_\infty^2 A\right)$
C_L'	sectional RMS lift coefficient, $F_L' / \left(\frac{1}{2}\rho U_\infty^2 A\right)$
D	large cylinder diameter [m]
d	small cylinder diameter [m]
$E_{u'u'}$	normalized energy spectrum of u
$E_{v'v'}$	normalized energy spectrum of v
$E_{w'w'}$	normalized energy spectrum of w
f	vortex shedding frequency [Hz]
f_K	von Karman vortex shedding frequency [Hz]
f_L	large cylinder vortex shedding frequency [Hz]
f_S	small cylinder vortex shedding frequency [Hz]
f_{SL}	frequency of Kelvin-Helmholtz instability vortices [Hz]
$f_\#$	numerical lens aperture
F_D	drag force [N]
F_D^S	drag force on a uniform circular cylinder of diameter d [N]
F_D^L	estimated drag force on the large cylinder [N]
F_L	RMS of lift force fluctuations [N]
F_L'	sectional lift force [N]
F_L^S	lift force on a uniform circular cylinder of diameter d [N]
g	discrete phase signal, g(k) [rad]

H	dual step cylinder spacing [m]
L	cylinder length [m]
L_{crit}	critical aspect ratio [m]
L_D	streamwise distance from the cylinder to the outlet of the domain [m]
L_f	length of the formation region in the streamwise direction [m]
L_u	streamwise distance from the cylinder to the inlet of the domain [m]
m	number of planar velocity fields obtained
$M1$	mesh spacing at domain inlet [m]
$M2$	mesh spacing in the near wake of cylinder [m]
$M3$	mesh spacing around the cylinder circumference [m]
$M4$	mesh spacing in radial direction at the cylinder wall [m]
n	number of planar fields in each bin
N	number of bins used for phase averaging
P	large cylinder spacing [m]
p	pressure [Pa]
Q	second invariant of the velocity gradient tensor
r	unfiltered reference signal
r_f	filtered reference signal
R_i	correlation coefficient between two planar vorticity fields
$\bar{R}$	average correlation coefficient for a set of vorticity fields
R_{xy}	correlation coefficient between two planar velocity fields
Re_D	Reynolds number based on large cylinder diameter, $U_\infty D/\nu$
Re_d	Reynolds number based on small cylinder diameter, $U_\infty d/\nu$
St	Strouhal number, fD/U_∞
t	experiment or simulation time [s]

t^*	dimensionless time, tf
T	data acquisition period
U_∞	free stream velocity component [m/s]
u	streamwise velocity component [m/s]
U	streamwise mean velocity component [m/s]
U^t	template velocity field for correlation analysis [m/s]
$\overline{U^t}$	mean velocity of template field [m/s]
U^b	instantaneous velocity field b used for correlation analysis [m/s]
$\overline{U^b}$	mean velocity of instantaneous field b [m/s]
u'	fluctuating component of streamwise velocity [m/s]
u_{RMS}	RMS velocity field [m/s]
v	transverse mean velocity component [m/s]
v′	fluctuating component of transverse velocity [m/s]
$\vec{v}$	two-dimensional wake velocity field, $\vec{v}(x, y, t)$ [m/s]
$\vec{v}_\theta$	phase-averaged representation of wake velocity field, $\vec{v}_\theta(x, y, \theta(t))$ [m/s]
$\vec{v}'$	coherent part of two-dimensional field, $\vec{v}'(x, y, t)$ [m/s]
$\vec{v}''$	random turbulent fluctuations in the two-dimensional field, $\vec{v}''(x, y, t)$ [m/s]
$\vec{v}'''$	base flow variation in the wake velocity field, $\vec{v}'''(x, y, t)$ [m/s]
$\vec{V}$	two-dimensional mean wake velocity field, $\vec{V}(x, y)$ [m/s]
$\vec{V}_{ROM}$	reduced order model of the velocity field [m/s]
w	spanwise velocity component [m/s]
W	transverse distance from cylinder to the free slip wall boundary [m]
w'	fluctuating component of spanwise velocity [m/s]
x, y, z	streamwise, transverse, and spanwise coordinates, respectively [m]
Δf	frequency resolution of velocity spectra [Hz]

$\Delta x, \Delta y, \Delta z$	measurement volume size in x, y, and z directions [Hz]
Δs	spanwise spacing between horizontal planes [Hz]
$\Delta\theta$	phase angle resolution for each bin [rad]
θ	phase pertaining to a reference signal [rad]
θ_L	phase in the large cylinder wake [rad]
θ_S	phase in the small cylinder wake [rad]
θ_{sep}	separation angle on the large cylinder [rad]
λ_i	eigenvalues (mode energy) obtained from POD of PIV data [1/s]
ϕ_i	spatial eigenfunctions (modes) obtained from POD of PIV data [m/s]
ε	average residual circulation error (%) in sets of planar vorticity fields
σ	standard deviation of a planar velocity field
φ	mean variation in phase angle along the span of a dual step cylinder [rad]
ρ	density of water [kg/m^3]
ν	kinematic viscosity of water [m^2/s]
ω	vorticity [1/s]

Chapter 1

Introduction

This thesis focuses on laminar and turbulent flows over cylindrical geometries. The simplest of such geometries is a uniform circular cylinder. Figure 1.1 shows a conceptual sketch of the flow past a circular cylinder. As fluid approaches a circular cylinder, the fluid is diverted around the cylinder, and boundary layers develop along the upper and lower surfaces. The boundary layer separates from the cylinder due to the presence of an adverse pressure gradient and forms a separated shear layer (Figure 1.1). If the Reynolds number (Re_D), is sufficiently high, then the separated shear layers roll-up into vortices behind the cylinder in a periodic fashion, forming a distinct pattern of vortices in the wake region. The periodic shedding of vortices affects the wake characteristics downstream of the cylinder, and exerts oscillating forces on the cylinder, both of which are important for engineering design.

Many cylindrical structures in engineering applications, e.g., off shore oil risers, suspension bridge cables, components of aircraft landing gears and wind turbine masts, etc., undergo significant flow-induced periodic loading generated from the well-studied vortex shedding phenomenon [1–3]. This can lead to early fatigue failure of the structure and can be a source of unwanted noise [4]. Conversely, the fluctuating loading on a cylindrical structure can also be used for energy harvesting by allowing flow-induced vibration to take place [5–8]. Over the past several decades, hundreds of

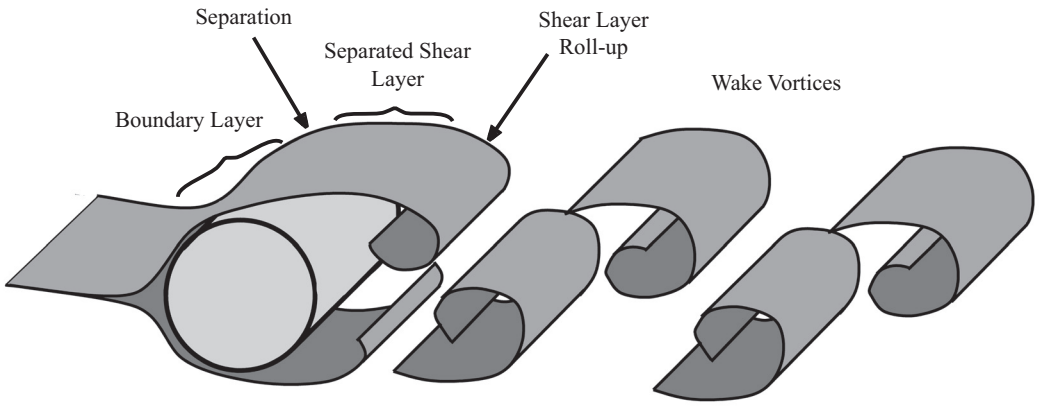

Figure 1.1 Flow development over a circular cylinder.

experimental and numerical investigations have considered methods of either mitigating or enhancing vortex shedding from cylindrical bodies [6,9]. Geometrical modifications to a uniform circular cylinder, for example, the addition of splitter plates, roughness elements, helical strakes, etc., can be used to alter vortex shedding characteristics, i.e., the spanwise coherence and strength of vortex shedding and even suppress vortex shedding [9–12]. Depending on the modifications made, the desired effect on the shedding can be achieved by controlling the: (i) boundary layer development, (ii) separated shear layer development, or (iii) near wake development. Examples of these modifications include: (i) roughness elements placed within the developing boundary layer to significantly alter boundary layer development and subsequent wake characteristics [13], (ii) a wire placed within the separated shear layer to alter vortex formation and wake characteristics [14], and (iii) a splitter plate placed in the near wake region for effectively suppressing the roll-up and shedding of wake vortices [15]. While there are a variety of modifications which are used for the passive control of vortex shedding in engineering applications [9], new modifications continue to be discovered as engineering applications evolve.

This thesis is focused on the dual step cylinder geometry (Figure 1.2): a geometry which is ubiquitous in engineering applications, but has not been investigated for its potential use in the control of vortex shedding. Aside from the work completed as part of this thesis, to the best of the author's knowledge, there is only one investigation on the flow development past dual step cylinders [16]. This study [16] was limited to Reynolds numbers within the laminar vortex shedding regime, which are not directly applicable to the abovementioned engineering applications involving cylindrical structures. A study by Nakamura & Igarashi [17] on multi-step cylinders in turbulent flow, provided some insight into the potentially beneficial effects of utilizing step changes in diameter for altering flow characteristics, namely, reducing mean and unsteady loading. Nakamura & Igarashi [17] showed that for a narrow range of geometric and flow parameters, substantial reduction (up to 15%) in the mean drag on a cylindrical structure can be achieved using multiple stepwise discontinuities in cylinder diameter.

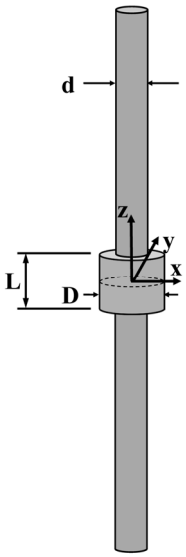

Figure 1.2 Dual step cylinder geometry.

For complex bluff body geometries such as that of a dual step cylinder, the flow development and vortex shedding is often highly three-dimensional [18,19]. Moreover, under turbulent flow conditions, which are ubiquitous in engineering applications, there are often spatial and temporal variations in vortex strength, coherence, and frequency [20]. Hence, in order to investigate such flows experimentally, quantitative measurements of the three-dimensional flow field are required. Such measurements can be carried out using tomographic PIV, three-dimensional Particle Tracking Velocimetry (PTV), multi-plane scanning PIV, and holography [21]. However, these techniques are often restricted by spatial and temporal resolution limits, and are not yet common research tools in experimental facilities world-wide, which rely on more conventional techniques, such as 2D PIV. Over the last few decades, several techniques of 2D PIV data analysis have proved useful for studying three-dimensional vortical structures in turbulent flows, including: (i) phase-averaging of dominant periodic structures [22,23], (ii) vortical structure identification through Proper Orthogonal Decomposition (POD) [24–26], (iii) pattern recognition methods [27–29], and combinations of these techniques. Each of the listed techniques require some subjective analysis based on where spatial and/or temporal variations in the velocity field are known to occur. Due to this subjectivity in the analysis, it has been difficult to reach a consensus on the most effective techniques for investigating three-dimensional

vortical flows. A study which compares these methodologies, and considers new approaches for investigating three-dimensional vortex dynamics in turbulent flows would be an important step towards focusing research efforts in the future.

1.1 Motivation

The present work is motivated by the following aspects: (i) Despite being found in a number of engineering applications where the understanding of flow development is of critical importance in engineering design, the dual step cylinder geometry has not been well-studied. Thus, there is a need to investigate dual step cylinder wake development and structural loading in turbulent flow. (ii) The research by Nakamura & Igarashi [17] on the use of multi-step cylinders for drag reduction has provided an indication of the potential benefits of using dual steps in cylinder geometry as a passive flow control tool. In order to expand their work to a wider range of geometrical parameters and Reynolds numbers, first, there is a need for a better understanding of the fundamental mechanisms involved in controlling wake development using discontinuities in diameter. This can be achieved by investigating the dual step cylinder geometry. (iii) For the vast majority of experimental facilities world-wide, three-dimensional flow measurement systems are not readily available due to the complexity of setup and cost of implementation. Far more common are two-dimensional planar measurement systems, which are easier to implement, but are presently limited in their ability to provide information about three-dimensional flow characteristics. Thus, there is a need for developing robust methods of investigating complex three-dimensional flows using planar measurement systems.

1.2 Objectives

This thesis presents an investigation of the flow development and structural loading on dual step cylinders (Figure 1.2). Based on the foregoing introduction to the thesis topic and motivation, the objectives are listed as follows:

1. Provide a comprehensive characterization of the effects of dual step cylinder geometry (D/d and L/D) and Reynolds number (Re_D), on wake development and structural loading in turbulent flows.

2. Develop data acquisition and data processing methodologies for investigating vortex dominated flows containing one or more dominant frequencies using solely two-dimensional PIV measurements. Specifically, reconstruct the dominant three-dimensional coherent vortical structures and their interactions in the wake of a dual step cylinder using conditional phase-averaging of planar PIV measurements and conditional averaging of planar PIV measurements via pattern recognition analysis.

3. Obtain three-dimensional tomographic PIV measurements of dual step cylinder wakes in order to uncover the instantaneous three-dimensional wake topology, provide insight into the observed changes in flow topology that occur with D/d, L/D, and Re_D, and validate the proposed three-dimensional flow reconstruction techniques based on planar PIV measurements.

1.3 Overview of the study

This thesis is organized into eight chapters. A review of relevant literature is presented in Chapter 2. First, literature pertinent to the flow development over uniform and complex cylindrical geometries is reviewed, focusing on vortex dynamics and mean and unsteady loading characteristics. Then, the state of the art in data processing methodologies utilized for investigating complex three-dimensional bluff body flows is briefly discussed. Chapter 3 describes the methods of investigation, which include experimentation in wind tunnel and water channel facilities. Chapter 3 also provides the mathematical framework used for all experimental data analysis.

The main experimental results are presented in Chapters 4, 5 and 6. In Chapter 4, dual step cylinder flow development is investigated through the analysis of flow visualizations, quantitative velocity measurements, and force balance measurements. The dual step cylinder wake development is classified into distinct flow regimes based on observed changes in large cylinder wake characteristics. A two-dimensional map of these flow regimes is proposed, which serves as a guideline for estimating the flow regime for a given D/d and L/D. Chapter 5 presents the results from tomographic PIV measurements performed on a limited set of dual step cylinder models. The focus of the Chapter is to provide insight into wake vortex dynamics as well as phenomena which were left

unexplained in Chapter 4. The tomographic PIV measurements spanned a larger Reynolds number range, enabling further investigation of the effects of Reynolds number on dual step cylinder wake development. Chapter 6 is dedicated to investigating methodologies of reconstructing three-dimensional flow topology solely from 2D PIV measurements obtained in multiple, closely spaced planes. The experimental results are compared with the tomographic PIV measurements presented in Chapter 5..

In Chapter 7, conclusions are drawn from the study, and in Chapter 8, recommendations are made for the future use of the experimental data analysis techniques developed, as well as for the application of the obtained experimental data to practical engineering applications.

1.4 Author's Current Contributions

It is acknowledged that portions of the work presented in Chapters 3-6, and Appendices A-H, are adapted from the following articles:

1. Morton, C., Yarusevych, S. (2014) "Three-dimensional flow and surface visualization using hydrogen bubble technique," *Journal of Visualization*, DOI 10.1007/s12650-014-0219-0, pp. 1-12.
2. Morton, C., Yarusevych, S. (2014) "Vortex dynamics in the turbulent wake of a single step cylinder," *Journal of Fluids Engineering*, Vol. 136, Issue 3, 031205.
3. Morton, C., Yarusevych, S. (2014) "Vortex shedding from low aspect ratio dual-step cylinders," *Journal of Fluids and Structures*, Vol. 44, pp. 251-269.
4. Morton, C., Yarusevych, S. (2014) "Analyzing three-dimensional wake vortex dynamics using time-resolved planar PIV," *17th International Symposium on Applications of Laser Techniques to Fluid Mechanics*, Lisbon, Portugal.
5. Morton, C., Yarusevych, S., Scarano, F. (2014) "Tomographic PIV investigation of the flow around dual step cylinders," *2014 Canadian Society for Mechanical Engineering International Congress*, Toronto, Canada.
6. Morton, C., Yarusevych, S. (2014) "Reconstructing 3D wake topology of complex cylindrical geometries using velocity field correlation," *1000 Islands Fluid Mechanics Meeting*, May 30-June 1, Gananoque, Canada.
7. Morton, C., Yarusevych, S. (2013) "Turbulent vortex shedding from a dual-step cylinder: Influence of diameter ratio and aspect ratio," *Proceedings of TSFP-8*, August 27-30, Poitiers, France.

8. Morton, C., Yarusevych, S. (2013) "Extracting dominant three-dimensional coherent structures from time-resolved planar PIV measurements in the wakes of cylindrical bodies," *Proceedings of the 10th International Symposium on Particle Image Velocimetry – PIV2013*, July 1-3, Delft, The Netherlands.

9. Morton, C., Yarusevych, S. (2013) "A dual step cylinder in cross-flow: wake and surface visualizations," *1000 Islands Fluid Mechanics Meeting*, April 26-28, Gananoque, Canada.

10. Morton, C., Yarusevych, S. (2012) "An Experimental Investigation of Flow Past a Dual Step Cylinder," *Experiments in Fluids*, Vol. 52, Issue 1, pp. 69-83.

11. Morton, C., Yarusevych, S. (2012) "Vortex shedding from low aspect ratio dual step cylinders," *Proceedings of the ASME 2012 Fluids Engineering Division Summer Meeting*, July 8-12, Rio Grande, Puerto Rico.

Chapter 2

Literature Review

Literature on the cross-flow over a dual step cylinder as well as other similar geometries, e.g., uniform cylinders, cantilevered cylinders, and cylinders with free ends, is reviewed in this Chapter. The main focus is to review aspects of the flow development which play an important role in determining unsteady loading characteristics as well as wake vortex dynamics, which, for bluff bodies, is largely dictated by the vortex shedding from the body.

2.1 Uniform circular cylinders

The flow over a uniform circular cylinder involves the development of boundary layers, shear layers, and wake vortices [30]. For Reynolds numbers (Re_D) greater than about 50, the separated shear layers roll-up into vortices behind the cylinder in a periodic fashion, forming a distinct vortex shedding pattern, as depicted in Figure 1.1. The vortex shedding from a circular cylinder is two-dimensional and laminar in the range $50 < Re_D < 190$ [30]. For $Re_D \geq 190$, a secondary (Mode A) instability leads to the deformation of spanwise vortices at formation [30], resulting in the development of streamwise vortices. The streamwise vortices form in pairs, with a spanwise wavelength of approximately 3-4D [30]. $Re_D \approx 240$ marks the transition to a Mode B secondary instability that is associated with smaller-scale deformations of the spanwise vortices at formation. With increasing Reynolds number up to about 1000, the arrangement of streamwise vortices becomes less organized. Transition to turbulence occurs in the wake region, and with increasing Re_D the location of transition moves upstream towards the near wake. For about $1x10^3 \leq Re_D \leq 2x10^5$, transition to turbulence occurs in the shear layers, and the point of transition continues to move upstream with increasing Re_D. This also corresponds to the range of Re_D common to many practical engineering applications relevant to the present study. A compilation of experimental data for uniform circular cylinders is provided in Figure 2.1. The data presentation in Figure 2.1 has been adapted from the review papers of Lienhard [31], Oertel [32], and

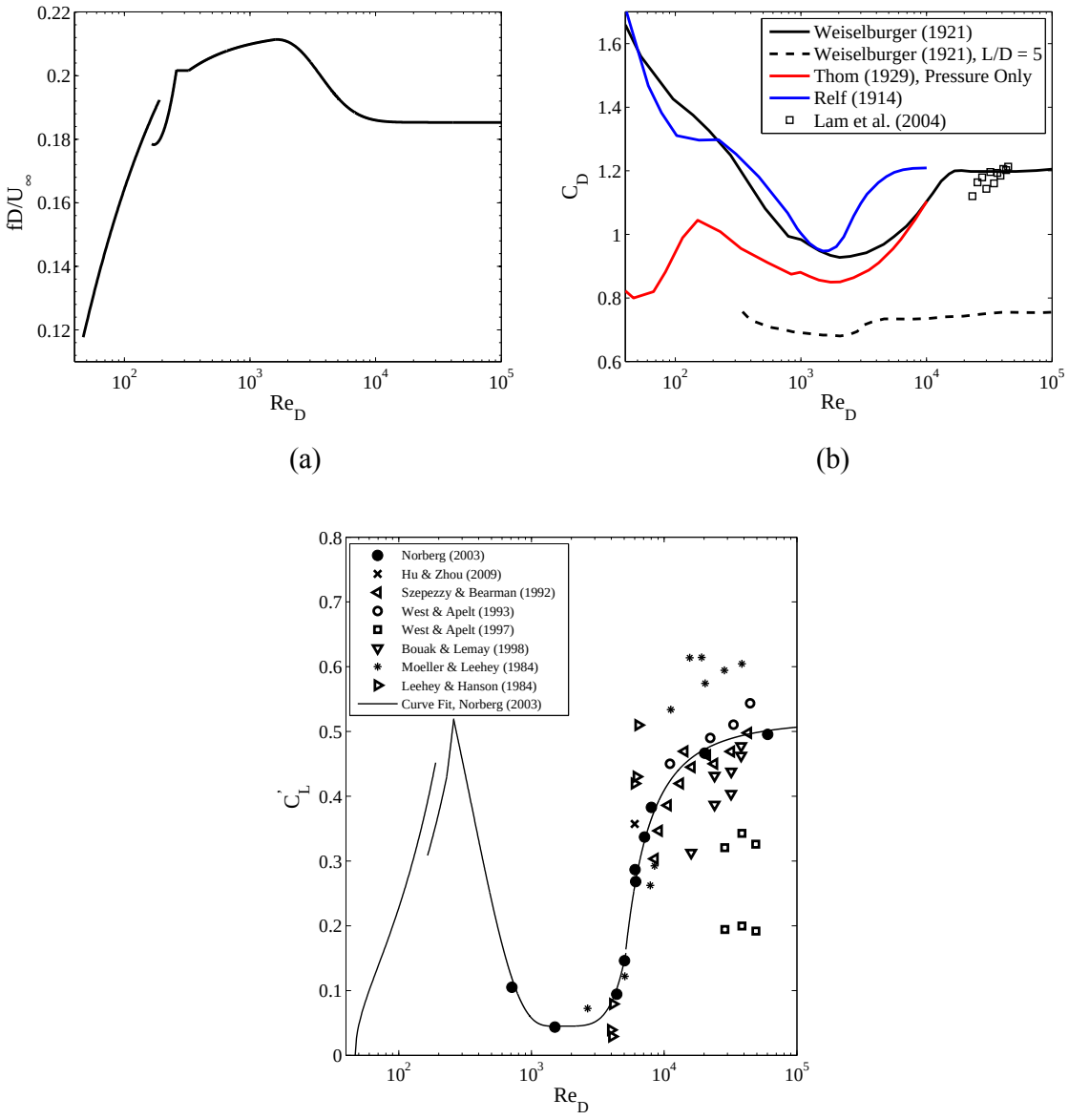

Figure 2.1 Experimental data on characteristics of uniform circular cylinders in cross-flow for $40 \leq Re_D \leq 1x10^5$: (a) Strouhal number (St) [33], (b) Drag coefficient (C_D) [68,143,144,156,157], and (c) RMS lift coefficient ($C_{L'}$) [33,158–164].

Norberg [33]. The results show that the Strouhal number (St), the drag coefficient, C_D, and the sectional RMS lift coefficient, C_L', all change significantly with Re_D. Moreover, at higher Reynolds numbers relevant to common engineering applications, i.e., $Re_D \geq 10^3$, there is considerable variation in the drag and lift measured by different researchers (Figure 2.1). For the drag data presented in Figure

2.1b, this variation is attributable primarily to changes in the contributions of pressure and friction drag towards the overall drag on the cylinder. There are also notable changes in drag coefficient with cylinder aspect ratio (L/D), for example, the results of Wieselburger at L/D = 5 in Figure 2.1 are significantly lower than the corresponding results for an infinitely long circular cylinder. For the fluctuating sectional lift coefficient data presented in Figure 2.1c, there is more substantial scatter in the data than for drag and Strouhal number data. The sectional lift coefficient is defined as the normalized lift force fluctuations acting on an infinitesimally small spanwise section of the cylinder. The observed scatter in data is attributed to differences in techniques for estimating the sectional lift, as well as model aspect ratio, end effects, and experimental facility conditions [33]. In engineering applications, of practical relevance is the total RMS lift coefficient for the entire body, which is application dependent, and cannot be displayed on a comprehensive plot like that shown in Figure 2.1c.

2.1.1 Influence of end conditions and aspect ratio on vortex shedding

In any experimental study, there are limitations in the physical dimensions of the testing area. Typically, a fixed aspect ratio model is placed in the flow and assumed to be representative of an infinite aspect ratio model in an infinite flow field. Naturally, the larger the aspect ratio of the model used, the more closely this approximation holds. However, it is also possible to use specific conditions at the ends of the model that minimize the effects of the ends on the overall flow development. This allows researchers to use fixed aspect ratio models while still achieving a reasonable approximation to infinite aspect ratio conditions. Previous experimental studies on uniform circular cylinders [34–40] show that thin circular or rectangular plates attached to both of the cylinder ends minimize end effects. Endplates, whether they are circular or rectangular, still induce a non-uniformity in the flow across the model span. When boundary layers develop along the surface of the endplates, the vortices forming behind the cylinder near the endplate have a lower convective velocity. Thus, over time, the vortex cores near the cylinder ends will move in and out of phase with the vortices shed along the central part of the cylinder. This can equivalently be described distinct differences in the vortex shedding frequency along the span. Specifically, a low frequency vortex shedding cell forms near the

cylinder ends, and a higher frequency vortex shedding cell forms near the central part of the cylinder, as illustrated in Figure 2.2. If the aspect ratio of the cylinder is significantly smaller than that depicted in Figure 2.2, it is possible for the spanwise regions of lower shedding frequency near the ends to merge, such that no central cell exists with periodic vortex shedding resembling that of an infinite cylinder. Gerich & Eckelmann [41] show that in laminar shedding conditions, a region extending up to 10D from each of the cylinder ends sheds vortices at a lower frequency, but if the aspect ratio of the cylinder is less than 30, these regions of low frequency shedding merge. It can be inferred from the results in Norberg [42] that a slightly larger critical aspect ratio exists in the turbulent vortex shedding regime. There is, however, practical limitations in adhering to these minimum aspect ratio requirements due to facility size restrictions, and research efforts to experimentally measure details of boundary layer, shear layer, and near wake characteristics. Therefore, an acceptable compromise is to

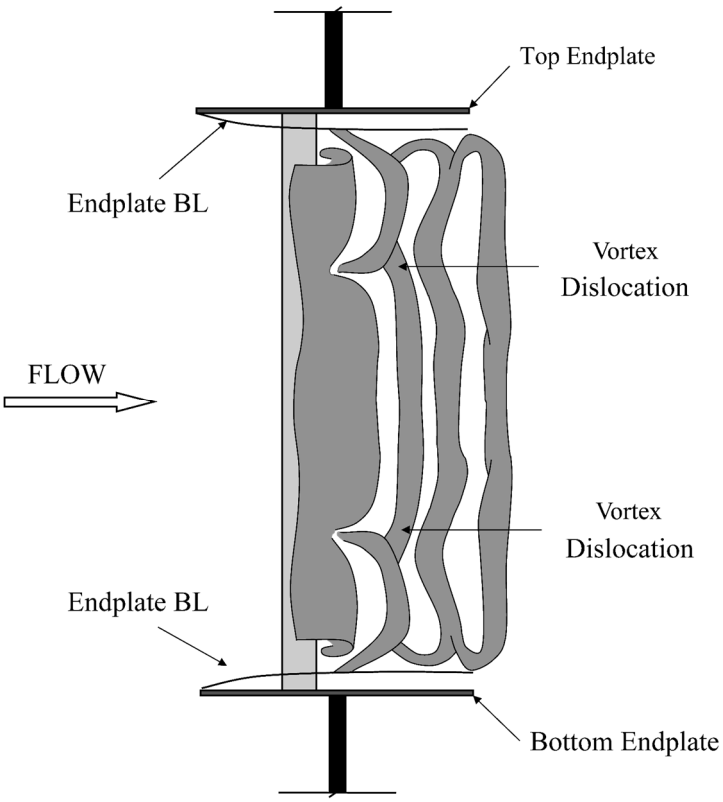

Figure 2.2 Vortex shedding from a cylinder mounted between circular endplates, adapted from [36].

determine the aspect ratios required to achieve nominally two dimensional flow conditions at the cylinder mid-span. The results by Fox & West [39] for $3.3x10^4 \leq Re_D \leq 13.2x10^4$ show that for low aspect ratio uniform cylinders ($7 \leq L/D \leq 35$) mounted between endplates designed following recommendations of Mair & Stansby [34], the cylinder base pressure is affected in a spanwise region extending just 3.5D from the cylinder ends. Their results suggest that to achieve nominally two-dimensional flow conditions at the mid-span of a circular cylinder in turbulent flow, the aspect ratio must be greater than about 7D [39]. As mentioned above, at such low aspect ratios, the low frequency vortex shedding cells forming near the ends of the model merge, and therefore, the vortex shedding frequency and associated wake characteristics will not match that found for an infinitely long uniform circular cylinder. Thus, corrections are applied to quantitative data based on the model aspect ratio used [43].

One additional point of importance regarding end effects is the design of the endplates. The end conditions studied by Norberg [42], included circular endplates whose diameter ranged between 10 to 30 cylinder diameters. The results showed that in general, smaller endplates performed better, i.e., convergence of wake characteristics occurred at lower L/D, except for one unique set of conditions that is relevant to the present study: Norberg [42] reported that for L/D = 7, and an endplate size of 10 cylinder diameters, the flow development becomes bi-stable, with regular vortex shedding being replaced with an "irregular flow" at moderate $Re_D \approx 2000$. The bi-stable flow behavior was speculated to be caused by the downstream edge of the endplates roughly matching the length of the vortex formation region downstream of the cylinder. This can be avoided by using a larger endplate, or by offsetting the cylinder so that the downstream distance to the edge of the endplate extends well beyond the formation region, as shown in Figure 2.2.

2.1.2 Vortex dislocations and vortex dynamics in cylinder wakes

The sketch in Figure 2.2 shows a single snapshot of the dominant vortex structures and their interactions in the wake of a circular cylinder mounted between endplates. The vortex dynamics can be described in a simplified form using Helmholtz vortex theorems, specifically the conservation of circulation. As mentioned previously, the vortex shedding near the ends of the cylinder model in

Figure 2.2 occurs at a lower frequency than the vortex shedding at the mid-span. As a result, over several vortex shedding cycles, the vortex cores near the ends will move out of phase with the vortex cores at the mid-span. In order to preserve circulation in the wake, when vortices move out of phase, they must stretch and tilt in order to maintain their vortex connections. Vortices may also split into multiple smaller filaments, and divide their circulation among neighboring vortices through direct or looped connections. Such events in the flow field are termed vortex dislocations [16], and may also be characterized as a vortex 'knot' [36,44] or vortex splitting [36]. One example of a vortex dislocation is identified in Figure 2.2. Based on the numerous accounts of vortex dynamics occurring between vortices shed at different frequencies in cylinder flows [16,19,36,44,45], vortex dislocations often involve a combination of vortex stretching, tilting, splitting, looping, and merging. The arrangement and occurrence of these phenomena in the wake depends upon the Reynolds number of the flow, the rate at which the vortices move in and out of phase, as well as the three-dimensional vortex topology at formation.

Vortex dynamics at a cylinder-wall junction

At the junction of a cylinder with an endplate, junction vortices form [46], and are characterised as a pair of counter-rotating streamwise vortices which may interact with the spanwise vortices. Downstream of vortex formation, the spanwise vortices must either terminate at the endplate boundary, form a connection with a subsequently shed spanwise vortex, or become intertwined in a vortex braid that maintains connection with the junction vortex at the step [36,40,47–49]. Experimental and numerical results on circular cylinders in cross-flow suggest that all three of these vorticity topologies can occur [36,40,47–49]. For large aspect ratio cantilevered cylinders, the numerical simulations by Krajnovic [47] and experiments by Bourgeois [49] show spanwise vortices terminating at a wall-boundary in turbulent vortex shedding conditions. In Figure 2.2, the presence of the endplate boundary layers inhibit spanwise vortices from terminating at the cylinder boundaries, leading to a continuous band of looped connections which preserve circulation (see also [36]). Finally, in the experimental studies by Williamson [40], flow visualizations indicate that the vortices form a continuous braid connecting back to the cylinder junction.

2.2 Complex cylindrical geometries

For complex cylindrical geometries, e.g., cantilevered cylinders, single step cylinders and multi-step cylinders, changes in cylinder geometry significantly complicate the vortex shedding along the span when compared to that of a circular cylinder. The model length and end conditions also have a significant influence on wake development. This section reviews the state of the art in the understanding of the flow development, wake vortex dynamics, and structural loading characteristics on complex cylindrical geometries similar to that of a dual step cylinder.

2.2.1 Cantilevered Cylinders

Uniform flow over cantilevered cylinders has been investigated extensively under turbulent vortex shedding conditions [41,47,50–56]. The aspect ratio plays an important role in the formation and shedding of spanwise vortices [41,50]. In particular, distinct changes in the wake development occur as the aspect ratio is decreased: (i) $L_{1,crit}/D \approx 20-30$, the critical aspect ratio for which vortex shedding from the cylinder transitions from shedding in multiple distinct cells to a single cell along the span [41,50,55], and (ii) $L_{2,crit}/D \approx 7$, the critical aspect ratio for which the vortex shedding from the cylinder ceases or becomes irregular [41,50,51]. Figure 2.3 presents topological sketches of the wake topology of a cantilevered cylinder for different cylinder aspect ratios. The sketches in Figure 2.3 are treated as illustrations only, as the values of $L_{1,crit}$ and $L_{2,crit}$ are approximate, and cantilevered cylinder wake topology at very low aspect ratios ($L/D < 7$) is still under debate [41,47,52,53,57–60].

Experimental studies have shown that for cantilevered cylinders with aspect ratios in the range $20 < L/D \leq 30$ and for $3000 < Re_D < 260{,}000$ (Figure 2.3a), near the cylinder ends, vortex shedding is highly three-dimensional and occurs at a lower frequency than vortex shedding at the cylinder mid-span [41,50,51]. The shedding near the cylinder mid-span occurs at frequency closer to that expected for an infinitely long circular cylinder. Similar to the findings on uniform cylinders mounted between endplates (cf. Figure 2.3a and Figure 2.2), the difference in vortex shedding frequency at the mid-span and near the cylinder ends leads to periodic vortex dislocations. At lower aspect ratios (Figure 2.3b), $6 < L/D \leq 20$, only a single vortex shedding frequency is detectable across the cylinder span owing to the merging of the regions of lower frequency vortex shedding near the cylinder ends. The shedding

frequency then decreases with decreasing cylinder aspect ratio [41] and, for L/D less than about seven, the flow becomes irregular. According to the experimental results of Okamoto & Yagita [52], for $1.5 \leq L/D \leq 6$, the typical alternating vortex shedding is replaced with symmetric shedding of vortices. On the other hand, Fox & Apelt [60], show no signature of vortex shedding in their fluctuating surface pressure measurements obtained for a cantilevered cylinder at L/D = 7, and speculate that vortex shedding ceases altogether. Recent Large Eddy Simulation (LES) results of Krajnovic [47] show another type of periodic vortex shedding from cantilevered cylinders for L/D = 6, where the spanwise vortices deform into "arch-like" structures as they are shed and preserve circulation in the wake by connecting to the ground plane. Thus, in three separate studies covering similar cantilevered cylinder aspect ratios, three-different wake topologies are observed [47,52,60]. The Reynolds number within the turbulent shedding regime and boundary layer thickness in the cylinder ground plane are two important quantities that are known to influence the wake development of cantilevered cylinders [57,61], but there are too few comprehensive experimental studies to determine if these quantities are responsible for the differences observed in the wake topology for the same aspect ratio.

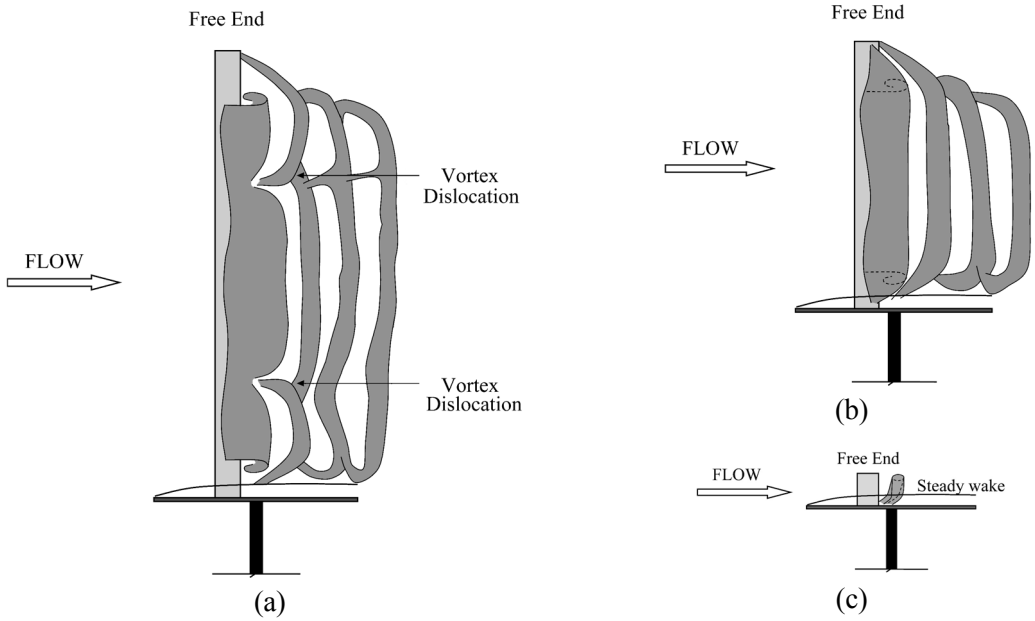

Figure 2.3 Sketches of vortex shedding from a cantilevered cylinder mounted to a ground plane. (a) large aspect ratios, $L > L_{1,crit}$, (b) moderate aspect ratios, $L_{2,crit} < L < L_{1,crit}$, (c) low aspect ratios, $L < L_{2,crit}$, adapted from [59].

In addition to the shedding of spanwise vortices from cantilevered cylinders, streamwise vortices form at the cylinder boundaries. In particular, similar to results on uniform cylinders mounted between endplates, junction vortices form at the base of a cantilevered cylinder and its ground plane. Downstream of the model, the junction vortex manifests as a pair of counter-rotating streamwise vortices which may interact with the main spanwise rollers, though the exact nature of such vortex interactions continues to be debated [62–65]. On the other hand, at the free end, another pair of streamwise vortices referred to as tip vortices forms. The strength and persistence of both junction and tip vortices in the instantaneous and mean field topology depend significantly on the cylinder aspect ratio, Reynolds number, and boundary layer thickness [46,47,53,57,58,61,66].

Mean and unsteady loading on cantilevered cylinders

The past experimental studies on the mean and unsteady loading on cantilevered cylinders have provided clear insight into local and global trends in these quantities with cylinder geometry and Reynolds number, but limited insight into how these trends relate to changes in vortex shedding characteristics.

Three comprehensive studies focused on the mean and unsteady loading characteristics of cantilevered cylinders in a cross-flow are those of Okamoto & Yagita [52] for $Re_D = 1.4x10^4$, Fox & West [67] for $Re_D = 4.4x10^4$, and Farivar [50] for $Re_D = 7x10^4$. In these studies, the variation of the local drag force due to pressure was measured along the span of cantilevered cylinders of varying aspect ratios in the range $4 \leq L/D \leq 30$. The results show that the local drag coefficient increases within approximately three diameters of the free end, and, except for a short spanwise region within about 0.5D of the free end, remains lower than that expected for an infinite cylinder. As a result, the overall mean drag across the entire span is lower than that found for a uniform circular cylinder.

The fluctuating components of the local drag and lift due to pressure on cantilevered cylinders have been investigated in detail by Fox & Apelt [60] for $Re_D = 4.4x10^4$ and Farivar [50] for $Re_D = 7x10^4$. Up to an aspect ratio of L/D = 30, the RMS of the drag and lift fluctuations varies significantly along the span. In particular, the local RMS lift and drag decrease with distance from the

free end until reaching a minimum at a location of 7D from the free end. In addition, with increasing cylinder aspect ratio, the RMS of the drag and lift fluctuations increases.

2.2.2 Cylinders with two free ends

A limited number of experimental studies that have been completed on the flow development over cylinders with two free ends: the two studies completed by Zdravkovich [18,20] for $6x10^4 < Re_D < 2.6x10^5$ and $0.025 \leq L/D \leq 8$ and the pioneering drag measurements completed by Weiselsburger [68] for $4 < Re_D < 1x10^6$ and $L/D = 5$ which are presented in Figure 2.1b.

Zdravkovich [20] found that, for $2 \leq L/D \leq 8$, vortex shedding in the wake of the cylinder is irregular and the frequency of shedding varies with time. This results in a distribution of wake energy content across a range of frequencies and makes it difficult to specify a single vortex shedding frequency [20]. For much smaller coin-like cylinders at $0.025 \leq L/D \leq 1$, Zdravkovich et al. [18] found the flow topology to be steady, consisting of two pairs of counter-rotating streamwise vortices emanating from each of the cylinders flat ends.

Recently, low Re_D laminar simulations of Inoue and Sakuragi [69] on the flow development past cylinders with two free ends have provided some additional insight into the flow development, particularly the vortex dynamics [69]. For $50 < Re_D < 200$ and $L/D \geq 20\text{-}30$, the vortex shedding and vortex interactions are similar to that found for a long cantilevered and circular cylinders. In particular, vortex shedding near the cylinder ends occurs at a lower frequency, and vortex dislocations occur between vortices shed near the end and those shed near the mid-span of the cylinder. In contrast, vortices are shed at a single frequency across the entire span at smaller L/D in the range $10 \leq L/D < 20\text{-}30$. The frequency of vortex shedding decreases with decreasing L/D, in agreement with the results of Gerich & Eckelmann [41] for cantilevered cylinders. The wake development for cylinders with two free ends becomes highly three-dimensional for $L/D \leq 8\text{-}10$. Distorted, highly three-dimensional vortex shedding is observed for $2 < L/D < 10$ [69]. Depending on the Reynolds number, two distinct flow patterns emerge for $0.5 < L/D \leq 2$ within the laminar shedding regime: (i) vortices may shed from the flat ends of the cylinder, i.e., traditional spanwise vortex shedding no longer occurs, or (ii) vortex shedding is suppressed.

Mean and unsteady loading on cylinders with two free ends

Experimental drag measurements on cylinders with two free ends have been reported for $L/D \geq 0.025$ [18,20,68]. The result indicate that the drag coefficient decreases with decreasing L/D for $1 < L/D < \infty$, agreeing with the results on cantilevered cylinders [50,55]. However, a further decrease in aspect ratio below L/D = 1 and the drag coefficient then increases [18]. This is attributed to an increase in the contribution of the skin friction drag generated by the flat ends of the cylinder. Thus, it is more appropriate to compute the drag coefficient using the cross-sectional area of the cylinder ends for $L/D \leq 1$ [18].

2.2.3 Single Step Cylinders

A single step cylinder is comprised of two different diameter cylinders joined co-axially. At the cylinders junction lies a single step change in diameter. The flow development past a single step cylinder is dependent on Re_D, and the ratio between the cylinder diameters, D/d [19,45,70]. At sufficiently high Re_D, vortex shedding occurs from both the large and small diameter cylinders, and the vortices interact in a region downstream of the step discontinuity [70]. In the laminar shedding regime, Lewis & Gharib [70] identified two different modes of vortex interactions depending on D/d. In the direct mode, occurring for $D/d < 1.25$, vortices shed from the small and large cylinders interact in a narrow region downstream of the step discontinuity. The difference in shedding frequency between the large and small cylinder vortices results in vortex dislocations between the wake vortices. During a vortex dislocation, vortices shed from the large cylinder split into multiple vortex filaments, while vortices shed from the small cylinder form either direct connections with large cylinder vortices or looped connections with adjacent small cylinder vortices in order to preserve circulation, as illustrated in Figure 2.4a [70]. In the indirect mode, occurring for $D/d > 1.55$, the wake of the large cylinder becomes more complex, with the vortices in the vicinity of the step shed at a lower frequency than those shed far from the step. Lewis & Gharib [70] referred to the region of lower frequency shedding as the 'modulated' zone, because the spanwise extent of the zone fluctuated with time. Dunn & Tavoularis [45] investigated the vortex dynamics within the modulated zone. Their results characterized the modulated zone as a region of lower frequency vortex shedding, similar to that

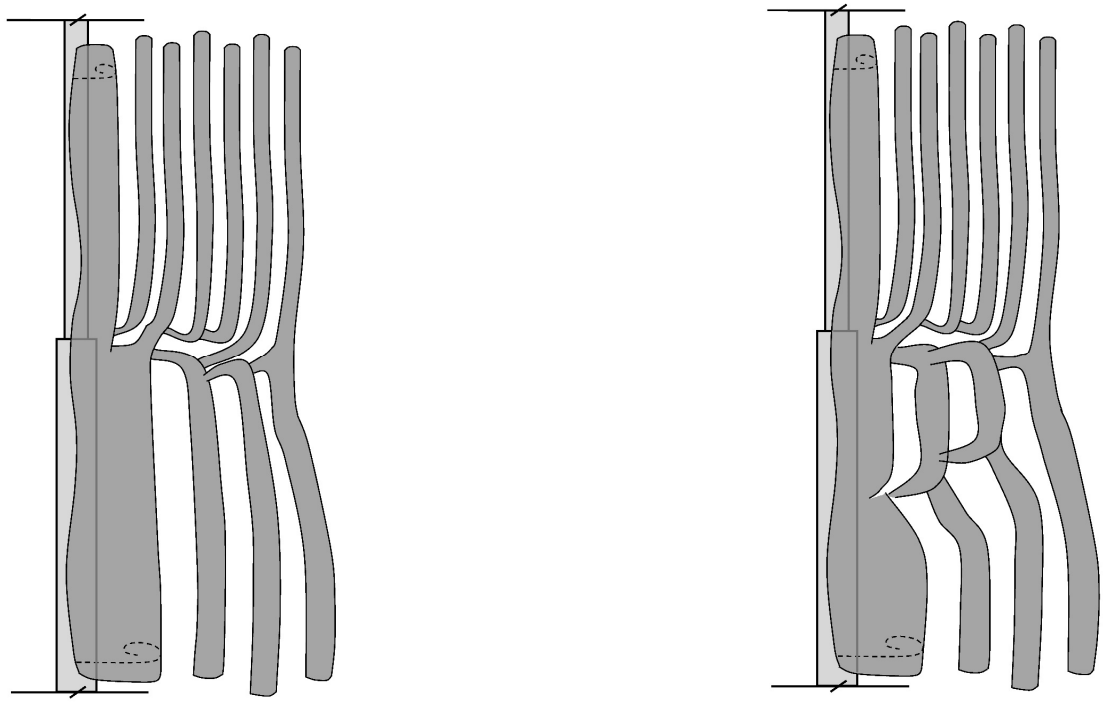

(a) direct mode (b) indirect mode

Figure 2.4 Vortex shedding from a single step cylinder: (a) direct mode interactions, (b) indirect mode vortex shedding. Adapted from Lewis & Gharib [70], Dunn & Tavoularis [45], and Morton & Yarusevych [19].

observed near the ends of uniform cylinders and cantilevered cylinders [36,40,69]. The vortex dynamics consists of vortex dislocations occurring periodically at the boundaries between the three identified vortex shedding cells, as illustrated in Figure 2.4b.

Several experimental investigations have also been completed on single step cylinders under turbulent vortex shedding conditions [71–76]. The results indicate that depending on D/d, either direct or indirect mode vortex shedding occurs in the wake. Flow visualizations by Morton & Yarusevych [73,77] for $Re_D = 1050$ and D/d = 2, show that the vortex dynamics in the near wake is similar to that observed in laminar flow. In particular, the vortex dislocations occurring between the spanwise vortex cells involve vortex splitting, vortex stretching and tilting, and half-loop vortex connections. The main difference observed between laminar and turbulent flows is the rate at which these vortex interactions

break down in the near wake due to turbulent transition. Additional quantitative results presented in Morton & Yarusevych [73,77] are discussed in Appendix D.

The only known force measurements on single step cylinders are those of total pressure drag reported by Chua et al. [76] at $Re_D = 4720$, and D/d = 2. While the measurements are comparable to the drag expected for uniform circular cylinders, the aspect ratio of the single step cylinder model is less than 10D, suggesting that end effects significantly influence the flow development and measured structural loading.

2.2.4 Dual Step Cylinders

A dual step cylinder is comprised of uniform cylinder of a diameter (d) with a larger diameter cylinder mounted at its mid-span (Figure 1.1). Apart from the experimental and numerical work completed as part of this thesis, to the best of the author's knowledge, there are two previous experimental studies focused on dual step cylinder flow development [16,77].

Williamson [16] investigated wake development of a dual step cylinder for $Re_d \leq 200$, D/d = 1.1 - 2.0, and L/d = 0.5. The aim of his work was to force vortex dislocations through the attachment of a larger diameter cylinder with low aspect ratio to the mid-span of a uniform circular cylinder. His results showed that periodic vortex dislocations form on both sides of the large diameter cylinder, and the frequency of dislocations is related to the difference in vortex shedding frequency in the wake of the small and large cylinders [16]. In the case where the small cylinder vortex shedding frequencies on both sides of the large cylinder match, vortex dislocations on both sides of the large cylinder occur simultaneously and at the same frequency. However, if a small difference in shedding frequency exists, the dislocations no longer occur at the same frequency, and hence, do not occur in phase [16]. Williamson [16] investigated the influence of D/d and Re_d on the topology and frequency of vortex dislocations. The results indicate that the frequency of dislocations decreases with decreasing D/d. Williamson [16] proposed a model describing vortex interactions involved in a vortex dislocation based on the difference in circulation of vortices in the large and small cylinder wakes and the difference in the vortex shedding frequencies. In this model, vortex interactions involved in a vortex

dislocation include vortex stretching, deformation, and vortex splitting, but do not include looped connections between consecutive vortices like those shown in Figure 2.2 for the wake of a circular cylinder near its wall boundary.

Morton & Yarusevych [77] investigated the effect of L/D on vortex shedding past a dual step cylinder for $Re_D = 1050$, D/d = 2, and $0.2 \leq L/D \leq 17$. The focus of the work was on identifying how the large cylinder flow development changes with L/D. Four distinct flow regimes were identified. (i) For $L/D \geq 15$, three vortex shedding cells form downstream of the large diameter cylinder. The vortex dislocations occurring between adjacent cells were similar to those observed in the wake of a single step cylinder by Dunn & Tavoularis [45]. (ii) For $8 \leq L/D \leq 14$, a single vortex shedding cell forms in the large cylinder wake, and the frequency of the cell decreases with decreasing L/D. The mechanism for transitioning between three cells and one cell is linked to the merging of low frequency vortex shedding cells forming near the ends of the large cylinder [77], similar to that observed in uniform and cantilevered cylinder flows [42,78]. (iii) For $2 \leq L/D \leq 6$, vortex shedding from the large cylinder is highly three-dimensional, with large cylinder vortices deforming as they are shed into the wake. There is also a substantial reduction in the coherence and strength of the large cylinder vortices in this L/D range. (iv) For $0.2 \leq L/D \leq 1$, similar to the findings of Williamson [16] vortex dislocations occur periodically between small cylinder vortices. Morton & Yarusevych [77] found no evidence of periodic vortex shedding occurring from the large diameter cylinder, and speculate that vortices visible in the large cylinder wake are in fact small cylinder vortex filaments connecting across the wake of the large cylinder. The vortex dynamics involved in vortex dislocations were found to involve half-loop vortex connections, which were not observed by Williamson [16].

2.2.5 Multi-step cylinders

Nakamura & Igarashi [17] investigated the aerodynamic forces acting on multi-step cylinders. The Reynolds numbers investigated were in the range of 3000 to 38000, and the geometric parameters of the multi-step arrangement (aspect ratio, L/d; diameter ratio, D/d; large cylinder spacing, H/d) were varied in order to identify trends in structural loading characteristics. For an optimal set of geometric parameters, $D/d \approx 1.3$, $L/d \approx 1.0$, and $H/d \approx 5.0$, the drag force is 15% lower than that expected for a

uniform cylinder of diameter d. Drag reduction is attributed to changes in the flow separation characteristics, which are linked to changes in surface pressure variation measured on each of the models [17]. It should be noted that the degree of drag reduction was also dependent on the Reynolds number [17].

The multi-step cylinder is an extension of the dual step cylinder geometry. While there have been no comprehensive investigations on multi-step cylinder wake development, it can be speculated that for adequately large spacing (H/d) between the large diameter cylinders, the flow regimes identified by Morton & Yarusevych [77] would also exist for a multi-step cylinder arrangement.

2.3 Investigating wake topology in highly three-dimensional flows

The flow development and vortex shedding from complex cylindrical geometries is highly three-dimensional [18,19]. To investigate the three-dimensional wake characteristics, quantitative measurements of the three-dimensional flow field can be carried out using tomographic Particle Image Velocimetry (PIV), three-dimensional Particle Tracking Velocimetry (PTV), multi-plane scanning PIV, and holography [21]. Holography and tomographic PIV measurement techniques are largely restricted by the physical size of the measurement volume which can be adequately illuminated and imaged. This depends largely on the quality of the laser and imaging systems being employed [21]. Particle Tracking Velocimetry has significant spatial resolution limits since a sparse particle distribution is required for adequate Lagrangian particle tracking algorithms. Finally, multi-plane scanning PIV has substantial temporal and spatial resolution limits due to the discrete time interval between consecutive planar images. As such, all three-dimensional flow measurement tools are still under development, and are not yet common research tools in experimental facilities world-wide.

One of the primary objectives of the present thesis, is to explore methods of using two-dimensional PIV measurements to uncover information about three-dimensional flow characteristics in the wakes of complex cylindrical bodies. Over the last few decades, several techniques of planar PIV data analysis have proved useful for studying vortical structures. The techniques include: phase-averaging of dominant periodic structures [22,23], vortical structure identification through Proper

Orthogonal Decomposition (POD) [24–26], pattern recognition methods [27–29], and combinations of these techniques. Such techniques have successfully been applied to planar PIV measurements [22,23,26] and extended into three dimensions through analysis of planar PIV measurements acquired in multiple planes which are closely spaced [79–81]. In this thesis, the above listed data analysis techniques are used to conditionally average PIV measurements and reconstruct the dominant three-dimensional vortical structures and their interactions in the wake of a dual step cylinder.

In periodic flows, phase-averaging of PIV measurements is performed using a fixed reference signal measuring the phase variation of the periodic phenomena of interest [22,23,25,26,79,82]. Reference signals commonly used in previous studies include surface pressure signals [22], wake velocity signals [23], actuator signals [79], and the temporal coefficients of the Proper Orthogonal Decomposition (POD) of the velocity field [26]. While phase-averaging has proven to be particularly useful in vortex dominated flows, the quality of the results in highly three-dimensional, turbulent flows is limited by three factors: (i) Bluff body wakes have a limited spanwise correlation length [33], and hence, there is a practical limitation of the ability of a fixed reference signal to adequately predict the presence and phase of coherent structures which are shed at spanwise distances greater than the spanwise correlation length. In other words, there are temporal variations in the spatial arrangement of the coherent structures, which a single reference signal is not capable of resolving. (ii) The periodic structures detected in the flow field may not adequately represent the instantaneous wake topology. In weakly periodic flows (e.g., [20]), conditional averaging may be less advantageous in uncovering features of the wake vortex dynamics since the coherent component of interest in the flow does not contribute significantly to the overall energy content of the flow. (iii) Bluff body wakes often contain coherent structures shed at different frequencies, i.e., in the vast number of bluff body flows containing distinct vortex shedding cells (e.g., [16,36]). In this case, a single reference signal is only capable of detecting the phase variation of coherent structures shed at one frequency, and cannot reconstruct the interactions of adjacent vortex cells.

An alternative to phase-averaging is the use of pattern recognition for conditional averaging. In comparison with the numerous investigations employing phase-averaging, there are far fewer

investigations on pattern recognition based conditional averaging techniques. The use of pattern recognition analysis (PRA) for the detection, identification, and classification of organized structures in turbulent wake flows was first described in detail by Ferre and Giralt [29]. Experimental studies have shown that pattern recognition using the correlation of planar velocity or vorticity fields can be used to identify coherent structures in the wakes of blunt bodies, e.g., a circular cylinder and a backward facing step [27,29,83]. In addition, PRA has been used recently for the detection of coherent structures in tomographic PIV measurements [84], and for the tracking of hairpin vortices in turbulent boundary layers [85]. One of the main challenges in the implementation of a PRA is the selection of a template velocity or vorticity field from which all other fields are correlated [27]. The aim is to use a template field which is representative of a coherent structure in the flow. In previous investigations the template field(s) used for PRA include: mathematical models of the coherent structure [29], a conditional average of instantaneous fields [27], or a spatial eigenfunction obtained from the POD [29]. In all cases, a priori knowledge or direct measurement of the flow properties is required to construct the template. Once all flow fields matching with the template are identified, they are averaged. The result is a conditionally averaged flow field that is representative in some way to the selected template used for the analysis.

The success of PRA for the detection and tracking of coherent structures in planar and three-dimensional PIV measurements in turbulent wakes (e.g., [27–29,84,86]), suggests that it can also be applied to multi-plane PIV processing. In the present study, PIV measurements in multiple closely spaced planes are processed using PRA in order to reconstruct the three-dimensional coherent structures in a dual step cylinder wake.

Chapter 3

Methods of Investigation

An experimental study of the three-dimensional wake development and structural loading on dual step cylinders was completed in two facilities: the University of Waterloo Water Flume Facility, and the open-loop, low speed wind tunnel facility (W-Tunnel) at TU Delft. Numerical modeling was carried out using the commercial code, ANSYS CFX 13.0.

3.1 Experiments in the Water Flume Facility

The test section of the water flume is 2.4m long, with a cross section of 1.2m x 1.2m. The walls of the test section are constructed of glass, allowing for optical access. The water level in the channel was maintained at 0.8m for all experiments. Models were placed vertically within a low turbulence, uniform flow region, between a water depth of 0.2m and 0.6m (Figure 3.1). The mean turbulence intensity in this region is less than 1% and the flow uniformity is within 3% [19], and primarily caused by a gradual decrease in free stream speed with water depth. Models were mounted between circular Lexan endplates, designed following the recommendations in Refs. [39,42] (Figure 3.1). In particular, the endplates were 200mm in diameter, 3mm thick, and contained 60° chamfered edges. The models were mounted offset from the flume centerline to increase optical access for the various laser-based measurement systems employed. The vertical alignment of the cylinder models and horizontal alignment of the endplates was achieved using a digital level with an accuracy of 0.1°. As shown in Figure 3.1, the origin (x,y,z) is positioned along the model axis at its mid-span.

The uniform cylinder and dual step cylinder model configurations investigated as part of the work in the water flume facility are summarized in Tables 3.1-3.3. A summary of the specific experimental measurements obtained for each of the models is indicated in each table. The uniform and dual step cylinder models were constructed of stainless steel and aluminum. For the dual step cylinders, a solid small diameter cylinder (d) is 40cm in length and made of stainless steel. Larger diameter cylinders

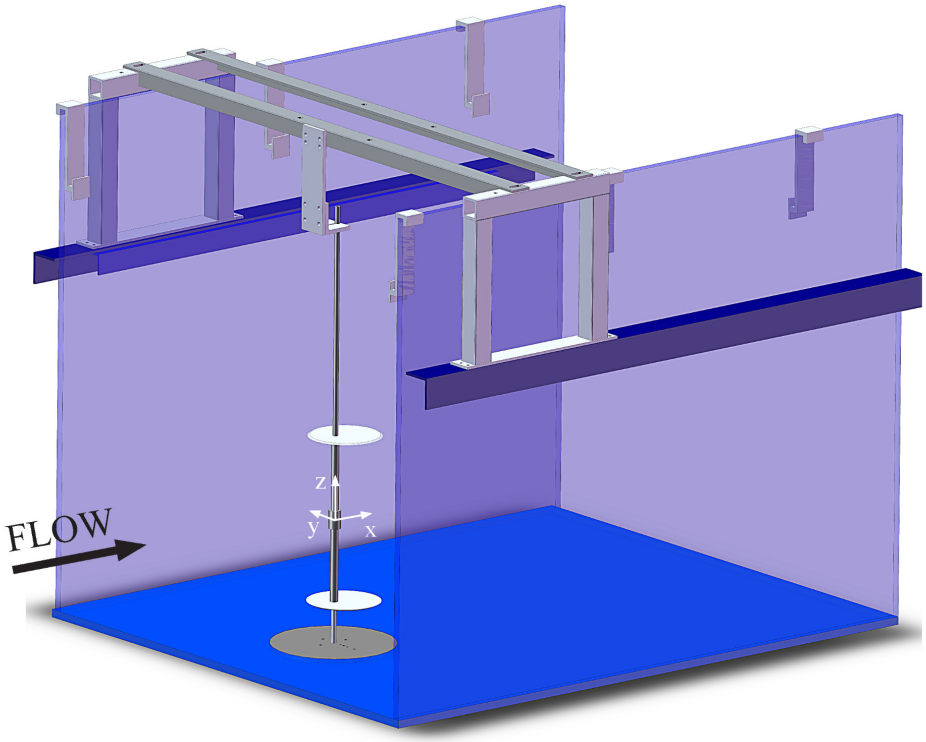

Figure 3.1 Water flume facility test section and model mounting arrangement.

(D) are made of aluminum with holes bored through the center, enabling a sliding fit on the smaller cylinder. The large diameter cylinders are placed in a fixed position at the mid-span of the smaller diameter cylinder, creating the dual step cylinder configuration shown in Figure 1.2. All of the models were sanded with 1600 grit sand paper and finished with aluminum polish. Some models are painted

Table 3.1 Uniform cylinder model configurations and associated experimental measurements completed. ✓[1] – horizontal (x-y) planar PIV data, ✓[2] – vertical (x-z) planar PIV data.

Uniform Cylinders			Experimental Techniques			
Re_D	D (mm)	L/D	LDV	2D-PIV	Forces	Flow Visualization
500	6.35	66	✓		✓	✓
750	9.53	44	✓		✓	
1000	12.70	33	✓	✓[1]	✓	✓
1250	15.88	26	✓		✓	
1500	19.05	21	✓		✓	
2000	25.40	16	✓	✓[1]	✓	✓

Table 3.2 Dual step cylinder model configurations and associated experimental measurements completed at Re_D = 2100. The diameter of the large cylinder was fixed at D = 25.4mm. ✓[1] – horizontal (x-y) planar PIV data, ✓[2] – vertical (x-z) planar PIV data, ✓[3] – simultaneous vertical and horizontal planar PIV data.

Dual Step Cylinders at Re_D = 2100		Experimental Techniques			
L/D	D/d	LDV	2D-PIV	Forces	Flow Visualization
0.2	2.00	✓	✓[1,2]	✓	✓
0.5	1.33	✓			
0.5	1.60	✓		✓	
0.5	2.00	✓	✓[1,2]	✓	✓
0.5	2.67	✓	✓[1]	✓	✓
0.5	4.00	✓	✓[1]	✓	
1	1.33	✓			
1	1.60	✓	✓[1]	✓	✓
1	2.00	✓	✓[1,2,3]	✓	✓
1	2.67	✓	✓[1]	✓	✓
1	4.00	✓	✓[1]	✓	
2	1.33	✓			
2	1.60	✓	✓[1]	✓	✓
2	2.00	✓	✓[1,2]	✓	✓
2	2.67	✓	✓[1]	✓	✓
2	4.00	✓	✓[1]	✓	
3	1.33	✓	✓[1,2]		✓
3	1.60	✓	✓[1]	✓	
3	2.00	✓	✓[1,2]	✓	✓
3	2.67	✓		✓	✓
3	4.00	✓	✓[1]	✓	
5	1.33	✓	✓[1]		
5	1.60	✓	✓[1]	✓	
5	2.00	✓	✓[1]	✓	
5	2.67	✓	✓[1]	✓	
5	4.00	✓	✓[1]	✓	

black in order to minimize reflections of laser light. The thin layer of paint alters the diameter of the cylinder by no more than 0.05mm.

3.1.1 Flow and surface visualization

Flow visualization was carried out using a hydrogen bubble technique. Background on the principles of the hydrogen bubble technique, as well as details of its use in the present study are provided in Appendix A. In the present study, hydrogen bubbles were generated on a thin, 0.085mm diameter stainless steel wire via electrolysis by applying a DC voltage of about ten to twenty volts. The cylindrical aluminum rod acting as the upper support for the models (Figure 3.1) served as the anode in the hydrogen bubble circuit. The models were insulated from the circuit through plastic threaded-rod connections. While producing adequate flow visualization, the generated bubbles had a sufficiently small rising velocity (less than 5% of free stream velocity) to ensure insignificant displacement due to buoyancy within the wake region of interest. The hydrogen bubble wire, shown in Figure 3.2 with a dashed black line, was positioned less than 0.7D upstream of the model and offset slightly from the model axis to visualize vortices on one side of the wake for both the uniform and dual-step cylinder models. The Reynolds number based on the wire diameter was less than ten. This minimizes adverse effects of the wire on the flow development around the model since no shedding of vortices occurs

Table 3.3 Dual step cylinder model configurations and associated experimental measurements completed at $Re_D = 1050$. The diameter of the large cylinder was fixed at D = 12.7 mm.

Dual Step Cylinders at Re_D = 1050		Experimental Techniques			
L/D	D/d	LDV	2D-PIV	Forces	Flow Visualization
0.2	2	✓			✓
0.5	2	✓			✓
1	2	✓			✓
2	2	✓			✓
3	2	✓			✓
5	2	✓			✓
6	2	✓			✓
7	2	✓			✓
8	2	✓			✓
10	2	✓			✓
13	2	✓			✓
14	2	✓			✓
17	2	✓			✓

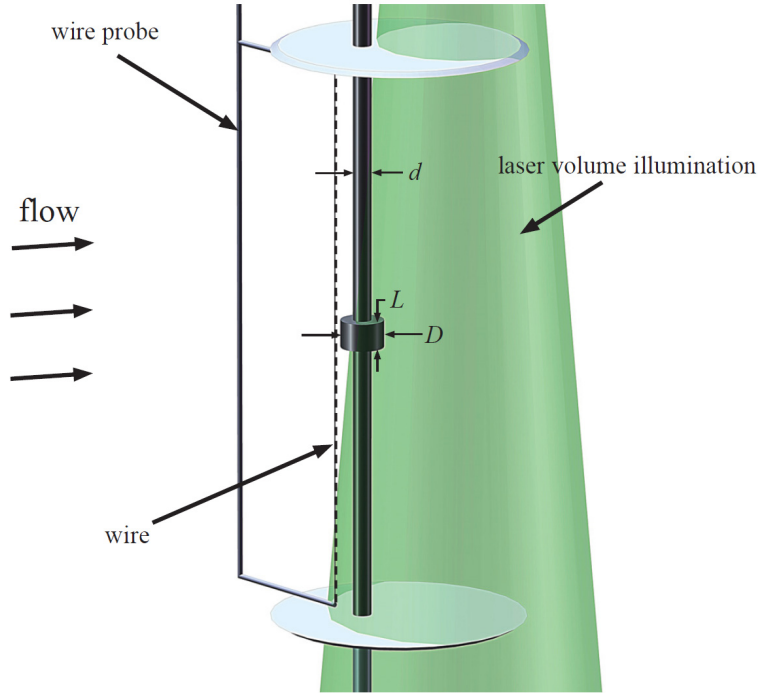

Figure 3.2 Experimental arrangement for hydrogen bubble flow visualization

from the wire. In addition, to minimize flow disturbances due to wire supports, the wire was mounted on a rigid probe that extended upstream of the cylinder model at an angle of approximately forty-five degrees (Figure 3.2).

To enable three-dimensional visualizations of the wake, a laser volume illumination of the hydrogen bubbles was achieved using a two-watt continuous wave Spectra-Physics laser. The laser source passed through two consecutive cylindrical lenses in order to generate the conical illumination volume depicted in Figure 3.2. The images were recorded using a 1024x1024 pixels Photron SA4 camera, equipped with a 50mm focal length Nikon lens, operating at 100 Hz, which is more than twenty-five times the highest frequency of interest for the models investigated.

Surface visualization with hydrogen bubble technique

A new technique of surface visualization has been developed using the hydrogen bubble technique setup shown in Figure 3.2. Validation of the techniques use on uniform and dual step cylinders can be found in Appendix A, with a brief description of the methodology provided in this section.

The new technique relies on the electrochemical reactions present during the process of electrolysis. Specifically, insoluble deposits of hydroxides and salts form on anode and cathode surfaces while voltage is being applied. These deposits remain fixed to the cathode wire [87] (Figure 3.2), but can be released from the wire by operating the hydrogen bubble system on a 50% duty cycle. Once the deposits are released from the wire, they impact on the surface of the model, and leave a white residue which acts as the surface visualization agent (see Appendix A for more details). Surface visualizations were performed on a limited set of uniform cylinder and dual step cylinder models for $Re_D = 1050$ & 2100, $D/d = 2$, and $0.2 \leq L/D \leq 3$. Preliminary investigations on different cylinder model materials (Appendix A) revealed that surface deposits accumulate more quickly on aluminum models [88]. As a result, for each model investigated, the large cylinder was constructed of aluminum. The base cylinder (of diameter d) was constructed of stainless steel as surface visualizations on the base cylinder were not the main focus.

3.1.2 Velocity measurements with LDV

Laser Doppler Velocimetry (LDV) is a single point velocity measurement technique that requires the illumination of tracer particles within a small measurement volume of fluid created by the intersection between two or more coherent, polarized laser beams [89]. Measurement of the frequency of the reflected light relative to the emitted light, referred to as the Doppler frequency, is linked to the tracer particle velocity. Further details on the fundamental principles in the operation of this technique can be found in Tavoularis [89]. In the present study, single point velocity measurements were carried out using a two-component Dantec LDV system and a single-component Measurement Science Equipment (MSE) miniLDV system. The Dantec system is comprised of a 5W Argon-Ion laser that is split into two green beams at 514.5 nm and two blue beams at 488nm. One of the beams in each pair is frequency shifted in order to resolve flow direction in the measurement volume. The Dantec system also contains a specialized beam expander which increases the focal length of the beams to beyond 600mm, enabling measurements across the half-width of the water flume test section. This optical configuration results in a maximum measurement volume size of approximately ($\Delta x/D$, $\Delta y/D$, $\Delta z/D$) = (0.006, 0.05, 0.006). The MSE system, on the other hand, is comprised of a 140mW diode

laser at 658nm wavelength that is split into two equal intensity red beams. The beam conditioning optics has a fixed focal length of 400mm in air, which is increased to approximately 530mm for measurement in water. The maximum measurement volume size is estimated to be ($\Delta x/D$, $\Delta y/D$, $\Delta z/D$) = (0.003, 0.02, 0.003). The flow is seeded with hollow glass particles by with a mean diameter of 10 μm. These particles are approximately neutrally buoyant (SG $\approx$ 1.05) with the water and also have optical properties which improve the performance of laser-based measurements. The uncertainty in the free stream velocity measurement with LDV was estimated to be less than 0.5% and is primarily attributed to minor changes in the facility conditions with time. The uncertainty in wake velocity measurements are estimated to be less than 4% and is attributed primarily to velocity bias errors (Appendix I). The mean data acquisition rate was greater than 50 Hz for all LDV measurements. Velocity data were re-sampled at 25Hz using a sample-and-hold technique [90] in order to facilitate spectral analysis of velocity fluctuations. For spectral analysis, the re-sampled data were divided into 48 non-overlapping segments of 1024 velocity points, which were then averaged. The corresponding frequency resolution for velocity spectra is approximately $\pm$ 0.003 fD/U_∞. For spectrogram analysis, re-sampled data were divided into segments of 128 velocity points, resulting in a frequency resolution of about $\pm$ 0.03 fD/U_∞.

3.1.3 Two-dimensional PIV Measurements

Two-dimensional Particle Image Velocimetry (PIV) is a technique used to estimate two components of velocity in a given measurement plane. The technique is carried out by first illuminating and imaging tracer particles in a two-dimensional field using a pulsed laser sheet. Velocity components within the two-dimensional field are estimated through image processing algorithms employing cross-correlation to determine the displacements of particles between pairs of particle images which are closely spaced in time. The reader is referred to the works of Willert & Gharib [91], Westerweel [92], Scarano & Riethmuller [93], and Raffel et al. [94] for details on the operating principles, as well as general recommendations for performing 2D PIV measurements. Sources of uncertainty in PIV measurements originate from the experimental setup, image acquisition, and image processing [94]. There is no generally accepted method for estimating the overall uncertainty in PIV measurements due

to the large number of error sources in image acquisition and image processing [94]. A brief discussion of the PIV uncertainty estimates are provided in Appendix I. In the free stream, the uncertainty in the measured velocity is less than 1.5%, and in the wake it is less than 5% (Appendix I).

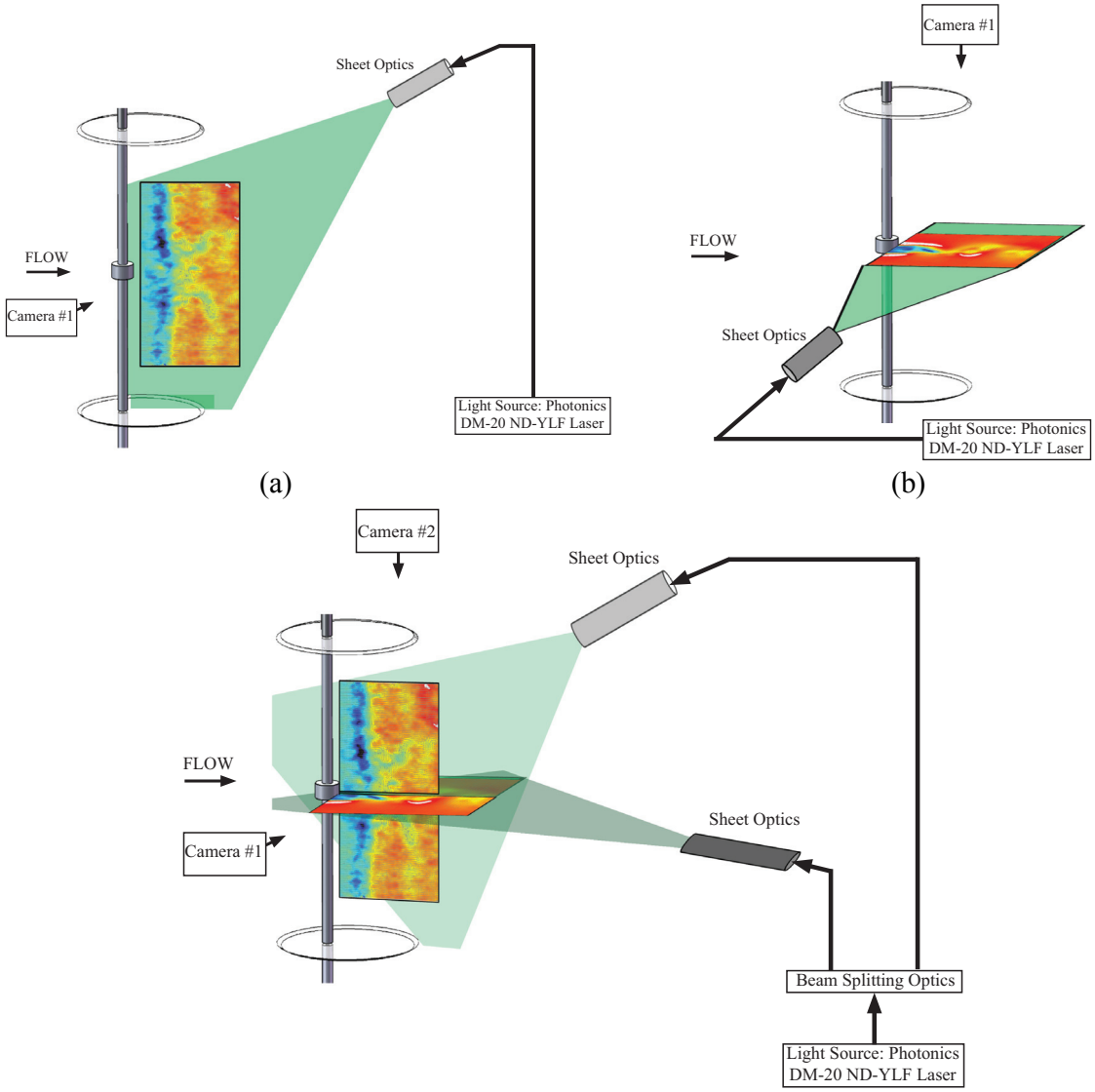

Figure 3.3 Experimental arrangement for PIV measurements: (a) single plane, 2D PIV in a vertical arrangement, (b) single plane, 2D PIV in a horizontal arrangement, (c) dual plane 2D PIV in simultaneous horizontal and vertical planes. Instantaneous velocity fields have been shown in place of the raw particle images for illustrative purposes.

In the present work, a LaVision PIV system was used to measure the velocity field in two-dimensional planes in the near wake of each model. The PIV system consists of a Photonics DM-20 Nd:YLF pulsed laser synchronized with up to two high frame rate Photron SA4 cameras equipped with 50mm focal length Nikon lenses. The same seed particles used with the LDV system were also used for PIV. Three different PIV system setups employed in the present study are illustrated in Figure 3.3. Time-resolved (TR) PIV measurements were performed on dual step cylinders in vertical planes (Figure 3.3a), horizontal planes (Figure 3.3b), and both planes simultaneously (Figure 3.3c). Uniform cylinder models were tested in the horizontal plane configuration shown in Figure 3.4. Specific details on the locations of the PIV measurements and specific data analysis techniques employed are discussed in the Results.

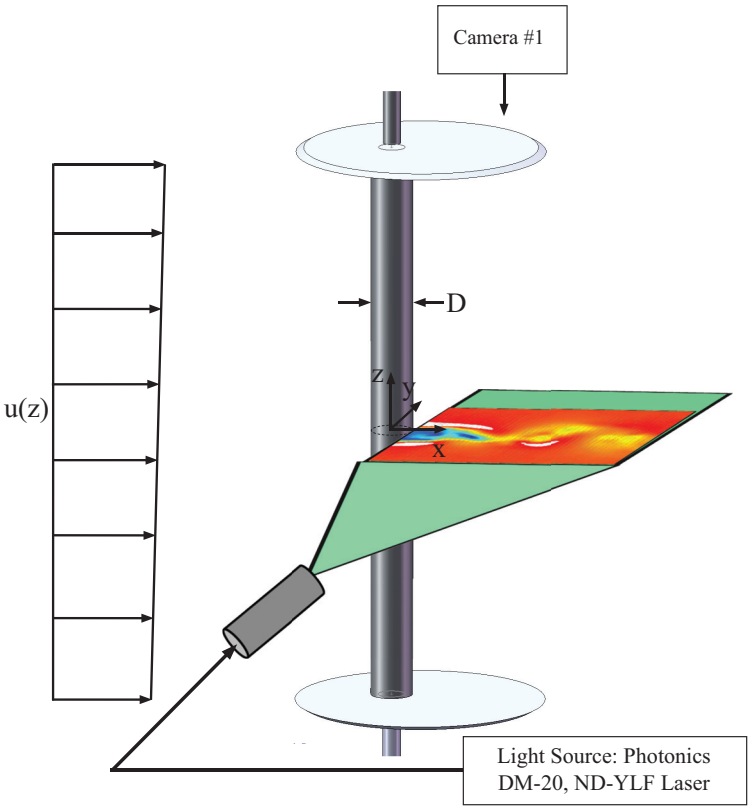

Figure 3.4 Experimental arrangement for PIV measurements in the wake of a uniform circular cylinder. An instantaneous velocity fields is shown in place of a raw particle image for illustrative purposes.

Each PIV data set contained between 5456 and 6400 images acquired at a fixed rate of 100 Hz and processed using LaVision DaVis 8 software. The interrogation window size was selected to maximize the vector resolution while simultaneously ensuring the direction and displacement of particles in each window was nearly constant and the mean number of particles within each window was equal to ten [95]. Using these criteria, cross-correlation was performed using an iterative multi-grid technique (WIDIM, [93]), so that the final interrogation window size was 16x16 pixels. A 75% overlap was applied between adjacent interrogation windows, resulting in a vector spacing of approximately 0.03D for both vertical and horizontal measurement planes. The velocity data were post processed using a universal outlier detection technique [96].

3.1.4 Force Measurements

The drag and lift on uniform and dual step cylinder models were computed using a cantilever-beam strain gauge force balance, as illustrated in Figure 3.5. In both lift and drag directions, four strain gauges were configured to create a Wheatstone bridge circuit. High resistance (350 Ω) precision strain gauges from Vishay Measurement Group were used, all of which contained the same gauge factor of 2.05. Futek CSG110 amplifiers were used to amplify the signal output from the Wheatstone bridge

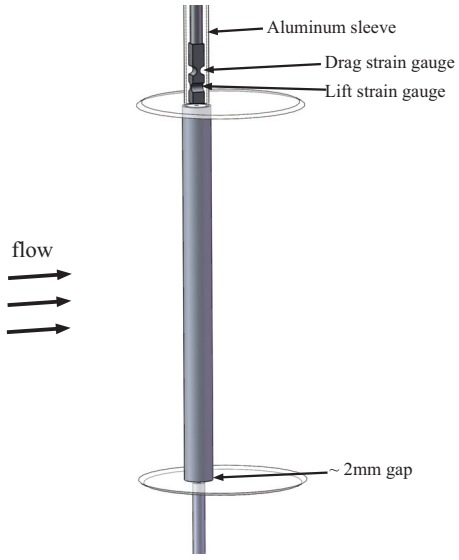

Figure 3.5 Experimental arrangement for force measurements.

and were used with a gain of 0.5 mV/V for a range of 10V. Data were acquired through a National Instruments (NI) model 6320 Data Acquisition System (DAQ). The sensitivity of the DAQ is ±0.67mV. A complete description of the setup, calibration, and validation of force data acquired on uniform circular cylinders is given in Appendix C. The results provided in Appendix C indicate that error in the mean drag measurements is less than 10%, while error in fluctuating lift measurements is less than 100%.

3.2 Experiments in the W-Tunnel Facility at TU Delft

A series of experiments involving Tomographic Particle Image Velocimetry (Tomo-PIV) measurements in the wakes of dual step cylinders were performed in a low-speed open jet wind tunnel (W-Tunnel) at TU Delft. The wind tunnel has a test section of 0.4 m x 0.4 m located at the exit of the tunnel. The free stream velocity can be varied between about 4 m/s and 20 m/s while maintaining a free stream turbulence intensity of less than 0.5 %. Dual step cylinder models with D = 8mm were investigated for L/D = 0.5, 1, 2, and 5, D/d = 1.33, 1.6, and 2.0, and Re_D = 2000, 3500, and 5000. The models were mounted between rectangular endplates, as shown in Figure 3.6.

Tomographic PIV, described in detail by Scarano [97] and Elsinga et al. [98], was employed for investigating the three-dimensional wake development. A schematic of the experimental setup arrangement is shown in Figure 3.6a. The flow was seeded with a smoke generator at the inlet of the wind tunnel, introducing smoke particles of approximately 1μm in diameter. The particle image density was maintained between 0.04 and 0.05 particles per pixel (ppp). A measurement volume (Δx, Δy, Δz) of approximately 38x11x55 mm^3, corresponding to 4.8D x 1.4D x 6.8D, was illuminated using a Spectra-Physics PIV-400 Nd:Yag laser with an output of 400mJ per pulse and a repetition rate of 5Hz. One spherical lens and two cylindrical lenses followed by knife edge filters were utilized to condition the laser beam. A mirror was installed in the top endplate to enhance the light intensity inside the measurement volume (Figure 3.6). Six LaVision Imager LX CCD cameras (1628 x 1236 pixels) were placed in an arc-like configuration. The cameras were equipped with 75mm focal length lenses and Scheimpflug adapters. A numerical aperture of $f_\# = 11.2$ was employed, resulting in a focal depth of greater than 12mm for all the cameras. Laser illumination and image recordings were controlled

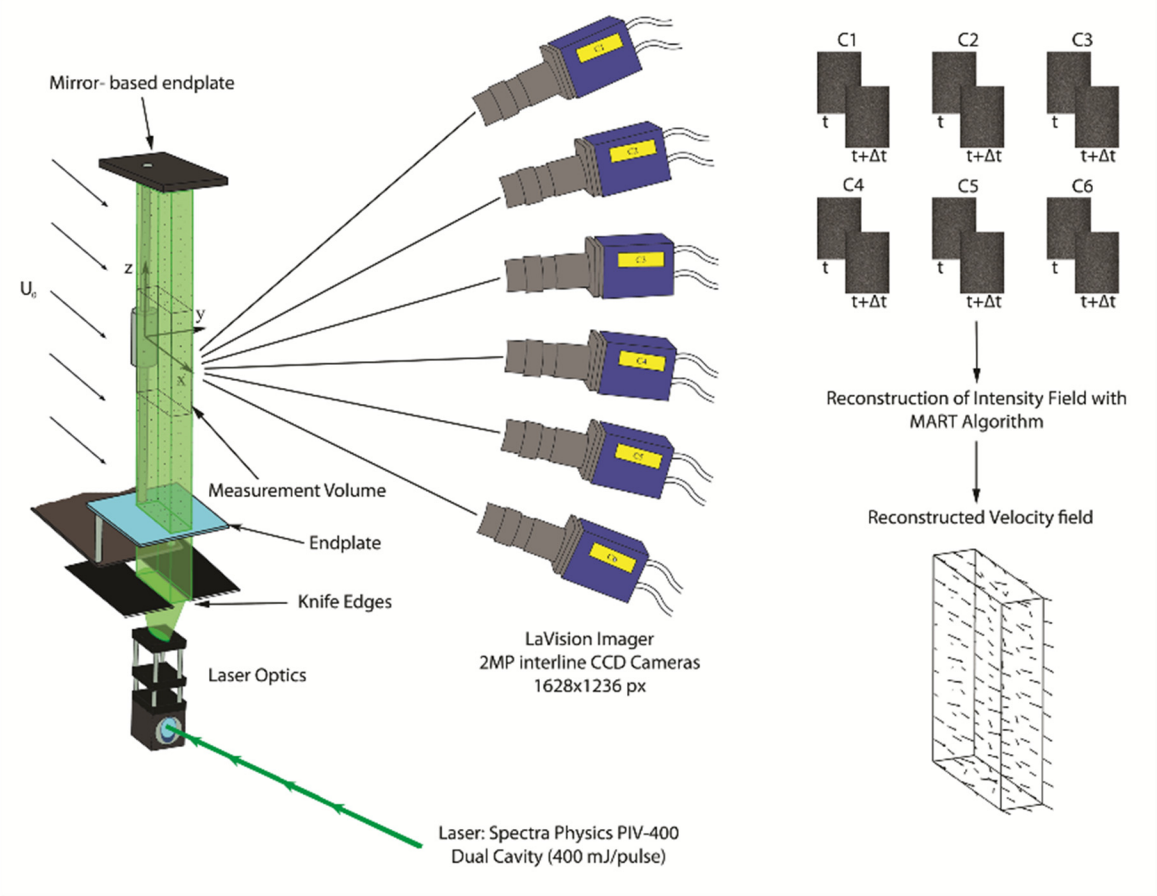

(a) (b)

Figure 3.6 Experimental arrangement and data processing methodology for Tomographic PIV measurements.

using a LaVision programmable timing unit and DaVis 8.3 software. For each set of experimental conditions, 500 double-frame recordings were acquired at 5 Hz, sufficient for obtaining converged flow statistics. A calibration of the system was performed using a calibration target, which was sequentially placed at three x-z planes within the measurement volume. The generated 3D mapping function was then improved using self-calibration [99], which reduced calibration errors below 0.1 pixels.

Figure 3.6b depicts the steps performed to obtain a single three-dimensional velocity field. First, a Multiplicative Algebraic Reconstruction Technique (MART) [100] was applied iteratively to the particle images to generate a 3D light intensity map in discretized physical space (Figure 3.6b). The

signal to noise ratio (SNR) was verified to be greater than two, similar to that in Scarano & Poelma [101]. Cross-correlation analysis was performed using a Volume Deformation Iterative Multigrid (VODIM) technique, which is an extension of the WIDIM technique [93] into three-dimensions. The final interrogation volume size was 48x48x48 voxels, where one voxel is equivalent to a single pixel in three dimensions. A 75% overlap was applied between adjacent interrogation volumes, yielding a velocity grid containing approximately 80x24x106 points with a vector pitch of about 0.06D. The reconstructed velocity data were post processed using a universal outlier detection technique [96].

3.3 Framework for Data Analysis

This section provides the mathematical background for all advanced data analysis methods employed in the present study. First, the Reynolds decomposition and extensions of this decomposition are introduced. Following this, general data analysis techniques are discussed, including Fourier decomposition, signal filtering, and Proper Orthogonal Decomposition (POD). POD is introduced for the identification of coherent structures in turbulent flows, as postulated by Lumley [102]. The chapter ends with a mathematical implementation of pattern recognition analysis using cross-correlation.

3.3.1 Problem Formulation

It is of interest to develop a statistical representation of periodic wake flows which extend on the traditional Reynolds decomposition. Given a bluff body wake velocity field, $\vec{v}(x,y,t)$, which is composed of strongly periodic coherent structures as well as underlying random turbulence, a triple decomposition of the flow field is written as follows [83,103,104]:

$$\vec{v}(x,y,t) = \vec{V}(x,y) + \vec{v}'(x,y,t) + \vec{v}''(x,y,t) \tag{3.1}$$

where $\vec{V}(x,y)$ is the mean flow field, $\vec{v}'(x,y,t)$ is the contribution due to coherent structures, and $\vec{v}''(x,y,t)$ contains random turbulent fluctuations. In many bluff body flows which are strongly periodic, a narrow frequency band can be used to define the energy associated with the dominant coherent structures. In this case, it is possible to perform a triple decomposition on the flow field as long as a reliable reference signal pertaining to the coherent contribution can be extracted from the flow field data. Results are conditionally averaged based on the phase of the obtained reference signal, $\theta(t)$. Over a large sample, the random turbulent fluctuations average to zero, resulting in the phase-averaged representation of the flow, $[\vec{v}(x,y,t)]_{phase\ averaged} = \vec{v}_\theta(x,y,\theta(t))$. The accuracy of phase-averaged flow field results depends on the ability of the reference signal to record the presence of coherent structures in the flow. As shown in Eq. 3.2, the reference signal is periodic and centered on a single frequency whose phase variation is described by $\theta(t)$:

$$\vec{v}_\theta(x,y,\theta(t)) = \vec{V}(x,y) + \vec{v}'(x,y,\theta(t)) \tag{3.2}$$

In more complex wake flows, such as those of a dual step cylinder, the coherent structures are comprised of two or more dominant frequencies. In this case, one approach to conditionally average the flow field is to decompose the coherent motion into its individual frequency components. Results are then conditionally averaged based on the relative phase variation of the dominant frequencies. The result is a conditionally phase-averaged flow field where coherent structures are described by the phase variation of each dominant frequency in the flow:

$$\vec{v}_\theta(x, y, \gamma(t)) = \vec{V}(x, y) + \vec{v}'(x, y, \gamma(t)) \tag{3.3}$$

$$\gamma(t) = f\big(\theta_1(t), \theta_2(t), \dots \theta_n(t)\big) \tag{3.4}$$

Where $\gamma(t)$ is a function of the relative phase variation of each of the dominant frequencies, $\theta_i(t)$.

In the present work (Chapter 4 and 6), the triple decompositions expressed in Equations 3.2 and 3.3 are obtained by conditionally averaging PIV measurements obtained in the wakes of dual step cylinders. To do this, reference signals are extracted directly from velocity measurements in the flow field, which must be post-processed in order to extract the phase-variation of the dominant coherent structures.

It should be noted that previous experimental investigations on bluff body flows have also identified a low frequency oscillatory component which contributes significantly to the overall wake energy content, and is referred to as the base flow [105]. In the interest of reconstructing the time evolution of coherent structures in the flow, there exists a modified triple decomposition which incorporates variations in this base flow [105–107]:

$$\vec{v}(x, y, t) = \vec{V}(x, y) + \vec{v}'(x, y, t) + \vec{v}''(x, y, t) + \vec{v}'''(x, y, t) \tag{3.5}$$

where the base flow variation is described by $\vec{v}'''(x, y, t)$, and can be obtained using a Gaussian filter [105].

Reference signal analysis

An example reference signal is shown in Figure. 3.7a. The signal is periodic, and contains low amplitude noise across a wide frequency band. For the given reference signal, $r(t)$, a Fourier analysis

can be performed to identify the band of frequencies associated with coherent motions of the velocity field. Following this, a Fourier decomposition is completed in order to reconstruct the components of the reference signal pertaining to coherent motion.

$$r_f(t) = \sum_{n=k}^{l} [a_n \cos(n2\pi f_n t) + b_n \sin(n2\pi f_n t)] \tag{3.6}$$

where $r_f(t)$ is the filtered reference signal (Figure. 3.7b), and k and l define the upper and lower frequency bounds pertaining to the coherent motion. This type of signal filtering has been successfully applied to wake velocity signals [23] and surface pressure measurements [49] in order to phase-average two-dimensional velocity field data. In order to extract phase information from the filtered reference signal, $r_f(t)$, the Hilbert transform is used:

$$DHT\{r_f(k)\} = g(k) = \begin{cases} \frac{2}{N} \sum_{k=0,2,4,\ldots} r_f(k) coth[(k-i)\pi/N]; \\ \frac{2}{N} \sum_{k=1,3,5,\ldots} r_f(k) coth[(k-i)\pi/N]; \end{cases} \tag{3.7}$$

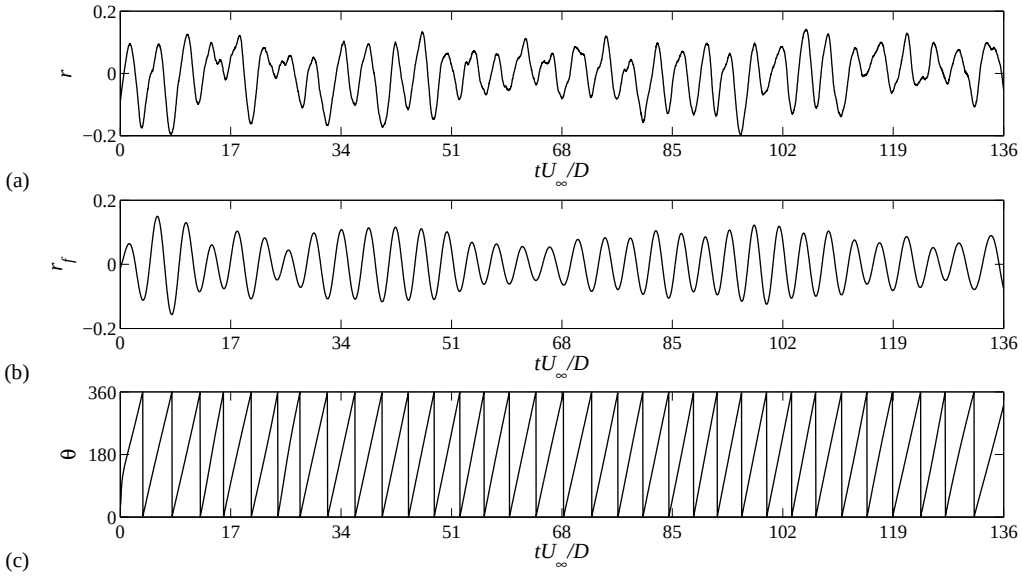

Figure. 3.7 Signal filtering and phase extraction from a reference signal. (a) raw reference signal, (b) filtered signal, (c) reference signal phase angle computed from the Hilbert transform.

By comparing the original signal, $r_f(k)$, with the Hilbert transform, $g(k)$, the phase variation of the signal at any instant in time can be obtained (Figure. 3.7c).

Loss of coherence in reference signals

In some cases, a reference signal may contain instances when amplitude and/or periodicity of the signal is reduced. An example of this is shown in Figure 3.8a, where the amplitude of a filtered reference signal is reduced substantially for tU_∞/D = 102-119, and the corresponding phase signal contains significant irregularities. These instances in wake measurements are attributed to transient phenomena in wake development, and should be discarded from any phase-averaging analysis since it is not possible to reliably determine the phase of the coherent structures. As a means of detecting such irregularities, a spectrogram analysis is proposed. A spectrogram involves performing a short time Fourier transform of discrete segments of reference signal data in order to establish the following: (i) how the amplitude of a given frequency component varies with time, and (ii) how the frequency of the coherent part of the flow varies with time. A spectrogram of the data presented in Figure 3.8a is shown

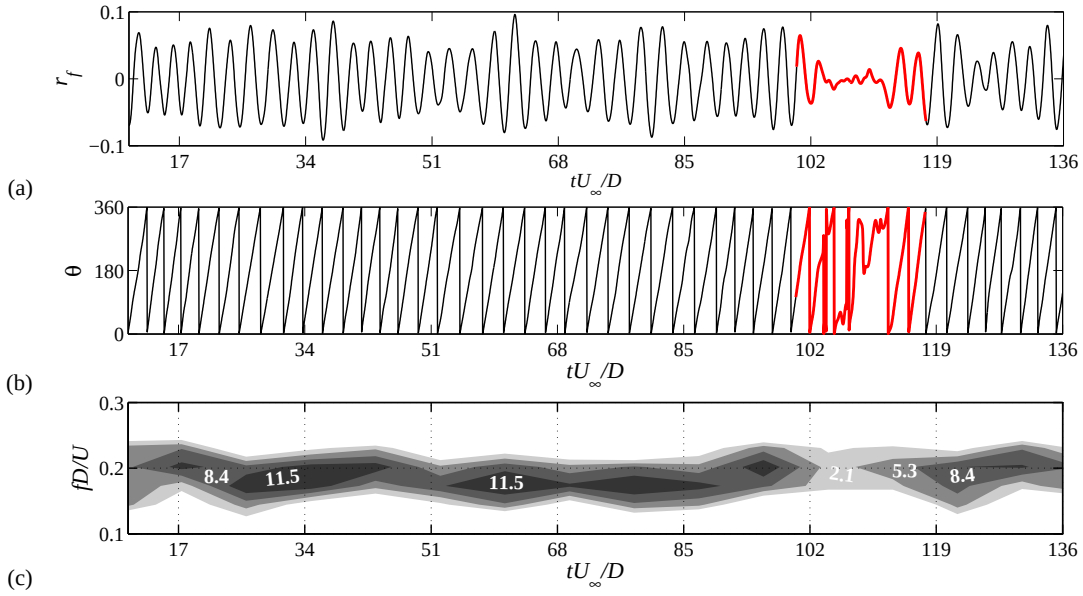

Figure 3.8 Analysis of a filtered reference signal containing irregularities. (a) filtered signal, r_f, (b) vortex shedding phase angle, and (c) spectrogram plot of r_f signal. Transient segments of the signals in (a) and (b) are highlighted in red.

in Figure 3.8c. The window used for each Fourier transform in the spectrogram contains data capturing approximately five periodic cycles of the coherent part of the reference signal, resulting in adequate spatial and temporal resolution. Data are excluded from the analysis if the following two criteria are satisfied: (i) the frequency of the dominant energy content differs from the average by more than the frequency resolution of the spectrogram, or (ii) the dominant energy content is less than 10% of the dominant energy content of the average spectrum of the entire signal. The result of post-processing is illustrated in Figure 3.8, where data corresponding to the segment of the reference signal highlighted in red is discarded from the analysis.

Partitioning phase signals into discrete bins

A given phase reference signal can be partitioned into a finite number of phase angle bins, with each bin defined by a bin width in degrees. In the present study, phase reference signals are used to phase-average PIV data as follows. Given a discrete data set containing thousands of 2D PIV fields, each PIV image is allocated to a bin based on its corresponding phase angle. Choosing an appropriate size for the bin is a compromise between averaging statistics and phase resolution. For the present work, most data sets to be phase-averaged contain m = 5456 PIV images. Assuming an even distribution of data points across all phase angles, a bin size of $\Delta\theta$ produces $N = 2\pi/\Delta\theta$ bins, with each bin containing approximately $n = m\Delta\theta/2\pi$ velocity fields to be averaged. Since the statistical error present in the phase average scales with the inverse root of n, it is desired to maximize n. In addition, to ensure only one velocity field per phase cycle is assigned to a particular bin, i.e., to eliminate averaging bias, the expected periodic oscillation frequency of the reference signal, f, as well as the data acquisition rate, f_{acq}, must be known. In the present study, f is expected to be in the range of 0.9-2.67 Hz, and f_{acq}= 100 Hz. One velocity field per phase cycle can be guaranteed as long as $\Delta\theta \leq 2\pi f/f_{acq}$. For the data analysis completed in this study, $\Delta\theta = 5°$ is used, which corresponds to approximately n = 150 velocity fields assigned to each bin. The selected parameters guarantee between one and two velocity fields per phase cycle depending on the periodic oscillation frequency, which minimizes statistical smearing of the data which are being averaged. In addition, the averaging of n = 150 velocity fields is statistically converged to within 2.5% of the estimated final values [108].

3.3.2 Proper Orthogonal Decomposition

As described in the previous section, phase-averaging is one of the common techniques of conditionally averaging data in order to investigate the development of coherent structures in wake flows. An alternative is the investigation of coherent structures through Proper Orthogonal Decomposition (POD). A short description of the principles of POD is provided in this section, and additional details can be found in a variety of review papers and other texts [24,109,110]. The POD [111] was proposed by Lumley [102,112] to be used as a means of detecting coherent structures in turbulent flows. The POD is an energy-based decomposition of the velocity field [113]. A set of vector fields with zero mean, $\vec{v}'(x,y,t)$, is approximated as a finite sum in which the independent variables are in a separated form as follows:

$$\vec{v}'(x,y,t) = \sum_{i=1}^{N} a_i(t)\overrightarrow{\emptyset_i}(x,y) \tag{3.8}$$

The basis functions, $\vec{\emptyset}_i(x,y)$, are the eigenfunctions of the velocity autocorrelation operator, and the details of its mathematical form can be found in Ma et al. [113]. The obtained eigenfunctions are ordered by their corresponding energy content (eigenvalue), and the temporal coefficients a_i are obtained from the projection of the velocity field $\vec{\boldsymbol{v}}'(x,y,t)$ onto the ith eigenfunction (also called the ith spatial mode). Three important mathematical properties of the POD arise from its formulation: (i) the eigenfunctions remain orthonormal (Eq. 3.9), (ii) the eigenfunction fields are divergence free (Eq. 3.10), and (iii) the variance of the ith temporal coefficient signal is equal to the corresponding eigenvalue (Eq. 3.11).

$$\iint \vec{\emptyset}_{\boldsymbol{i}}(\boldsymbol{x},\boldsymbol{y}) \cdot \vec{\emptyset}_{\boldsymbol{j}}(\boldsymbol{x},\boldsymbol{y})dxdy = \underbrace{\mathbf{1}}_{\boldsymbol{if\ i=j}} \quad \underbrace{\mathbf{0}}_{\boldsymbol{if\ i\neq j}} \tag{3.9}$$

$$div\ \vec{\emptyset}_{\boldsymbol{i}} = 0 \tag{3.10}$$

$$\overline{a_i a_i} = \lambda_i \tag{3.11}$$

In a strongly periodic wake flow, the first pair of spatial modes combined with the mean flow gives a low order approximation of the dominant coherent wake structures [25]. This reduced order model of the velocity field is given by:

$$\vec{V}_{ROM}(x,y,t) = \vec{V}(x,y) + a_1(t)\vec{\emptyset}_1(x,y) + a_2(t)\vec{\emptyset}_2(x,y) \tag{3.12}$$

where $\overline{U}$ is the mean velocity field, a_1 and a_2 are the first two temporal coefficients, and $\emptyset_1$ and $\emptyset_2$ are the first two spatial modes.

It has been shown by previous experimental and numerical studies that the first two temporal coefficients pertaining to a periodic wake flow can be used to identify the phase variation of the coherent structures [25,26,113]. To illustrate this, it is first instructive to consider the wake of a uniform cylinder. Figure 3.9 shows a plot of a_1 versus a_2, where each data point corresponds to a single planar velocity field. Both temporal coefficients exhibit strong periodicity related to vortex shedding, as depicted in Figure 3.10a for a_1. Thus, Figure 3.9 features a locus of data points centered about an ellipse given by:

$$\frac{a_1^2}{2\lambda_1} + \frac{a_2^2}{2\lambda_2} = 1 \tag{3.13}$$

where λ_1 and λ_2 are the first two eigenvalues obtained from the POD. The phase angle of the vortex shedding can be estimated using equation (3.14) and the result is illustrated in Figure 3.10b.

$$\theta = arctan\left[\sqrt{\frac{\lambda_1}{\lambda_2}}\frac{a_2(t)}{a_1(t)}\right] \tag{3.14}$$

Hence, the cross plot of temporal coefficients (Figure 3.9) can be used to conditionally select planar fields which correspond approximately to the same phase angle. For phase-averaging PIV data, the data points in Figure 3.9 are separated into discrete phase angle bins and the planar velocity fields within each bin are averaged. A single phase angle bin is illustrated in Figure 3.9, with the width of the bin being exaggerated for illustration purposes. For the case of a dual step cylinder, post processing of temporal coefficients is required prior to phase averaging due to instances when amplitude and/or

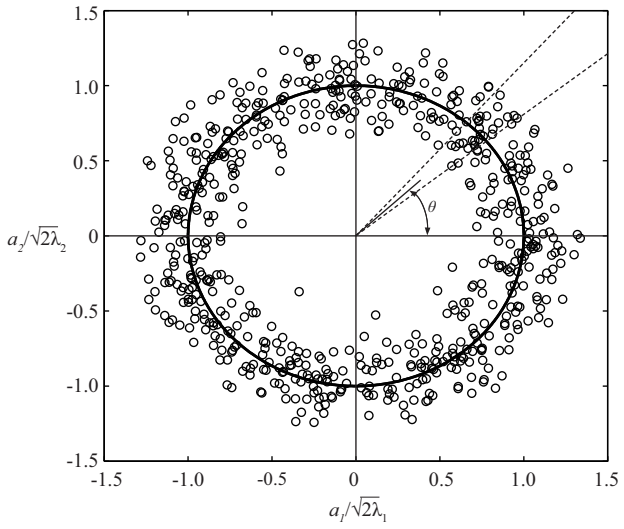

Figure 3.9 Cross plot of temporal coefficients a_1 and a_2 from POD analysis of PIV data for a uniform circular cylinder.

periodicity of the temporal coefficients are reduced.

3.3.3 Pattern recognition analysis of velocity fields in turbulent wakes

An alternative approach to the detection and conditional averaging of coherent structures is the use of pattern recognition analysis based on cross-correlation of velocity or vorticity fields [27–29]. A pattern recognition technique of identifying organized structures in turbulent signals is described in detail by Ferre & Giralt [29] and has been successfully applied to identify coherent patterns in the wakes of circular cylinders [28], identify coherent structures downstream of a backward facing step [27], and

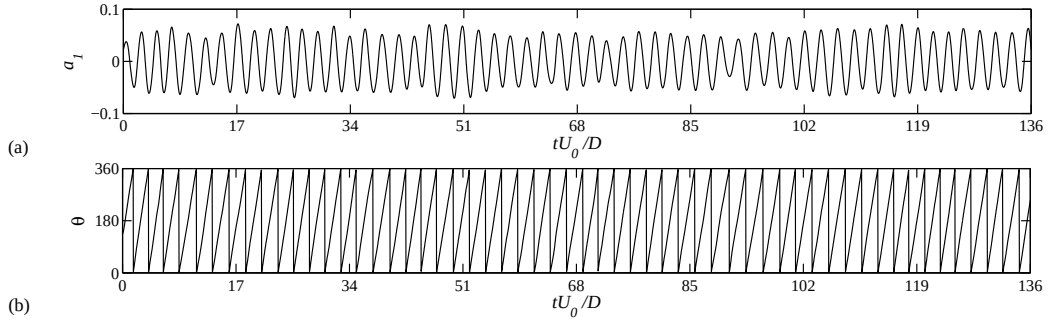

Figure 3.10 POD analysis of PIV data for a uniform circular cylinder. (a) temporal coefficient signal a_1, (b) vortex shedding phase angle.

track vortices in a turbulent boundary layer [85] and in the wake of a sharp trailing edge [84]. When a pattern recognition analysis is applied to planar velocity or vorticity fields, e.g., [27], one of the main challenges is the selection of a template planar velocity or vorticity field from which all other fields are correlated [27]. A correlation coefficient R_{xy}, between a template planar field and all instantaneous fields is used to identify 'matching' planar fields following Eq. 3.15.

$$R_{xy} = \frac{cov(U^t, U^b)}{\sigma_t \sigma_b} = \frac{\sum_{i=1,}^{m} \sum_{j=1}^{n} \left(U_{ij}^t - \overline{U^t}\right)\left(U_{ij}^b - \overline{U^b}\right)}{\sum_{i=1,}^{m} \sum_{j=1}^{n} \left(U_{ij}^t - \overline{U^t}\right)^2 \sum_{i=1,}^{m} \sum_{j=1}^{n} \left(U_{ij}^t - \overline{U^b}\right)^2} \tag{3.15}$$

where R_{xy} is the correlation coefficient between the template, *t*, and velocity field *b*, $cov(U^t, U^b)$ is the covariance function, and σ_t and σ_b are the standard deviations of each of the corresponding planar fields. The template represents the structure of the flow field that is being sought. In the context of coherent structure identification, the template is a planar footprint of a coherent structure. The template can be an instantaneous snapshot of the flow field, a mathematical model representing the coherent structure [27], a conditional average of instantaneous fields obtained from a set of raw data [29], or a spatial eigenfunction obtained from the POD [29]. To minimize bias errors in the detection of coherent structures, instantaneous snapshots of the flow field are typically not selected as templates. In the present study, it will be shown that using a reduced order model of instantaneous snapshots for template fields produces results which are similar to using a conditional average of instantaneous fields. For all forms of template fields, a priori knowledge or direct measurement of the flow properties is required to construct the template. Flow fields which are matching with the template are identified based on a correlation coefficient exceeding a certain threshold value. Once all matching flow fields are identified, they are averaged. The result is a conditionally averaged flow field that is representative in some way to the selected template used for the analysis.

In the present study, PIV measurements in multiple closely spaced planes in the wake of a dual step cylinder (Figure 3.3c) are processed using PRA with the aim of reconstructing the three-dimensional coherent structures and there interactions in the wake using a reduced order model for planar velocity field templates.

Chapter 4

A dual step cylinder in a cross-flow

This Chapter presents experimental results on dual step cylinder geometries investigated experimentally in the Water Flume Facility at the University of Waterloo. Flow and surface visualizations were carried out with hydrogen bubble technique (Figure 3.2), and velocity measurements were completed using Laser Doppler Velocimetry (LDV) and Particle Image Velocimetry (PIV) (Figure 3.3). For LDV, measurements of the free stream velocity were obtained at a fixed point, 5D downstream of the model. PIV measurements were obtained in a single horizontal plane at z/D = 0 (Figure 3.3b) and a single vertical plane at y/D = 0 (Figure 3.3a). This chapter is divided into three sections: (i) overview of the flow development and identification of dominant flow regimes, (ii) detailed investigation of wake vortex shedding, and (iii) structural loading. Preliminary investigations completed on uniform and single step cylinder geometries are discussed in detail in Appendix D.

4.1 Overview of flow development

Flow over a dual step cylinder is investigated for $1050 \leq Re_D \leq 2100$, $1.33 \leq D/d \leq 4$, and $0.2 \leq L/D \leq 17$. The aspect ratio and diameter ratio are found to have a profound effect on wake vortex shedding. Six distinct flow regimes were identified based on changes in the large cylinder wake topology and are discussed in detail in this section. The qualitative features of the wake development are described first through a review of flow visualization results. Following this, a detailed analysis of quantitative data acquired for each of the investigated flow regimes is used to provide further insight into the wake development.

4.1.1 An overview of the flow regimes

Shown in the center of Figure 4.1 is a two-dimensional map of the main flow regimes encountered for a dual step cylinder geometry. The flow regimes are defined based on changes observed in the large cylinder wake topology with D/d and L/D, since the wakes of the small diameter cylinders above and below the large cylinder remain invariant to changes in large cylinder geometry.

Markers are placed in the map in Figure 4.1 to identify the D/d and L/D parameters investigated. The boundaries between different regimes are marked by solid and dashed lines, with the latter drawn based on extrapolation of the present data and results from other relevant studies [20,36,41,42,47,50,60,67,69]. A more detailed discussion of the regime boundaries is completed in section 4.2. Insets are placed outside of the map to describe important qualitative and quantitative features of the flow development for four of the identified flow regimes. Each inset includes: (i) a representative flow visualization image, (ii) a wake velocity spectrum, (iii) the mean velocity field in the wake of the large cylinder at z/D = 0, and (iv) an instantaneous vorticity field in the wake of the large cylinder at z/D = 0. The remaining flow regimes are extensions of the flow regimes identified by the insets. As shown in Figure 4.1, data acquired at $Re_D = 1050$ extends to higher L/D for a fixed D/d = 2, while the data acquired at $Re_D = 2100$ encompasses a wide range of D/d values for $L/D \leq 5$. In Chapter 5, it is shown that the flow regimes also extend to Reynolds numbers up to $Re_D = 5000$, and are expected to persist for even higher Reynolds numbers. The Reynolds number has a minor effect on the L/D and D/d boundaries between each of the identified flow regimes but does not alter the presence of each of the identified flow regimes (Figure 4.1).

The flow regimes are described briefly as follows:

CS – Cellular vortex Shedding occurs from the large cylinder. Multiple vortex shedding cells are detectable downstream of the large cylinder. The vortex dynamics downstream of each stepwise discontinuity matches that found in the wake of the large cylinder in a single step cylinder configuration (Appendix D).

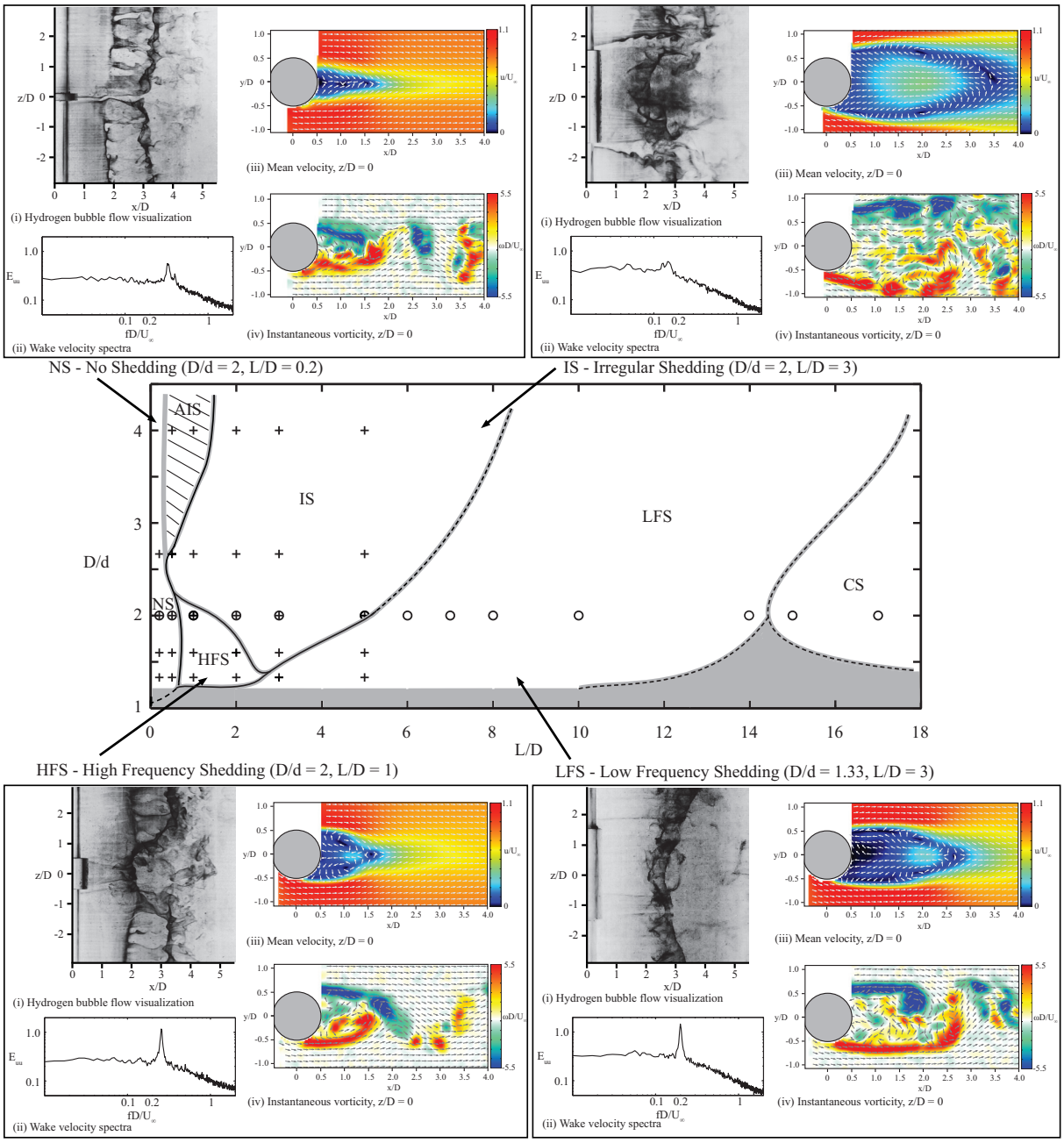

Figure 4.1 Diagram of large cylinder wake regimes expected for a dual step cylinder. The boundaries between different regimes are marked by solid and dashed lines, with the latter drawn based on extrapolation of the present data and results from other relevant studies [20,36,42,47,60,67,69]. + symbols represent the L/D and D/d investigated at $Re_D = 2100$, ○ symbols represent the L/D and D/d investigated at $Re_D = 1050$. The hatched region labeled AIS is an intermediate flow regime whose wake characteristics are similar to both the NS and IS regimes. Solid gray regions identify locations where the dual step cylinder flow regime is unknown.

LFS – Low Frequency vortex Shedding occurs from the large cylinder. The vortex shedding frequency can be up to 10% lower than that found for a uniform cylinder of diameter D. Vortex interactions between large and small cylinder vortices take place downstream of each discontinuity in diameter and are similar to those found downstream of a single step cylinder (Appendix D).

IS – Irregular vortex Shedding occurs from the large cylinder. The coherence and strength of vortex shedding is reduced substantially, and the vortex shedding frequency varies with time. There is minimal interaction between vortices shed from the small and large diameter cylinders, with large cylinder vortices deforming substantially as they are shed into the wake into hairpin-like structures.

HFS – High Frequency vortex Shedding occurs from the large cylinder. Vortex shedding from the large cylinder occurs at a frequency that is up to 30% higher than the shedding frequency of a uniform circular cylinder of diameter D. Vortex interactions occur between vortices shed from the small and large cylinders downstream of each stepwise discontinuity in diameter.

NS – No vortex Shedding occurs from the large cylinder. The vortices shed from the small diameter cylinders interact through complex vortex connections across the wake of the large cylinder.

AIS – Asymmetric, Irregular vortex Shedding occurs from the large cylinder. Vortices are only shed from one side of the large cylinder, creating an asymmetry in the flow development. On the shedding side, the vortices have a reduced coherence when compared to that of a uniform cylinder, similar to that observed in the IS regime. On the no-shedding side, the wake topology resembles that found for the NS regime.

The results presented in the following sections will show that for the region of overlap between data collected at both Reynolds numbers ($0.2 \leq L/D \leq 5$ and $D/d = 2$ in Figure 4.1), similar topological changes in the large cylinder wake occur at roughly the same critical L/D values. Hence, it is expected that the flow regimes and their L/D and D/d boundaries identified for $Re_D = 2100$ persist for lower Reynolds numbers.

4.1.2 Cellular Shedding regime (CS)

The wake development for the CS regime is illustrated by a sequence of flow visualization images shown in Figure 4.2. Comparing the flow visualization results in Figure 4.2 with those obtained for a single step cylinder at $Re_D = 1050$ and D/d = 2, it can be seen that the flow development for z/D > 0 and z/D < 0 resembles that found for a single step cylinder (Appendix D). In the large cylinder wake, lower frequency N-cells form near the step discontinuities in diameter, and a higher shedding frequency, L-cell, forms near the mid-span of the large cylinder, bounded by the two N-cells. The N-cells develop cyclically near each of the step discontinuities, leading to periodic vortex dislocations between N-cells and the L-cell, and between N-cells and vortices shed from the small diameter cylinders (S-cells) (Figure 4.2). The nature of vortex interactions at cell boundaries is similar to that found for a single step cylinder, namely, depending on the relative phase alignment of the vortex cells,

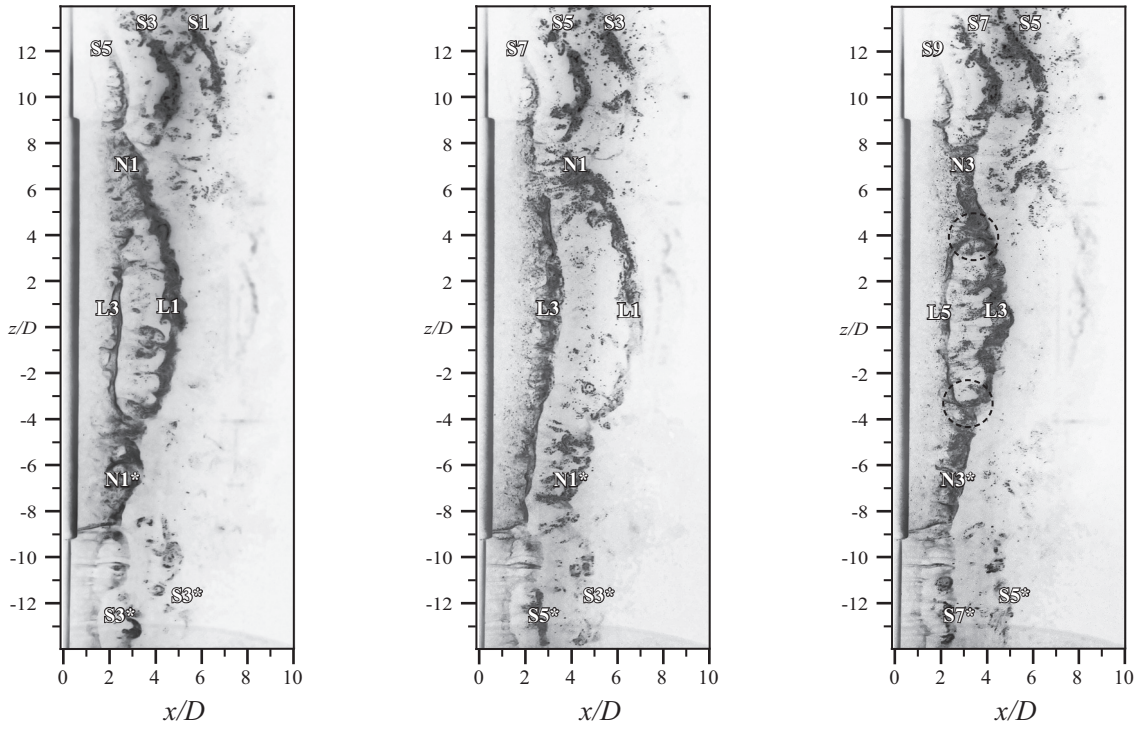

(a) t*=0 (b) t*=2.07 (c) t*=3.94

Figure 4.2 A sequence of hydrogen bubble flow visualization images depicting cellular vortex shedding in the wake of a dual step cylinder in the CS regime for L/D = 17, D/d = 2, and $Re_D = 1050$.

N-cell and L-cell vortices may split into multiple vortex filaments to conserve circulation (e.g., the circled region in Figure 4.2c), while S-cell vortices either form half-loop connections with adjacent S-cell vortices or interact directly with N-cell vortices (the half-loop connections are not easy to identify in the instantaneous flow visualization images, and were detected through the analysis of the flow visualization video recordings). The N-cell development is cyclic, and is similar to that observed for single step cylinders (Appendix D). In particular, N-cell vortices periodically move in and out of phase with L-cell vortices, and the N-cells spanwise extent also fluctuates on the same period. The cyclic flow development is referred to as the N-cell cycle [45]. The N-cells maximum spanwise extent is limited to a region extending about 5-6D from each of the step discontiniuties and into the large cylinder wake. Analysis of video records showed that there is a slow variation in the phase alignment of each N-cell. Similar minor variations in the phase alignment of vortex cells are observed in the wakes of circular cylinders and low aspect ratio dual step cylinders as well [16,36,40], and are attributed to minor non-uniformities in the upstream flow conditions along the model span. As a result, it is common to observe one-sided N-cell cycle development or simultaneous development of two N-cells (Figure 4.2). The large cylinder wake development in this regime is also comparable to that found for a cylinder with two free ends for $L/D > 20$ [69] and for a uniform circular cylinder mounted between endplates for $L/D > 20$-30 [42]. These geometries have been shown to exhibit cellular vortex shedding patterns, with low frequency cells forming near each of the ends and a higher frequency cell forming near the cylinder mid-span. Note, however, that the mechanism for the formation of multiple distinct vortex shedding cells may be different for different cylindrical geometries.

4.1.3 Low Frequency Shedding regime (LFS)

In this regime, vortex shedding from the large cylinder occurs in a single cell (L-cell) across the entire span (Figure 4.3). The transition between the CS and LFS regimes involves the merging of N-cells as L/D decreases beyond a certain threshold, resulting in a single vortex shedding cell. The same phenomenon takes place for free end and uniform cylinder geometries [42,69]. In particular, for a cylinder with two free ends at approximately $L/D < 20$ [69] and for a uniform circular cylinder mounted between endplates for about $L/D \leq 20$-30 [42], the low frequency end cells merge and lead

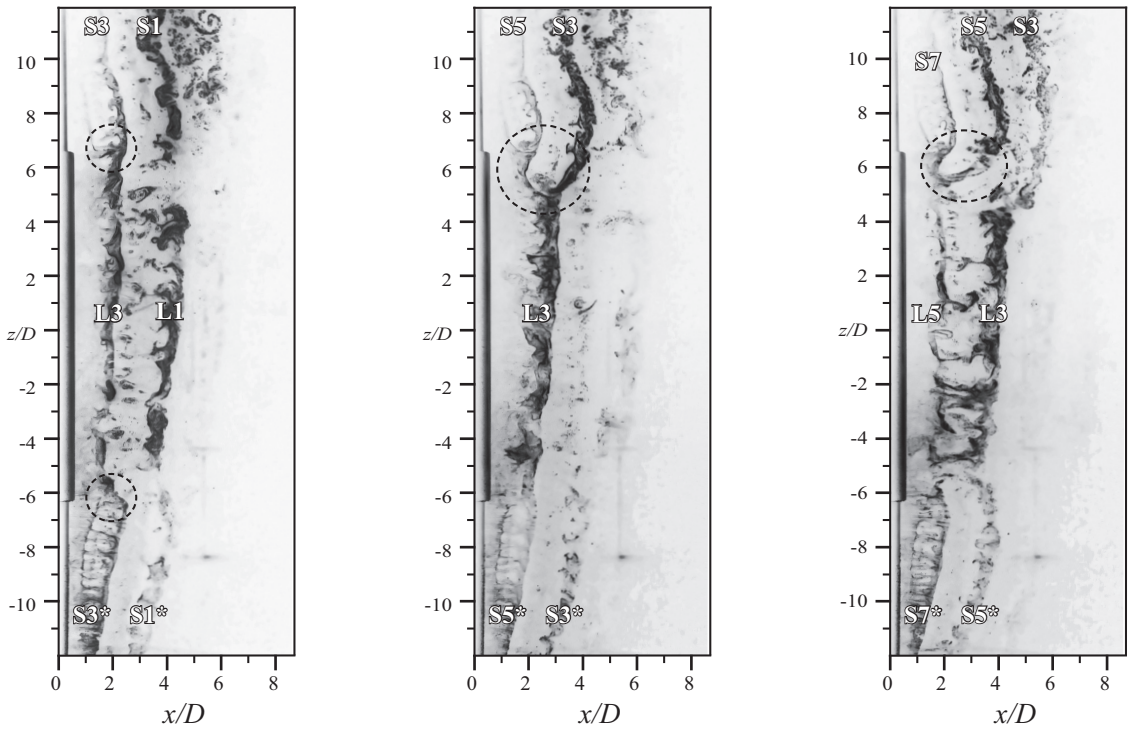

(a) t*=0 (b) t*=1.95 (c) t*=3.90

Figure 4.3 A sequence of hydrogen bubble flow visualization images depicting vortex shedding in the wake of a dual step cylinder in the LFS regime for L/D = 14, D/d = 2, and Re_D = 1050.

to the formation of a single vortex shedding cell along the span. As shown in Figure 4.3a, vortices in the large cylinder wake are shed nearly parallel to the cylinder axis and form direct vortex connections with small cylinder vortices, e.g., vortices L3 and S3 in Figure 4.3a. Large cylinder vortices are stronger than their small cylinder counterparts, which results in all vortices in the large cylinder wake splitting into at least two vortex filaments in order to conserve circulation (e.g., vortex L3 connects to both S3 and S5 in Figure 4.3b, and vortex L5 connects to both S5 and S7 in Figure 4.3c). Figures 4.3b and 4.3c also illustrate the transient nature of the vortex interactions. For example, vortex S5 initially connects to vortex L3 in Figure 4.3b, but is unable to maintain this connection as the vortices are shed from the body (Figure 4.3c). The difference in vortex shedding frequency between the L-cell and S-cells leads to a continuous variation in phase between these cells. As a result, periodic vortex dislocations occur downstream of the step discontinuity. Such dislocations are comparable to those observed in the wake of a single step cylinder (Appendix D) and in the CS regime (Figure 4.2).

4.1.4 Irregular Shedding regime (IS)

In the irregular shedding regime, no consistent vortex shedding pattern is observed in the large cylinder wake. As seen in the flow visualization image sequences in Figure 4.4 for Re_D = 1050 and Figure 4.5 for Re_D = 2100, the spatial arrangement of the large cylinder vortices is difficult to identify. In contrast, small cylinder vortices form nearly parallel to the cylinder axis and are easily identifiable in the near wake (e.g., S1 and S2 in Figure 4.4). Morton [78] speculates that the large cylinder vortices deform into hairpin-like structures as they are shed from the large cylinder, and a review of the present flow visualization video records confirmed this to be the case at both Reynolds numbers investigated. In the vicinity of the large cylinder vortex formation region, small cylinder vortex filaments terminate at the stepwise discontinuities and/or connect with vortex filaments in the large cylinder wake, as shown in the circled region in Figure 4.4a and Figure 4.4c. Analysis of flow visualization video records showed that, beyond the vortex formation region, small cylinder vortices can form half-loop vortex connections in a continuous fashion but they may also form direct connections with large cylinder vortices. This implies that the large cylinder vortices may also form vortex loops. Although the initial deformation of the large cylinder vortices into hairpin-like structures can be seen through flow visualization, vortex loops, which presumably form further downstream, cannot be detected.

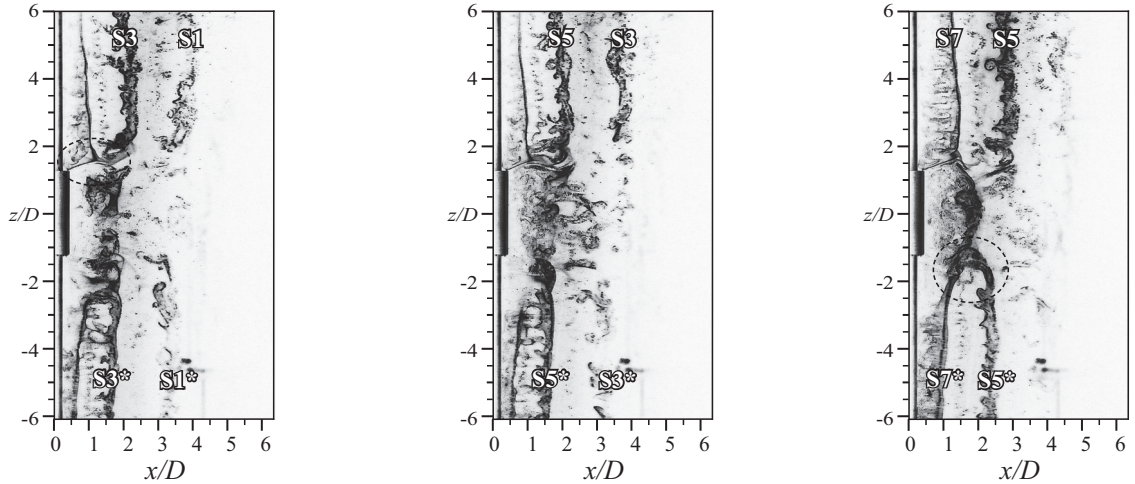

(a) t*=0 (b) t*=1.0 (c) t*=2.0

Figure 4.4 A sequence of hydrogen bubble flow visualization images depicting vortex shedding in the wake of a dual step cylinder in the IS regime for L/D = 3, D/d = 2, and Re_D = 1050. t* is the number of small cylinder vortex shedding periods.

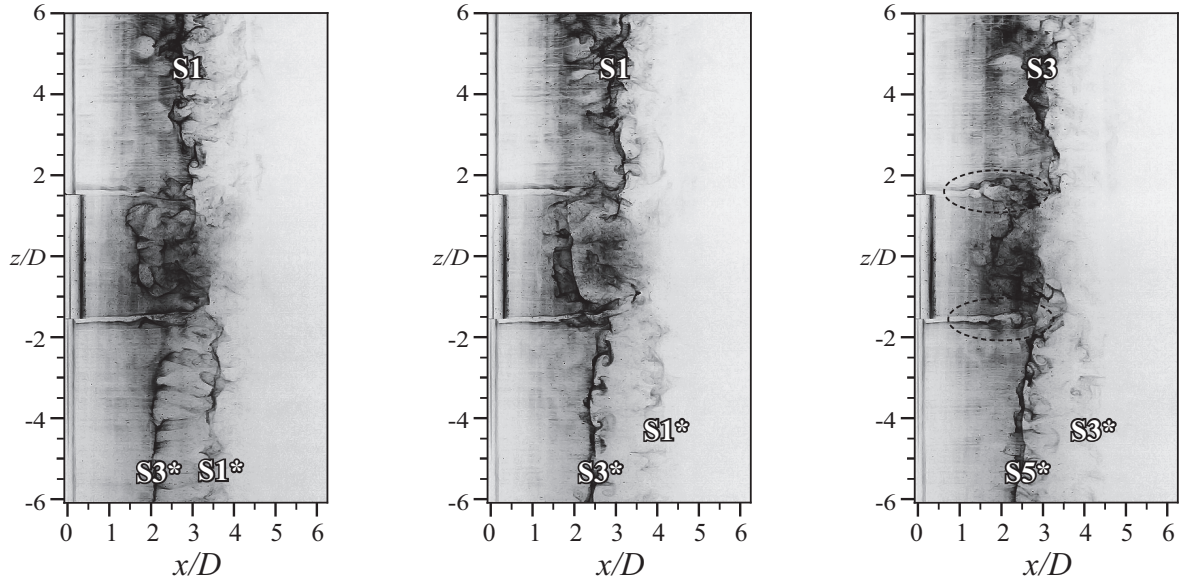

(a) t*=0 (b) t*=1.0 (c) t*=2.0

Figure 4.5 A sequence of hydrogen bubble flow visualization images depicting vortex shedding in the wake of a dual step cylinder in the IS regime for L/D = 3, D/d = 2, and Re_D = 2100.

Notable changes in the topology of the IS regime occur with Reynolds number. In particular, at the boundary between the large and small cylinder wakes, smaller scale Kelvin-Helmholtz vortices can be seen within transverse oriented shear layers emanating from each stepwise discontinuity at Re_D = 2100, as shown, for example, within the circled regions in Figure 4.5c. In addition, at Re_D = 2100, upstream of vortex formation, Kelvin-Helmholtz instability vortices can also be seen rolling up in the separated shear layers. This occurs across a limited range of L/D and D/d within the IS regime. The effects of L/D on the flow topology are illustrated in Figure 4.6, and effects of D/d are illustrated in Figure 4.7. For L/D = 1 (Figure 4.6a), there is no evidence of spanwise vortices being shed from the large cylinder. Vortices in the large cylinder wake could only be seen intermittently through analysis of flow visualization video records. Evidently, the absence of large cylinder vortices for L/D = 1 (Figure 4.6a) leads to consecutive small cylinder vortices forming half-loop vortex connections at formation in order to preserve circulation in the wake (e.g., see the circled regions in Figure 4.6a). For L/D = 2 and 3 (Figure 4.6b-c) and the same diameter ratio (D/d = 2.67), large cylinder vortex shedding takes place, but the near wake is dominated by Kelvin-Helmholtz instability vortices which can be seen forming within the large cylinder separated shear layers (i.e., spanwise-oriented K-

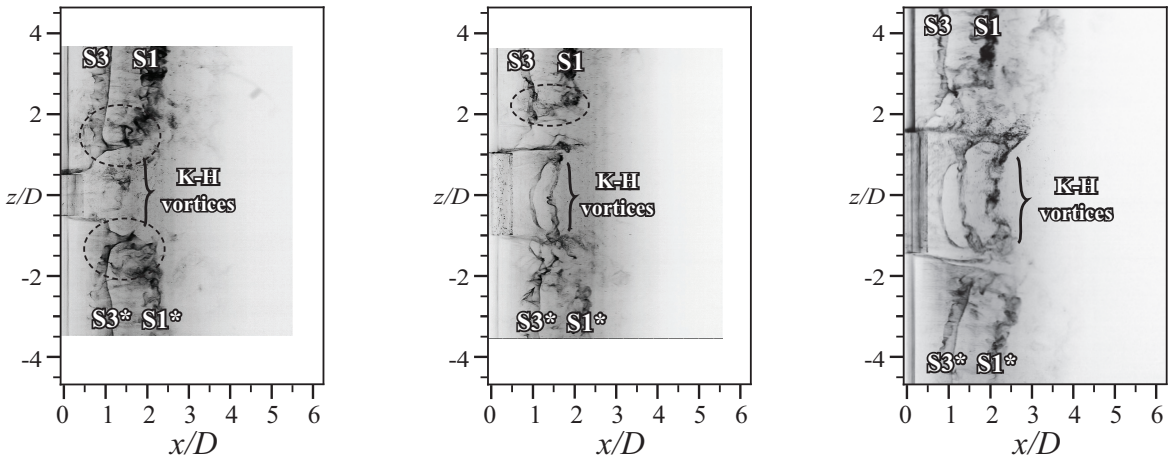

Figure 4.6 Changes in the vortex shedding pattern in the IS regime with L/D at D/d = 2.67 and Re_D = 2100: (a) L/D = 1, (b) L/D = 2, (c) L/D = 3.

H vortices). Transverse-oriented K-H vortices on the other hand, could not be detected at this D/d. For D/d = 2 and all L/D investigated within the IS regime (e.g., Figure 4.7b), both spanwise-oriented and transverse-oriented K-H vortices are observed in the flow visualizations. At lower D/d = 1.6 (Figure 4.7a), only spanwise-oriented K-H vortices form. The flow visualization video records were used to estimate the ratio of the frequency of K-H vortices in the separated shear layer (f_{SL}) to spanwise vortices (f_K). For the cases where K-H vortices were observed (e.g., Figures 4.6 and 4.7), the frequency ratio, f_{SL}/f_K, is between 3.4 and 4.2. This is in good agreement with the expected value

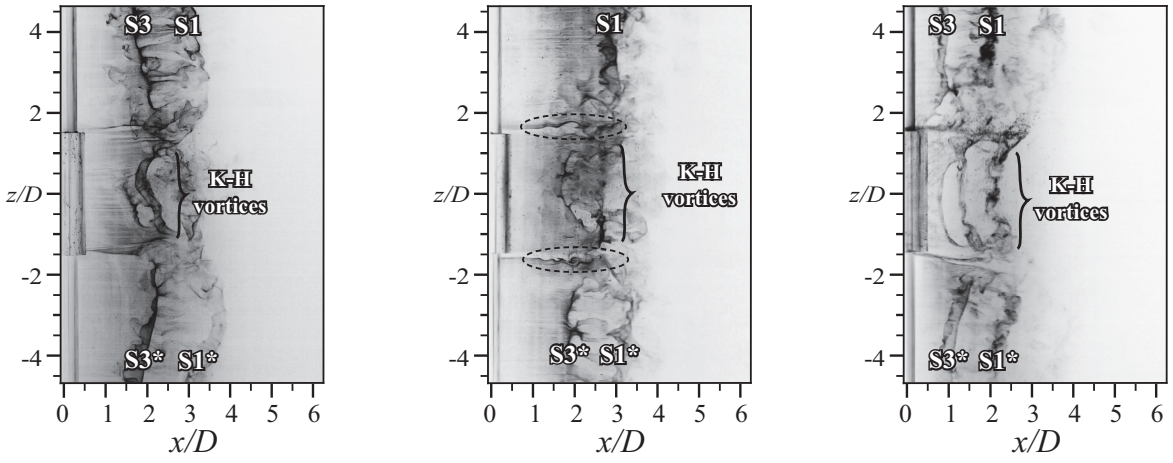

Figure 4.7 Changes in the vortex shedding pattern in the IS regime with D/d at L/D = 3 and Re_D = 2100: (a) D/d = 1.6, (b) D/d = 2, (c) D/d = 2.67.

of f_{SL}/f_K = 4.0 for a uniform circular cylinder at the same Reynolds number [114,115]. Since no K-H vortices were observed in the preliminary investigations on uniform circular cylinders in the range 525 ≤ Re_D ≤ 2100, the results suggest that an earlier amplification of disturbances occurs within the separated shear layers in the IS regime (Figure 4.6 and Figure 4.7).

Asymmetric Irregular Shedding regime (AIS)

The AIS regime is characterized by an asymmetry in the mean and instantaneous wake development in the x-y plane, which cannot be adequately visualized via hydrogen bubble flow visualization in the x-z plane. As such, qualitative and quantitative features of this flow regime will be discussed in detail when PIV measurements are presented.

4.1.5 High Frequency Shedding regime (HFS)

The HFS regime occurs for a narrow range of D/d when the aspect ratio of the large cylinder is within about 1 ≤ L/D ≤ 2 (Figure 4.1). Rather unexpectedly, large cylinder vortex shedding is intensified in this regime. The representative flow visualization image sequence in Figure 4.8 shows the well-defined roll-up of the large cylinder separated shear layer and shedding of vortices into the wake. Similar to the LFS regime, small and large cylinder vortices interact in the large cylinder wake through direct vortex connections which involve vortex stretching of small cylinder vortices and vortex splitting of large cylinder vortices as the vortices in the two wakes move in and out of phase. For

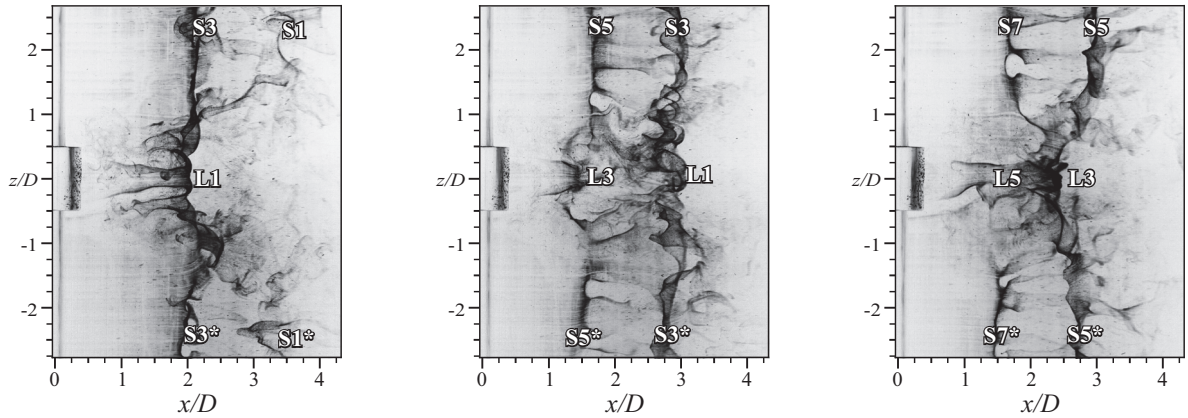

(a) t*= 0 (b) t*= 0.77 (c) t*= 1.65

Figure 4.8 A sequence of hydrogen bubble flow visualization images depicting vortex shedding in the wake of a dual step cylinder in the HFS regime for L/D = 1, D/d = 2, and Re_D = 2100.

example, vortex L1 connects directly small cylinder vortex S3 in Figure 4.8a, but vortex L3 splits to form connections with two consecutive small cylinder vortices S5 and S7 in Figure 4.8c. Vortex dislocations occur periodically and are speculated to be manifested by small cylinder vortices forming half-loop connections, similar to that observed in the LFS and CS regimes.

4.1.6 No Shedding regime (NS)

For about L/D < 1, the shear layers forming on the large cylinder do not roll up into spanwise structures, and hence, vortex shedding from the large cylinder is effectively suppressed. This is illustrated in the flow visualization image sequences in Figures 4.9 and 4.10. Some small cylinder vortices form vortex connections across the wake of the large cylinder. However, the presence of the large cylinder perturbs the development of such connections and leads to the formation of periodic vortex dislocations. These are manifested by small cylinder vortices forming half-loop vortex connections in the large cylinder wake, as shown in Figure 4.10c with solid lines. It is important to note that the present results suggest that no distinct spanwise shedding occurs from the large cylinder at such low aspect ratios. Thus, although the occurrence of vortex dislocations is caused by the presence of the large cylinder, they involve spanwise vortices forming on the small cylinder.

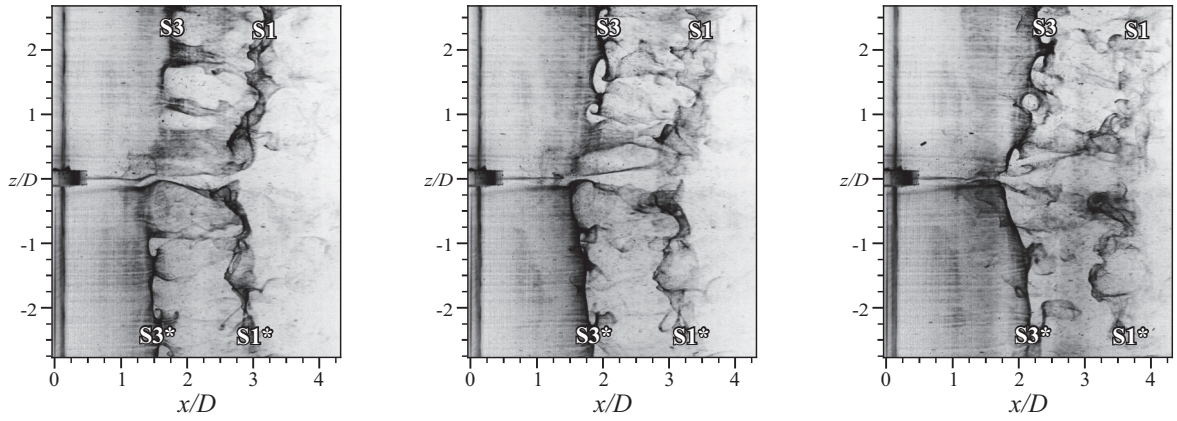

(a) t*= 0 (b) t*= 5.21 (c) t*= 6.42

Figure 4.9 A sequence of hydrogen bubble flow visualization images depicting vortex shedding in the wake of a dual step cylinder in the NS regime for L/D = 0.2, D/d = 2, and Re_D = 2100.

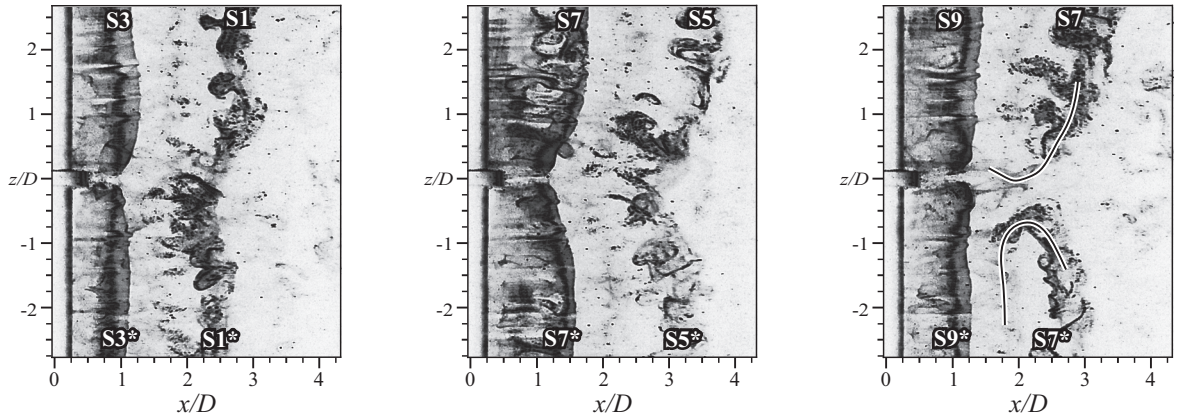

(a) t*= 0 (b) t*= 0.21 (c) t*= 0.42

Figure 4.10 A sequence of hydrogen bubble flow visualization images depicting vortex shedding in the wake of a dual step cylinder in the NS regime for L/D = 0.2, D/d = 2, and Re_D = 1050.

4.2 Flow regime boundaries

Figure 4.11 shows the two-dimensional map of flow regimes introduced in Figure 4.1. The D/d and L/D boundaries for each flow regime are marked by solid and dashed lines. Solid boundary lines represent an extrapolation between data points in the present study. The uncertainty in the placement of the boundary lines can be inferred based on the spacing between adjacent data points in D/d and L/D directions (Figure 4.11). Dashed lines are an extrapolation between results in the present study and the results of studies on similar geometries (e.g., [20,36,41,42,47,50,60,67,69]). In particular, for the limiting cases of $D/d \rightarrow \infty$ and $D/d \rightarrow 1$ the dual step cylinder approaches the geometry of a free end cylinder and uniform cylinder, respectively.

Experimental studies on cylinders with two free ends under turbulent flow conditions by Zdravkovich [18] & Zdravkovich et al. [20], and laminar flow conditions by Inoue & Sakuragi [69], form the basis for the extrapolation of the flow regime boundaries for $D/d \rightarrow \infty$. In particular, for very low aspect ratio coin-like cylinders whose aspect ratio is less than about L/D = 1 [18,69] no vortex shedding occurs from the cylinder. This flow topology corresponds to the NS regime for a dual step cylinder (Figure 4.11). At higher L/D, in the range $2 \leq L/D \leq 8$, vortex shedding occurs from cylinders with two free ends [20]. The shedding is described by Zdravkovich [20] as irregular, with a variation in vortex shedding frequency with time. The characteristics of the wake development are similar to those observed in the IS regime in the present study. Therefore, a transition between the NS and IS

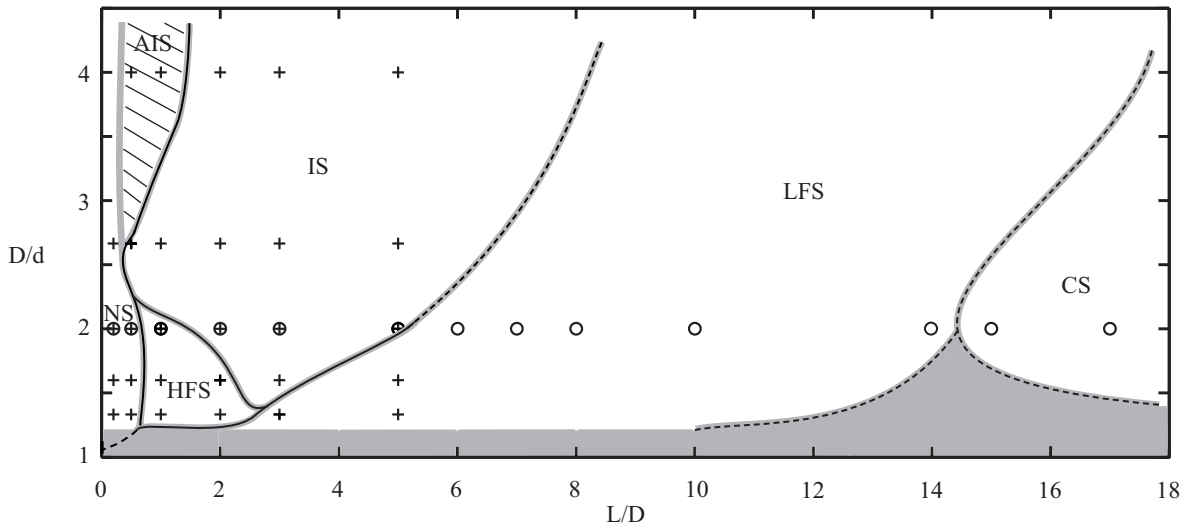

Figure 4.11 Diagram of large cylinder wake regimes expected for a dual step cylinder. The boundaries between different regimes are marked by solid and dashed lines, with the latter drawn based on extrapolation of the present data and results from other relevant studies [20,36,42,47,60,67,69]. + symbols represent the L/D and D/d investigated at $Re_D = 2100$, ○ symbols represent the L/D and D/d investigated at $Re_D = 1050$. Solid gray regions identify locations where the dual step cylinder flow regime is unknown.

regime is expected to occur within $1 < L/D < 2$ for $D/d \rightarrow \infty$ (Figure 4.11). On the other hand, the IS regime will persist up to at least $L/D \approx 8$. The results in Zdravkovich [20] suggest that with increasing L/D in the range $2 \leq L/D \leq 8$, the coherence of the vortex shedding increases. For $L/D > 8$, it is speculated that this trend continues, and a transition from the IS to the LFS flow regime will occur for $L/D \approx 10$ (Figure 4.11). Under laminar shedding conditions, Inoue & Sakuragi [69] found that vortex shedding from a cylinder with two free ends occurs in a single vortex shedding cell up to $L/D \approx 20$. Three distinct vortex shedding cells form in a free end cylinder wake for $L/D > 20$ [69]. This critical aspect ratio is similar to that reported for cantilevered cylinders under both laminar and turbulent shedding conditions (e.g., [41,50]), and, hence, with increasing D/d the boundary between the LFS and CS regime is expected to asymptotically approach $L/D \approx 20$ for $D/d \rightarrow \infty$, as shown in Figure 4.11. In our experiments at $D/d = 2$, transition from the LFS regime to the CS regime occurs at approximately L/D = 14-15 (Figure 4.11). Hence, for $2 < D/d < \infty$, results are extrapolated between L/D = 14.5 and 20 (Figure 4.11). For $D/d < 2$, insight into the L/D boundary between the LFS and CS regime can be gained from experimental data available for single step cylinders [70]. In the CS regime, the flow development within $z/D > 0$ and $z/D < 0$ matches that found for a single step cylinder for the

same diameter ratio and Reynolds number (Appendix D). According to Lewis & Gharib [70], for a single step cylinder geometry with D/d greater than about 1.55, under laminar vortex shedding conditions, a low frequency vortex shedding cell forms near the step discontinuity in the large cylinder wake, and a higher frequency vortex shedding cell forms across the remainder of the large cylinder span. This wake topology corresponds with the CS regime due to the presence of multiple vortex shedding cells in the large cylinder wake. However, for $D/d < 1.25$, the low frequency is absent [70]. This suggests that for dual step cylinders with D/d less than about 1.25-1.55 [70], cellular shedding does not occur in the large cylinder wake and the wake topology would match that of the LFS regime. However, it is well documented that in uniform circular cylinder wakes, unless the end conditions are intentionally modified (e.g., suction at the ends or inclining endplates [40]), cellular shedding will take place for higher aspect ratio models greater than about $L/D \approx 30$ [41]. For lower aspect ratio models with $L/D < 10$, experimental results from numerous researchers suggest vortex shedding occurs at a single frequency along the entire span, irrespective of end conditions [20,36,41,42,47,50,60,67,69]. Thus, it is speculated that for dual step cylinders with $1 \leq D/d \leq 1.25\text{-}1.55$, transition from the LFS to the CS regime can occur for L/D up to 30 and possibly as low as 10. This is illustrated in Figure 4.11 with a solid gray region.

In the limiting case of $D/d = 1$, a dual step cylinder approaches the geometry of a uniform circular cylinder. The flow development depends on the aspect ratio of the entire dual step cylinder model since the small and large cylinder diameters match. For low large cylinder aspect ratios, $L/D < 10$, and low diameter ratios, $D/d < 1.33$, there is no data available to speculate on the flow regime boundaries and there transitions. As a result, this region of the map is also highlighted in gray (Figure 4.11).

4.3 Mean and instantaneous wake topology

The flow visualization results in the previous section outlined important qualitative features of each of the identified flow regimes. In this section, the main focus is on quantitative changes in mean and instantaneous wake characteristics. Measurements in the CS regime are not included in this section since results are comparable to those found in the LFS regime.

Figures 4.12 to 4.15 illustrate changes in the mean, RMS, and instantaneous wake topology of uniform and dual step cylinders through PIV measurements obtained at the mid-span of the large diameter cylinder in the x-y plane. It is of interest to compare the dual step cylinder results to those of a uniform circular cylinder. The uniform circular cylinder has a recirculation zone consisting of two counter-rotating eddies that are symmetric relative to the wake centerline (Figure 4.12a). The recirculation region extends about 2.5D downstream of the model axis, matching that expected for a uniform circular cylinder at the corresponding Reynolds number and aspect ratio [43]. The extent of the recirculation zone for a uniform cylinder may be used as an indicator for the vortex formation length [43]. Comparing the uniform cylinder results in Figure 4.12 to the dual step cylinder results in Figure 4.13, it can be seen that the extent of the recirculation zone in both streamwise and transverse directions downstream of the large cylinder is larger than that of a uniform circular cylinder in the LFS and IS flow regimes. On the other hand, in the HFS, AIS, and NS regimes, the recirculation zone can be substantially smaller, with the streamwise extent varying between 0.2D and 2.0D downstream of the cylinder axis (Figure 4.13e-h). Since the size of the recirculation zone changes substantially in each flow regime, so does the size and position of the pair of recirculation eddies. In the LFS and HFS regimes (Figure 4.13a,b,f), where periodic vortex shedding is known to take place from the large cylinder, the y/D position of the recirculation eddies are comparable to those seen for a uniform cylinder. In the IS regime, the recirculation eddies are displaced away from the wake centerline and are elongated in the streamwise direction (Figure 4.13c-d). This is accompanied by the presence of a larger and stronger reverse flow region when compared that of a uniform circular cylinder. In the AIS regime, there is only a single recirculation eddy behind the cylinder model, and the recirculation zone and wake velocity recovery is cambered by nearly ten degrees relative to the $y = 0$ axis. In the NS regime, there are no detectable recirculation eddies (Figure 4.13g-h).

The RMS velocity in the wake of a uniform circular cylinder consists of a well-defined region directly downstream of the cylinder where strong velocity fluctuations occur. The peak strength of velocity fluctuations reach approximately 30% of the free stream velocity (Figure 4.12b), and occur along the wake centerline. The x/D location of the maximum RMS velocity can be used as an indicator

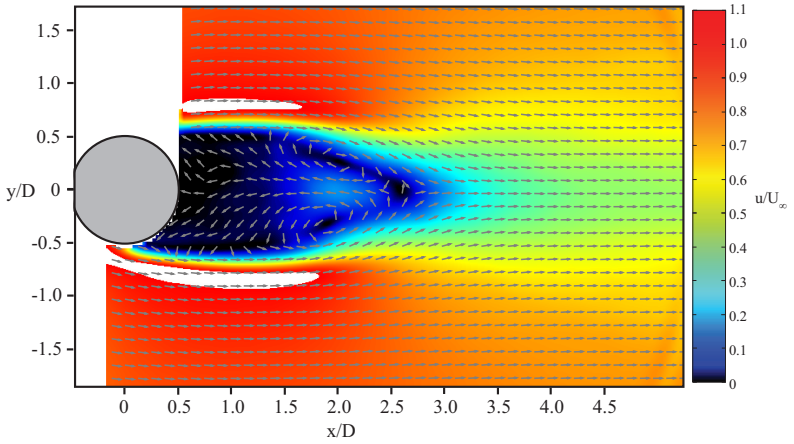

(a) Mean velocity

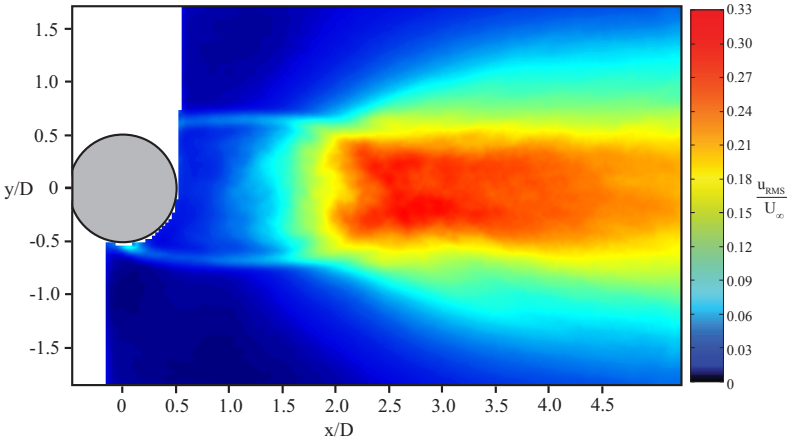

(b) RMS velocity

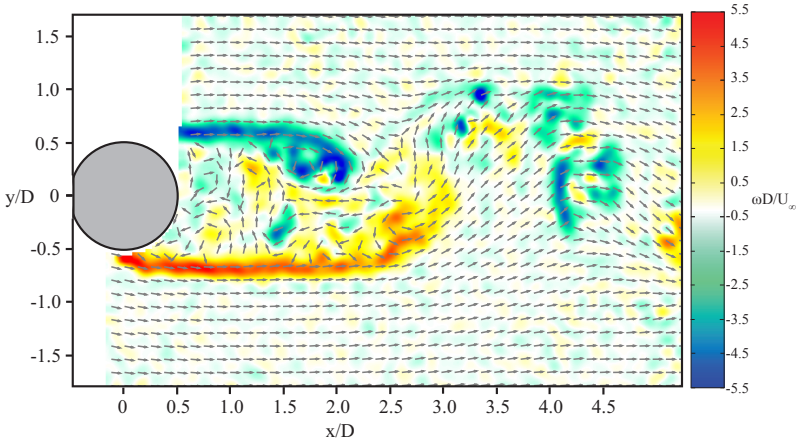

(c) Instantaneous vorticity

Figure 4.12 Mean, RMS and instantaneous wake topology of a uniform circular cylinder at $Re_D = 2100$.

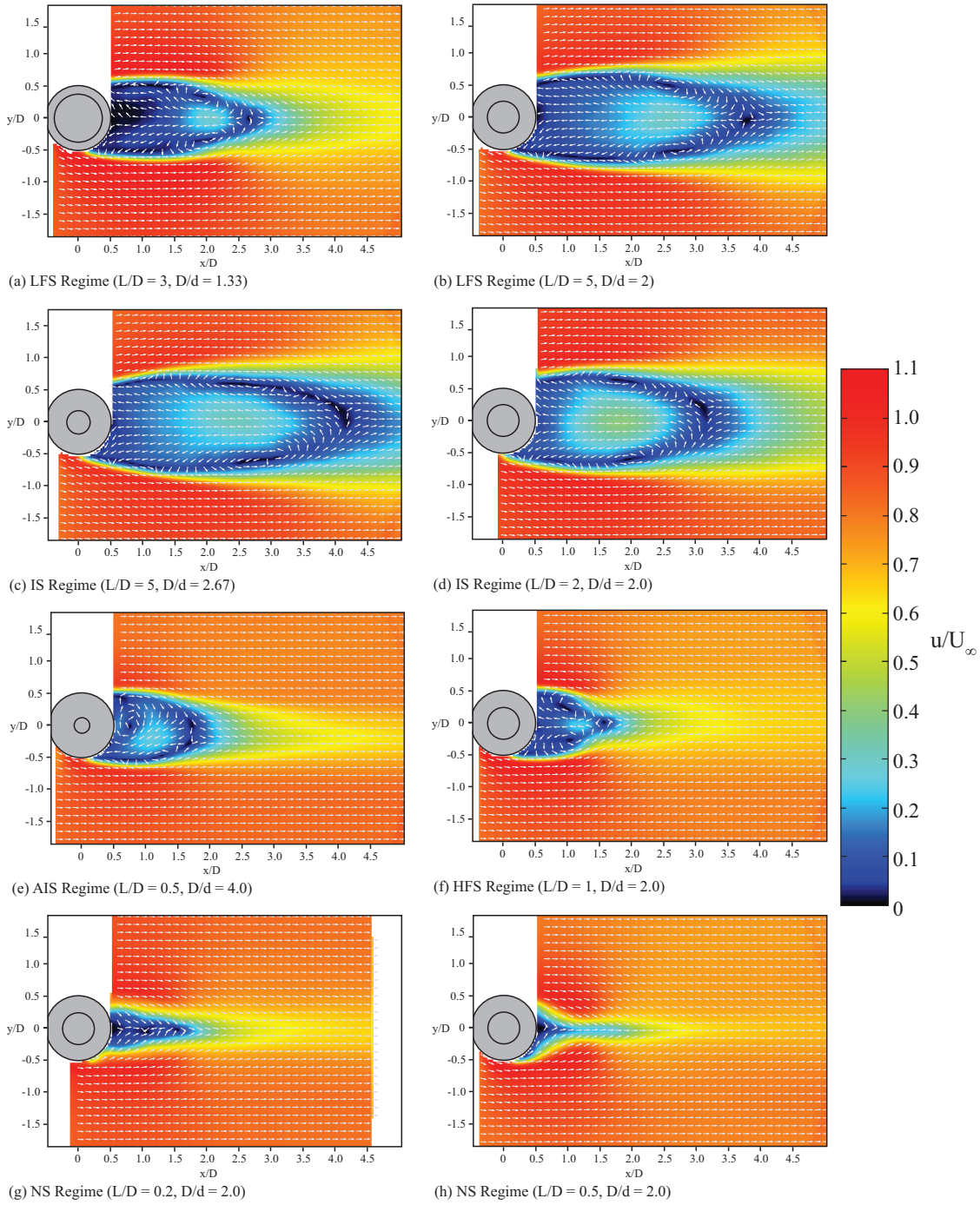

Figure 4.13 Changes in the mean velocity in the wake in the x-y plane for each identified flow regime at $Re_D = 2100$.

of the vortex formation length [43]. For the uniform cylinder at $Re_D = 2100$, this peak occurs approximately 2.5D downstream of the cylinder axis, matching the downstream location defined by

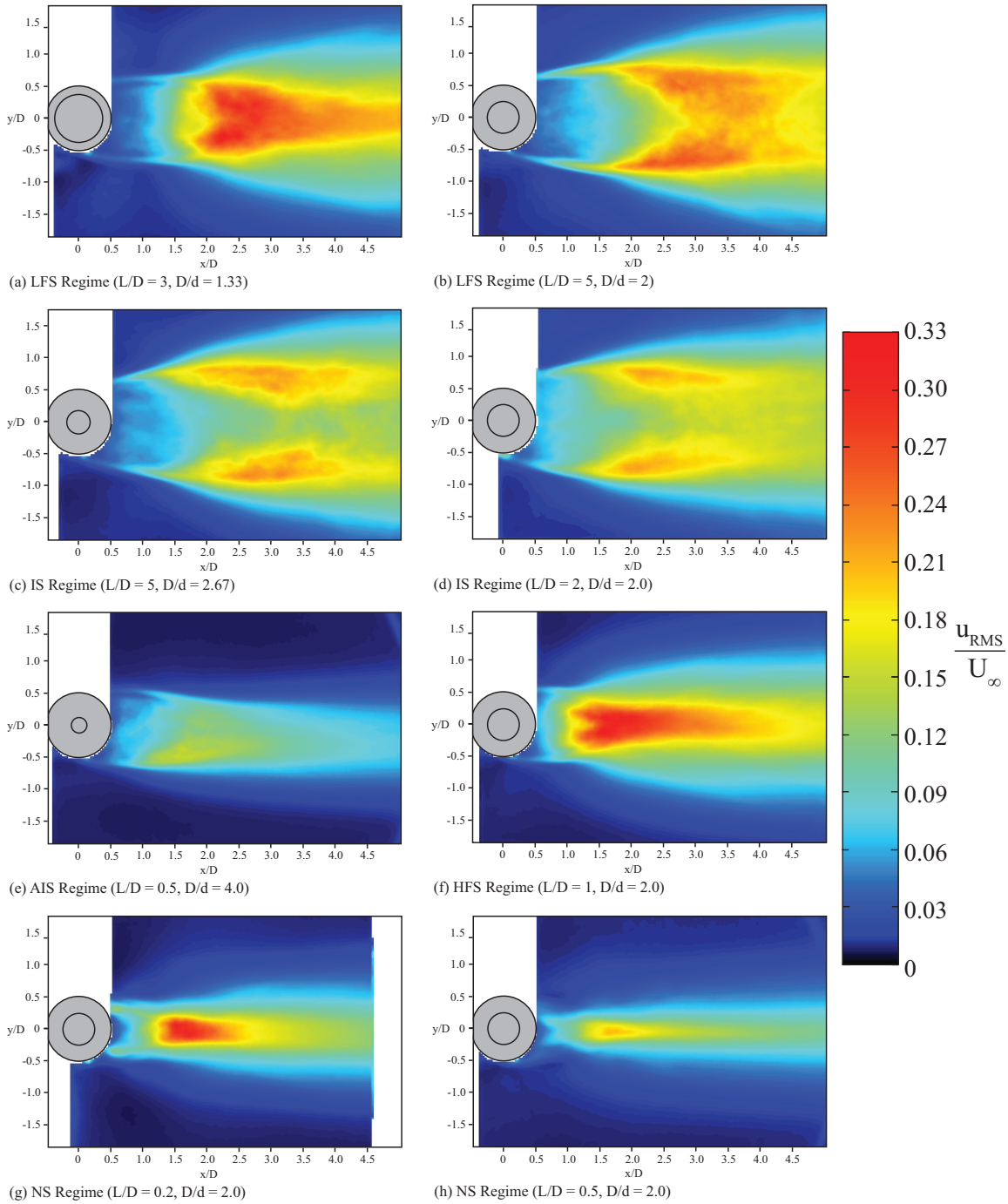

Figure 4.14 Changes in the RMS velocity in the wake in the x-y plane for each identified flow regime at $Re_D = 2100$.

the recirculation zone in Figure 4.12a. Compared to the dual step cylinder results in Figure 4.14, it can be seen that the location of high RMS velocity, as well as the magnitude of the RMS velocity changes substantially with each flow regime. In the LFS, HFS, and NS flow regimes, the peak RMS velocity

remains along the wake centerline (Figure 4.14a,b,f,g,h) and has a similar magnitude to as that of a uniform circular cylinder (Figure 4.12b). In the transition from the LFS and HFS regimes to the IS regime (e.g., Figure 4.14e,f,g), the RMS velocity along the wake centerline weakens, while the RMS velocity away from the wake centerline strengthens. In the IS regime, regions of high RMS velocity can be found on both sides of the wake centerline at a y/D location of about ±0.7(Figure 4.14a,b,c). The magnitude of the RMS velocity peaks in the IS regime are weaker than that found for a uniform circular cylinder. Agreeing with the mean flow topology results for the IS regime in Figure 4.13, the results in Figure 4.14 suggest that vortex formation occurs close to the large cylinder separated shear layers. However, the estimates of the vortex formation length, defined by either the streamwise extent of the recirculation region (Figure 4.13) or the x/D location of peak RMS velocity (Figure 4.14), do not agree in the IS regime. In the AIS regime, the peak RMS velocity is less than half that found for a uniform circular cylinder (Figure 4.14e). Due to the asymmetry of the wake in the AIS regime (Figure 4.13e), the peak in RMS velocity occurs on one side of the wake ($y/D < 0$). For the NS regime (Figure 4.14g-h), flow visualization results presented in the previous section show that small cylinder vortices periodically connect across the large cylinder wake. Given that the shape of the RMS velocity distribution in the NS regime is similar to that found for a uniform circular cylinder, it is likely the result of small cylinder vortex filaments connecting periodically across the large cylinder wake.

The instantaneous vorticity field in the wake of a uniform circular cylinder at $Re_D = 2100$ (Figure 4.12c) shows strong alternately signed shear layers rolling up into concentrations of vorticity that highlight the presence of vortical structures. As the vortices convect into the wake, they decay into weaker, smaller scale structures due to turbulent transition and viscous dissipation, as illustrated in the instantaneous image provided in Figure 4.12c. Select images of the instantaneous vorticity field in the wake of a dual step cylinder are provided in Figure 4.15. Where applicable, the images have been selected such that the large cylinder vortices are in approximately the same phase alignment. In the LFS and HFS regimes (Figure 4.15a,b,f) the images depict a vortex street. Apart from changes in the location of shear layer roll-up due to variations in the formation length, the vortex shedding is similar to that found for a uniform cylinder. In the IS regime (Figure 4.15c-d), the vorticity field is less

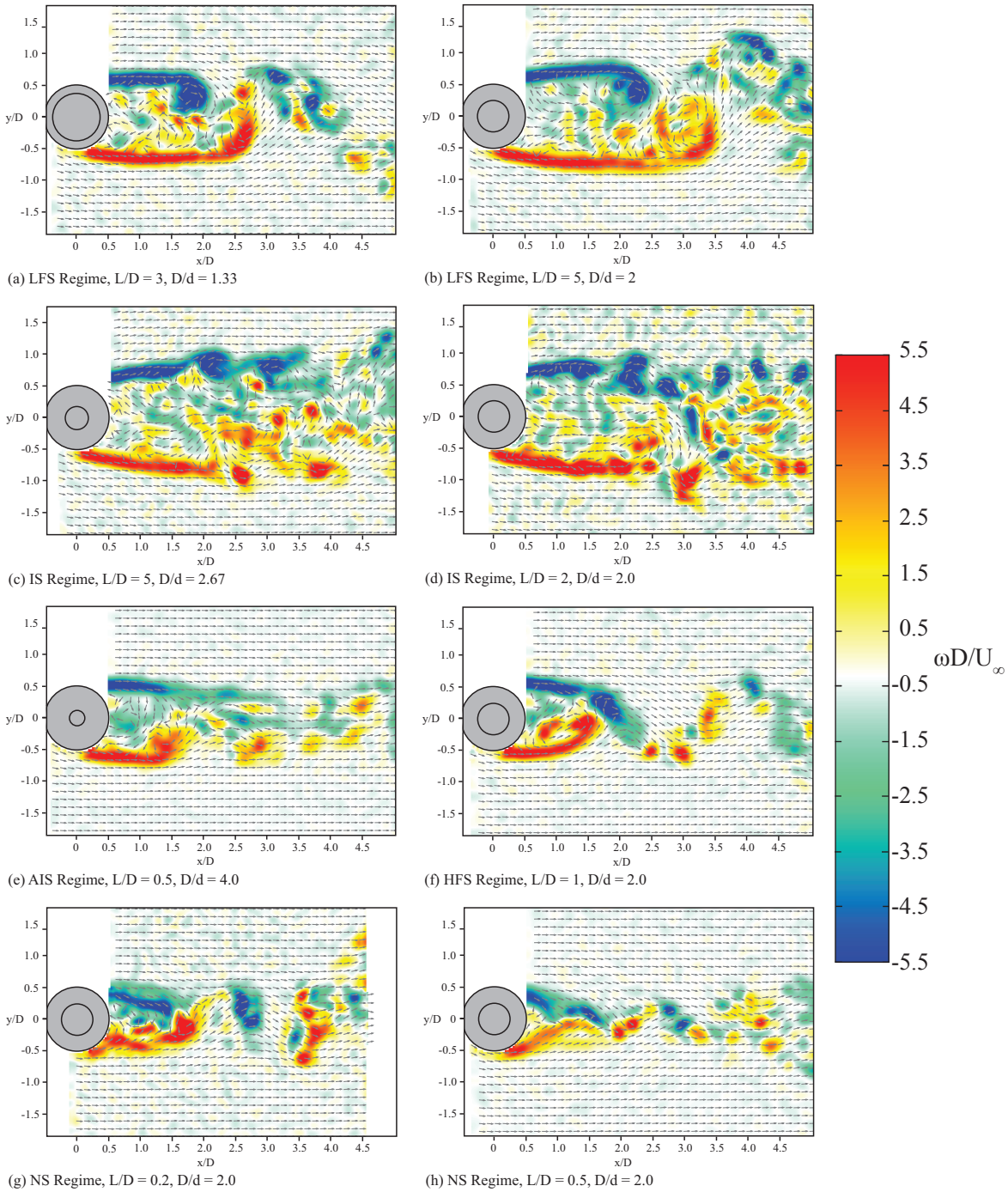

Figure 4.15 Changes in the instantaneous vorticity field in the x-y plane for each identified flow regime at $Re_D = 2100$.

coherent, and no large scale vortices can be seen forming in the wake. Instead, the results indicate that several consecutive smaller-scale shear layer vortices roll-up and are carried downstream with no

direct evidence of a global vortex shedding instability. These results are in agreement with the hydrogen bubble flow visualizations presented earlier, which showed several small-scale shear layer instability vortices forming in the near wake upstream of where vortex formation is expected to occur. In the AIS regime (Figure 4.15e), the upper shear layer ($y/D>0$) does not shed vortices, while the lower shear layer ($y/D < 0$) can be seen rolling up into distinct structures. In the NS regime (Figure 4.15a-b), the results show small-scale vortical structures in the wake, thought to be footprints of the small cylinder vortex filaments connecting across the large cylinder wake.

Figures 4.16 and 4.17 illustrate changes in the mean and RMS wake topology of dual step cylinders for four flow regimes using PIV measurements obtained in the x-z plane at $y/D = 0$. For all flow regimes, there is variation in the length of the recirculation zone, as well as variation in the peak RMS velocity along the span of the dual step cylinder. In the LFS regime (Figure 4.16a), there is a gradual change in the recirculation length between the large and small cylinder wakes. The x/D location of the peak RMS in the wake (Figure 4.17a) approximately matches the end of the recirculation region for any given z/D location. In the IS regime (Figure 4.16b), the recirculation region elongates substantially to $x/D \approx 4.0$, and contains two counter-rotating eddies downstream of both step discontinuities in the large cylinder wake ($x/D = 1.5$ and $z/D = \pm 1.25$ in Figure 4.16b). There also exists a region of high velocity magnitude emanating from the steps that creates a boundary between the large and small cylinder wakes. Near the step, this high velocity region is directed at an angle relative to the free stream and further downstream it attains a streamwise orientation (Figure 4.16b). The location of this high velocity region appears to nearly match the location and trajectory of transverse-oriented shear layer instability vortices that have been identified in hydrogen bubble flow visualizations (Figure 4.6). In the HFS regime (Figure 4.16c and Figure 4.17c), the recirculation zone extends up to 2D downstream of the cylinder axis in the large cylinder wake. The spanwise region affected by the presence of the large cylinder in the HFS regime includes the large cylinder wake, and spanwise regions extending into the small cylinder wakes near the step discontinuities, $0.5 \leq z/D \leq 1.0$, and $-1.0 \leq z/D \leq -0.5$ in Figure 4.16c. Wake velocity fluctuations are the highest near the step locations (Figure 4.17c), and correspond to where vortex interactions occur between large and small cylinder

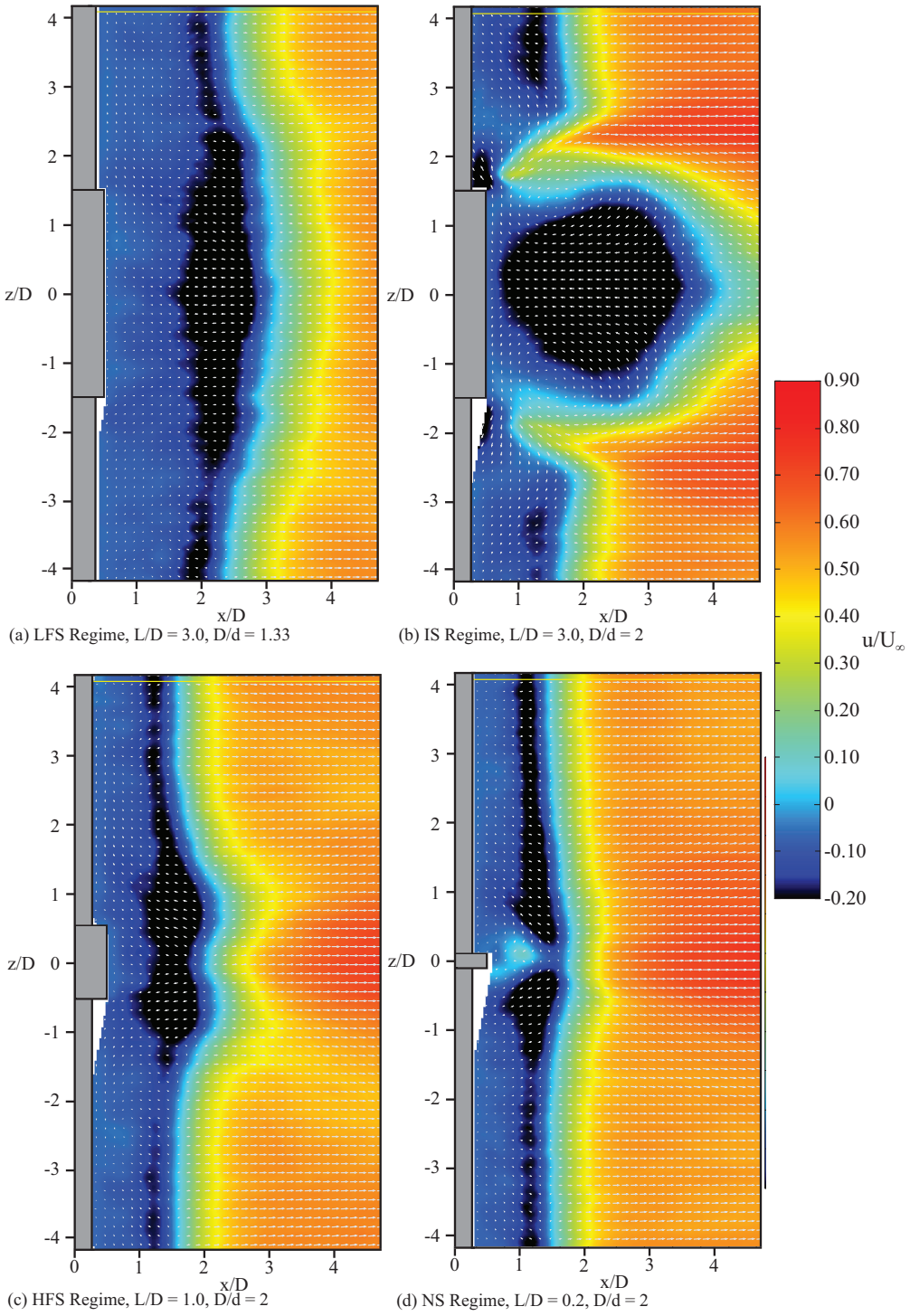

Figure 4.16 Changes in the mean wake velocity deficit in the x-z plane for each identified flow regime at $Re_D = 2100$.

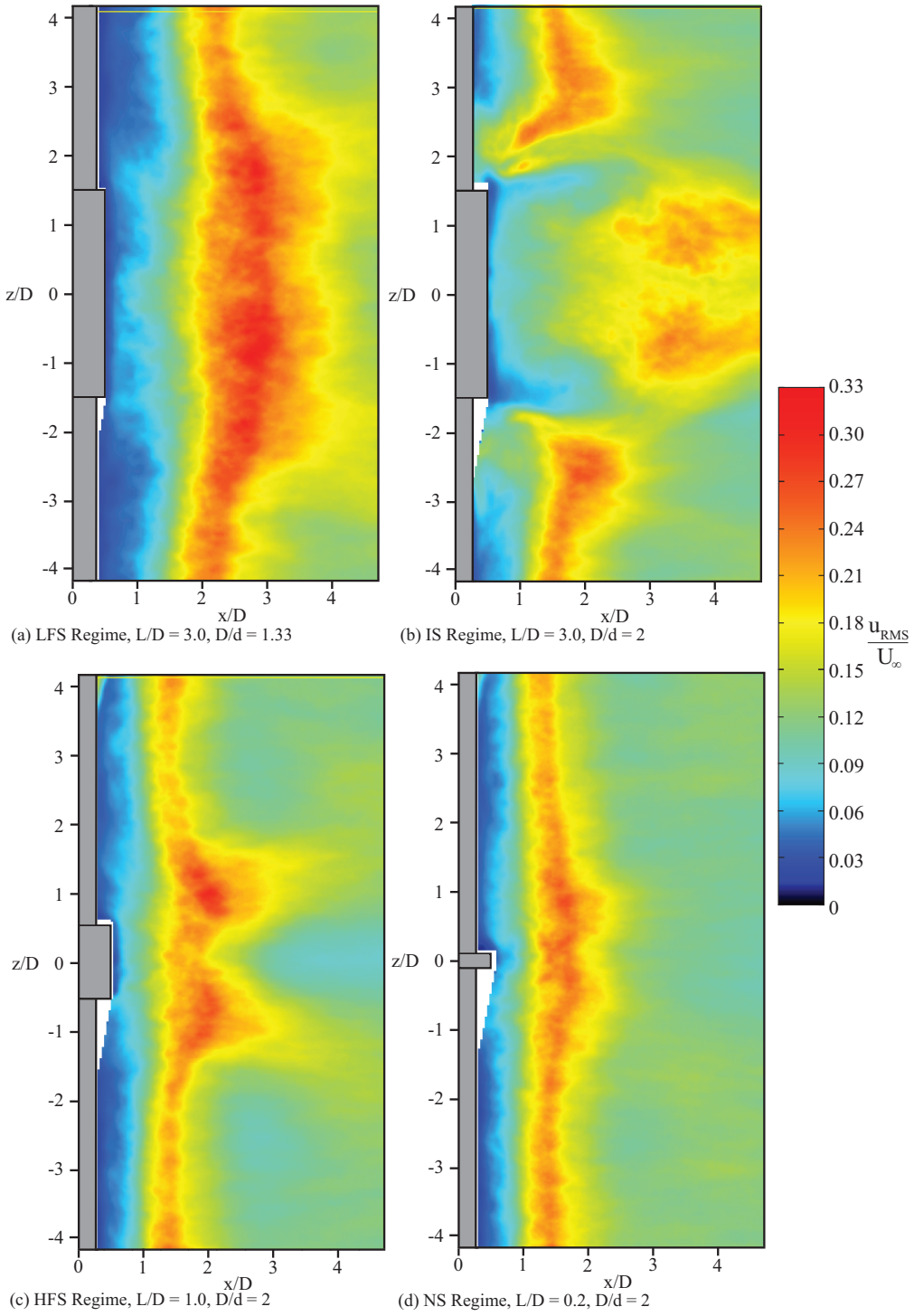

Figure 4.17 Changes in the RMS velocity in the x-z plane for each identified flow regime at $Re_D = 2100$.

vortices (e.g., Figure 4.4). Since the RMS field is largely governed by velocity fluctuations induced by vortex shedding, in order for the highest fluctuations to be recorded in the region where vortex interactions take place, they are likely both repeatable and strong. In the NS regime (Figure 4.16d and Figure 4.17d), the large cylinder is relatively small (in D/d and L/D) compared to other flow regimes, and has only a minor effect on mean and RMS wake topology. The main features of the near wake surrounding the large cylinder model consist of a slightly elongated recirculation zone when compared to that of the small cylinder. Beyond the recirculation region, the mean velocity in the wake of the large cylinder recovers to approximately 80% of the free stream velocity, and does so more quickly than in the small cylinder wakes. This is caused by more significant spatial variations in the vortex connections in the large cylinder wake, which, on the average, leads to a higher mean velocity downstream of the large cylinder.

4.3.1 Vortex formation in the large cylinder wake

To estimate vortex formation length, the extent of the recirculation zone was used as it provided results which were less ambiguous, and had a lower uncertainty when compared to using the streamwise location of the peak RMS velocity. Figure 4.18 presents the variation of the formation length with D/d and L/D for all models investigated. Also shown in the figure are formation length estimates for uniform small diameter circular cylinders at L/D = 0. For a given D/d, the formation length increases with increasing L/D, and for a given L/D, the formation length does not change significantly with D/d. For dual step cylinders with small L/D in the NS regime, the formation length is the smallest, and less than that found for a uniform small diameter cylinder (Figure 4.18). Peak values in the formation length are obtained for models investigated at L/D = 5 (Figure 4.18). However, it is expected that as L/D continues to increase, the formation length at the large cylinder mid-span will plateau and then decrease, eventually approaching that expected for an infinitely long uniform circular cylinder of diameter D.

To determine the dominant frequency in the large cylinder wake and gain better insight into the flow regimes depicted in Figure 4.1, spectral analysis of streamwise velocity data was performed and

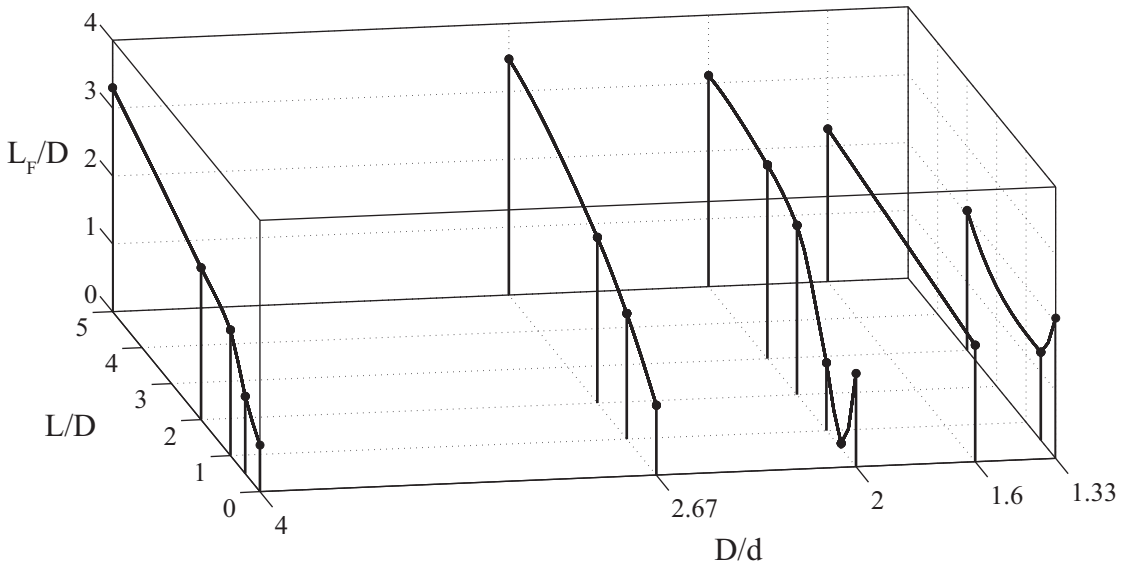

Figure 4.18 Variation in the vortex formation length in the x-y plane at z/D = 0.

the results are presented in Figure 4.19. All spectra were computed based on velocity data acquired in the wake of the large cylinder at *x/D = 5*, *y/D = 0.75*, and *z/D = 0*. As a reference, the dimensionless shedding frequency of a uniform cylinder of diameters d and D is included in the figure. For a uniform cylinder, dominant, narrow peaks appear in the spectra at the vortex shedding frequency (Figure 4.19), with the corresponding Stouhal numbers matching those reported by Norberg [33] ($St \approx 0.2$) to within the frequency resolution bandwidth. The results in Figure 4.19 illustrate that variations in dominant frequency occur in the wake of a dual step cylinder with both D/d and L/D. Consider, for example, spectra pertaining to D/d = 1.6 (Figure 4.19b). The velocity spectrum for L/D = 3 shows a broad peak centred on a frequency lower than that expected for a uniform cylinder at the same Reynolds number (Figure 4.19b). As the aspect ratio of the large cylinder is decreased to L/D = 2 and 1, the dominant frequency in the large cylinder wake increases, exceeding the vortex shedding frequency for a uniform cylinder (Figure 4.19b). Also, the energy content of the corresponding spectral peak increases, indicating an increase in coherence of wake structures. A further decrease in the large cylinder aspect ratio below L/D = 1, produces a dual peak in the spectrum, with one peak centred at a frequency matching the expected vortex shedding frequency of the small diameter cylinder and the other at a slightly lower frequency, as can be seen in the spectra pertaining to L/D = 0.5 in Figure 4.19b. At L/D

= 0.2, the energy content associated with the small cylinder shedding frequency becomes dominant (Figure 4.19b). These observed trends can also be seen for other diameter ratios investigated (Figure 4.19).

The changes in velocity spectra seen in Figure 4.19b are reflecting changes in the large cylinder wake topology within each of the identified flow regimes. Through a comparison of the velocity spectra with hydrogen bubble flow visualizations and PIV measurements shown earlier, each flow regime can be shown to have unique spectral characteristics associated with the dominant vortical structures detectable in the large cylinder wake. In the LFS regime, a single, narrow banded peak is observable in the spectra, but the central frequency of the peak is lower than that expected for a uniform circular cylinder. For example, for L/D = 3 and D/d = 1.33 the dimensionless shedding frequency is about 0.175, which is about 13% lower than that produced by a uniform cylinder of the same diameter. Velocity spectra pertaining to the IS and AIS regimes are characterised by low energy content centered on a single dominant peak, and is associated with a decrease in coherence of vortices shed from the large cylinder. In some cases, e.g., D/d = 4 (Figure 4.19e), there is no discernible peak in the spectra, despite the fact that there are organized structures in the near wake (Figure 4.15). The reduced coherence in the vortices shed in the IS and AIS regimes is the principle reason that it is difficult to identify their formation and shedding from the large cylinder. The HFS regime is characterised by a single, narrow peak in in the spectra whose frequency is higher than that expected for a uniform circular cylinder of the same diameter. For example, the dimensionless vortex shedding frequency for L/D = 1 and D/d = 2 (Figure 4.19) is approximately 0.26, about 30% higher than that produced by a uniform circular cylinder of the same diameter. The NS regime is characterized by a dual peak in the velocity spectra, one peak centred on the small cylinder vortex shedding frequency and the other centred on a slightly lower frequency (e.g., L/D = 0.2 and D/d = 2 in Figure 4.19). These spectral peaks detected in the streamwise velocity spectra for the NS regime are attributed to the periodic passage of small cylinder vortices linking across the wake of the large cylinder. Specifically, the vortex filaments linking across the wake have a reduced convective velocity when compared to the small cylinder vortices forming away from the step. It is these filaments that are responsible for the lower frequency

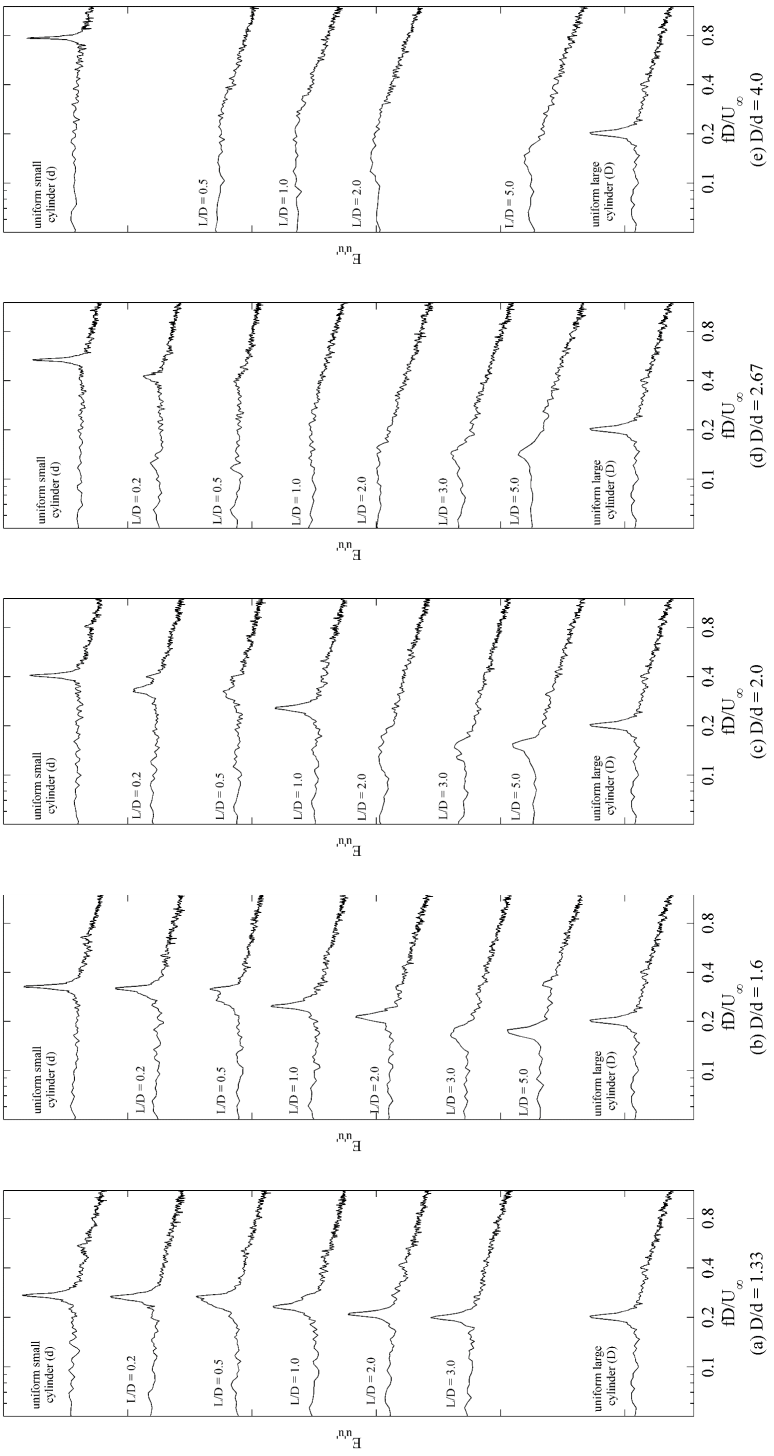

Figure 4.19 Spectral analysis of velocity measurements obtained in the wake of a dual step cylinder at x/D = 5, y/D = 0.75, z/D = 0, for Re_D = 2100.

peak in the spectra. The higher frequency peak in the spectra matches the small cylinder shedding frequency and is present due to the velocity fluctuations produced by the nearby shedding of small cylinder vortices. Not surprisingly, as the size of the large cylinder disturbance is reduced (e.g., L/D or D/d decreases), the dual peaks in the spectra begin to merge since the convective velocity of the vortex filaments are less retarded.

Figure 4.20 illustrates the variation in the dominant frequency and associated spectral energy content in the wake of the large cylinder. Note that at L/D = 0, the spectral energy content and frequency associated with uniform small cylinder vortices is shown for comparison. Note that in Figure 4.19, for some D/d and L/D, it is difficult to identify the dominant frequency in the large cylinder wake. Therefore, for these models, a spectral analysis of PIV measurements is used to estimate the dominant frequency. For such measurements, the resolution in the spectra is lower, but does not affect the interpretation of the results presented in Figure 4.20. The results shed further insight

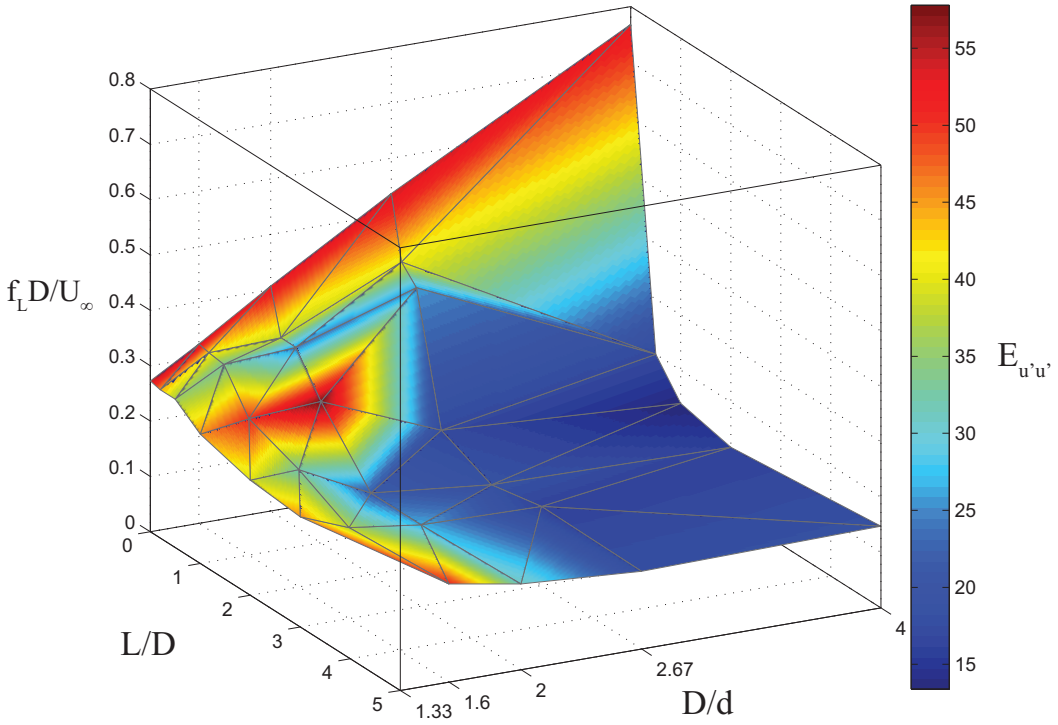

Figure 4.20 Variation in the dominant frequency and associated spectral energy content in the large cylinder wake at x/D = 5, y/D = 0.75, z/D = 0, for Re_D = 2100.

into the changes in energy content of the dominant wake structures. Comparing Figure 4.20 to the flow regime map produced in Figure 4.1, it can be seen that the large cylinder wake structures have a high energy content within the NS, HFS, and LFS regimes, while the IS regime produces both the lowest energy content and lowest dominant frequencies.

4.4 POD-Analysis

POD of the horizontal mid-plane PIV measurements are used to gain added insight into the formation and development of large scale coherent structures. Figure 4.21 shows the energy distribution over the first hundred POD modes for each investigated model, as well as a uniform circular cylinder of diameter D. Based on previous studies conducted on uniform cylinder geometries (e.g., [116]), a superposition of the mean flow and the first two POD modes serves to approximate vortex shedding in the cylinder wake. The results pertaining to a uniform cylinder at $Re_D = 2100$ show that the first two modes capture about 60% of the overall wake energy content, agreeing with results reported in the literature (e.g., [25,117]). For dual step cylinders, depending on L/D and D/d, the first two modes in the large cylinder wake account for 10% to 60% of the energy content (Figure 4.21), reflecting the changes in strength and coherence of the large cylinder vortices in different flow regimes (Figure 4.19 and Figure 4.21). In the LFS and HFS regimes, where coherent vortex shedding is known to take place from the large cylinder, the first two modes capture between 45% and 60% of the overall wake energy content, similar to that of a uniform circular cylinder (Figure 4.21). The IS and AIS flow regimes are characterised by low energy content in the first two modes (between 10% and 30% of the overall wake energy content in Figure 4.21), indicating that the dominant coherent structures are significantly weaker than those found for a uniform cylinder. Finally, for the NS regime, the energy content contained in the first two modes depends on the size of the large cylinder, with less than 25% for L/D = 0.5, and more than 40% for L/D = 0.2 for a fixed D/d = 2 (Figure 4.21). To verify if the first two POD modes capture the dominant vortical structures in the wake of the large diameter cylinder, it is instructive to investigate the first few spatial modes and corresponding temporal coefficients in more detail.

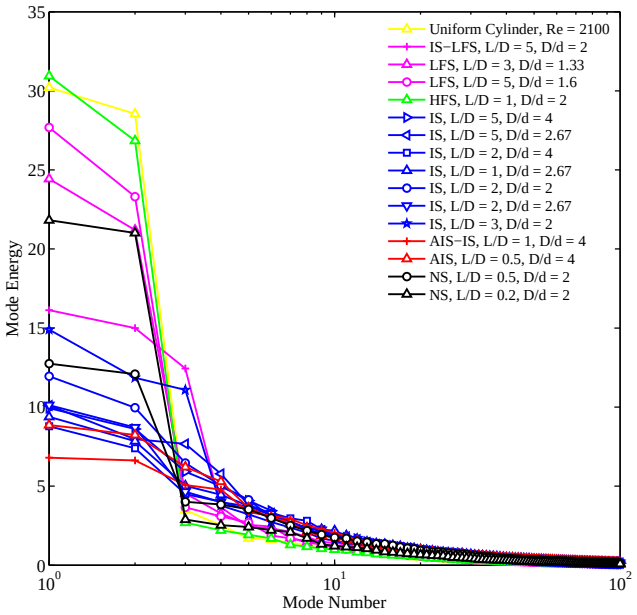

(a) Mode Energy vs mode number

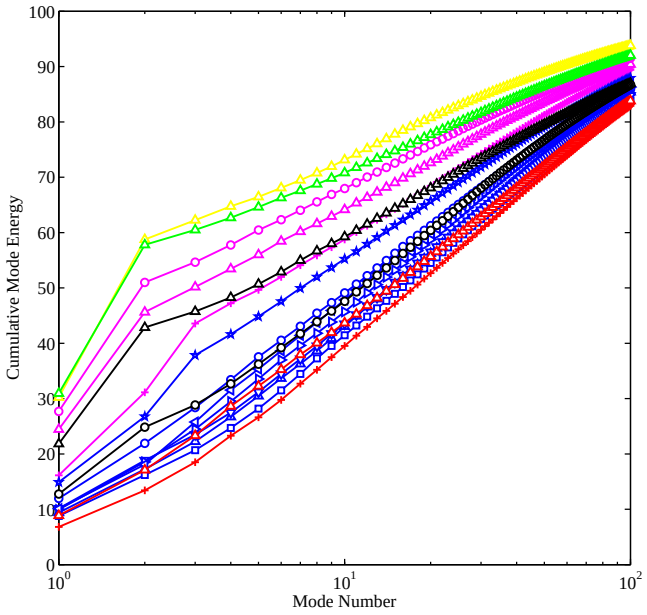

(b) Cumulative mode energy vs mode number

Figure 4.21 Distribution of eigenmode energy obtained from a POD analysis of 2D PIV measurements in the wake of a dual step cylinder in an x-y plane at z/D = 0. The legend in (a) applies to both images.

4.4.1 Characteristics of the spatial eigenfunctions and corresponding temporal coefficient signals

Figure 4.22 presents the first four spatial and temporal modes for a uniform circular cylinder, and Figures 4.23-4.27 present the same for the LFS, IS, HFS, AIS, and NS regimes, respectively. For a uniform circular cylinder, it was confirmed through spectral analysis of the first two temporal coefficient signals that these signals are directly linked to the frequency of vortex shedding, with each of the two signals having approximately the same spectral energy content, with one of the coefficients being shifted out of phase by $\pi/4$ radians (Figure 4.22e-f). The results are in agreement with experimental studies showing the POD analysis of cylinder wakes [25,26,113]. The first two spatial modes show large scale structures which are associated with the vortices shed periodically from the cylinder (Figure 4.22a-b), such that the superposition of the first two modes via equation 3.12 represents the lowest order approximation of the vortex shedding. The third and fourth temporal modes for a uniform circular cylinder (Figure 4.22g-h) show less periodicity than the first two, and the corresponding spatial modes depict asymmetric structures in the wake that are speculated to be related to three-dimensional effects including: oblique vortex shedding, vortex deformation, vortex stretching, and splitting of vortex filaments. Previous experimental studies on uniform circular cylinders and cantilevered cylinders have shown that in addition to modes associated with three-dimensional effects, some of the higher modes (ϕ_3 through ϕ_{10}) are often associated with low frequency modulations in the vortex formation length [80,107], and harmonics of the fundamental mode pair ϕ_1 & ϕ_2 [113,118]. An investigation of higher modes ϕ_5 to ϕ_{10} (not shown here) revealed harmonic modes as well as low frequency modes associated with the so-called base flow modulation [107].

For the results presented for each flow regime (Figures 4.23-4.27), the aim is to confirm that the dominant vortical structures in each regime are associated with vortices being shed periodically from the large diameter cylinders. In addition, it is possible to provide added insight into the wake development in each flow regime based on characterising the changes in the shape of the spatial modes and periodicity of the temporal coefficients. A spectral analysis of the first two temporal coefficient signals for each flow regime confirmed that the dominant frequency in each of the signals matched with the estimated vortex shedding frequency shown in Figure 4.19. In addition, for each pair of

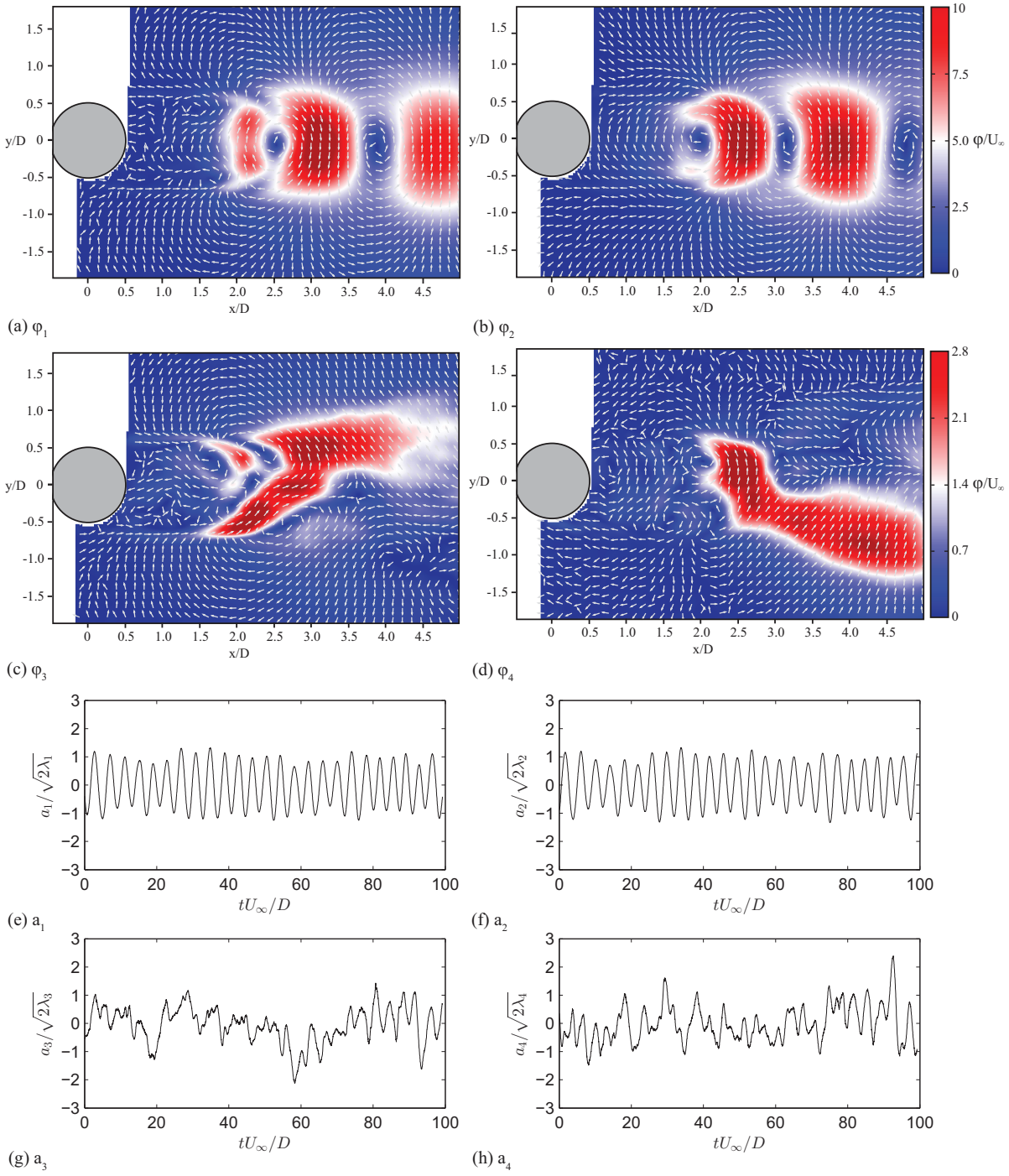

Figure 4.22 Characteristic spatial modes and temporal coefficients for a uniform circular cylinder at $Re_D = 2100$.

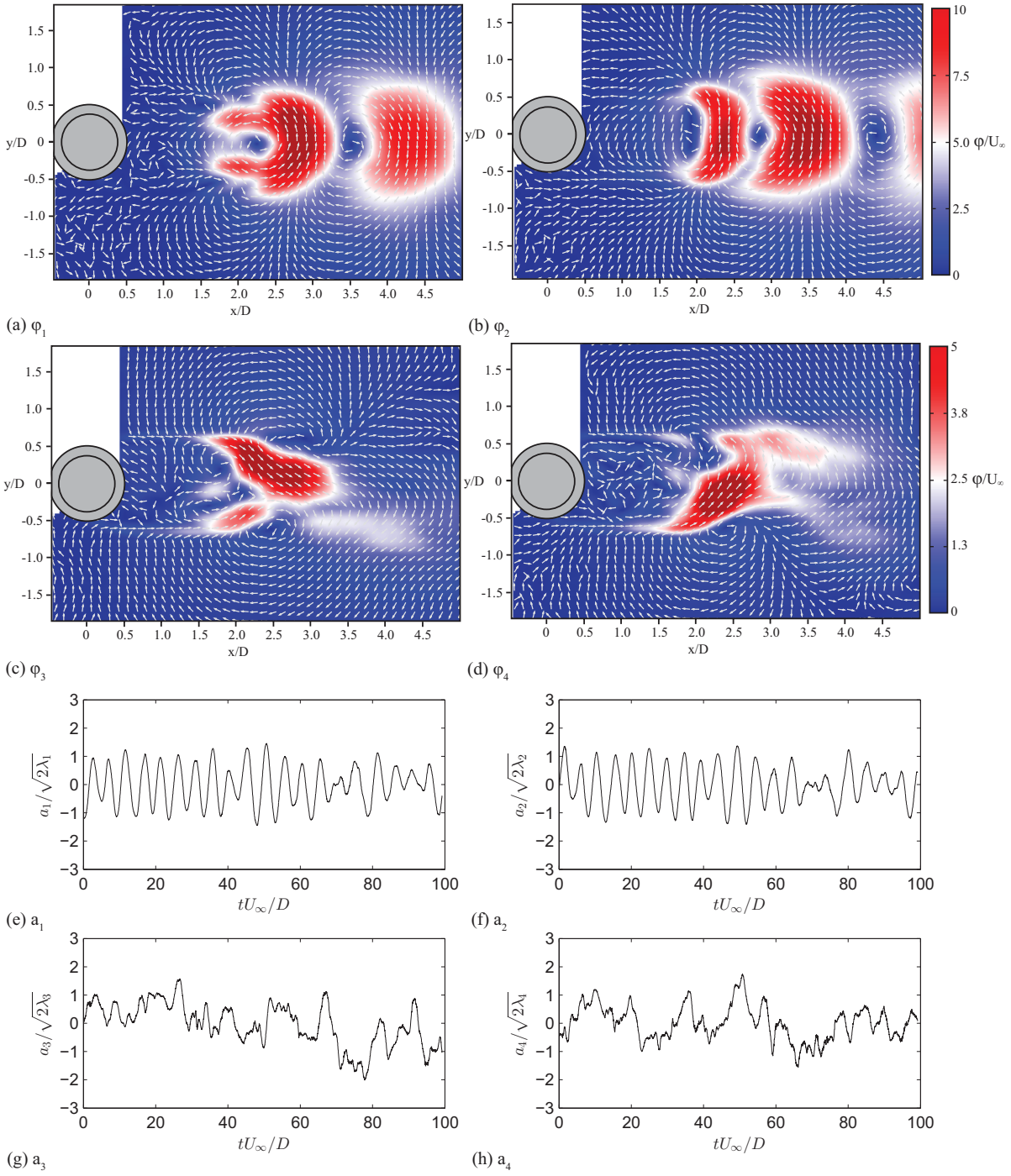

Figure 4.23 Characteristic spatial modes and temporal coefficients in the LFS regime for L/D = 3 and D/d = 1.33.

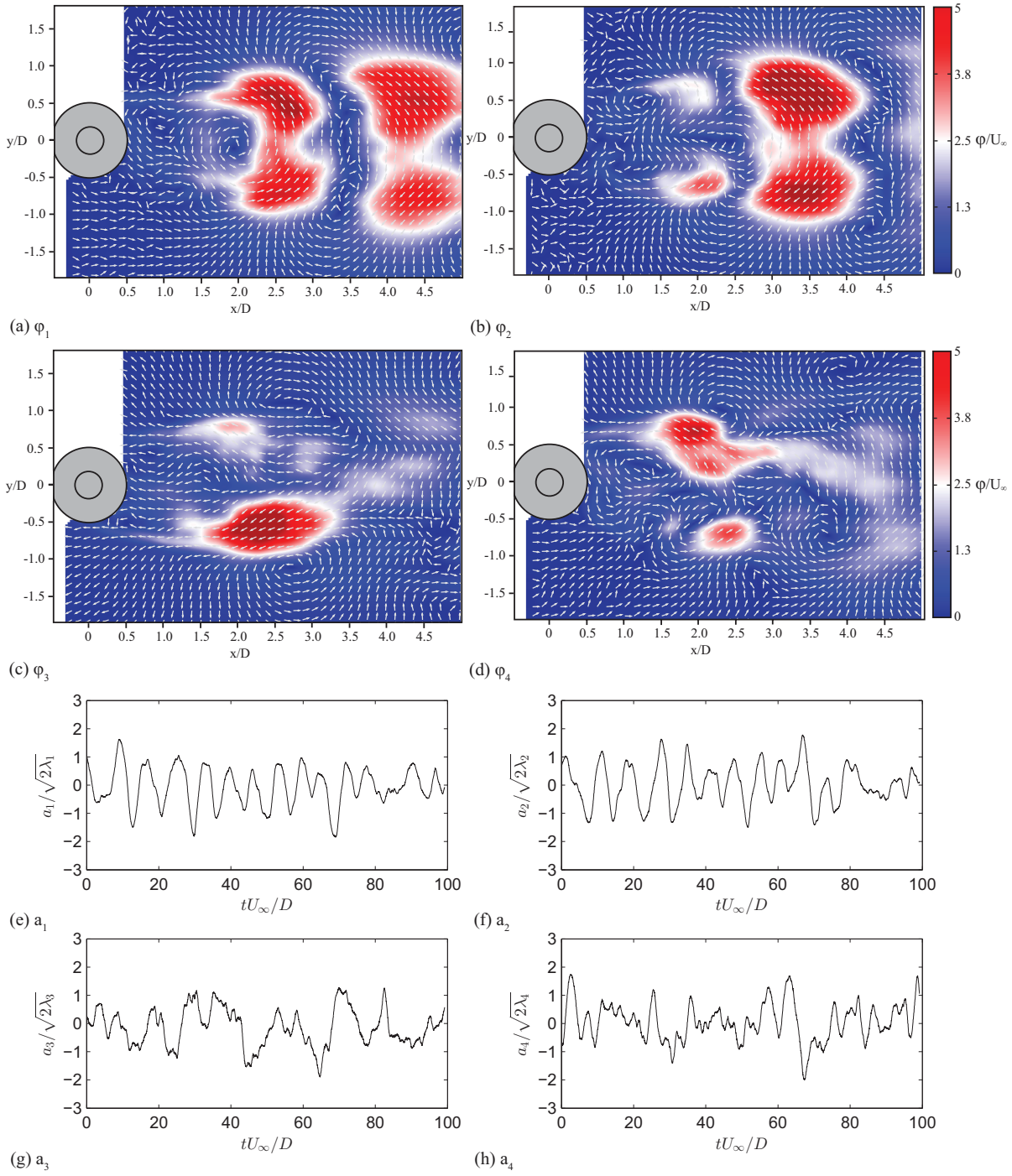

Figure 4.24 Characteristic spatial modes and temporal coefficients in the IS regime for L/D = 2 and D/d = 2.67.

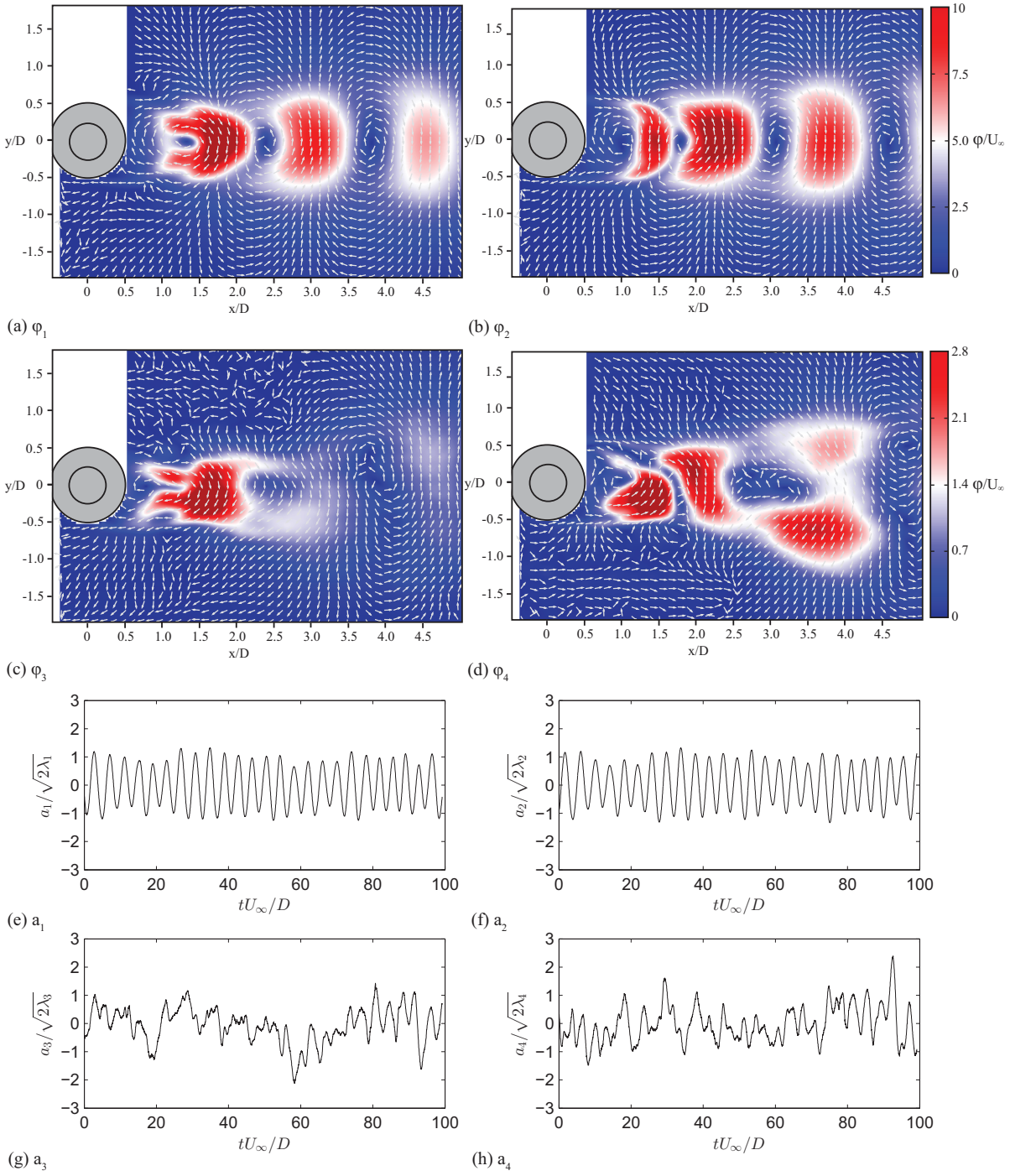

Figure 4.25 Characteristic spatial modes and temporal coefficients in the HFS regime for L/D = 1 and D/d = 2.

.

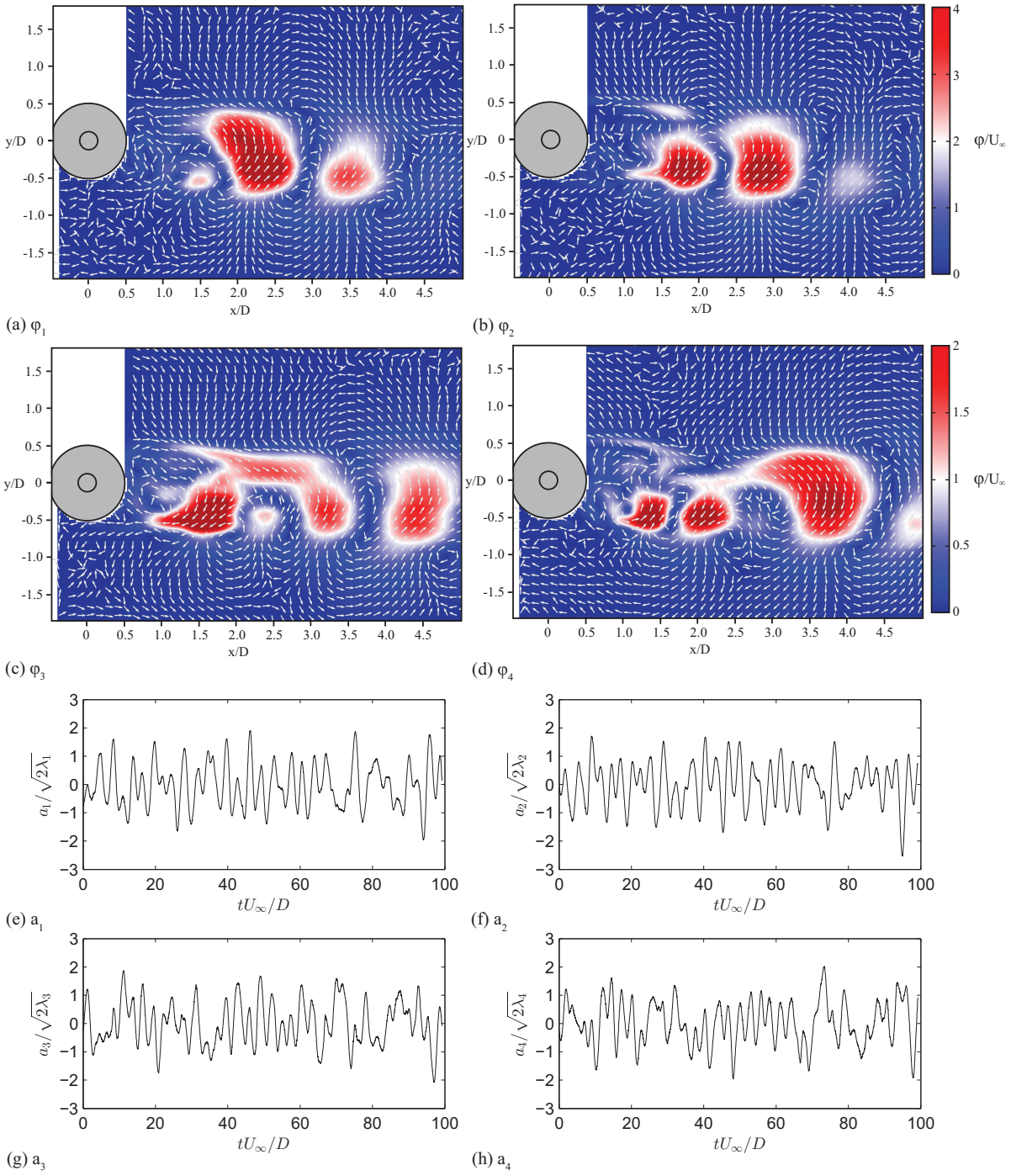

Figure 4.26 Characteristic spatial modes and temporal coefficients in the AIS regime for L/D = 0.5 and D/d = 4.0.

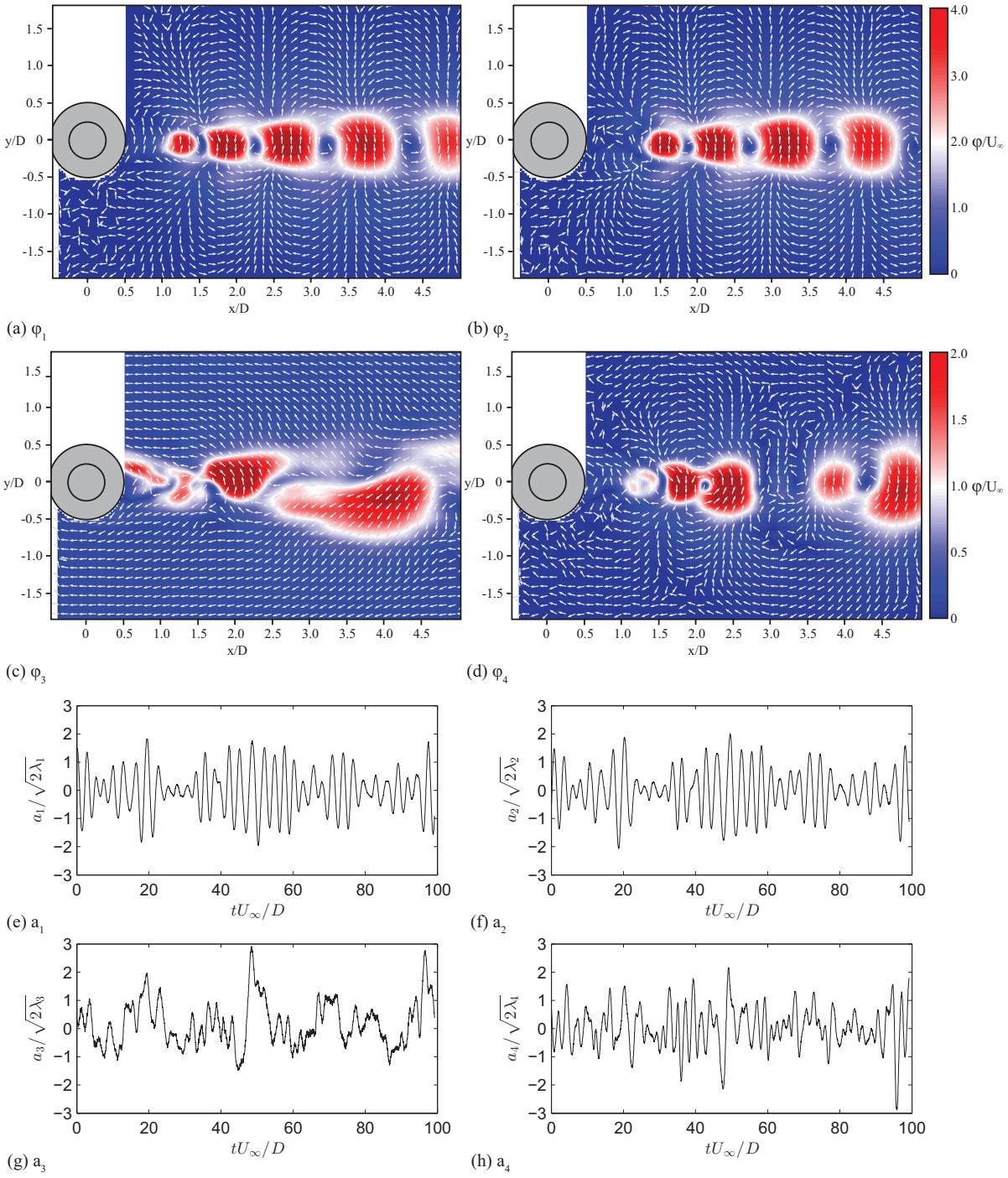

Figure 4.27 Characteristic spatial modes and temporal coefficients in the NS regime for L/D = 0.5 and D/d = 2.

temporal coefficient signals, the majority of the signals approximately match, with one of the signals being phase shifted by $\pi/4$ radians. The one exception is the AIS regime (Figure 4.26) where less than 50% of the temporal coefficient signals match with the prescribed $\pi/4$ radian phase shift. Comparing the uniform cylinder results with those in each flow regime (Figure 4.22-4.27), it can be seen that the first two spatial modes for each flow regime show large scale structures associated with the vortices convecting downstream of the large cylinder. These results confirm that for all flow regimes (except for the AIS regime), the first two modes combined with the corresponding temporal coefficients represent a reduced order model of the vortex shedding in the wake of the large cylinder. Similar to the results for uniform cylinders, the third and fourth temporal modes for each flow regime show less periodicity, and the corresponding spatial modes depict asymmetric structures in the wake that are linked to three-dimensional effects including oblique vortex shedding, vortex deformation, vortex stretching, splitting of vortex filaments, and base flow variation. For the AIS regime, the third and fourth modes are similar to the first two in terms of periodicity and energy content (Figure 4.26 and Figure 4.21) indicating that the development of vortical structures for this flow regime is more complex.

Additional insight into the nature of the vortex shedding occurring in each flow regime is obtained by inspecting the first two temporal coefficients in more detail. As shown in equation 3.11, the variance of a temporal coefficient signal is directly linked to the average energy content associated with the corresponding mode. Therefore, local changes in the amplitude or frequency of the first two temporal coefficient signals are directly linked to changes in the wake development. Large amplitude modulations occur in the first two temporal coefficient signals pertaining to the IS, AIS, and NS flow regimes. This suggests that these regimes exhibit more substantial variations in the strength and coherence of the vortex shedding. The amplitude modulations in the HFS and LFS flow regimes are much smaller, indicating that there is less cycle to cycle variation in the strength and coherence of the vortex shedding. The results are in agreement with results of spectral analysis of velocity data presented in Figure 4.19.

4.4.2 Phase averaging of dominant structures and reduced order models of the wake topology

Phase-averaged flow fields for each model investigated were estimated following the procedure outlined in Chapter 3.3, which utilizes the cross-plot of the first two temporal coefficients in order to extract the phase pertaining to each instantaneous planar velocity field. Upon examination of the results presented in the previous section, for some flow regimes the first two temporal coefficient signals exhibited strong modulations in amplitude and frequency. During these transient periods, topological changes in the wake are expected to occur, therefore, such 'transient' signal periods have been identified through a spectrogram analysis, as described in Chapter 3.4, and are discarded from the phase-averaging analysis. An example set of temporal coefficient signals and their corresponding 'transient' segments are presented in Figure 4.28. The maximum duration of the discarded signal segments is less than 50% of the overall signal length. The phase-averaged results serve to illustrate 'regular' flow topology based on the development of primary spanwise vortices in the large cylinder wake. Phase-averaging was performed on the raw PIV data. Additionally, a reduced order model of the flow field was constructed with the first twenty POD modes for comparison.

Figure 4.29 -4.33 present phase-averaged vorticity contours, as well as instantaneous vorticity field snapshots from a reduced order model containing the first twenty POD modes. The results illustrate the substantial changes in vortex formation and shedding that occur for a dual step cylinder. For most models investigated, the phase-averaged flow field is comparable to the reduced order model of the flow field containing twenty modes. For a uniform cylinder of diameter D (Figure 4.29), the shear layers roll up into spanwise vortices whose size scales with cylinder diameter (Figure 4.29a and b). The vortices form within about two and a half diameters downstream of the cylinder axis. The shear layer roll-up is well defined in the LFS regime as well (Figure 4.31). The results in Figure 4.31 show vortex formation similar to that seen for a uniform cylinder of the same diameter (Figure 4.29), which is also reflected in the marked increase in the energy content of the first two POD modes for these flow regimes (Figure 4.21). In the IS regime, the shear layer roll-up is more difficult to identify, and the attendant shedding of spanwise vortices is less coherent compared to that from a uniform circular cylinder, agreeing with the previous analysis of velocity spectra, flow visualization images,

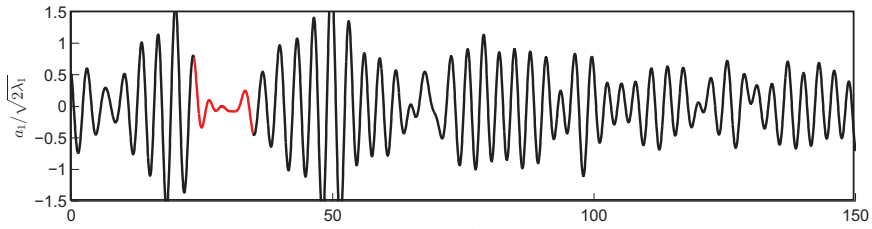

(a) NS, L/D = 0.5, D/d = 2

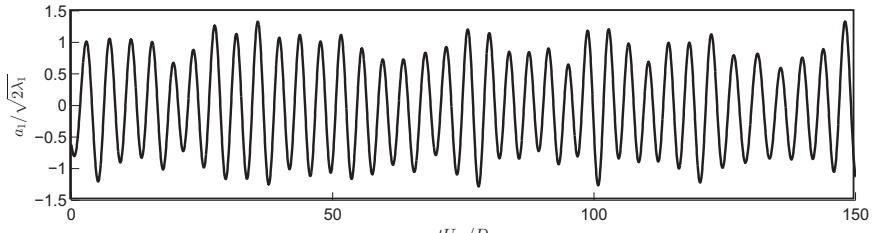

(b) HFS, L/D = 1.0, D/d = 2

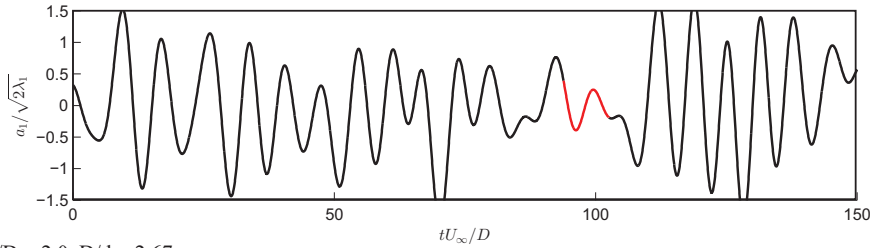

(c) IS, L/D = 2.0, D/d = 2.67

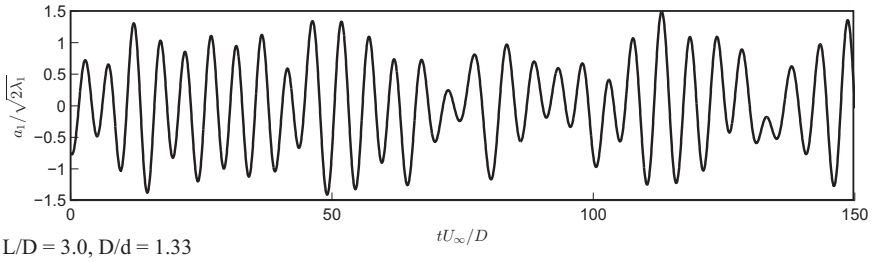

(d) LFS, L/D = 3.0, D/d = 1.33

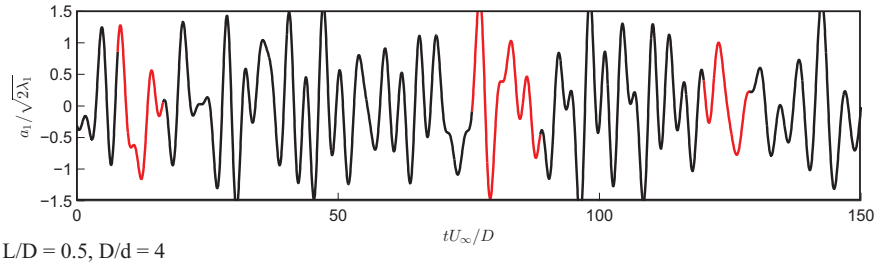

(e) AIS, L/D = 0.5, D/d = 4

Figure 4.28 Representative segments of the first temporal coefficient signal for each identified flow regime. Sections highlighted in red are identified as ‘transient’ segments which are removed from the analysis.

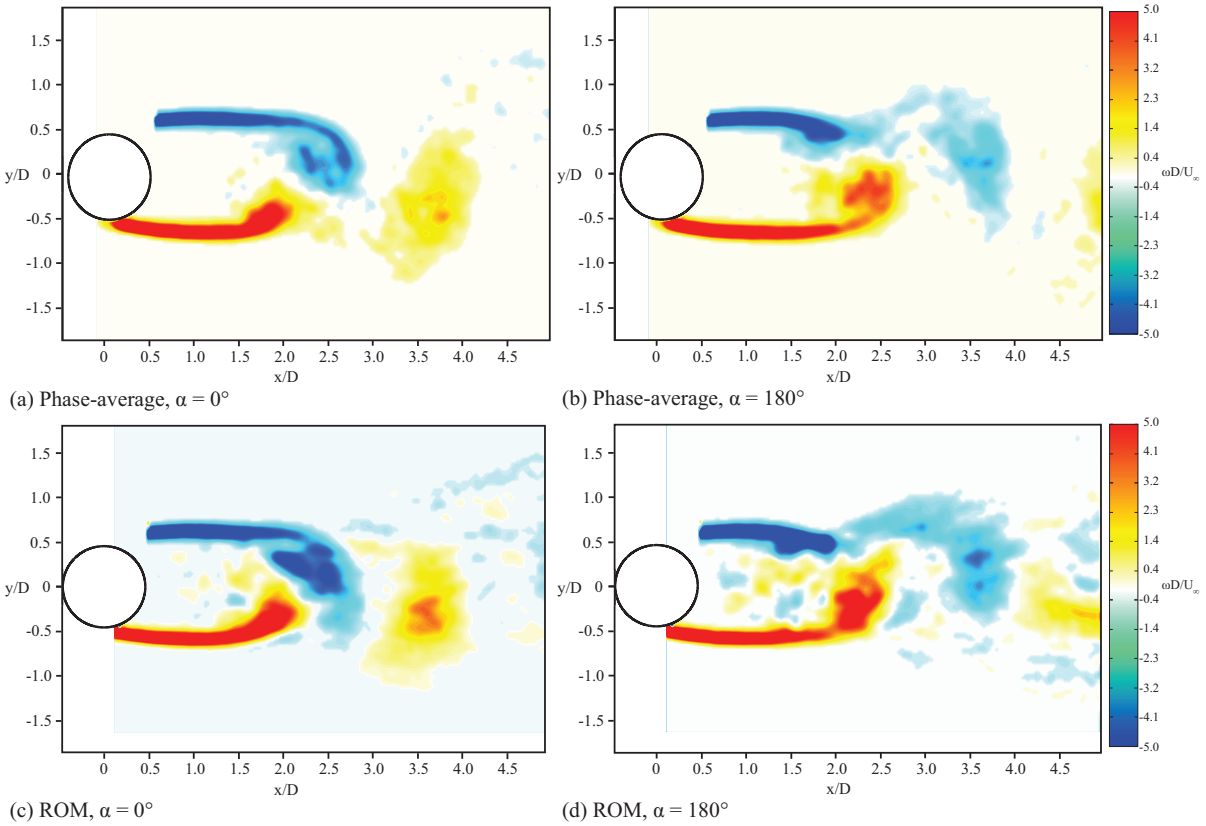

Figure 4.29 Phase averaged flow field and reduced order model of the flow field for a uniform circular cylinder at $Re_D = 2100$.

and results from POD. By comparing Figure 4.29 and Figure 4.30, it can be seen that the vertical distance between the separated shear layer cores in the IS regime is greater than that for a uniform cylinder of the same diameter (Figure 4.29). The implication here is that boundary layer separation occurs earlier, leading to a wider vortex formation region. This is similar to the results of Okamoto & Yagita [52], who found that, for free end cylinders with $6 \leq L/D \leq 12$, the separation point advances upstream with decreasing L/D. Furthermore, as with previous experiments on uniform and free end cylinders (e.g., [20,30,42,52]), the resulting widening of the vortex formation region leads to the decrease in vortex shedding frequency observed in the IS regime in the present study (Figure 4.20). In contrast with the IS regime, the shear layer roll up is well defined for HFS regime (Figure 4.32). The results in Figure 4.32 show vortex formation similar to that seen for a uniform cylinder of the same diameter (Figure 4.29). However, comparing Figure 4.29 and Figure 4.32, it can be seen that the distance between the separated shear layers is reduced for the HFS regime, indicating that boundary

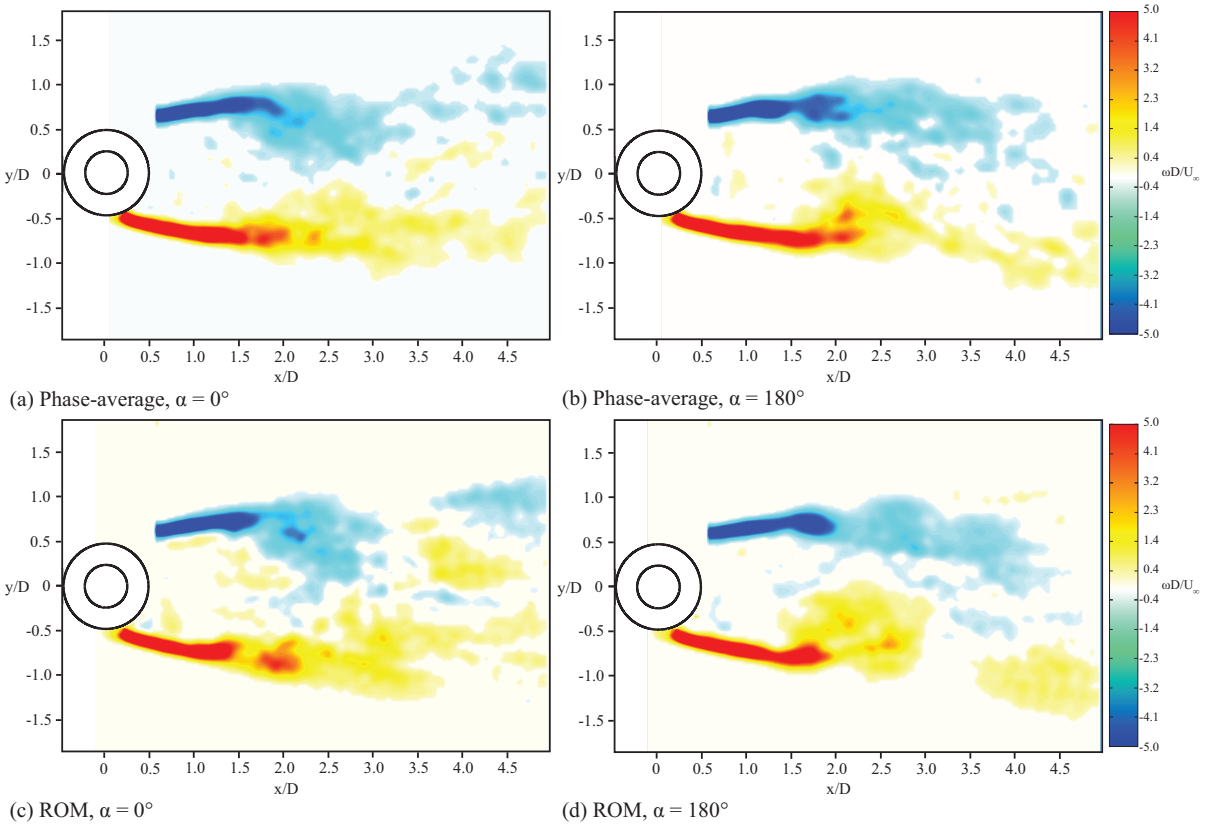

Figure 4.30 Phase averaged flow field and reduced order model of the flow field in the IS regime for L/D = 2, D/d = 2, and Re_D = 2100.

layer separation on the large cylinder is delayed slightly. As a consequence, the size of the formation region is decreased (cf. Figure 4.29a and Figure 4.32a), leading to an increase in vortex shedding frequency.

In the AIS regime, there are drastic changes in the large cylinder wake development, as the large cylinder no longer sheds vortices in an alternating fashion (Figure 4.33). The results indicate that vortices are shed from one side of the cylinder (y/D < 0) while the shear layer on the opposite side of the wake remains relatively steady (Figure 4.33a-b). In order to confirm that the phase-averaged flow field is representative of the actual wake development, a comparison is made with the reduced order model of the wake flow field in Figure 4.33c-d. In the reduced order model of the flow field containing twenty modes it can be seen that shear layer roll-up is only visible on one side of the wake, similar to the phase-averaged flow field results (y/D < 0 in Figure 4.33c-d).

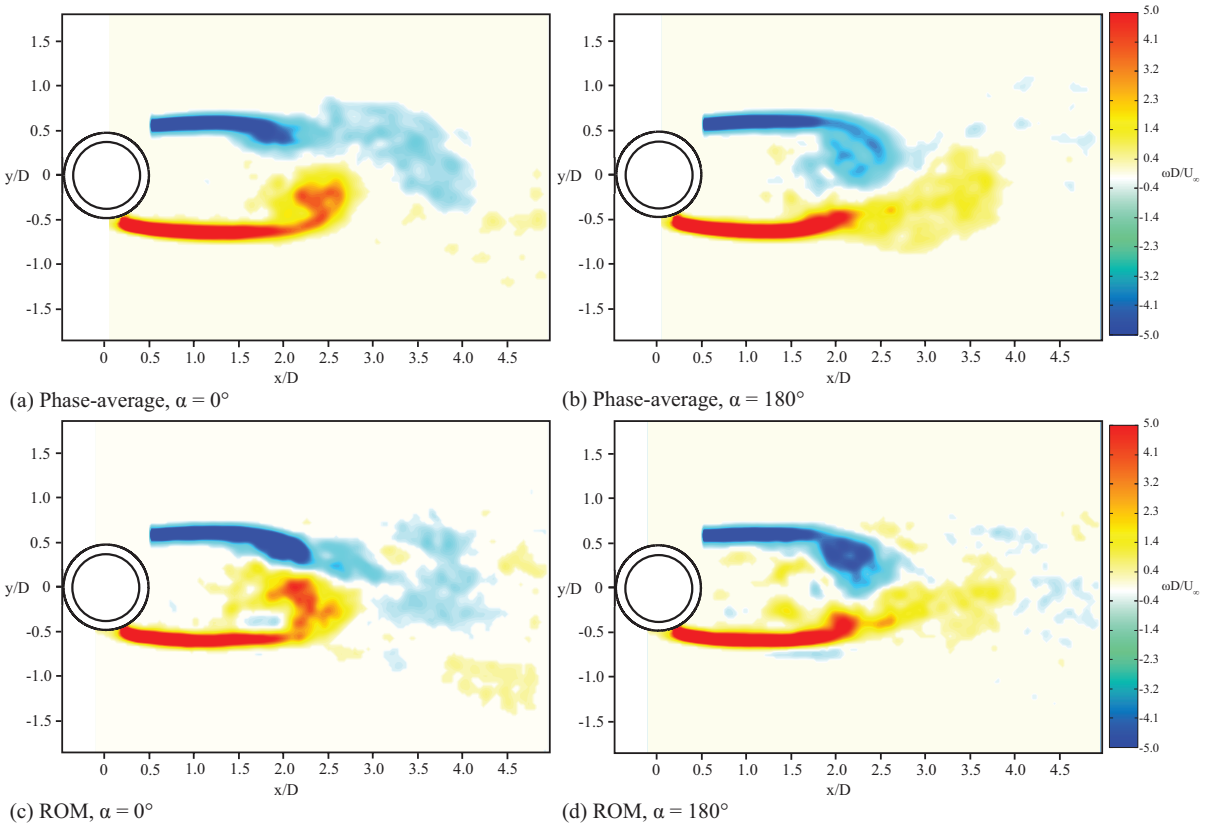

Figure 4.31 Phase averaged flow field and reduced order model of the flow field in the LFS regime for L/D = 3, D/d = 1.33, and Re_D = 2100.

In the NS regime, substantial changes in large cylinder wake development occur (Figure 4.34). The distance between the shear layers is decreased more substantially when compared to the HFS regime, indicating that boundary layer separation on the large cylinder surface is delayed further. For free end cylinders, previous experimental results (e.g., [52]) show that separation is delayed within about 0.5D from the free end of the cylinder. Hence, for dual step cylinders, delayed boundary layer separation at the mid-span of the large cylinder is expected to occur when the length of the large cylinder becomes comparable to the size of the regions of delayed separation near its ends. For L/D = 0.5 and D/d = 2 (Figure 4.34), the separation angle is so large that the shear layers collapse and form a quasi-steady recirculation zone in the near wake, with no evidence of vortex roll-up (Figure 4.34). However, beyond the recirculation zone ($x/D > 1.5$), footprints of vortices whose scale is comparable to the small cylinder diameter (d) can be seen (Figure 4.34a-d). These are produced by vortex filaments connecting small cylinder vortices across the wake of the large cylinder.

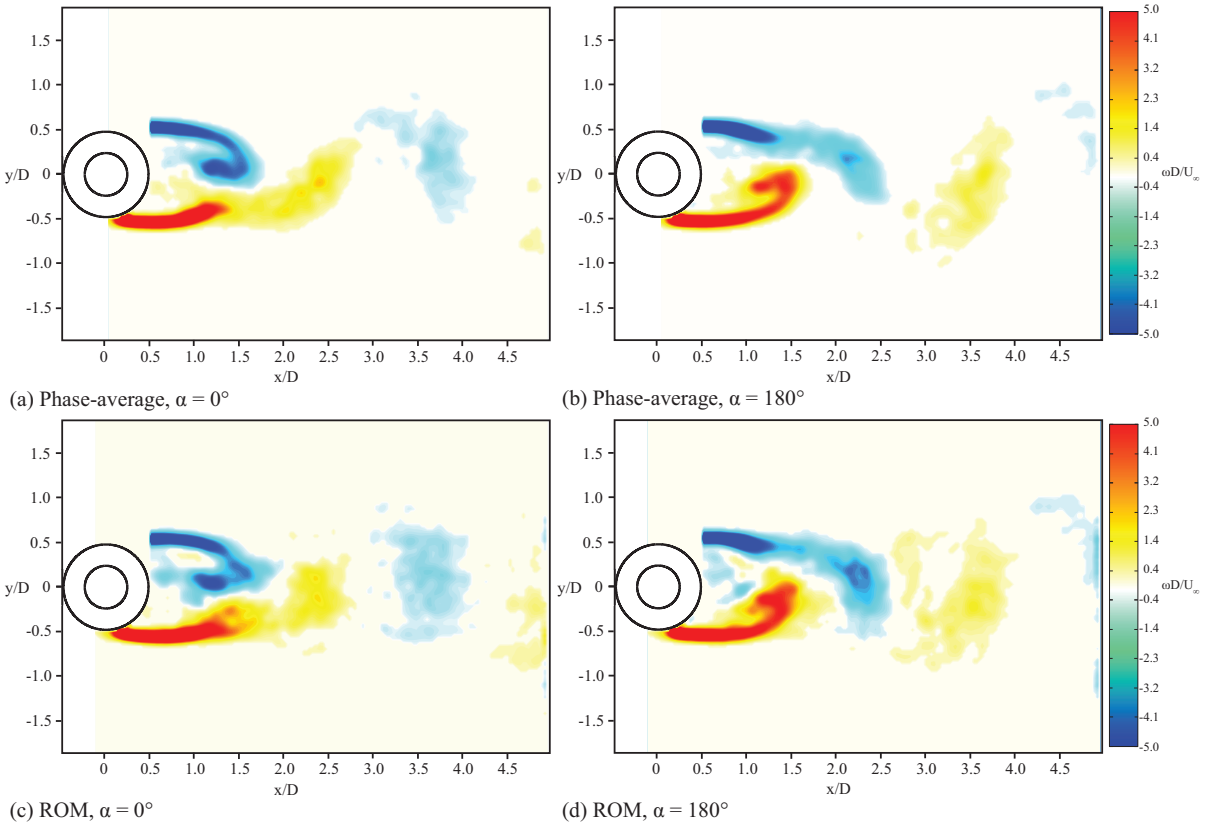

Figure 4.32 Phase averaged flow field and reduced order model of the flow field in the HFS regime for L/D = 1, D/d = 2, and Re_D = 2100.

Substantial changes in the wake topology are yet again observed when the aspect ratio is reduced further within the NS regime at L/D = 0.2 and D/d = 2 (Figure 4.35). Specifically, a shear layer roll-up can be observed, and the vortical structures shed in the near wake are comparable in size to the small cylinder diameter (d). To determine the origin of these vortices, it is instructive to compare the results in Figure 4.35 and those pertaining to a uniform cylinder of diameter d (Figure 4.36). For a uniform cylinder, during the roll-up process, a vortex grows until the supply of vorticity from the shear layer is cut off by a vortex forming on the opposite side of the wake (e.g., [119]). For example, this can be seen in Figure 4.36a, where the lower vortex forming at $x/D \approx 1.25$, $y/D \approx -0.125$ is cutting off the supply of vorticity to the upper vortex at $x/D \approx 1.75$, $y/D \approx 0.125$. However, examining Figure 4.35a, it can be seen that the circulation within the separated shear layers is significantly lower than

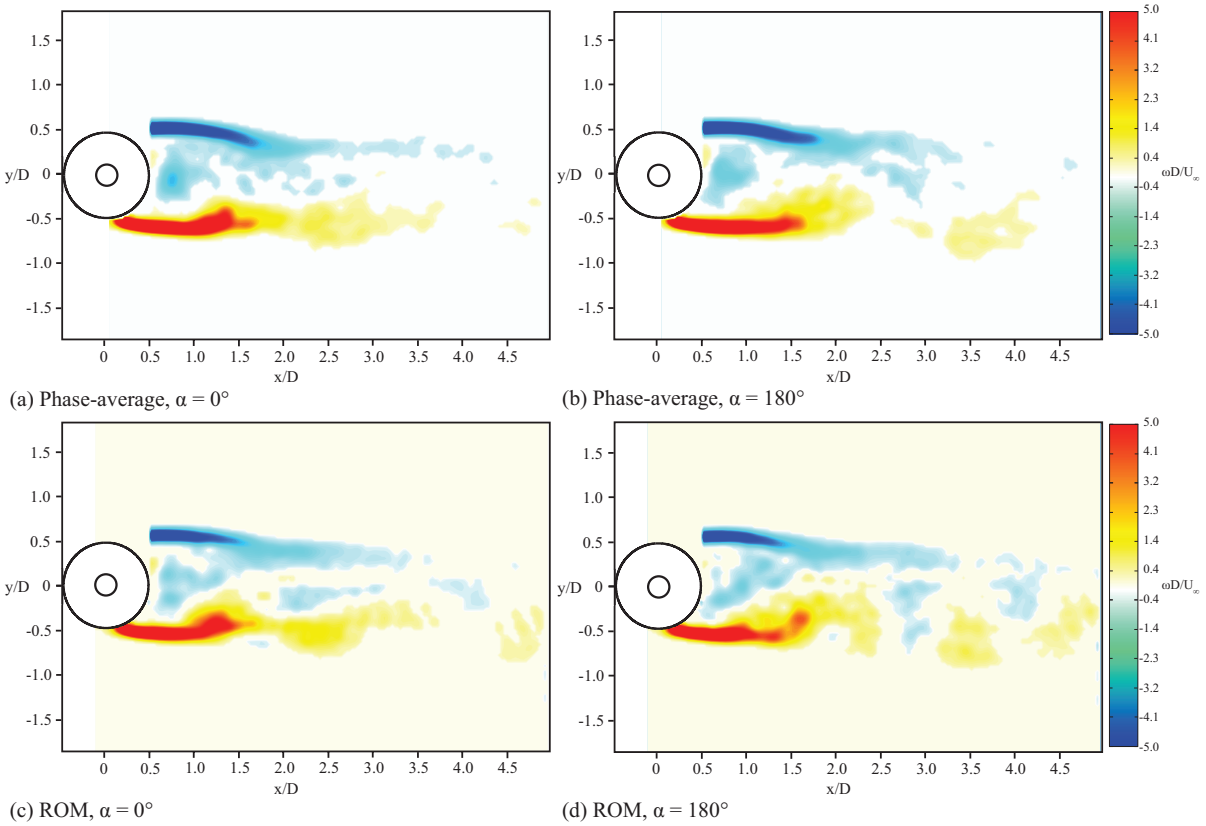

Figure 4.33 Phase averaged flow field and reduced order model of the flow field in the AIS regime for L/D = 0.5, D/d = 4, and Re_D = 2100.

that of the vortices for *L/D = 0.2*, suggesting that the vortices forming in the large cylinder wake cannot originate solely from the shear layers forming on the large cylinder. In fact, the strength of the shed vortices in the large cylinder wake is comparable to that of the vortices shed from the small cylinder (cf. Figure 4.35a-b and Figure 4.36a-b). This confirms that the structures observed in the large cylinder wake at these very low aspect ratios are small cylinder vortices. Furthermore, comparing the results in Figure 4.35 and Figure 4.36, it can be seen that, for *x/D* < *3*, the streamwise spacing of vortices is approximately the same, while the dominant frequency in the corresponding spectra in Figure 4.19 differs by about 20%. This confirms that, the presence of the large cylinder reduces the convective velocity of small cylinder vortices connecting across the large cylinder wake.

The results in Figure 4.34 and Figure 4.35 depict the passage of vortices in the large cylinder wake at a frequency that is slightly less than the shedding frequency of the small diameter cylinder (Figure 4.36). However, the results of spectral analysis show that the small cylinder shedding frequency also

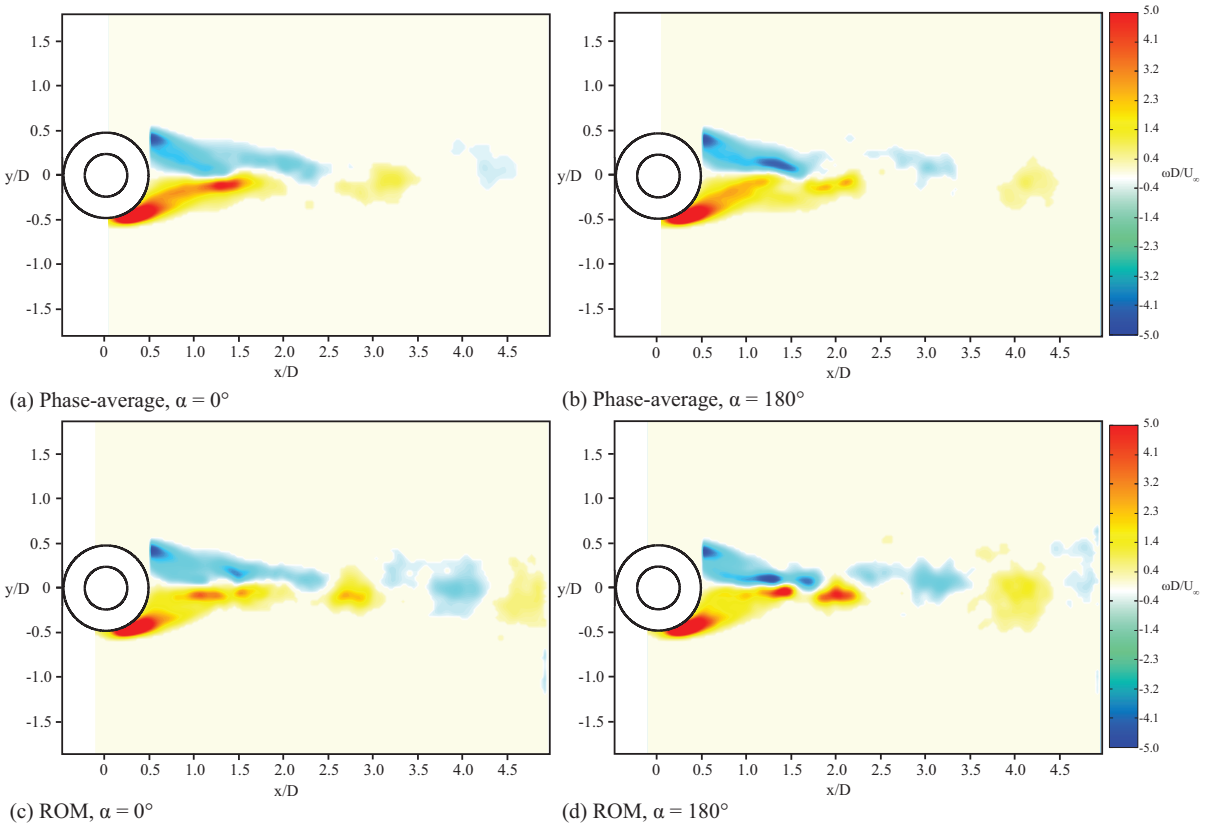

Figure 4.34 Phase averaged flow field and reduced order model of the flow field in the NS regime for L/D = 0.5, D/d = 2.

contributes to wake velocity fluctuations (Figure 4.19). A spectrogram analysis of the wake velocity measurements and temporal coefficient signals has shown that the appearance of energy content associated with small cylinder vortex shedding is intermittent, and has no clearly identifiable relationship to the fluctuations in energy content associated with the dominant frequency in the large cylinder wake. However, an underlying periodicity in the appearance of these frequencies may be masked by turbulent fluctuations in the wake.

In order to confirm the inferred changes in boundary layer separation between the IS, HFS, and NS flow regimes, surface visualizations of boundary layer separation were carried out. Details of the development of the surface visualization technique and its application to uniform cylinder and dual step cylinder flows can be found in Appendix A. Surface and flow visualization results are presented in Figure 4.37 for three flow regimes. The models are rotated from the stagnation point by about ninety

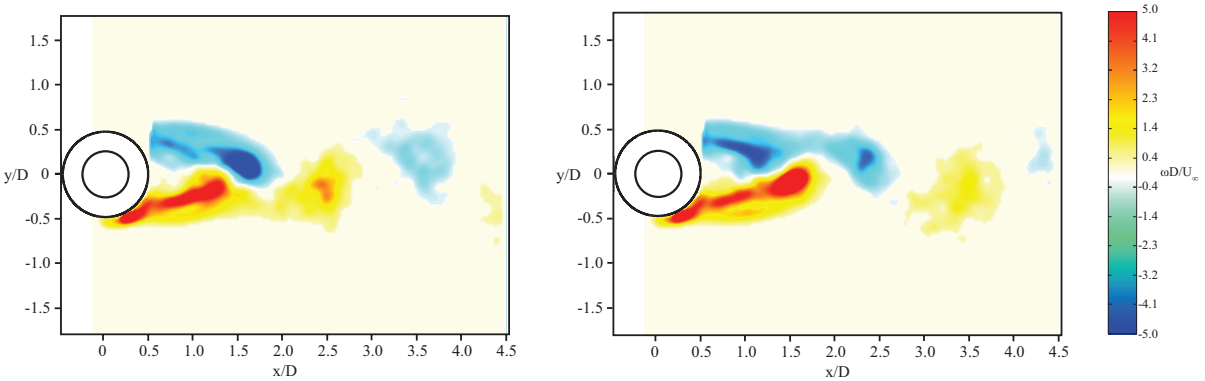

(a) Phase-average, α = 0° (b) Phase-average, α = 180°

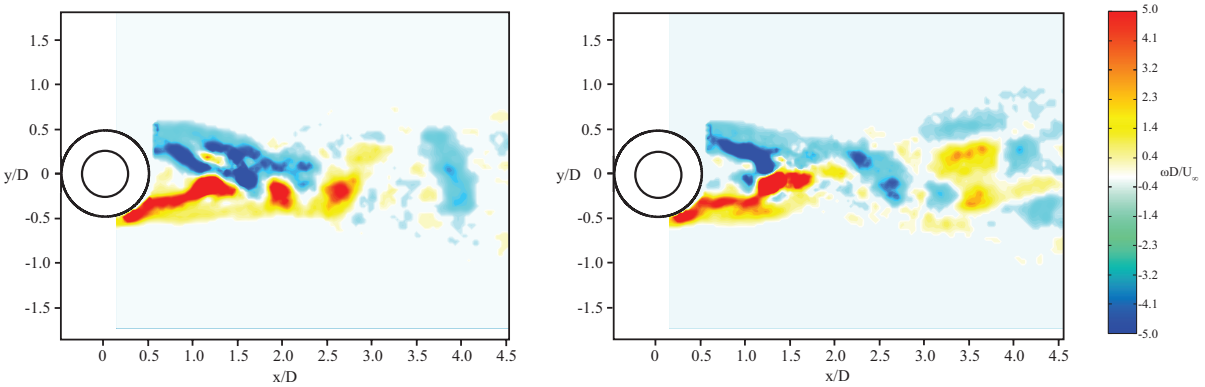

(c) ROM, α = 0° (d) ROM, α = 180°

Figure 4.35 Phase averaged flow field and reduced order model of the flow field in the NS regime at L/D = 0.2, D/d = 2.

degrees, allowing identification of the separation line. The results show that the separation angle increases with decreasing L/D, with $\theta_{sep} \approx 86°, 91°,$ and $105°$ for $L/D = 2, 1,$ and 0.5, respectively (Figure 4.37a,c,e). For comparison, the separation angle for a uniform circular cylinder at $Re_D = 2100$ was measured to be $\theta_{sep} \approx 89°$ (Appendix A). Hence, the results confirm the observed trends in the phase-averaged flow fields. Specifically, in the IS regime (Figure 4.37a-b), flow separation occurs earlier, leading to a wider and longer vortex formation region. For bluff body wakes, the size of the vortex formation region scales inversely with the vortex shedding frequency [114]. This explains the lower frequency vortex shedding measured in the IS regime. In the HFS regime, the separation is delayed (Figure 4.37c-d), the vortex formation region decreases in size, leading to a higher frequency vortex shedding. Finally, in the NS regime, the separation angle becomes delayed further, and the separated shear layers coalesce in the near wake (Figure 4.37e-f).

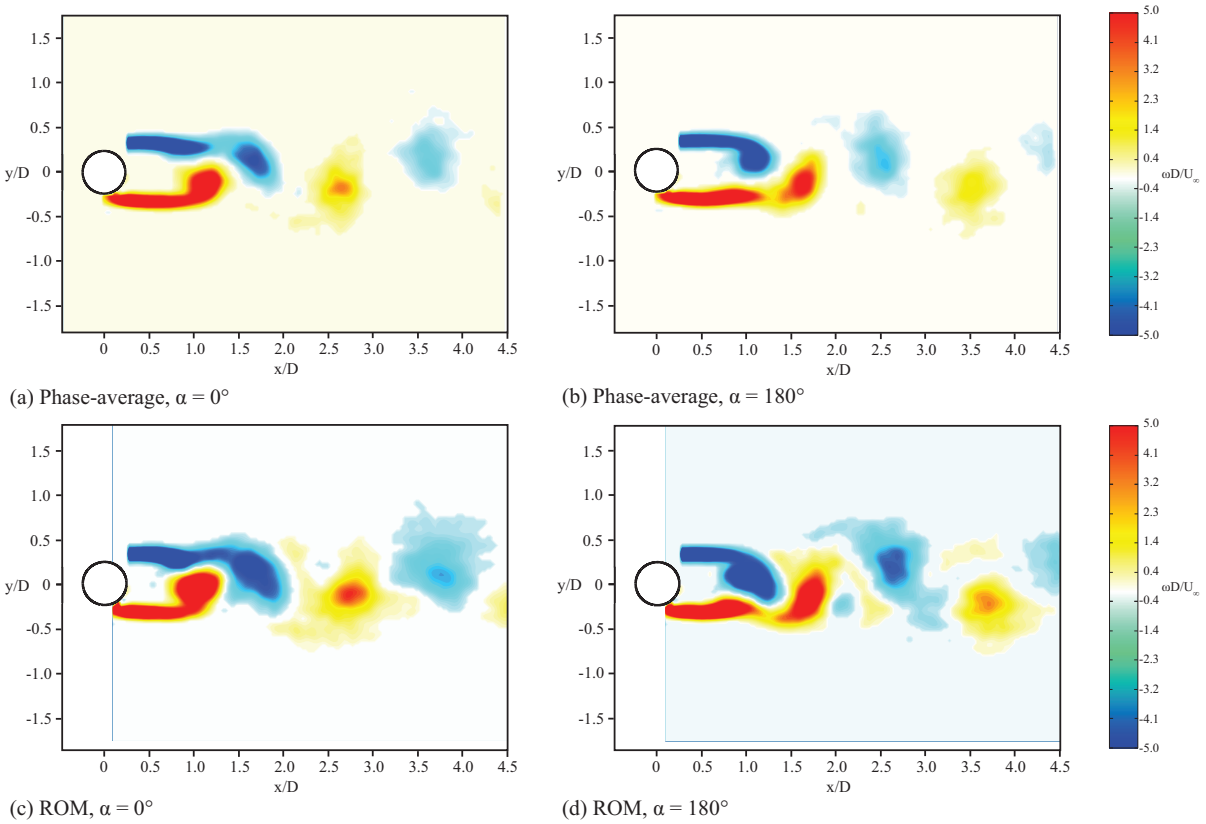

Figure 4.36 Phase averaged flow field and reduced order model of the flow field for a uniform circular cylinder of diameter d, $Re_d = 1050$.

4.4.3 Dual step cylinder wake topology during 'transient' flow periods

It is of interest to characterise large cylinder wake development during 'transient' time periods identified in POD results (Figure 4.28). Figure 4.38 facilitates a comparison of the instantaneous wake structure during 'regular' and 'transient' periods using vorticity fields reconstructed from the first twenty POD modes. During 'regular' periods, the results presented in the previous section show that the instantaneous characteristics of large scale wake structures are similar to those found in the corresponding phase-averaged flow fields. On the other hand, transient periods (Figure 4.38) show dramatically different wake patterns. For example, for the IS regime at $L/D = 2$ and $D/d = 2.67$ (Figure 4.38a), the alternate shedding of vortices is replaced with simultaneous shedding of vortices

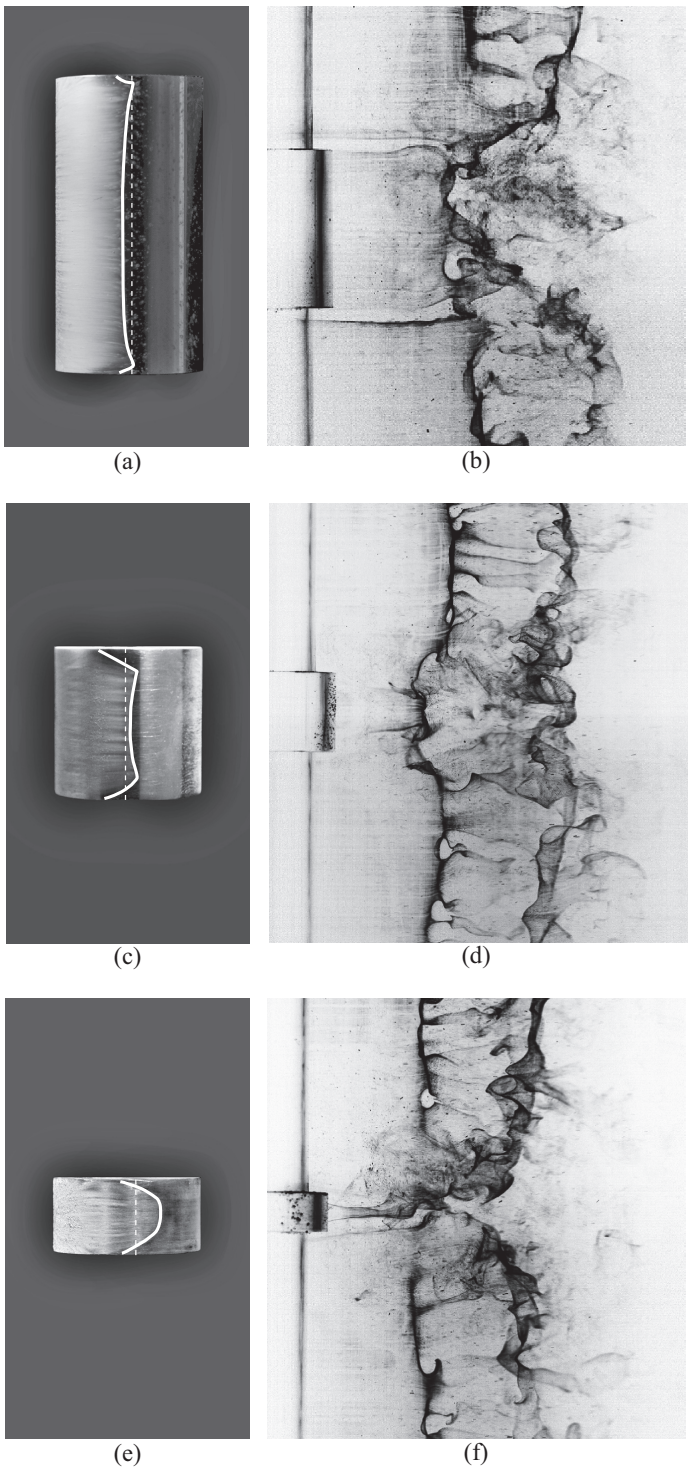

Figure 4.37 Surface and wake visualizations for dual step cylinders at Re_D = 2100: (a)-(b) the IS regime, L/D = 2, D/d = 2, (c)-(d) the HFS regime, L/D = 1, D/d = 2, and (e)-(f) the NS regime, L/D = 0.5, D/d = 2. The dashed white lines in (a),(c),(e), indicate $\theta \approx 90^{\circ}$. Solid white lines highlight the separation line.

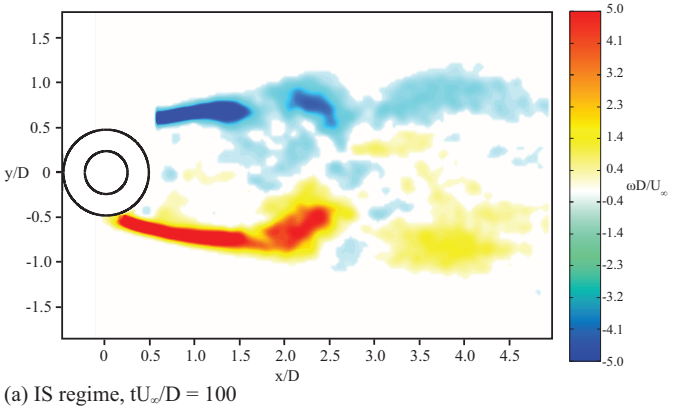

(a) IS regime, $tU_\infty/D = 100$

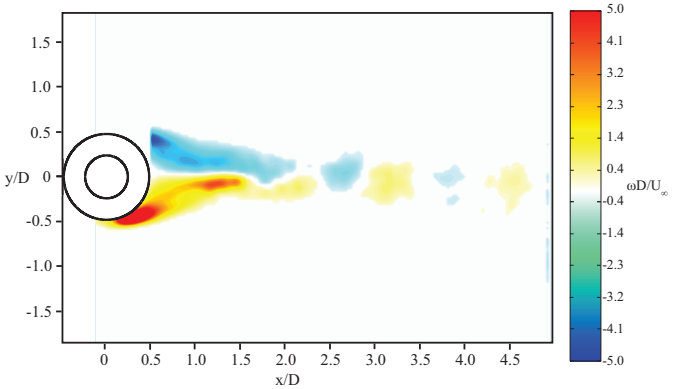

(b) NS regime, $tU_\infty/D = 26$

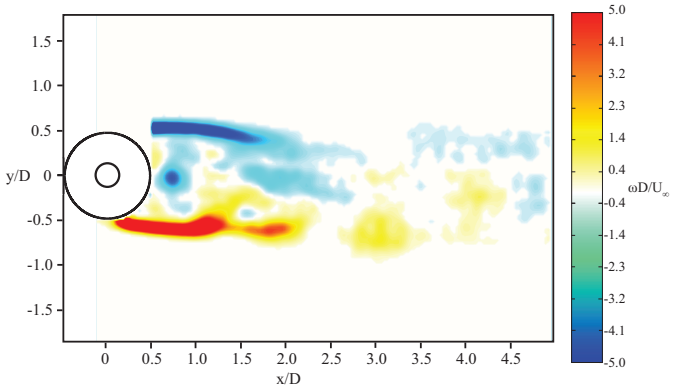

(c) AIS regime, $tU_\infty/D = 78$

Figure 4.38 Reduced order model of the vorticity topology in the wake of a dual step cylinder during 'transient' periods.

from both sides of the large cylinder. This topology was observed within 'transient' periods for all geometries investigated within the IS regime, and has been observed previously for low aspect ratio cantilevered cylinders [120]. In the NS regime, 'transient' periods are predominantly characterized by the doubling of the shedding frequency, resulting in approximately twice the number of alternately shed vortices in Figure 4.38b compared to that in Figure 4.34. Since planar vortices in the large

cylinder wake are the footprints of vortex filaments connecting small cylinder vortices across the wake of the large cylinder, the observed doubling in the frequency of the vortical structures suggests that 'transient' periods are associated with continuous splitting of vortex filaments. For the IS regime (Figure 4.38c), 'transient' periods show a distinct increase in the number of vortices present, indicating that the frequency of vortex shedding changes significantly. As a result, the spacing and arrangement of vortices in the wake changes, making it impossible to obtain a representative phase-averaged flow field that retains the presence of vortical structure beyond the vortex formation region. The results in Figure 4.38 confirm that significant changes in regular wake patterns occur for a dual step cylinder in the NS, IS, and AIS flow regimes. Such changes are manifested by substantial alterations in the shedding characteristics of primary structures, and can be identified through the analysis of the first two temporal coefficient signals extracted from the POD of the PIV data.

4.5 Forces on dual step cylinders in uniform flow

Simultaneous drag and lift force measurements were performed on dual step cylinder models for $Re_D = 2100$, $1.6 \leq D/d \leq 4$, and $0.5 \leq L/D \leq 5$. Additionally, measurements of drag and lift were performed on uniform circular cylinders in order to validate the force balance setup (Appendix D). The aim of this section is to characterize forces induced on the cylinder and relate them to the flow regimes identified earlier.

4.5.1 Drag on dual step cylinders

Figure 4.39 shows the effect of diameter ratio and aspect ratio on the drag coefficient for a dual step cylinder. In Figure 4.39a, the data at D/d = 1 corresponds to the drag coefficient measured for a uniform circular cylinder of diameter D, and, in Figure 4.39b, the data at L/D = 0 corresponds to the drag coefficient measured for a uniform circular cylinder of diameter d. The results in Figure 4.39a show that, for $L/D \geq 2$, the drag coefficient decreases with increasing D/d up to D/d = 2.67, and, for $D/d \geq 2.67$, the drag coefficient remains approximately constant. On the other hand, for $L/D \leq 1$, the drag coefficient does not change significantly with increasing D/d up to D/d = 2.67 (Figure 4.39a) and beyond D/d = 2.67, the drag coefficient increases. For a given D/d, the drag coefficient decreases with

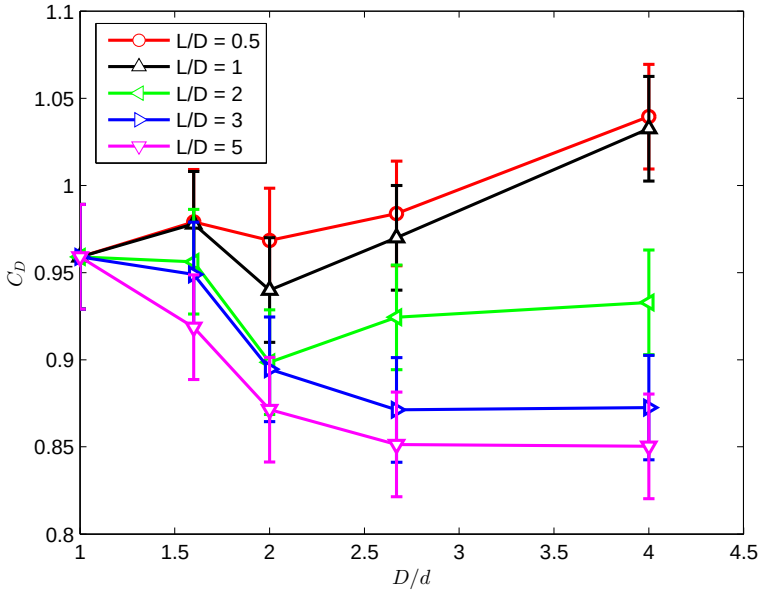

(a)

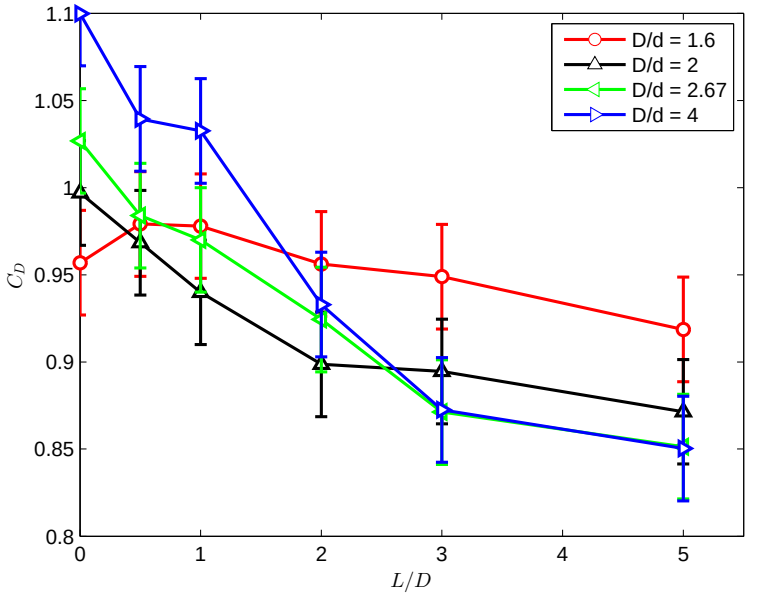

(b)

Figure 4.39 Effects of diameter ratio and aspect ratio on the drag coefficient for a dual step cylinder: (a) C_D vs D/d, (b) C_D vs L/D. The drag coefficient is computed based on the frontal area of the dual step cylinder model. Data at L/D = 0 in (b) pertains to a uniform cylinder of diameter d, while data at D/d = 1 in (a) pertains to a uniform cylinder of diameter D. The vertical bars at each point in the figures represent the estimated measurement uncertainty. C_D is defined based on the frontal area of the dual step cylinder models.

increasing L/D (Figure 4.39b). To establish how the drag coefficient trends are linked to changes in the flow development in the large cylinder wake, Figure 4.40 presents a contour plot of the drag coefficient values overlaid with the two-dimensional map of flow regimes introduced earlier in this chapter. The contour plot shows that the drag coefficient decreases with increasing D/d and L/D towards the IS regime (Figure 4.40). Within the IS regime, the drag coefficient reaches a minimum for L/D = 5 and D/d = 4 (Figure 4.40).

In order to evaluate the influence of the large cylinder on the drag of the dual step cylinder, the drag force on the large cylinder is estimated by subtracting the drag produced on the small cylinders of diameter d above and below the large cylinder from the measured dual step cylinder drag force. The drag produced on the small cylinders is estimated using uniform cylinder drag data (Appendix D). A validation of the large cylinder drag estimation method is illustrated in Figure 4.41. The results in Figure 4.41 show that as D/d increases, the estimated drag coefficient on the large cylinder decreases

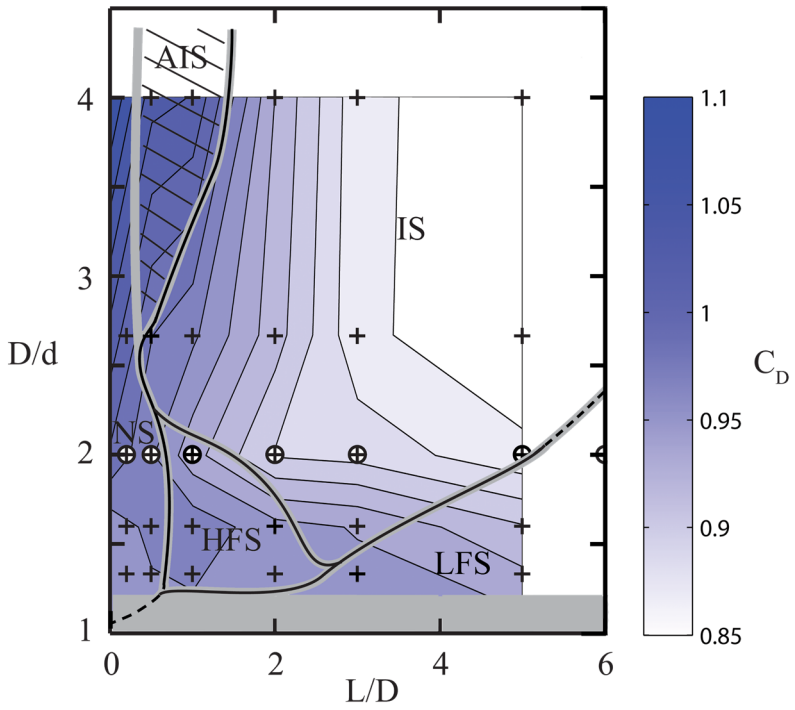

Figure 4.40 Contour plot of the drag coefficient for a dual step cylinder. The boundaries between different regimes are marked by solid and dashed lines, with the latter drawn based on extrapolation of the present data and results from other relevant studies. + symbols represent the L/D and D/d investigated at Re_D = 2100, ○ symbols represent the L/D and D/d investigated at Re_D = 1050.

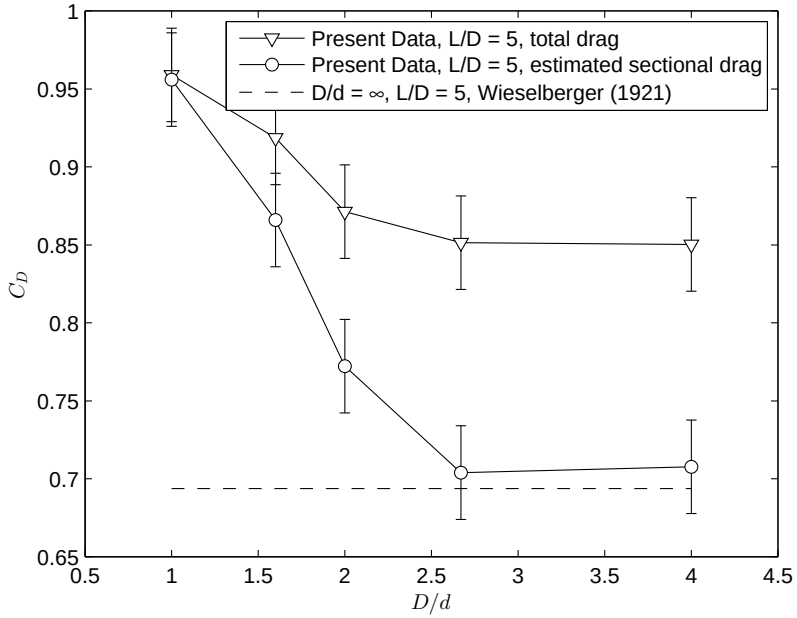

Figure 4.41 Estimates of the drag coefficient for L/D = 5. The vertical bars at each point in the figures represent the estimated measurement uncertainty.

to a value approximately matching that obtained by Wieselberger [68] for L/D = 5 and D/d = ∞ (Figure 4.41). As D/d increases, the effect of the small diameter cylinders on the large cylinder wake development and structural loading becomes negligible, i.e., for about D/d ≥ 2.67 in Figure 4.41. It can be inferred from the results in Figure 4.40 that the drag force on the large cylinder can be estimated for all dual step cylinder models.

The drag force on the large cylinder for all models is obtained using the above described force estimation approach. Figure 4.42 shows the estimated drag coefficient for the large cylinder, and Figure 4.43 shows the drag force on the large cylinder relative to that of a uniform cylinder of the same length and diameter d. The data at D/d = 1 in Figure 4.42 corresponds to the measured drag coefficient for a uniform cylinder of diameter d. The results in both Figure 4.42 and 4.43 show that for L/D = 0.5, 1.0, 2.0, and 3.0, a local minimum in the large cylinder drag occurs for D/d = 2. The lowest drag on the large cylinder occurs at L/D = 0.5 and D/d = 2, and approximately corresponds to the drag on a uniform cylinder of diameter d, $F_D^L/F_D^S \approx 1$ (Figure 4.43). While none of the models result in a drag force that is smaller than that found for a uniform circular cylinder of diameter d, there remains a

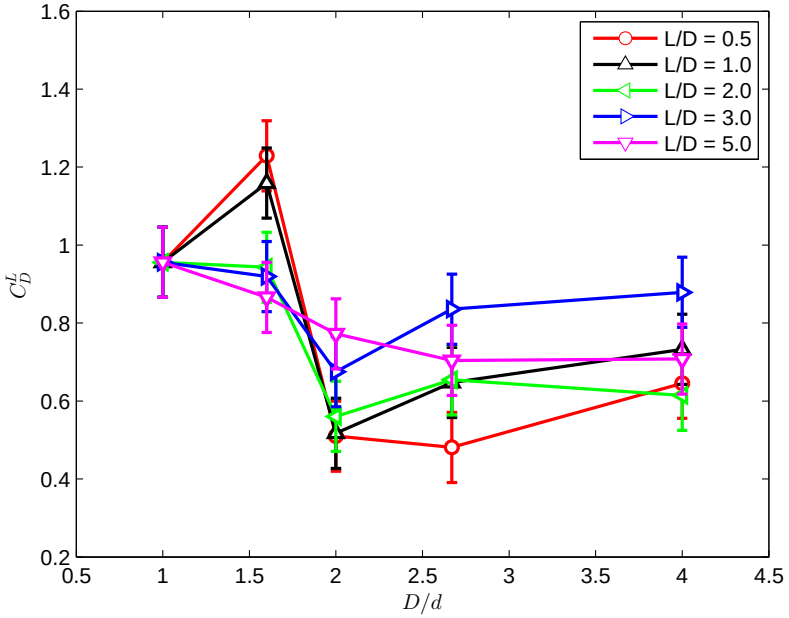

Figure 4.42 Estimates of the drag coefficient on the large cylinder. The vertical bars at each point in the figures represent the estimated measurement uncertainty.

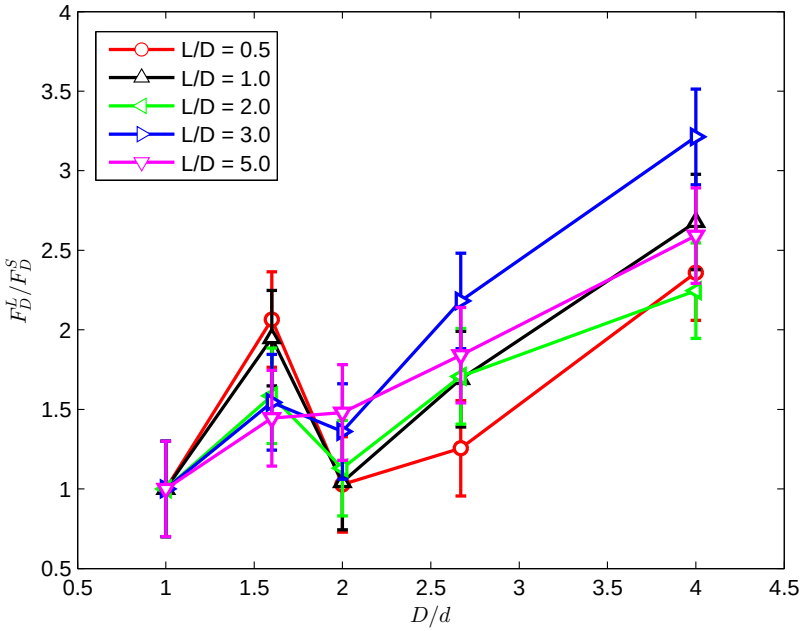

Figure 4.43 Estimates of drag force on the large cylinder relative to that of a small diameter cylinder with the same length. The vertical bars at each point in the figures represent the estimated measurement uncertainty.

possibility that intermediate geometrical parameters result in drag reduction or are not resolved due to the relatively high measurement uncertainty.

In order to illustrate how the estimated drag on the large cylinder changes with each flow regime, Figure 4.44 and 4.45 present contour plots of the large cylinder drag data overlaid with the map of flow regimes introduced at the beginning of this chapter. The results show that the minimum large cylinder drag values are produced near the intersection of the HFS, NS, and IS flow regimes (Figure 4.45). Additionally, the results show that substantial changes in the large cylinder drag occur within each flow regime. In the IS regime, the drag force can be between one and three times that found for a uniform small diameter cylinder (Figure 4.45). In the HFS, AIS, and NS regimes, the drag on the large cylinder ranges between about one and two times that found for a uniform small diameter cylinder (Figure 4.45). In the LFS regime, the drag is about 1.5 times larger than that found for a uniform small diameter cylinder.

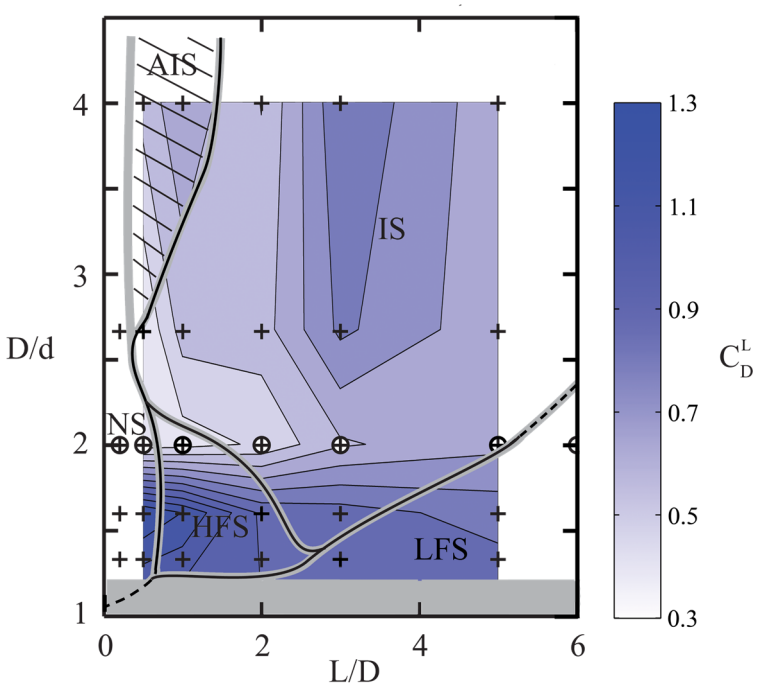

Figure 4.44 Contour plot of drag coefficient estimates for the large cylinder. Note, the boundaries between different regimes are marked by solid and dashed lines, with the latter drawn based on extrapolation of the present data and results from other relevant studies. + symbols represent the L/D and D/d investigated at $Re_D = 2100$, ○ symbols represent the L/D and D/d investigated at $Re_D = 1050$.

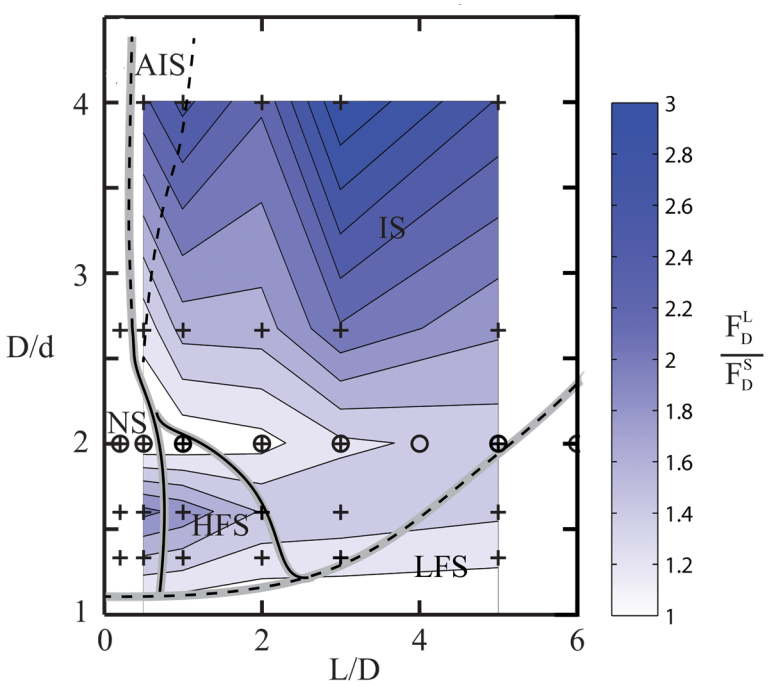

Figure 4.45 Contour plot of the estimated drag on the large cylinder relative to a uniform cylinder of diameter d with the same length. Note, the boundaries between different regimes are marked by solid and dashed lines, with the latter drawn based on extrapolation of the present data and results from other relevant studies. + symbols represent the L/D and D/d investigated at Re_D = 2100, ○ symbols represent the L/D and D/d investigated at Re_D = 1050.

It should be noted that the presence of the large diameter cylinder affects the flow development in the wake of the small diameter cylinders as well, especially near the step discontinuities (e.g., Figure 4.16). Therefore, the structural loading on the small diameter cylinders will be affected by the presence of the large cylinder. While this is not expected to significantly impact the results presented in Figures 4.43 to 4.45, it should be acknowledged that the actual drag force on the large cylinder may vary from the reported values.

4.5.2 Lift on dual step cylinders

Figure 4.46 presents the RMS lift on the dual step cylinder models normalized by the RMS lift measured for a uniform small diameter cylinder (Appendix D). The results show that the lift fluctuations are reduced for all D/d and L/D investigated when compared to the lift fluctuations produced on a uniform base cylinder of diameter d. This is attributed to the presence of the discontinuities in diameter which disrupt the coherence of the vortex shedding along span of the model.

In particular, the small cylinder vortex shedding above and below the large cylinder will continuously move in and out of phase due to small differences in the shedding frequency above and below the large cylinder, leading to the observed reduction in lift RMS. The largest reduction in lift force fluctuation of 60% is found within the IS regime for high L/D and D/d values. This is expected, since in the IS regime, shear layer roll-up is displaced away from the wake centerline and further downstream (Figure 4.13 and 4.14). As a result, near wake velocity fluctuations are weaker at base of the large cylinder when compared to those of a uniform cylinder. This reduces the fluctuating forces on the large cylinder, leading to the observed reduction in RMS lift. Moreover, the vortices shed from the large cylinder in the IS regime are substantially weaker than those found in all other flow regimes. This helps to explains why the fluctuating lift force in the IS regime is the smallest of all flow regimes. Note that for smaller D/d and L/D within the IS regime the lift force fluctuations are substantially higher. This attributed to aspect ratio effects on lift force fluctuations on each of the small diameter cylinders.

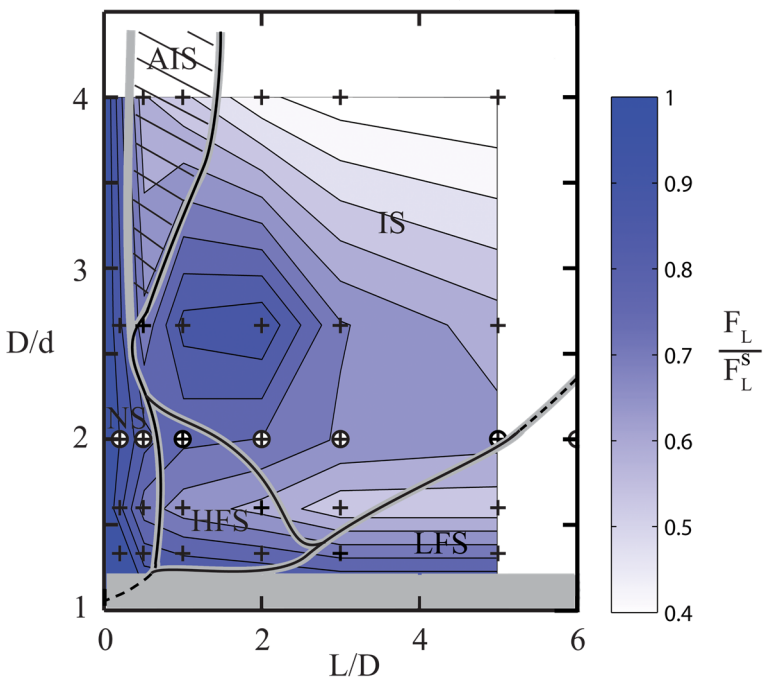

Figure 4.46 Contour plot of the lift force fluctuations on the dual step cylinder relative to a uniform cylinder of diameter d. Note, the boundaries between different regimes are marked by solid and dashed lines, with the latter drawn based on extrapolation of the present data and results from other relevant studies. + symbols represent the L/D and D/d investigated at $Re_D = 2100$, ○ symbols represent the L/D and D/d investigated at $Re_D = 1050$.

It should be noted that the lift RMS measurements reported here have a substantially higher uncertainty when compared to the drag measurements, at approximately ±50% of the measured values (Appendix C). This needs to be considered when interpreting the trends in measured RMS lift with D/d, L/D or between different flow regimes.

4.6 Conclusion

The flow over dual step cylinders has been investigated experimentally using flow visualization, LDV measurements, PIV measurements, and drag and lift force measurements for two Reynolds numbers, Re_D = 1,050 and 2,100, a range of aspect ratios, $0.2 \leq L/D \leq 17$, and diameter ratios, $1.33 \leq D/d \leq 4$. Through an analysis of the qualitative and quantitative measurements, six distinct flow regimes have been identified based on observed changes in the flow development downstream of the large cylinder. While there are slight variations in the large and small cylinder wake topologies within each flow regime, it is of interest to develop a generalized three-dimensional sketch of the overall wake development for each regime. Using the data presented in this chapter, simplified models of the wake development are constructed for each regime and presented in Figures 4.47 to 4.51. The nature of vortex interactions depends primarily on the circulation of vortices at formation and its rate of decay, the frequency of vortex shedding, and three-dimensional effects due to the presence of the step discontinuities. For turbulent flows, cycle-to-cycle variation in the circulation of vortices in the wake of a dual step cylinder are expected to be up to 50% [121,122], which can impact the vortex connectivity at any given instant. Therefore, the presented sketches are an average depiction of the observed wake development pertaining to a given flow regime.

In the LFS and CS regimes (Figure 4.47 and Figure 4.48), which occur for high aspect ratio dual step cylinders, vortex shedding from the large cylinder occurs in one or more distinct cells, with the coherence and strength of the vortex shedding resembling that of a uniform circular cylinder. The vortex shedding frequency is slightly lower than that found for uniform circular cylinders, which is attributed to slightly earlier boundary layer separation along the large cylinder. The vortex interactions between the distinct cells in these flow regimes is similar to that observed in the wakes of single step

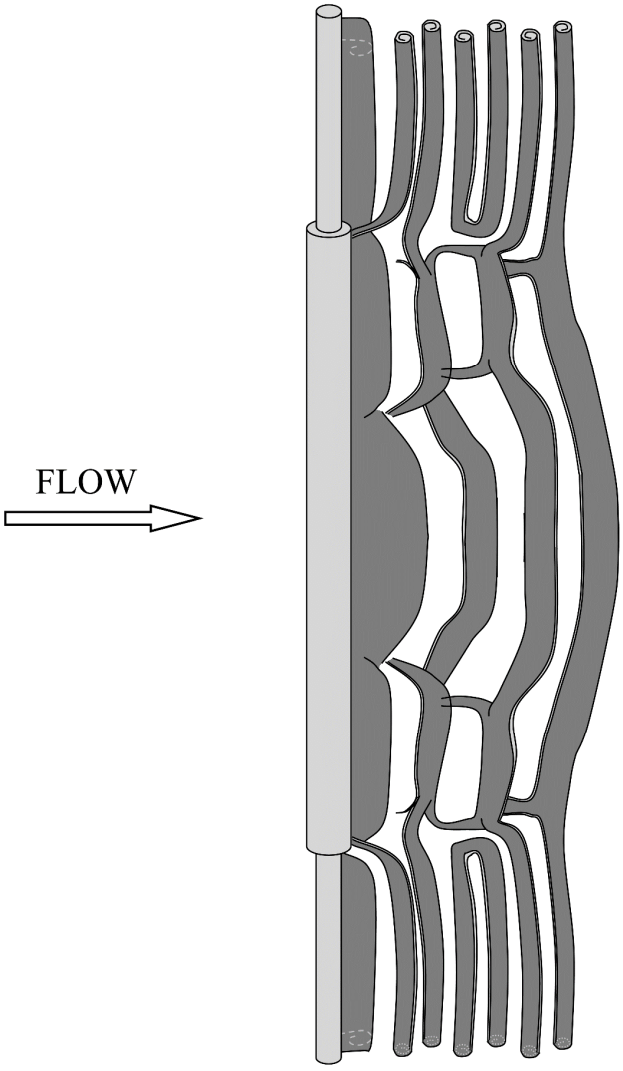

Figure 4.47 Topological sketch of the flow development past a dual step cylinder in the CS regime.

cylinders and cantilevered cylinders, where vortex dislocations occur periodically and are manifested by both vortex splitting and half-loop vortex connections.

At lower L/D, a transition to the IS regime occurs. In this regime (Figure 4.49), at the mid-span of the large cylinder, the vortex formation region is wider when compared to that found for a uniform cylinder of the same diameter, and is attributed to earlier boundary layer separation. The vortex shedding frequency is lower and the shedding is highly three-dimensional, being characterized by lower coherence compared to vortex shedding from a uniform circular cylinder. The wake vortex dynamics involves small cylinder vortices primarily forming a continuous band of half-loop vortex

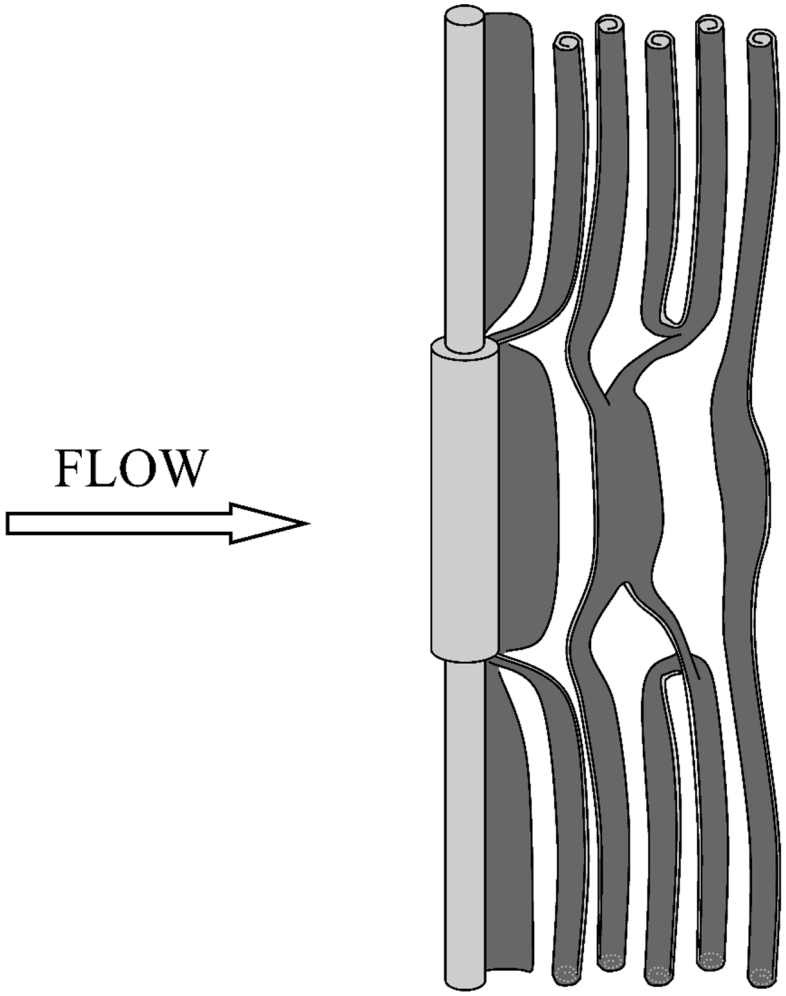

Figure 4.48 Topological sketch of the flow development past a dual step cylinder in the LFS regime.

connections in the wake, while the large cylinder vortices terminate on themselves, forming vortex loops (Figure 4.49). Kelvin-Helmholtz instability vortices intermittently form within the separated shear layers of the large cylinder, as well as within transverse-oriented shear layers forming downstream of each step discontinuity (Figure 4.49).

When the aspect ratio and diameter ratio of the large cylinder is reduced and the HFS regime is approached, the vortex formation region at the mid-span of the large cylinder begins to narrow, indicating that the boundary layer separation starts to shift downstream. This occurs due to the increasing influence of the flow near stepwise discontinuities, since, similar to free-end cylinders (e.g., [52]), separation is delayed significantly within about *0.5D* of the large cylinder ends. As a result, the

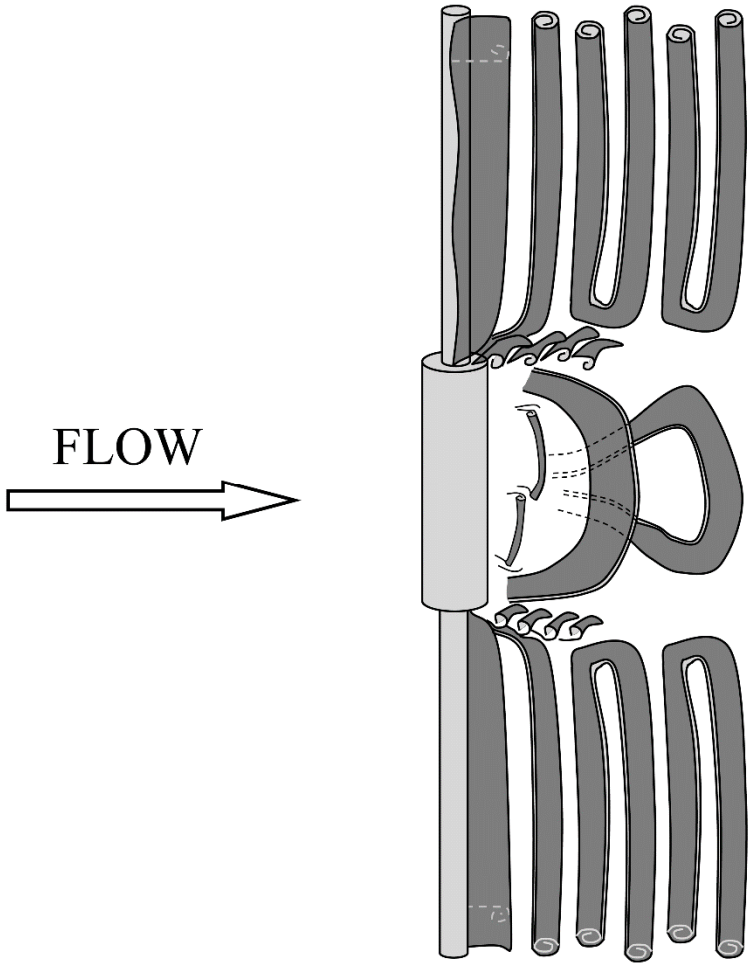

Figure 4.49 Topological sketch of the flow development past a dual step cylinder in the IS regime.

shedding frequency in the large cylinder wake starts to increase with decreasing L/D. Within a narrow range of diameter ratios around L/D = 1.5, the coherence and strength of the shed vortices increases, with well-defined periodic vortex shedding occurring from the large cylinder at a frequency higher that that expected for a uniform cylinder (Figure 4.50). In this HFS regime, small and large cylinder vortices form vortex connections downstream of each step discontinuity in diameter, and vortex dislocations occur periodically due to the difference in their shedding frequencies.

When *L/D* is reduced below about one, the wake narrows, and vortex shedding from the large cylinder can become asymmetric and one-sided (AIS regime), or cease entirely (NS regime) (Figure 4.51). When vortex shedding has ceased (NS regime), small cylinder vortices connect across the large

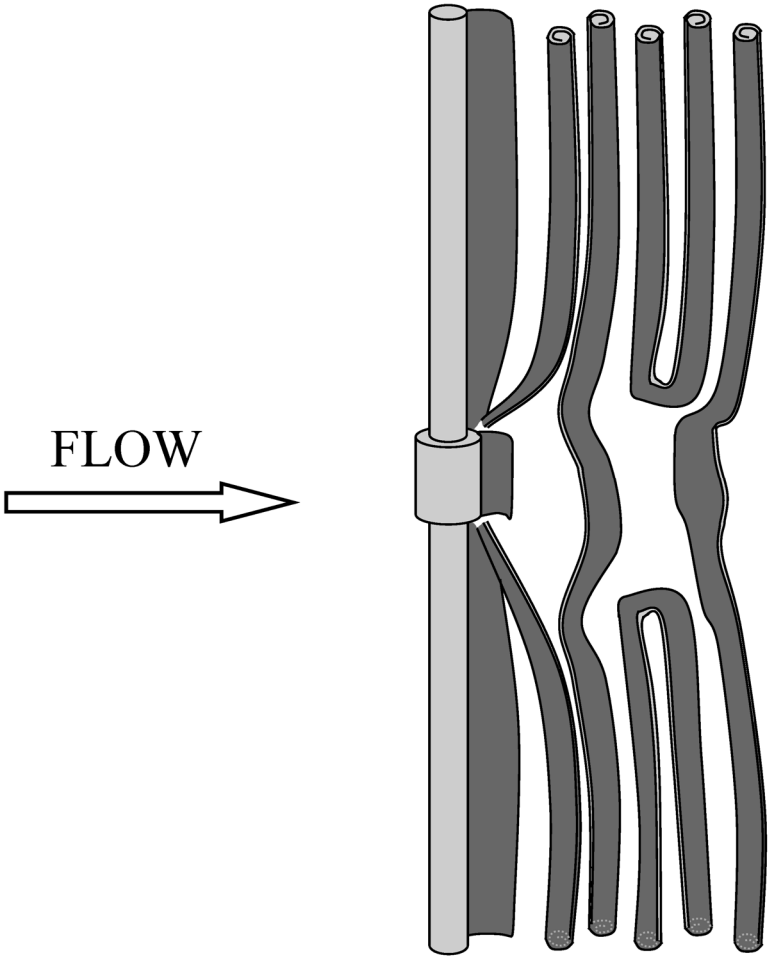

Figure 4.50 Topological sketch of the flow development past a dual step cylinder in the HFS regime.

cylinder wake, and, hence, the dominant frequency in the large cylinder wake is attributed to the passage of these vortex filaments. However, the presence of the large cylinder affects their convective velocity. This results in progressive deformation of vortex filaments and periodic formation of vortex dislocations, manifested by half-loop vortex connections (Figure 4.51). With decreasing *L/D*, the dominant frequency in the large cylinder wake approaches the small cylinder shedding frequency, and the frequency of vortex dislocations decreases.

It should be noted that Reynolds number has an effect on the wake characteristics within each regime, and the transition between flow regimes. In particular, there are minor differences in the appearance and transition between the main wake topologies depending on Re_D. Within the IS regime, at $Re_D = 2100$, shear layer instability vortices intermittently form within the separated shear layers and

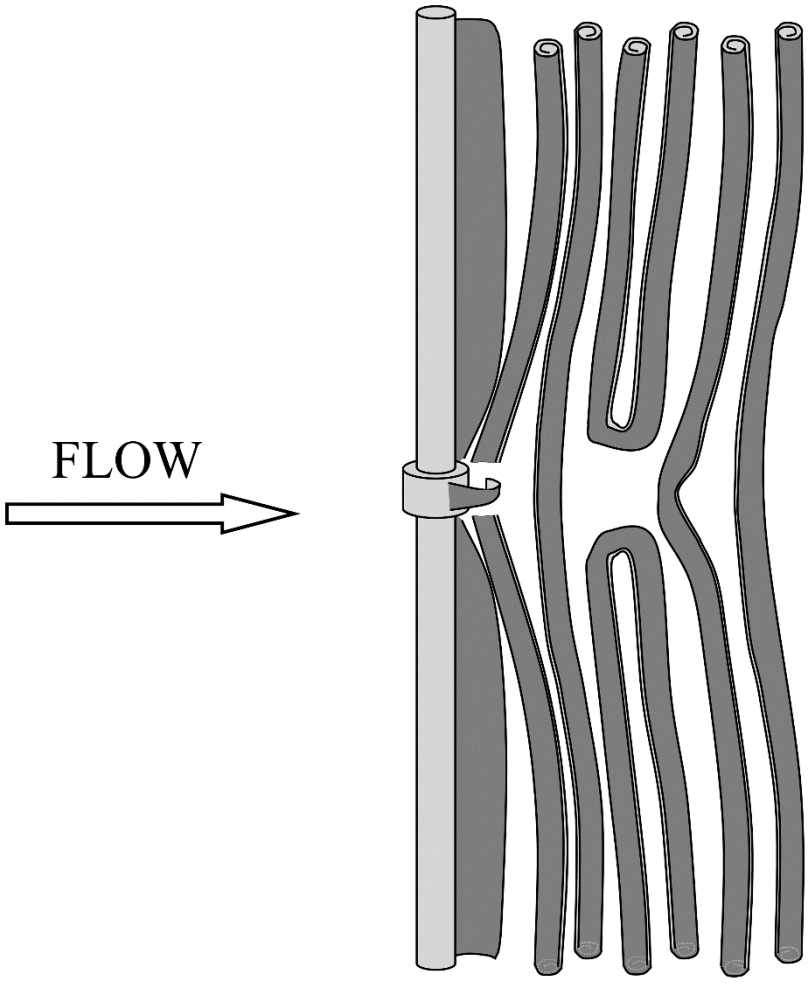

Figure 4.51 Topological sketch of the flow development past a dual step cylinder in the NS regime.

downstream of each step discontinuity. At lower Reynolds numbers, shear layer instability vortices do not form. In addition, for a given *L/D*, the effect of the Reynolds number on the dominant frequency in the large cylinder wake is often greater than that expected for a uniform cylinder.

Chapter 5

A Tomographic PIV investigation of the flow development over dual step cylinders

Chapter 4 provides a detailed investigation of the flow development and loading characteristics on dual step cylinder models. In order to gain further insight into the three-dimensional flow physics, a tomographic Particle Image Velocimetry (PIV) study of the dual step cylinder wake development was carried out. Dual step cylinder models were investigated for $0.5 \leq L/D \leq 5$, $1.33 \leq D/d \leq 2$, and $2000 \leq Re_D \leq 5000$. Details of the experimental setup employed for Tomographic PIV are provided in section 3.2. A subset of the full compilation of tomographic PIV data is presented in this chapter and organized into three main sections: (i) mean flow field measurements, (ii) analysis of vortex dynamics through visualizations of the instantaneous vortical structures, and (iii) specific three-dimensional characteristics of the irregular vortex shedding (IS) regime. A larger compilation of the tomographic PIV data can be found in Appendix H.

The tomographic PIV results were first analysed and classified into distinct flow regimes based on a comparison with the results in Chapter 4. The results agree well with those presented in Chapter 4, with the same flow regimes occurring for the same L/D and D/d ranges (Figure 4.1).

5.1 Mean wake topology

Figure 5.1 presents mean streamwise velocity contours for multiple two-dimensional planes in the wake of a dual step cylinder. Also shown in the plots are the size and extent of the re-circulation zone in the wake of each model, which is identified via an iso-surface defined by zero free stream velocity. The results illustrate the significant changes in three-dimensional mean flow topology that occur

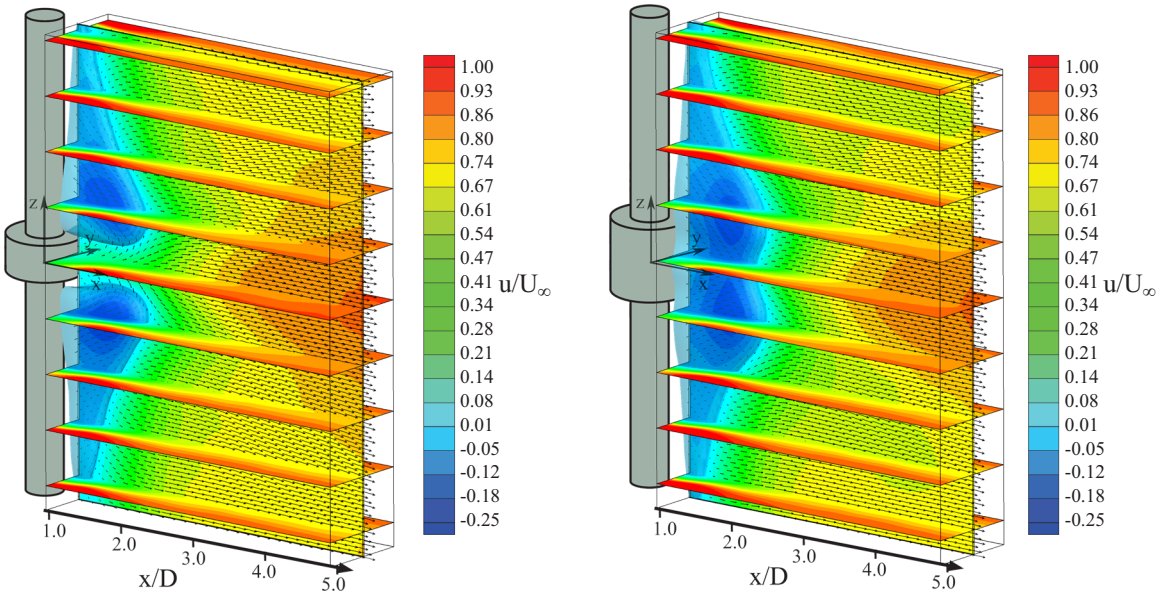

(a) NS regime, L/D = 0.5, D/d = 2

(b) HFS regime, L/D = 1, D/d = 2

(c) IS regime, L/D = 2, D/d = 2

(d) LFS regime, L/D = 2, D/d = 1.33

Figure 5.1 Planar contours of mean streamwise velocity in the wake of a dual step cylinder at Re_D = 2000. Isosurfaces of $u = 0$ are shown to illustrate the three-dimensional extent of the recirculation zone in the wake.

between each flow regime (Figure 5.1). Of particular interest are the changes in the size and extent of the recirculation zone, which can be used as an estimate of the size of the vortex formation region.

The mean wake topology is approximately symmetric about the x-y and x-z planes for all models (Figure 5.1). It can be seen in Figure 5.1 that in the NS regime, there is no discernible recirculation zone in the wake of the large cylinder (Figure 5.1a). This is attributed to the collapse of the large cylinder separated shear layers in the near wake, agreeing with the results presented in Chapter 4. On the other hand, in the wake of the small cylinders near the step discontinuities, the recirculation zones increase in size, with their streamwise extent increasing up to 2D downstream of the steps. In the HFS regime (Figure 5.1b), the mean flow topology in the small cylinder wakes is comparable to that found for the NS regime. Downstream of the large cylinder, on the other hand, the recirculation zone is present and extends beyond x/D = 2 (Figure 5.1b). There is an abrupt increase in the size of the recirculation zone in the large cylinder wake in the IS regime (Figure 5.1c). In fact, the recirculation zone exceeds the size of the measurement volume in the transverse direction, and in the streamwise direction, extends beyond x/D = 3 (Figure 5.1c). However, within about 1.5D from the step in the wake of the small diameter cylinders, the recirculation zone is absent, indicating that small cylinder vortex formation may not occur in this region (Figure 5.1c). In the LFS regime (Figure 5.1d), the mean wake topology shows that a recirculation zone exists along the entire dual step cylinder span, similar to the HFS regime. In the streamwise and transverse directions, the recirculation zone approximately matches with that of a uniform cylinder of the corresponding diameter (Figure 5.1d). The mean three-dimensional flow field results for all of the regimes are in excellent agreement with the corresponding planar results presented in Chapter 4.

For all D/d and L/D investigated, the Reynolds number has only a minor effect on the flow development. In particular, for a given L/D and D/d, the corresponding flow regime does not change with Reynolds number. For example, at L/D = 1, and D/d = 2 (Figure 5.2a-b), the only discernible change in the mean flow topology is a slight increase in the strength of the re-circulation zone. The one exception is for L/D = 2, and D/d = 1.6 (Figure 5.2c-d). This model, as shown in the two-dimensional map in Figure 4.1, lies on the boundary between two flow regimes: the HFS regime and the IS regime. Through a careful analysis of instantaneous tomographic PIV flow images, an intermittent switching between the two flow regimes was observed for a Reynolds number of 2000.

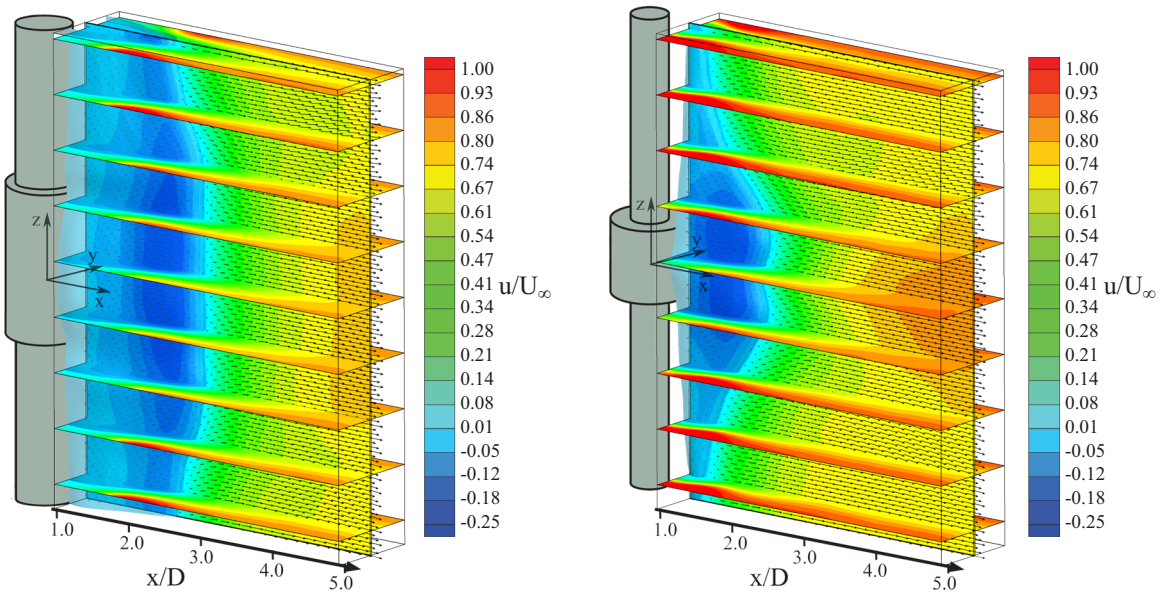

(a) $Re_D = 2000$ (b) $Re_D = 5000$

(c) $Re_D = 2000$ (d) $Re_D = 5000$

Figure 5.2 Planar contours of mean streamwise velocity in the wake of a dual step cylinder for: (a) and (b) HFS regime for L/D = 1, D/d = 2, (c) and (d) transitional HFS-IS regime for L/D = 2, D/d = 1.6. Isosurfaces of $u = 0$ are shown to illustrate the three-dimensional extent of the recirculation zone in the wake.

This results in the mean flow topology having characteristics of both flow regimes (cf. Figure 5.2c, Figure 5.1b-c). Specifically, the wake of the small cylinder has a small re-circulation zone near the

step discontinuities that is not present in any of the IS regime results (Figure 5.1c and Appendix H). On the other hand, instantaneous tomographic PIV results at $Re_D = 5000$ showed that the flow topology was consistently that of the IS regime. As shown in Figure 5.2d, the mean flow topology nearly matches that of the IS regime at D/d = 2 and L/D = 2 (Figure 5.1c), with the recirculation zone in the wake of the small cylinder being absent near the steps. The results obtained at this regime boundary location suggest that the boundaries between different flow regimes are sensitive to changes in Reynolds number.

5.2 Instantaneous wake topology

In order to investigate the instantaneous wake topology, a Proper Orthogonal Decomposition (POD) of the three-dimensional velocity field was employed so as to identify dominant coherent structures. POD was performed using the snapshot method [16]. Figure 5.3a shows the energy distribution over the POD modes for each model investigated, and Figure 5.3b shows the corresponding cumulative energy distribution. While modal energy content varies with aspect ratio, an analysis of the spatial structure of the modes revealed some distinct similarities across all the models investigated. In particular, of the first eight POD modes, six capture the dominant spatial structure of wake vortex shedding. However, not all of these modes form distinct mode pairs, reflecting a complex nature of vortex interactions expected for these geometries. Moreover, the majority of modes eight through sixteen also contain spatially periodic features, for example, harmonics of the dominant spatial modes, and modes pertaining to distinct streamwise structures. Thus, the attendant mode energy spectrum in Figure 5.3 is notably broader than that typically observed for periodic wake flows of two-dimensional models (e.g., [26,123,124]). For example, the energy content of the first pair of POD modes capturing planar wake vortex shedding from the large diameter cylinder (Chapter 4) is larger that found in Figure 5.3b for the same dual step cylinder models. However, the disparity in the cumulative energy content between each flow regime is consistent with the planar results in Chapter 4. This suggests that the changes in mode energy content between each flow regime in Figure 5.3b are due to changes in flow topology. It is important to note that, the fixed size of the measurement volume also impacts the mode

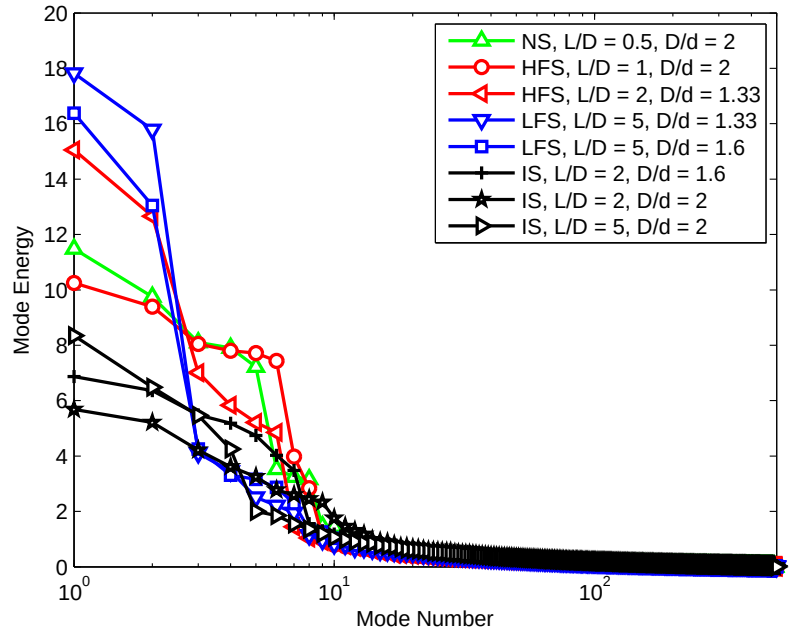

(a)

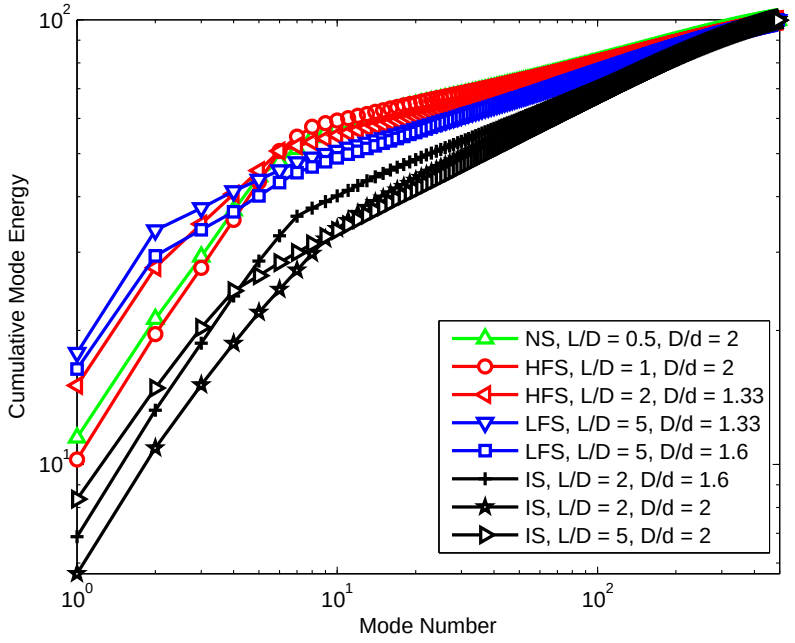

(b)

Figure 5.3 Energy distribution over the POD modes: (a) Mode energy, (b) Cumulative mode energy.

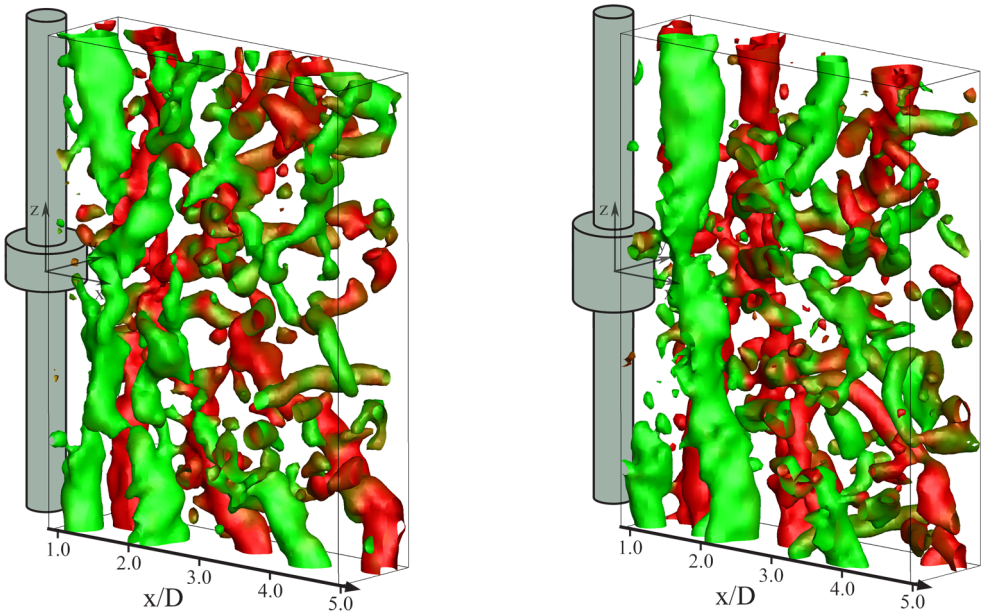

(a) L/D=0.5, D/d=2 (b) L/D = 1, D/d=2

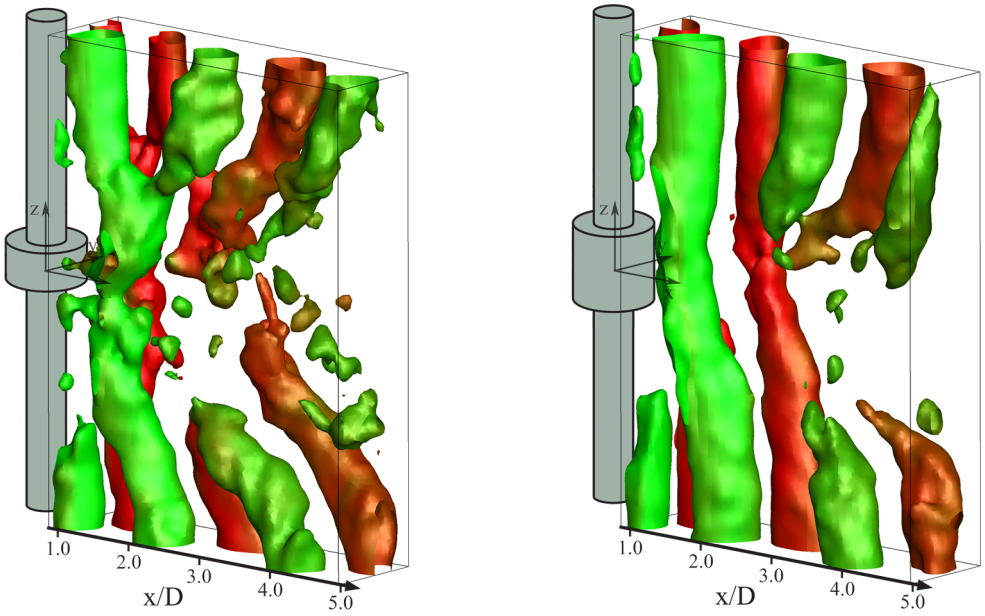

(c) L/D=0.5, D/d=2 (d) L/D = 1, D/d=2

Figure 5.4 Q-criterion isosurfaces colored by spanwise vorticity in the wake of a dual step cylinder: (a)- (b) instantaneous isosurfaces at $Q = 0.2$, (c)-(d) corresponding reduced order model isosurfaces at $Q = 0.075$.

energy distributions since the span of the small diameter cylinders within the measurement volume changes with D/d.

Instantaneous snapshots of the three-dimensional vortical structures in the wakes of dual step cylinders are presented for each flow regime in Figures 5.4a-b and 5.5a-b. To more clearly visualize the arrangement of the dominant vortical structures and their interactions in the wake, Figures 5.4c-d

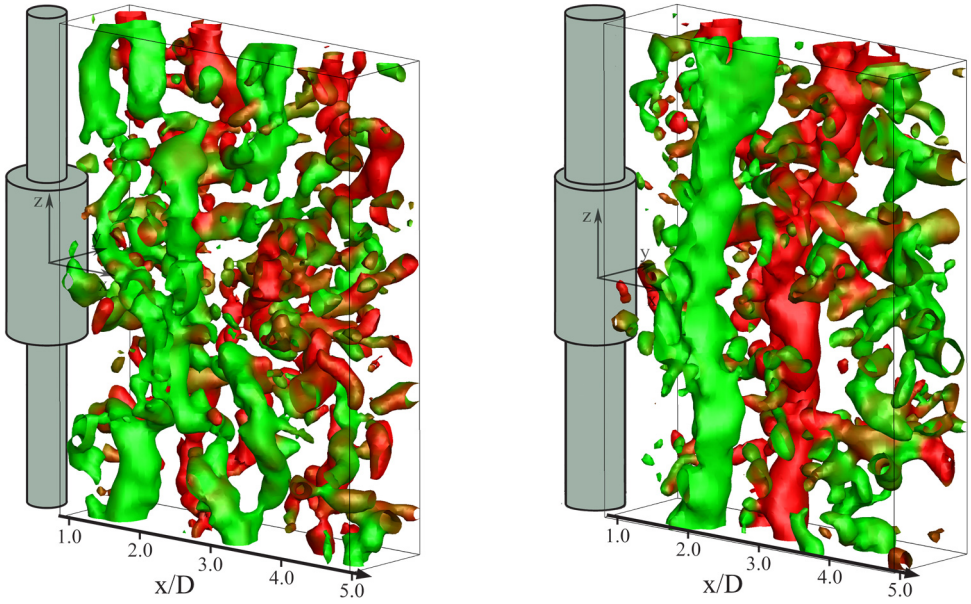

(a) L/D=2, D/d=2

(b) L/D = 2, D/d=1.33

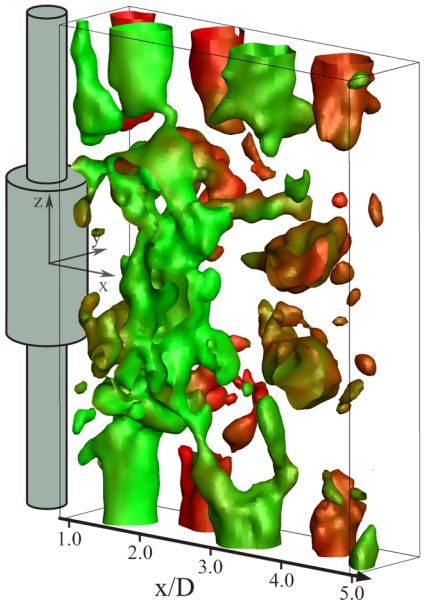

(c) L/D=2, D/d=2

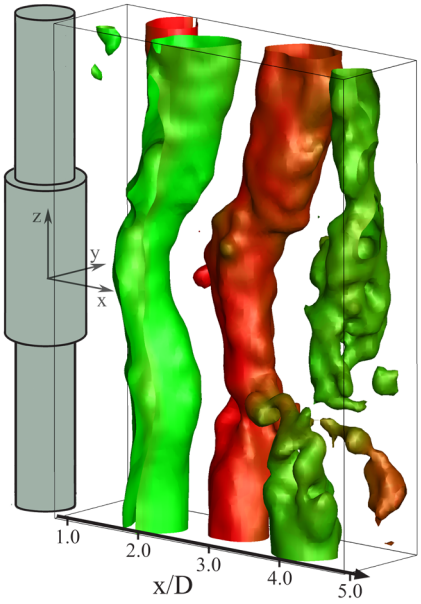

(d) L/D = 2, D/d=1.33

Figure 5.5 Q-criterion isosurfaces colored by spanwise vorticity in the wake of a dual step cylinder: (a)- (b) instantaneous isosurfaces at $Q = 0.1$, (c)-(d) corresponding reduced order model isosurfaces at $Q = 0.05$.

and 5.5c-d present a reduced order model constructed using the first twenty modes. The results are presented in Figure 5.4 and Figure 5.5 using Q-criterion isosurfaces, colored by the spanwise vorticity sign. The results in Figure 5.4 and Figure 5.5 show a complex three-dimensional turbulent wake topology for all aspect ratios. In addition to the primary vortical structures and their interactions, smaller scale streamwise vortices also form and connect between the spanwise rollers as a result of secondary instabilities.

Four instantaneous reconstructions of the wake vortex dynamics for each flow regime are presented in Figure 5.6 to Figure 5.9 by employing the reduced order model. For the NS regime (Figure 5.6), spanwise vortices shed from the small cylinders often connect across the large cylinder wake. However, the relative phase-alignment of the small cylinder vortices changes over time. This results in substantial variations in the spatial arrangement of vortex interactions which include oblique vortex shedding and vortex stretching (e.g., x/D = 3 in Figure 5.6a and x/D = 4 in Figure 5.6b), vortex splitting (e.g., downstream of the step at x/D = 1.5 in Figure 5.6c), and half-loop vortex connections (e.g., x/D = 4 in Figure 5.6d). The three-dimensional reconstructions of the wake vortex shedding are in good agreement with the proposed sketch in Chapter 4 (cf. Figure 4.51 and Figure 5.6d). For the HFS and LFS regimes (Figure 5.7 and Figure 5.9) similar vortex interactions are found to occur, however, they occur between the large cylinder and small cylinder vortices downstream of both stepwise discontinuities. When small and large cylinder vortices are out of phase in the LFS regime, the large cylinder vortices often split into two vortex filaments and connect to two consecutive small cylinder vortices of the same sign. On the other hand, in the HFS regime, the majority of large cylinder vortices do not split into multiple filaments. These subtle differences between the HFS and LFS regimes were also observed in the flow visualizations and are depicted in the corresponding sketches of the flow development in Chapter 4 (Figure 4.48 and Figure 4.50). For the IS regime (Figure 5.8), the wake vortex dynamics changes drastically. Large cylinder vortices initially form parallel to the cylinder axis (e.g., x/D = 2.5 in Figure 5.8b and 5.8d). As the vortices are shed into the wake, the results in Figure 5.8 suggest they either deform out of the field of view or rapidly break down into weaker vortical structures. In Chapter 4 and in Morton & Yarusevych [77], it was proposed that in the IS regime large cylinder vortices deform into hairpin-like vortical structures (Figure 4.48). Evidence

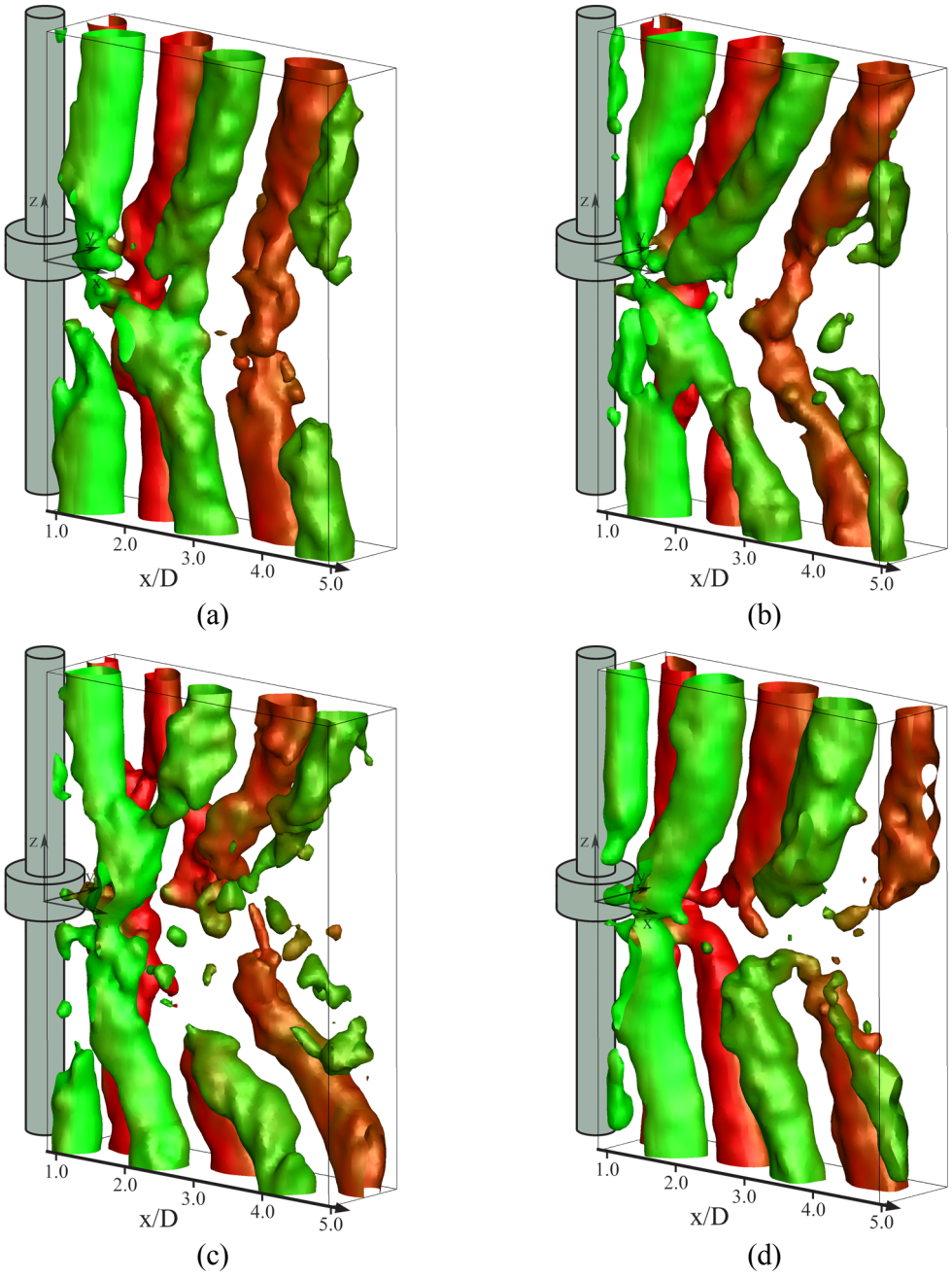

Figure 5.6 Visualizations of instantaneous vortex dynamics in the NS regime using isosurfaces of $Q = 0.05$ colored by spanwise vorticity for L/D = 0.5, D/d = 2, and Re_D = 2000.

of this can be seen in Figure 5.8c, where only 'legs' of the large cylinder vortex deformed out of the measurement volume are captured at about x/D > 4. This is more clearly illustrated by visualizing streamwise vorticity isosurfaces, which are presented in the next section. The vortices shed into the

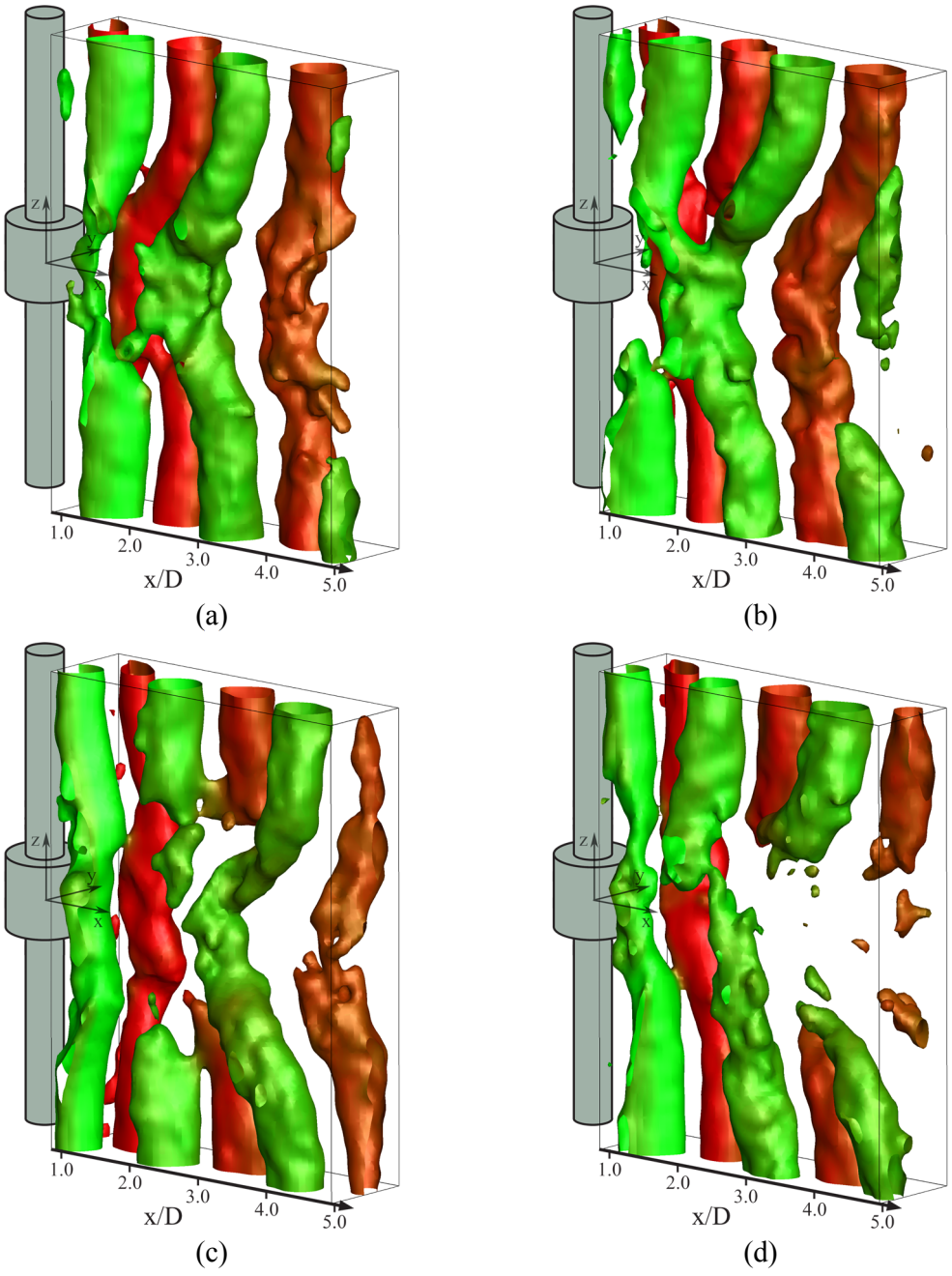

Figure 5.7 Visualizations of instantaneous vortex dynamics in the HFS regime using isosurfaces of $Q = 0.05$ colored by spanwise vorticity for L/D = 1, D/d = 2, and Re_D = 2000.

wakes of the small diameter cylinders in the IS regime either form weak connections with large cylinder vortices, or half-loop connections with an adjacent small cylinder vortex.

The global features of the observed elements of vortex dynamics agree well with qualitative flow visualization results discussed in Chapter 4, and the sketches of the vorticity topology proposed at the end of Chapter 4 (Figures 4.47-4.51).

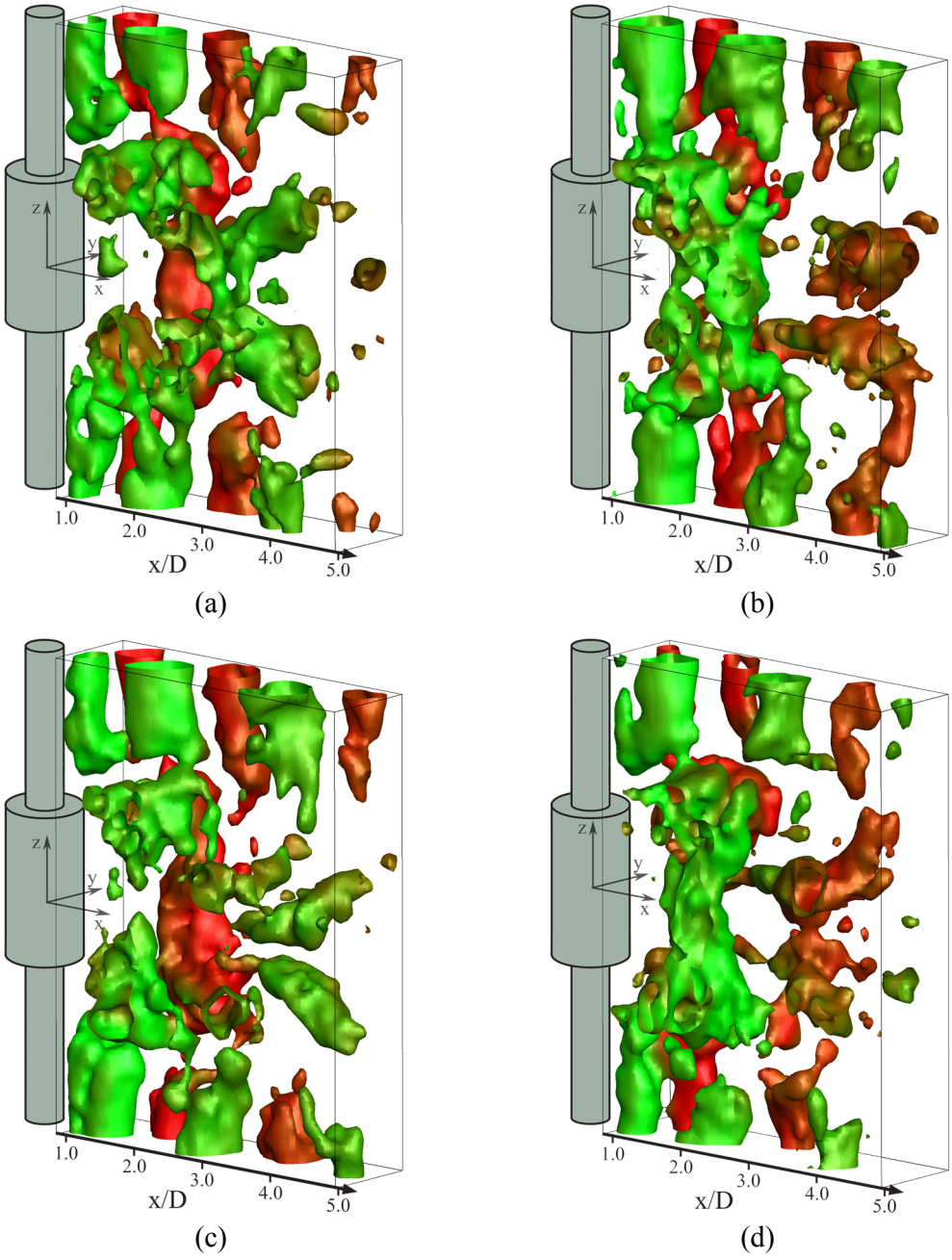

Figure 5.8 Visualizations of instantaneous vortex dynamics in the IS regime using isosurfaces of $Q = 0.05$ colored by spanwise vorticity for L/D = 2, D/d = 2, and Re_D = 2000.

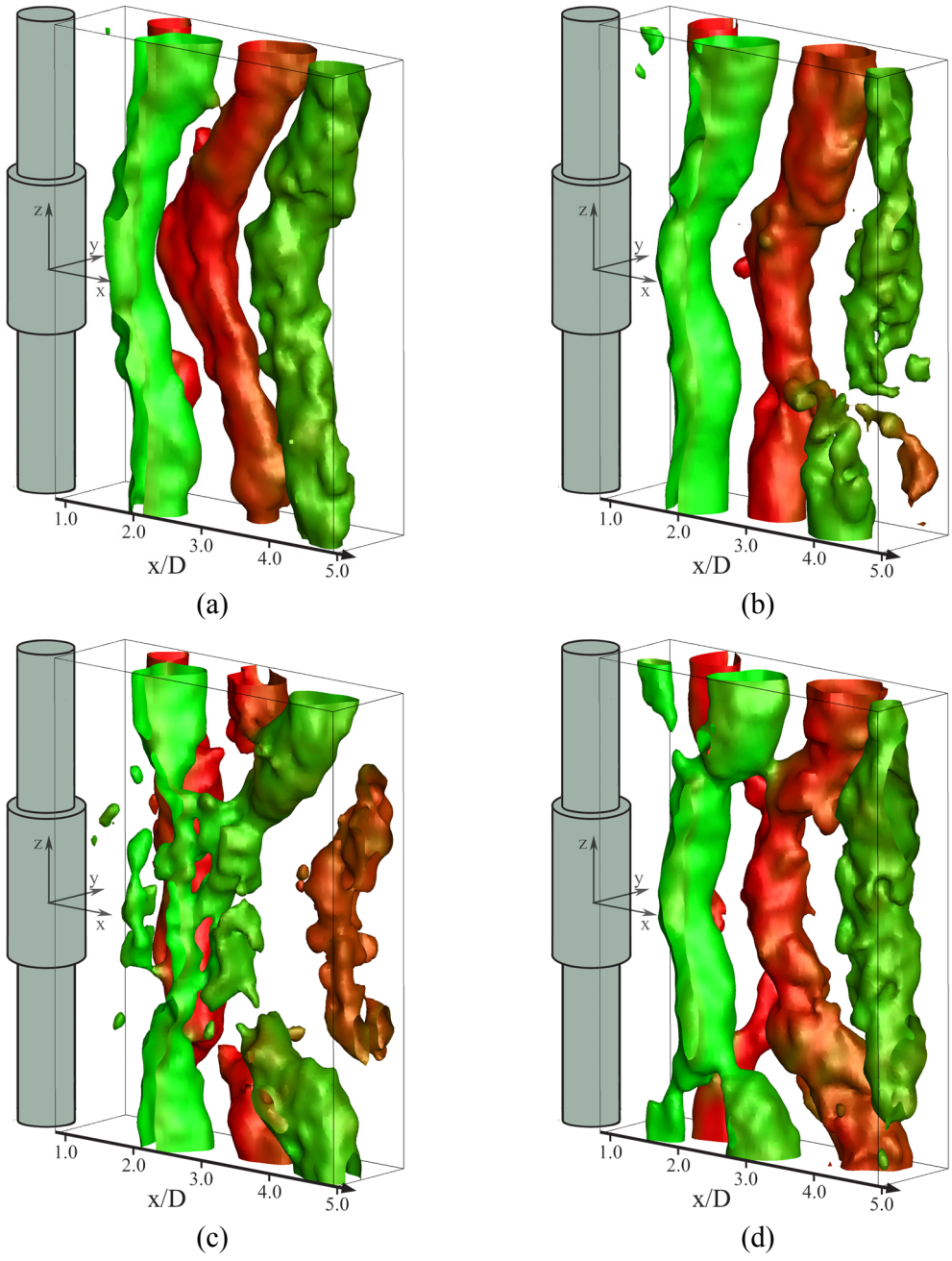

Figure 5.9 Visualizations of instantaneous vortex dynamics in the LFS regime using isosurfaces of $Q = 0.05$ colored by spanwise vorticity for L/D = 3, D/d = 1.33, and Re_D = 2000.

5.3 Streamwise and transverse vortices in the IS regime

The IS regime is of particular interest due to the wide range of dual step cylinder geometries where it occurs (Figure 4.1). The results presented in Figure 5.8 confirm previous speculations in Chapter 4: only weak interactions between small and large cylinder vortices occur, with most small cylinder vortices forming looped connections with adjacent small cylinder vortices, and large cylinder vortices deforming substantially as they are shed. In order to preserve circulation in the wake, it was speculated in Chapter 4 that large cylinder vortices may form vortex loops. In order to obtain an improved visualization of portions of the large cylinder vortices as they are shed into the wake, Figure 5.10a-b shows streamwise vorticity isosurfaces colored by the streamwise vorticity sign in the wake of the large cylinder. Overlapped on these images are Q-criterion isosurfaces which highlight the presence of vortical structures forming in the large and small cylinder wakes. In Figure 5.10b, a large cylinder vortex is forms on the opposite side of the wake for $x/D < 3$ and $y/D>0$. For about $x/D>2$, streamwise vorticity isosurfaces depict the 'legs' of the previously shed large cylinder vortex (Figure 5.10b). The results suggest that the 'legs' of the previously shed vortex do not form a vortex loop, they attain a streamwise orientation and appear to form connections with the large cylinder vortex forming on the opposite side of the wake (Figure 5.10a-b).

A unique feature of the flow development in the IS regime observed in flow visualizations is the presence of Kelvin-Helmholtz (K-H) instability vortices forming in the large cylinder separated shear layers, and forming downstream of the step discontinuities. As shown in Figure 5.1c, in the near wake downstream of each step discontinuity, there is a region of high velocity shear that acts as a boundary between the large and small cylinder wakes. This region of high velocity shear corresponds with the approximate location where K-H vortices were observed in the flow visualizations shown in Figure 4.7. In order to visualize the vorticity production in this region, Figure 5.10c and 5.10d show transverse (ω_y) isosurfaces of vorticity, colored by the transverse vorticity sign. Overlaid on the figures are the Q-criterion isosurfaces depicting vortical structures in the wake. The results in Figure 5.10c and 5.10d, as well as several other instantaneous visualizations show that the small cylinder vortices occasionally

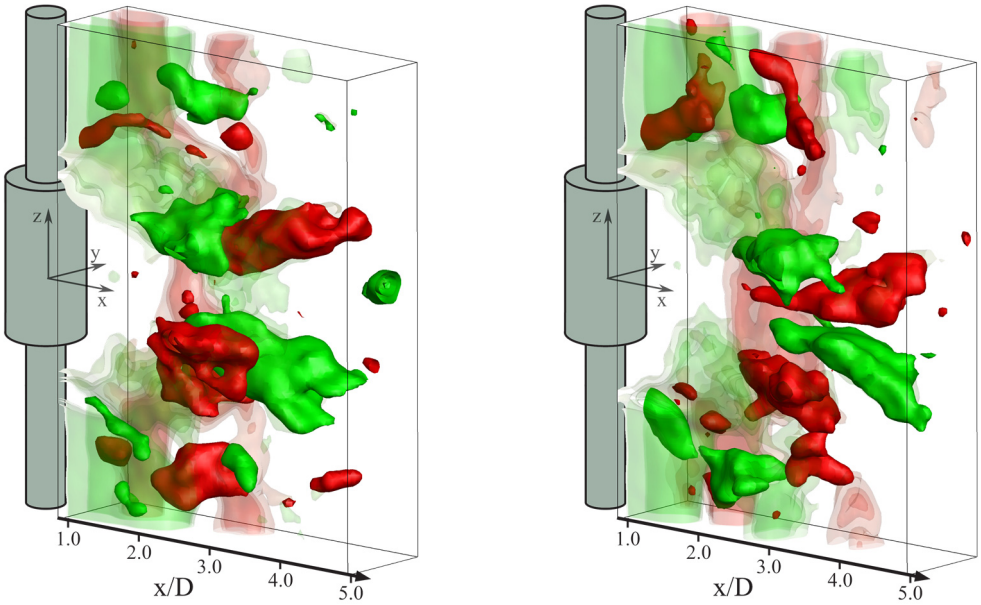

(a) Streamwise vorticity

(b) Streamwise vorticity

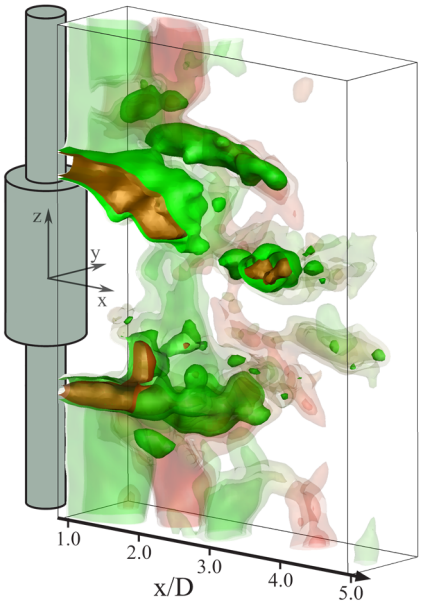

(c) Transverse vorticity

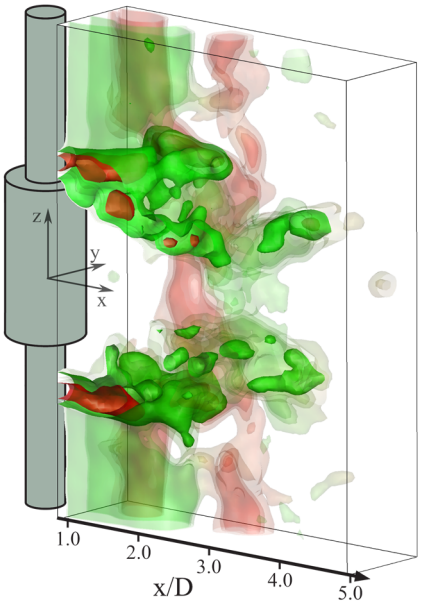

(d) Transverse vorticity

Figure 5.10 Visualizations of instantaneous vortex dynamics in the IS regime using vorticity isosurfaces with semi-transparent visualization of the vortical structures with Q-criterion for L/D = 2, D/d = 2, and Re_D = 2000.

connect into the shear layer, suggesting that vortical structures must also exist within the shear layer. It is speculated that the vortical structures within the shear layer are K-H vortices, but the resolution of the vector field in the tomographic PIV images is too low to confirm if this is the case.

5.4 Conclusion

Flow over a dual step cylinder was investigated experimentally using Tomographic PIV for $5000 < Re_D < 2000$, $1.33 < D/d < 2$, and $0.5 \leq L/D \leq 5$. The results provide insight into the mean wake characteristics and wake vortex dynamics. The mean flow results are in excellent agreement with experimental results presented in Chapter 4, and shed light on how the three-dimensional extent of the formation region in the wake varies with each flow regime. The results show that the two-dimensional map of flow regimes proposed in Chapter 4 is consistent with the present tomographic PIV data.

A POD-based reduced order model was used to investigate the dominant vortical structures and their interactions for each flow regime. The results demonstrate that, in the NS regime, spanwise vortices shed from the small cylinders often connect across the large cylinder wake. However, the presence of the large cylinder leads to periodic vortex dislocations forming downstream of the large cylinder, and involves complex vortex interactions including vortex stretching, splitting, and half-loop vortex connections. In the HFS and LFS regimes, vortex shedding occurs from the large cylinder and small cylinder. Vortex dislocations occur between the large and small cylinder vortex wakes, downstream of the step discontinuities, and involve similar vortex interactions as those observed in the NS regime. Vortex shedding from the large cylinder becomes highly three-dimensional in the IS regime, with large cylinder vortices deforming into hairpin-like structures in the near wake. The ‘legs’ of the hairpin vortices attain a streamwise orientation as they are shed into the wake, and connect to subsequently forming large cylinder vortices. The small cylinder vortices primarily form half-loop connections with adjacent small cylinder vortices, but may also form weak connections to large cylinder vortices. Strong shear layers form above and below the steps in model diameter and roll into transverse oriented rollers that interact with main spanwise vortices shed from the small diameter cylinders.

Chapter 6

Reconstructing three-dimensional flow topology from 2D time-resolved PIV measurements

In this chapter, two techniques are developed for conditionally averaging time-resolved planar PIV measurements. The aim is to reconstruct dominant three-dimensional vortical structures and their interactions in the wakes of complex cylindrical geometries. The techniques are validated on a dual step cylinder with L/D = 1, D/d = 2, and Re_D = 2100. The main features of the flow development for this geometry are illustrated through hydrogen bubble flow visualization images and quantitative planar PIV measurements presented in Chapter 4. For this geometry, both the large and small cylinders shed vortices periodically, but they do so at different frequencies. This results in the vortices continuously moving in and out of phase alignment, leading to complex vortex interactions which occur downstream of the step discontinuities.

The experimental arrangement used to obtain the results presented in this chapter is shown in Chapter 3 (Figure 3.3c). Planar velocity measurements are performed on one horizontal (x-y) and one vertical (x-z) plane simultaneously. While the vertical plane remains fixed, the horizontal plane is traversed to 18 locations along the z-direction in the range $-3.2 \leq z/D \leq 0$. The spanwise spacing between horizontal planes, Δz, varies within $0.1 \leq \Delta z/D \leq 0.5$.

6.1 POD-based conditional phase-averaging

The aim of POD-based conditional phase-averaging is to reconstruct the dominant vortical structures in the small and large cylinder wakes for a given relative phase alignment of the large and small cylinder vortices. The methodology presumes that the turbulent wake vortex dynamics between vortex

shedding cells depends predominantly on the relative phase alignment of the dominant vortical structures at formation. The first step in the methodology is to extract reference signals for the phase variation of the dominant vortical structures from the planar PIV data (Figure 6.1). As shown in Figure 6.1, a single or multiple reference signals can be used depending on the complexity of the flow being studied. For traditional phase-averaging, each planar PIV field is assigned a phase angle based on a single reference signal. The phase reference signal is divided into discrete phase angle bins from 0 to 2π, with the total number of bins being $N = 2\pi/\Delta\theta$ (section 3.3.1). All planar PIV fields are then sorted into their corresponding bins. The planar PIV data in each bin are averaged to obtain a phase-averaged representation of the two-dimensional flow field (Figure 6.1). Phase-averaged data from each of the horizontal planes are combined in order to reconstruct the three-dimensional flow field for a given phase angle. A similar approach can be extended to flows where more than one dominant frequency is present, as is the case for a dual step cylinder with two dominant frequencies. This requires two reference signals (Figure 6.1), so that each planar PIV field can be assigned two phase angles, one for each of the two reference signals. In this case, the planar data is conditionally binned based on a selected phase angle for each reference signal. This process is repeated for all spanwise measurement locations, and the three-dimensional field is reconstructed through a cubic spline interpolation of the data between each x-y plane.

A POD analysis of the planar PIV data is employed in order to extract reference signals pertaining to the phase variation of the small cylinder and large cylinder vortices, for a dual step cylinder at

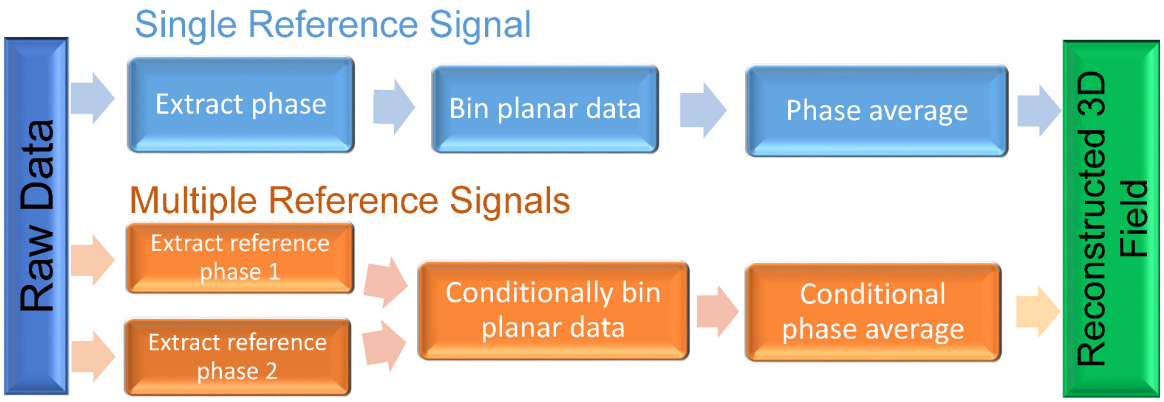

Figure 6.1 POD-based methodology.

L/D = 1, D/d = 2, and Re_D = 2100. Figure 6.2 shows the mode energy distribution and cumulative mode energy distribution for the first fifty POD modes at seven selected spanwise locations. The results indicate that, in the wake of the large diameter cylinder, as well as sufficiently far away from the step in the wake of the small cylinder (z/D < -1.8), the first two modes capture over 50% of the wake energy content (Figure 6.2b). However, between these regions, where vortex interactions take place, the energy content in the first two modes is considerably lower. The results are in good agreement with those obtained at lower Reynolds numbers pertaining to laminar vortex shedding (Appendix G).

Figure 6.3 presents the first two spatial modes obtained from the POD of x-y planar PIV data for three selected spanwise locations, z/D = 0, -1.0, and -3.2. At each spanwise location, the modes in Figure 6.3 are qualitatively similar to those found for a uniform circular cylinder (Figure 4.22). Figure 6.4 shows spectra for the first temporal coefficient at z/D = 0, -1.0, and -3.2. Note that the results for the second temporal coefficient feature similar spectral content and are not included for brevity. At z/D = 0 (Figure 6.4a), the majority of the energy content is centered on the large cylinder vortex shedding frequency, $fD/U_\infty \approx 0.26$. At z/D = -3.2 (Figure 6.4c), the dominant energy content of the first temporal coefficient signal is centered on the small cylinder vortex shedding frequency, $fD/U_\infty \approx 0.40$. Spectral analysis of temporal coefficients a_3 to a_{10} at z/D = 0 and -3.2 showed no evidence of

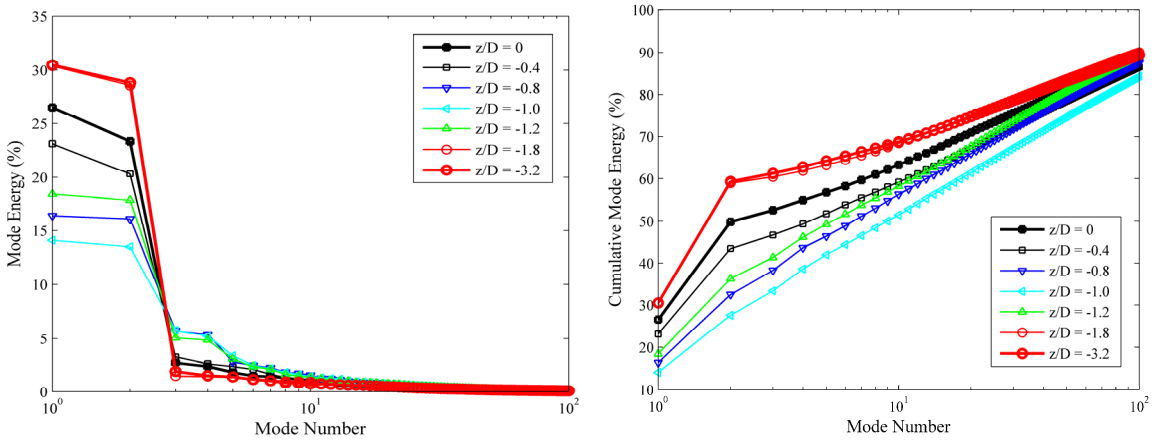

(a) (b)

Figure 6.2 Energy distribution over the POD modes for a dual step cylinder at L/D = 1, D/d = 2, and Re_D = 2100.

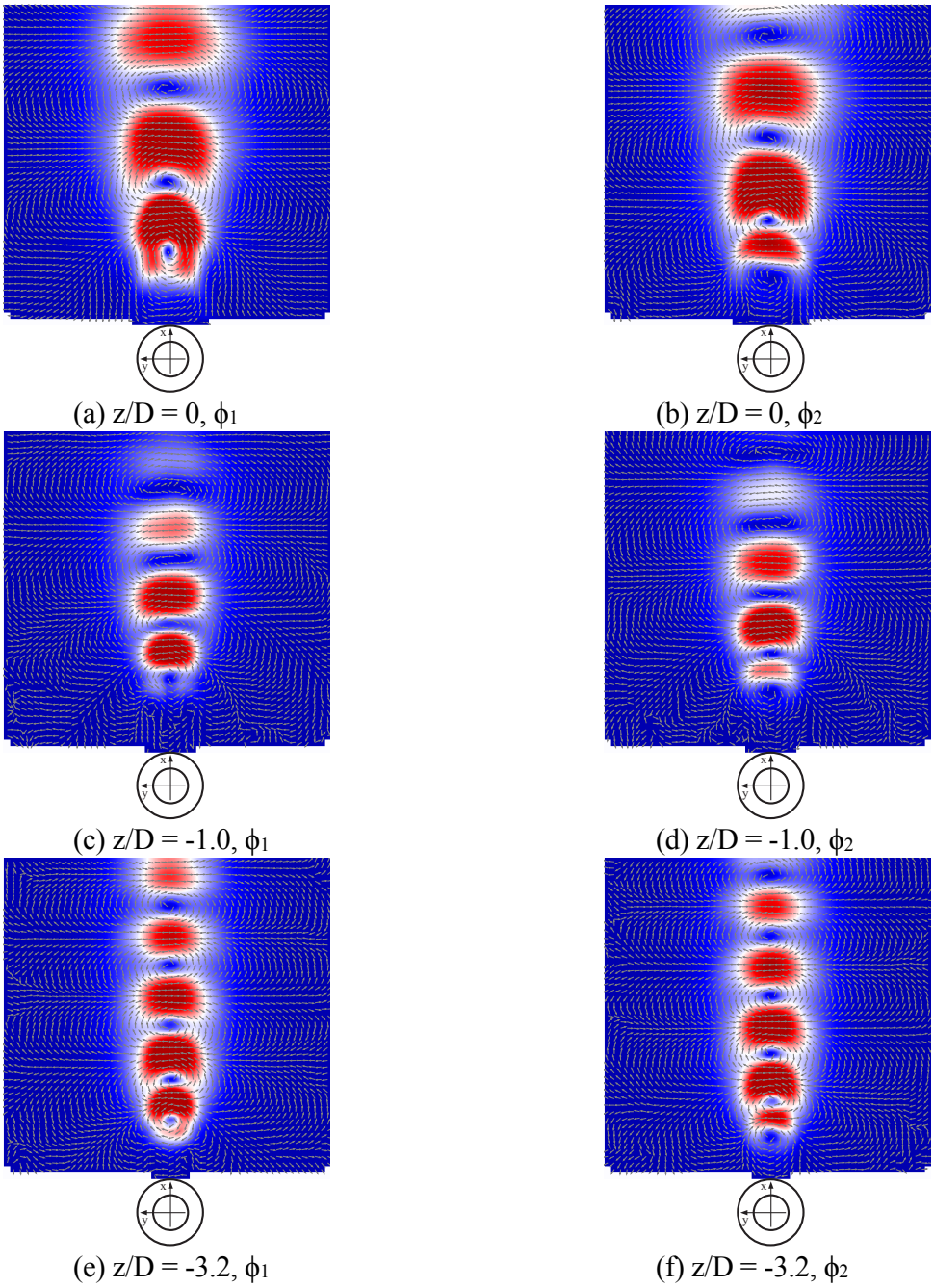

(a) z/D = 0, ϕ_1 (b) z/D = 0, ϕ_2

(c) z/D = -1.0, ϕ_1 (d) z/D = -1.0, ϕ_2

(e) z/D = -3.2, ϕ_1 (f) z/D = -3.2, ϕ_2

Figure 6.3 Spatial eigenmodes obtained from POD of x-y planar PIV data acquired in the wake of a dual step cylinder for L/D = 1, D/d = 2, and Re_D = 2100.

a secondary frequency-centred activity, aside from harmonics of the dominant frequency. Hence, it can be concluded that at these spanwise locations, a single vortex shedding phenomenon is present, i.e., the vortex shedding from the large cylinder at z/D = 0, and the vortex shedding from the small

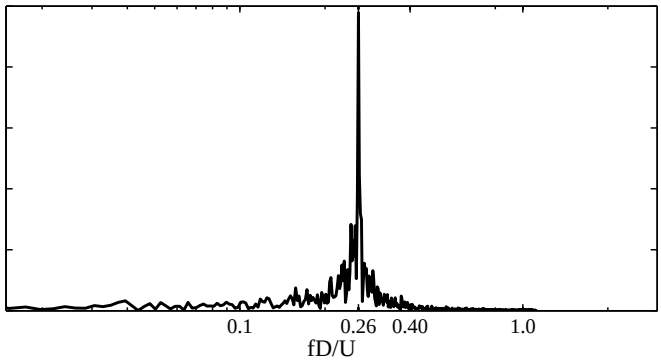

(a)

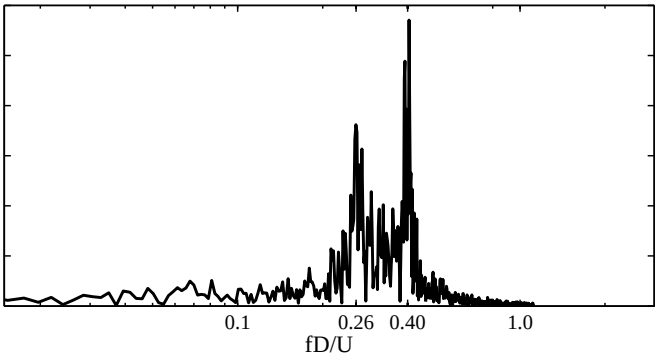

(b)

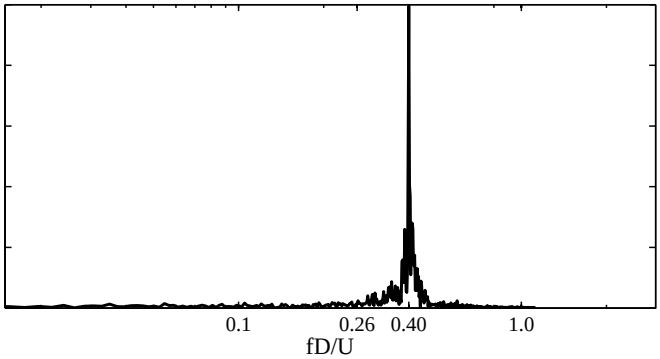

(c)

Figure 6.4 Spectra of the first temporal coefficient, a_1 for: (a) z/D = 0, (b) z/D = -1.0, and (c) z/D = -3.2.

cylinder at z/D = -3.2. In such a case, the planar wake topology can be reconstructed using a traditional POD-based phase-averaging with a single reference signal for the phase variation of the vortices (Figure 6.1), as outlined in section 3.4.2 and demonstrated in Chapter 4 (section 4.3). At z/D = -1.0, the temporal coefficient spectrum in Figure 6.4b contains energy contributions from two frequencies,

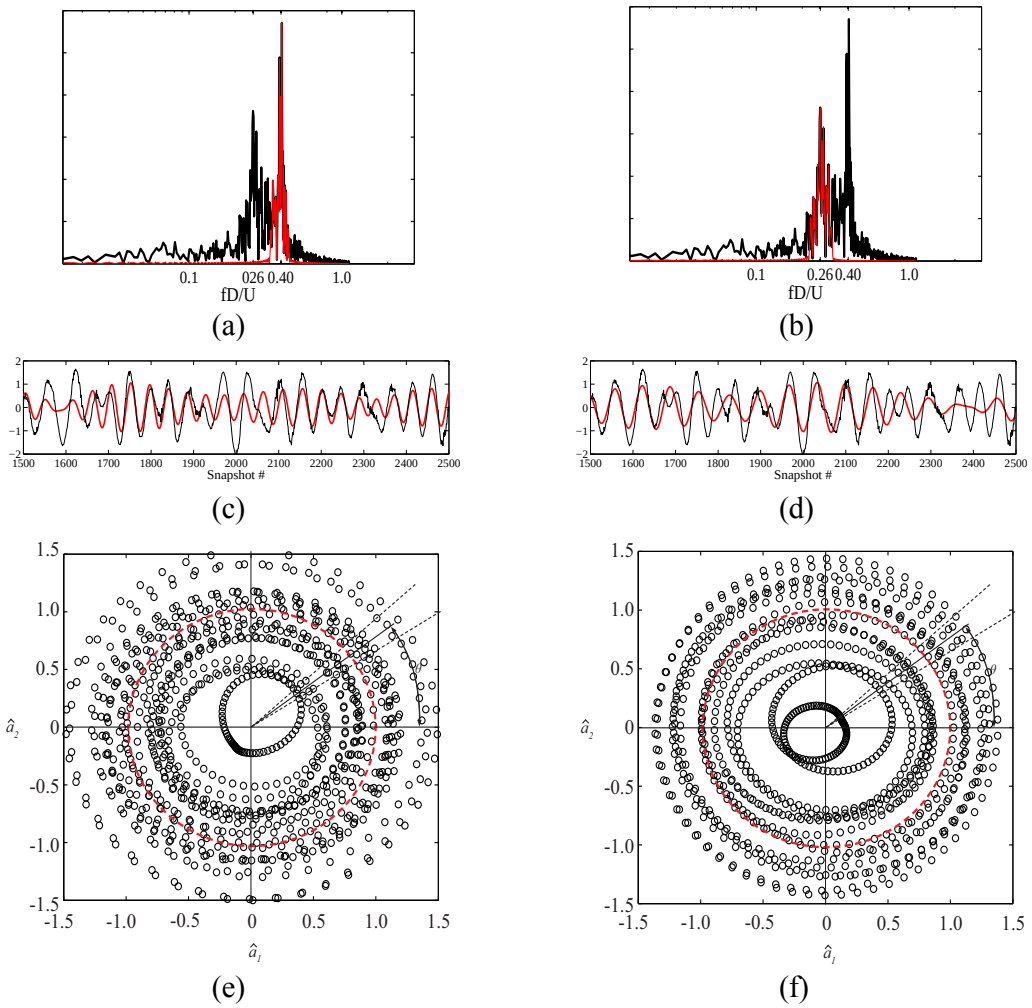

Figure 6.5 Analysis of temporal coefficients obtained from POD of x-y planar PIV data for z/D = -1.0. (a) Temporal coefficient spectrum of a_1 and filtered spectrum pertaining to $fD/U_\infty \approx 0.4$, (b) Temporal coefficient spectrum of a_1 and filtered spectrum pertaining to $fD/U_\infty \approx 0.26$, (c) & (d) Sample segment of temporal coefficient a_1 and filtered temporal coefficient, (e) & (f) Cross-plot of filtered temporal coefficients, $\hat{\boldsymbol{a}}_1$ and $\hat{\boldsymbol{a}}_2$. Filtered data are shown with red lines for (a)-(d). A red dashed line illustrating a unit circle is shown in (e)-(f).

namely, the large and small cylinder vortex shedding frequencies. It is important to note that the presence of two frequency-centred activities in the wake is not clear from the examination of the corresponding spatial modes (Figure 6.3c and Figure 6.3d), and the analysis of time resolved temporal coefficient is required. In this case, the coherent structures in the wake are defined by two dominant frequencies, and a conditional phase-averaging procedure is required. To perform conditional phase-

averaging, the temporal coefficient signals (a_1 & a_2) are band-pass filtered using a Fourier decomposition and signal reconstruction with a limited number of Fourier modes centered on each of the two dominant frequencies. This is illustrated in Figure 6.5a-d for signal a_1 at z/D = -1.0. Cross-plots of the normalized and filtered temporal coefficient signals are presented in Figure 6.5e and Figure 6.5f, where the phase variation pertaining to each of the dominant frequencies can be obtained directly. This enables implementation of the conditional phase-averaging methodology described in the beginning of this section (Figure 6.1).

The conditional phase-averaging methodology should be applied in the spanwise region where vortex interactions occur. In order to determine the extent of this region, temporal coefficient signals at all spanwise locations were band-pass filtered and reconstructed with a limited number of Fourier modes in the same way as Figure 6.5. Figure 6.6 depicts cross-plots of filtered temporal coefficients for a range of z/D locations spanning the flow region of interest. Within the large cylinder wake and in the adjacent part of the interaction region ($-1.4 \leq z/D \leq 0$), the temporal coefficients are filtered based on the large cylinder vortex shedding frequency (Figure 6.6a-d); whereas, in the small cylinder wake and within the adjacent interaction region ($-3.2 \leq z/D \leq -0.8$), the filter is centered on the small cylinder vortex shedding frequency (Figure 6.6e-h). As expected, the results show that there is a reduction in both the energy content (related to the magnitude of the temporal coefficients) and the periodicity (reflected in how well the data falls onto a circular fit in the cross plots) as the survey plane is moved away from the regions dominated by either of the two frequency-centred activities (Figure 6.6d & Figure 6.6h). Based on the results presented in Figure 6.6, the conditional phase-averaging methodology is applied for $-1.4 < z/D < -0.6$.

6.1.1 Extracting phase variation along the span using PIV measurements in the vertical plane

Although horizontal plane POD analysis is sufficient to phase-average planar velocity measurements in each individual plane, knowledge of the phase variation along the span is required for three-dimensional reconstruction. This is due to the fact that, in the energy-based decomposition, phase angles computed from the POD correspond to the same instant in the shedding cycle along the entire span of the model. In a 3D reconstruction, this artificially aligns the vortices to be in the same phase,

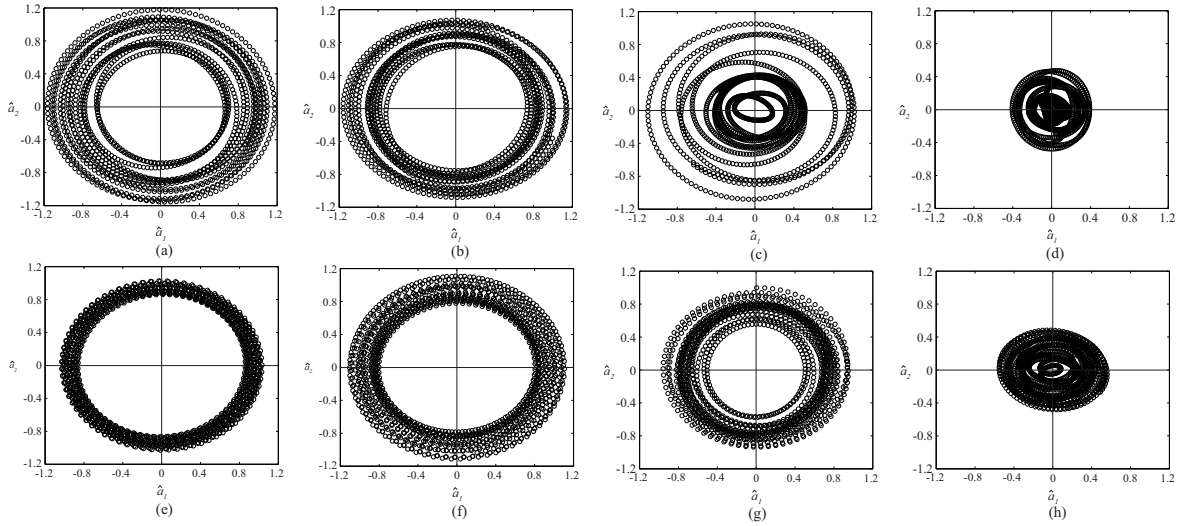

Figure 6.6 Cross plots of filtered temporal coefficient signals: (a)-(d) temporal coefficient signals filtered based on the large cylinder vortex shedding frequency for (a) z/D = 0, (b) z/D = -0.4, (c) z/D = -0.8, (d) z/D = -1.2. (e)-(h) temporal coefficient signals filtered based on the small cylinder vortex shedding frequency for (e) z/D = -2.4, (f) z/D = -1.6, (g) z/D = -1.2, (h) z/D = -0.8.

and parallel to the model axis. Thus, the spanwise variation of the phase angle of the vortex filaments needs to be determined to establish the relative phase alignment in the adjacent horizontal planes. This can be achieved based on the analysis of the acquired vertical PIV plane measurements. As shown in Figure 6.7, the first four spatial eigenmodes obtained from the POD of the vertical plane measurements give an indication of the average spatial arrangement of the dominant coherent structures based on the energy-based orthogonal decomposition of the planar data. However, it is not possible to obtain the average relative phase alignment of the large and small cylinder wake vortices from the spatial modes as it depends on the linear combination of the first four spatial modes and corresponding temporal coefficients (Figure 6.7). Therefore, a reduced order model of the vertical PIV planar fields is constructed using the first four POD modes. To determine spanwise phase variation, velocity measurements from the reduced order model were analyzed along a spanwise line at a downstream distance of x/D = 3, downstream of the vortex formation region. Fourier decomposition was applied to all data in order to extract the fluctuations pertaining to each of the two dominant frequencies in the wake. Following this, a Hilbert transform was applied to the data in order to obtain the instantaneous phase variation of the signal at each z/D location. For example, Figure 6.8 depicts the results for

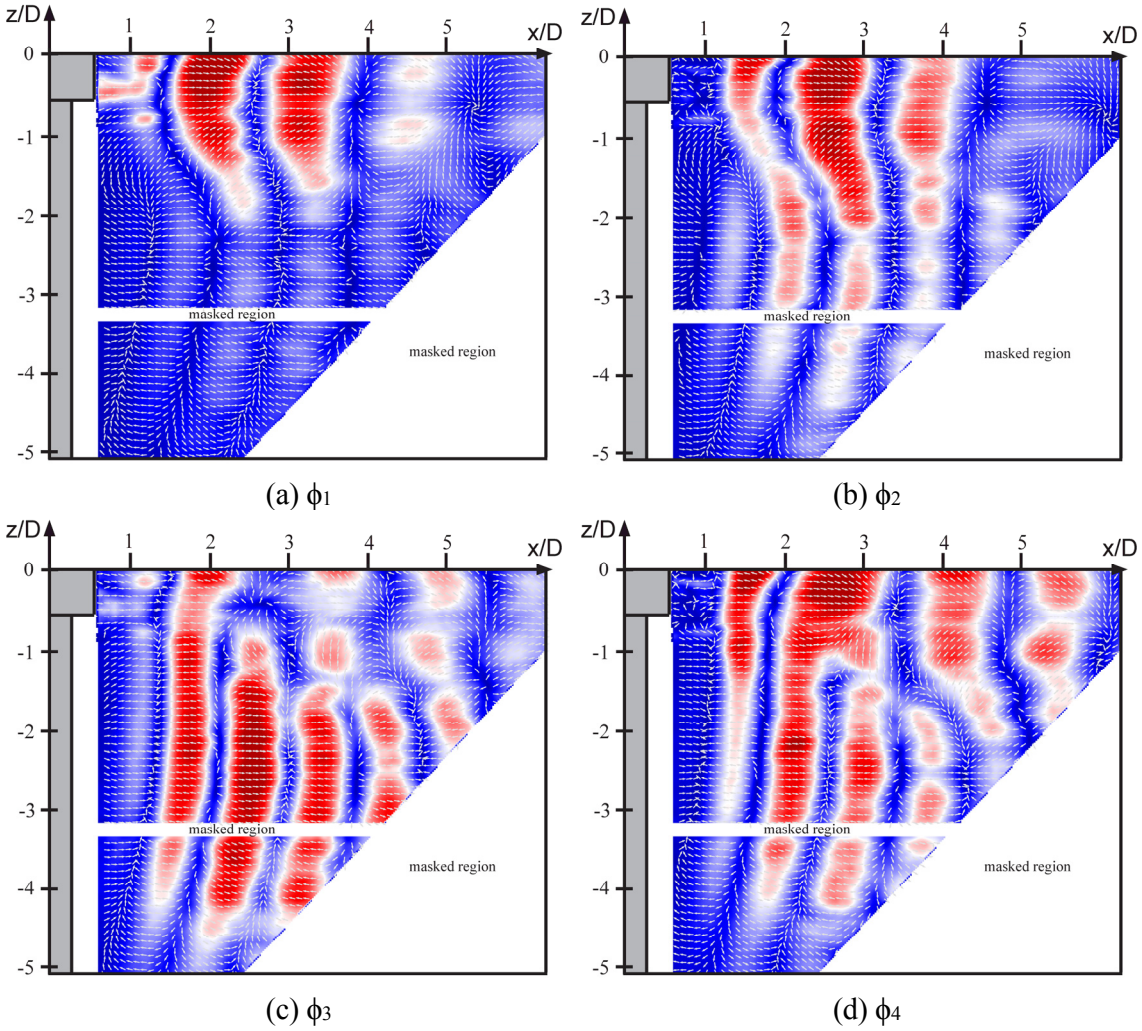

Figure 6.7 Vertical plane spatial eigenmodes obtained from POD of PIV data acquired in the wake of a dual step cylinder at y/D = -0.5.

z/D = -1.0, where two dominant frequencies are present in the velocity signal. The results are in agreement with the analysis of temporal coefficients completed at the same z/D location in Figure 6.5. In order to relate the obtained phase variation in the reference velocity signals to the physical changes in vortex core alignment along the model span, the phase of the reference velocity signals are compared with the phase variation of vortices at a specified z/D location. The resulting relative phase variation, φ, is representative of the spanwise variation in the mean phase angle of the small and large cylinder dominant wake frequencies. The results are presented in Figure 6.9, along with 95% confidence interval bands illustrating the variability in phase. The results illustrate that the mean phase angle based

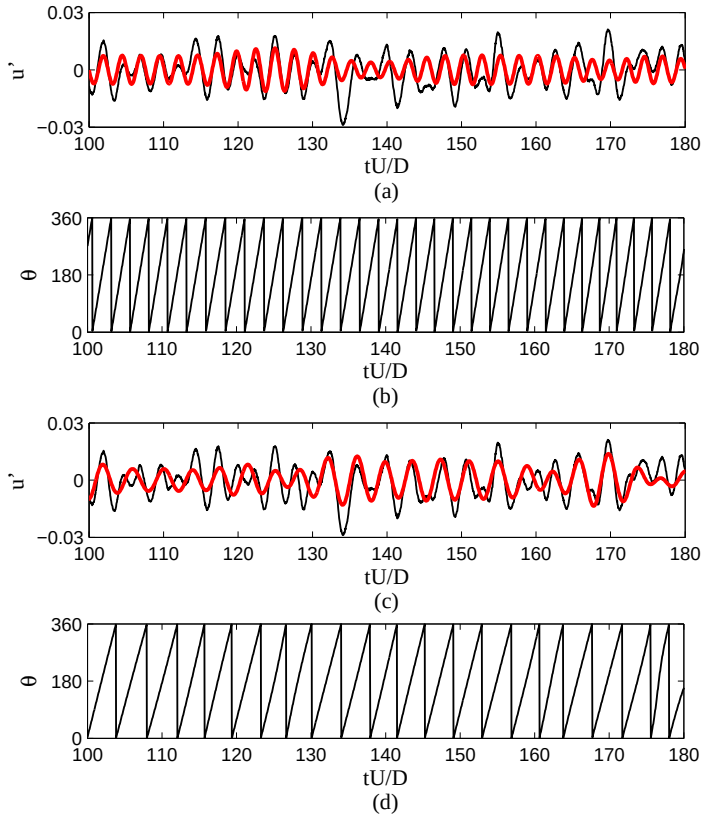

Figure 6.8 Analysis of fluctuating wake velocity data from a reduced order model of vertical plane PIV data for x/D = 3.0, z/D = -1.0. (a) Sample segment of velocity data and velocity data filtered based on a frequency band centred on the small cylinder vortex shedding frequency, (b) phase variation of the filtered velocity data in (a), (c) Sample segment of velocity data and velocity data filtered based on a frequency band centred on the large cylinder vortex shedding frequency, (d) phase variation of the filtered velocity data in (c). Filtered data are shown with red lines for (a) and (c).

on the small cylinder shedding frequency decreases with increasing z/D in the range $-50 < \varphi < 0$, while the mean phase angle based on the large cylinder shedding frequency does not vary significantly ($-10 < \varphi < 0$). As expected, for both frequency-centred activities, the most notable phase variation occurs within and near the vortex interaction region downstream of the step.

6.1.2 Three dimensional reconstruction of wake topology

To reconstruct the three-dimensional wake topology, all of the obtained reference signals are phase-shifted to match the results presented in Figure 6.9. Traditional phase-averaging of the planar (x-y)

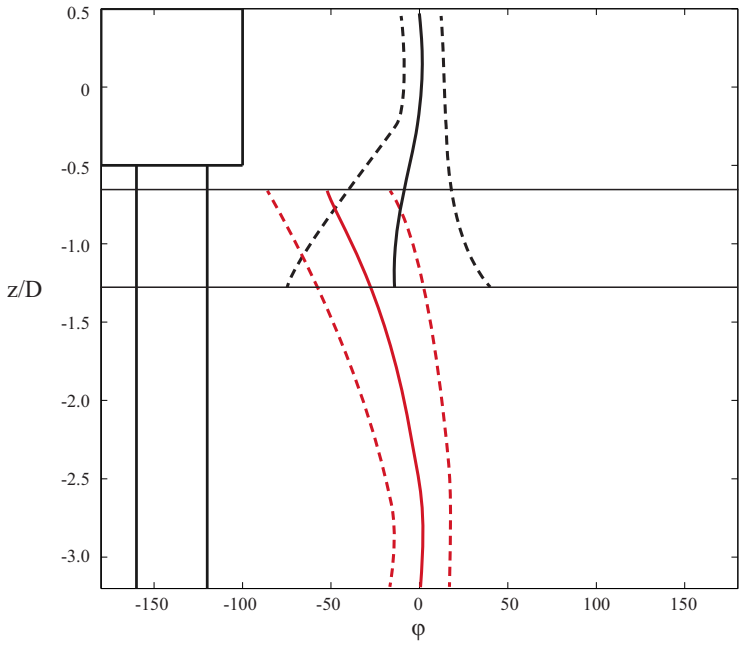

Figure 6.9 Variation in phase along the span of a dual step cylinder. Red solid and dashed curved lines represent the mean phase variation, and 95% confidence interval in the phase variation of the velocity signals filtered at the small cylinder vortex shedding frequency, respectively. Black solid and dashed curved lines represent the same for the velocity signals filtered at the large cylinder vortex shedding. The horizontal lines represent the spanwise extents of the vortex interaction region.

PIV data is performed in z/D locations where one dominant frequency is present, and conditional phase-averaging is performed in the z/D locations where two dominant frequencies are present.

The bin sizes for the phase reference signals were selected based on a compromise between minimizing statistical smearing due to the selected bin width and maximizing averaging statistics. In the large cylinder wake ($0 \geq z/D \geq -0.6$), the phase reference signals are divided into phase angle bins of 15 degrees in width. This results in about 227 instantaneous velocity fields, on the average, in each bin. In the small cylinder wake away from the interaction region ($-1.4 \geq z/D \geq -3.2$), the reference signals divided into phase angle bins of 22.5 degrees. Note, the phase angle bin size is selected so as to enable investigation of the wake vortex dynamics. On the average, for each 15 degree shift in phase in the large cylinder wake vortices there is a 22.5 degree phase shift in the small cylinder wake vortices due to the ratio of the large and small cylinder vortex shedding frequencies being about $f_S/f_L = 1.5$.

With the selected bin size of 22.5 degrees, this results in about 341 instantaneous velocity fields, on the average, in each bin. Within the interaction region, -0.6 > z/D > -1.4, the data is conditionally binned as follows. First, the reference signals are filtered at the large cylinder vortex shedding frequency, and divided into phase angle bins of 15 degrees in width. All planar fields in each bin are then re-distributed into conditional bins (22.5 degrees width) based on filtering the same reference signals at the small cylinder vortex shedding frequency. This conditional binning procedure leaves approximately 15 instantaneous planar fields to be averaged in each conditional bin. In order to maintain equal averaging statistics in regions where traditional phase averaging is performed, a 15 planar fields are randomly selected within each bin for phase-averaging. Each three-dimensional reconstruction of the wake topology is generated by selecting phase angles pertaining to the large and small cylinder wake vortices. The corresponding phase-averaged planar fields pertaining to the selected phase angles are combined in three-dimensions using a cubic spline interpolation. A sequence of three-dimensional reconstructions which are representative of experimental results is obtained by advancing the selected phase angles by the bin sizes of the corresponding reference signals. In this way, changes in the relative phase alignment between the large and small cylinder vortices matches what occurs, on the average, in an experiment. Figure 6.10 shows six three-dimensional reconstructions of the vorticity field in the wake of a dual step cylinder. Note that the reconstruction is mirrored about the x-y plane at z/D = 0. The results illustrate the dominant periodic vortex interactions occurring between the large and small cylinders in the near wake. On the average, small cylinder vortices incline back towards the step discontinuities as they are shed (e.g., Figure 6.10b and c). They consistently form vortex connections with large cylinder vortices in the near wake, though the arrangement of these connections is dependent upon the relative phase alignment of the large and small cylinder vortices. The consistent 'Y-type' connections between large and small cylinder vortices observed in the near wake agree with those observed in flow visualization results (e.g., Figure 4.8a-c). Farther downstream, vortex connections between large and small cylinder vortices are maintained when these vortices are aligned in phase (e.g., Figure 6.10d-f). When the phase separation becomes significant, e.g., Figure 6.10b, there is no evidence of direct connections being maintained. Based on the results presented in Chapter 4, in this case, consecutive small cylinder vortices form half-loop

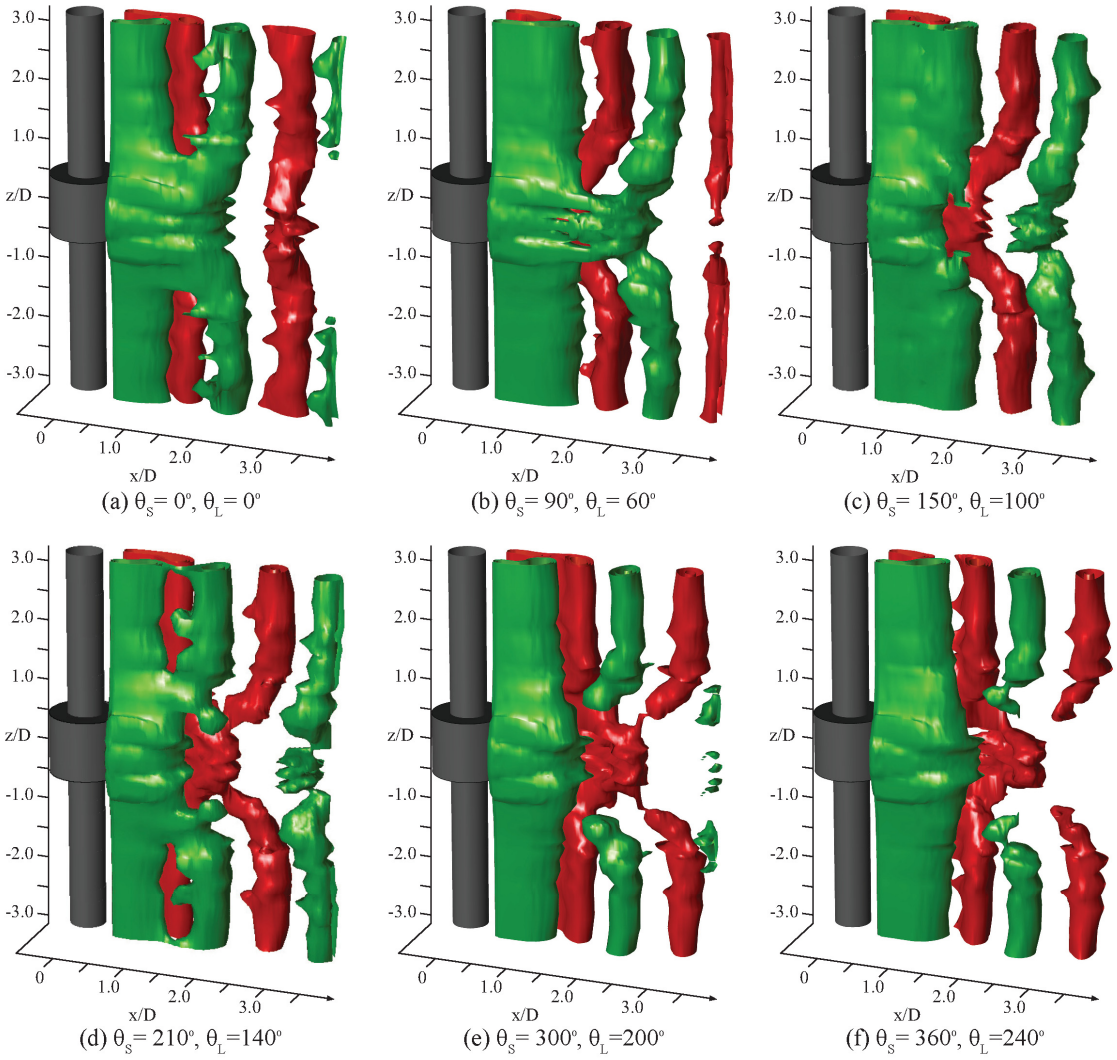

Figure 6.10 Reconstructed sequence of the three-dimensional wake topology of a dual step cylinder using isosurfaces of vorticity at $\omega U_\infty / D \approx 0.1$ for visualization. Note that the data has been mirrored about the z/D = 0 plane for illustrative purposes.

connections which cannot be properly resolved with spanwise vorticity isosurfaces due to the reorientation of the vortex core in the streamwise direction. Moreover, more significant cycle to cycle variations in the spatial arrangement of vortex connections are expected as x/D increases, and, hence, the conditional averaging cannot resolve such non-periodic features of vortex interactions. It is important to note that the sequence of images presented in Figure 6.10 are created from about 1% of the overall PIV data acquired. The images are chosen for illustrative purposes and represent just one

set of many different relative phase alignments of large and small cylinder vortices which can lead to substantially different sequences of vortex interactions.

6.1.3 Conclusion

A POD-based methodology for reconstructing three-dimensional wake topology from planar velocity measurements has been developed and evaluated experimentally. The technique is applicable primarily to strongly periodic flows which can consist of more than one dominant frequency. It relies on time-resolved planar velocity measurements acquired in multiple two-dimensional planes. Planar measurements must also be obtained in an orthogonal plane to determine quantitative information on the spatial and temporal phase variation of the vortical structures. Each of the two-dimensional planes is conditionally phase-averaged using the temporal coefficients obtained from the POD. The flow is reconstructed three-dimensionally for different relative phase of the dominant vortical structures.

A dual step cylinder in cross flow at $Re_D = 2100$, D/d = 2, and L/D = 1 was investigated to test the proposed methodology. The results show that the proposed conditional phase-averaging approach successfully reconstructs the dominant periodic vortex interactions between spanwise vortices in the wake of a dual step cylinder. This technique is a significant improvement over traditional phase averaging methods. In particular, traditional phase-averaging only allows the reconstruction of vortical structures which are described by a single frequency. In flows with multiple dominant frequencies, such as that of a dual step cylinder, the phase-averaged flow field will only resolve the dominant vortex cells in one of the two wakes, and will not resolve the dominant vortex interactions.

6.2 Conditional reconstruction through pattern recognition

The aim of the pattern recognition approach, is to reconstruct the dominant three-dimensional vortical structures and vortex interactions corresponding to any given instantaneous flow field template. The data set used in section 5.1 is used for the analysis in this section.

The first step in the pattern recognition methodology is to select a template (Figure 6.11). Vertical plane velocity fields constructed from a reduced order model of the instantaneous planar fields (e.g., Figure 6.12), are used as templates in the present study. For a given template (Figure 6.12), the next

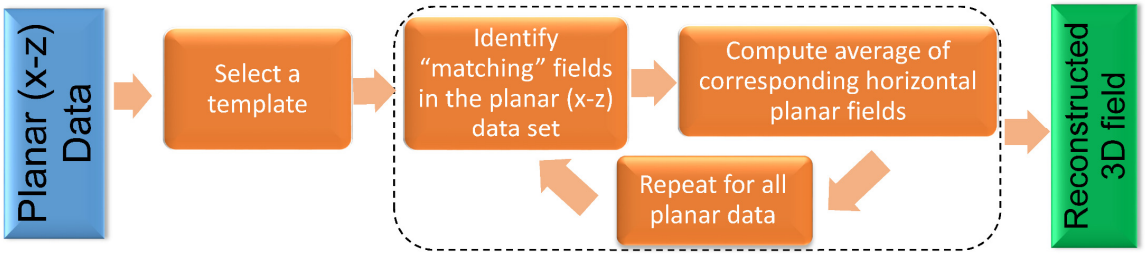

Figure 6.11 Pattern recognition methodology.

step is to conditionally bin all vertical plane velocity fields which approximately match the template field based on a cross-correlation analysis. In order to select 'matching' fields a threshold value of the correlation coefficient is selected, above which, the fields are deemed to be matching (Eq. 3.15). For the resulting set of matching vertical planar fields, there is a set of corresponding horizontal (x-y) planar fields for each horizontal measurement plane. These horizontal planar fields are averaged, and represent conditionally averaged two-dimensional flow fields pertaining to the selected template (Figure 6.11). Note that it is a common practice to use the conditionally averaged two-dimensional flow field as a template and iterate the correlation analysis until the conditionally averaged two-dimensional flow field is converged [27,28]. In the present study, no iterations in the correlation analysis were required. The reconstructed three-dimensional flow field pertaining to the template is obtained through a cubic spline interpolation between the conditionally averaged horizontal (x-y) planar fields (Figure 6.11).

The selection of a velocity field template used for correlation analysis is not a trivial process. The template should correspond to an event or feature of interest in the flow field. As can be seen in Figure 6.12, there are spatially periodic variations in velocity field. These correspond to locations of vortex cores in the dual step cylinder wake, and are produced by the vortex shedding. To focus on these spatially periodic variations in the velocity field, a rectangular region just downstream of vortex formation is selected (shown by a solid black line within the planar velocity field in Figure 6.12). It is this rectangular region of the velocity field that is used as the template for correlation analysis. The spanwise height of the template matches the region where horizontal (x-y) planar measurements have

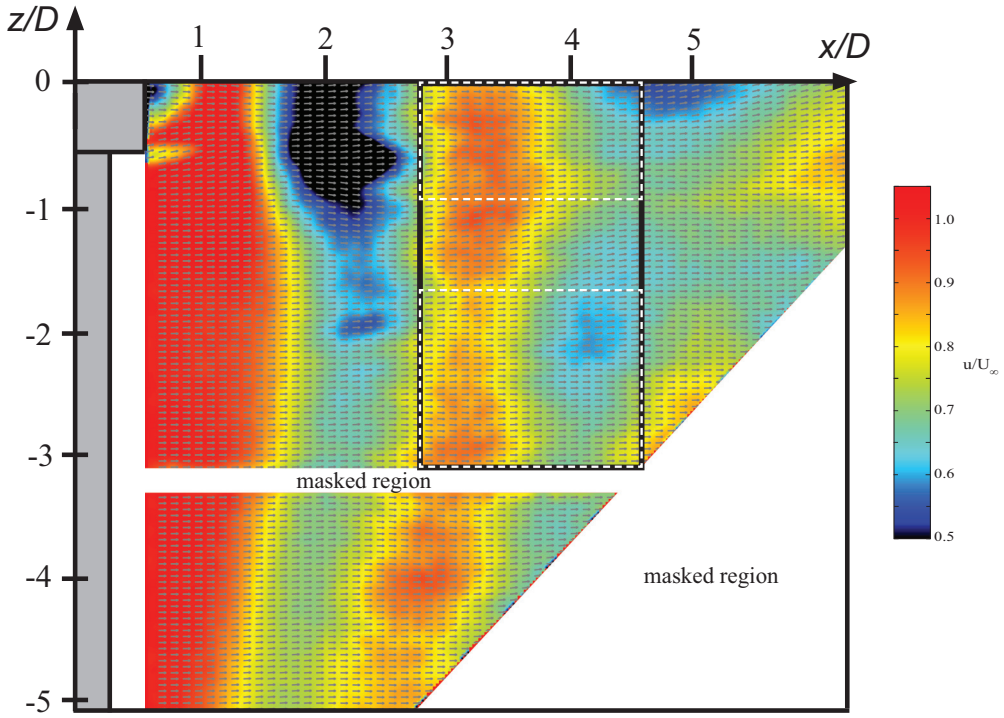

Figure 6.12 Vertical PIV planar velocity field constructed from a reduced order model of the instantaneous vertical planar fields containing the first twenty POD modes. The rectangular region used for correlation-based pattern recognition is illustrated with a solid black line. Alternative regions used for correlation analysis are indicated with white dashed lines. The vector resolution in the figure is ¼ of the true resolution in both x and y directions.

been acquired and the streamwise width of the template extends as far as possible downstream of the vortex formation region (Figure 6.12).

In order to select an appropriate threshold for the correlation coefficient, it is instructive to investigate the typical range of correlation coefficient values between the template in Figure 6.12 and all other instantaneous flow fields. Figure 6.13a shows the correlation coefficient variation between the template field shown in Figure 6.12, and the following 1000 planar fields. The results show that the correlation coefficient contains periodic fluctuations, which result from the periodic shedding of vortices from the small and large cylinders. The spectral analysis of the correlation coefficient reveals the presence of three dominant frequencies (Figure 6.13b): (i) the large cylinder vortex shedding frequency, (ii) the small cylinder vortex shedding frequency, and (iii) the beat frequency, or vortex dislocation frequency. It can be seen that the highest peaks in the correlation coefficient occur on

intervals of the vortex dislocation period. The results suggest that the wake development is linked to the occurrence of vortex dislocations, which has been confirmed experimentally in Chapter 4 and numerically in Appendix G. If the template region used for correlation analysis is selected in the large or small cylinder wakes only (see the white dashed lines in Figure 6.12), then the correlation coefficient fluctuations occur at a single frequency, the vortex shedding frequency in either the small or large

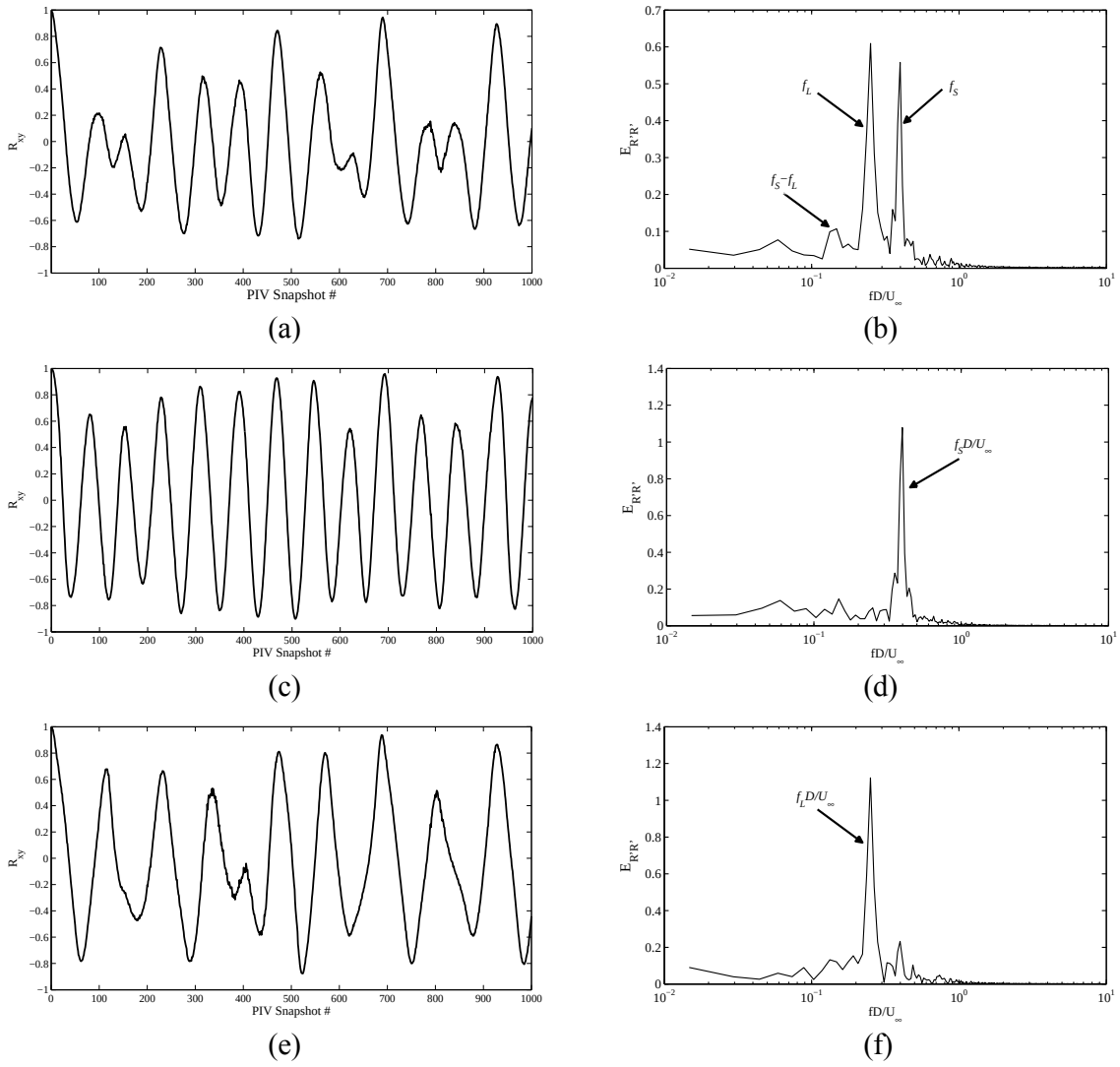

Figure 6.13 Correlation coefficient analysis in the dual step cylinder wake using the first PIV snapshot as a template: (a)-(b) whole field correlation and spectrum of the correlation coefficient, (c)-(d) small cylinder wake correlation and spectrum of the correlation coefficient, (d)-(e) large cylinder wake correlation and spectrum of the correlation coefficient. Approximately 135 snapshots covers one large cylinder vortex shedding cycle, and 85 snapshots covers one small cylinder vortex shedding cycle.

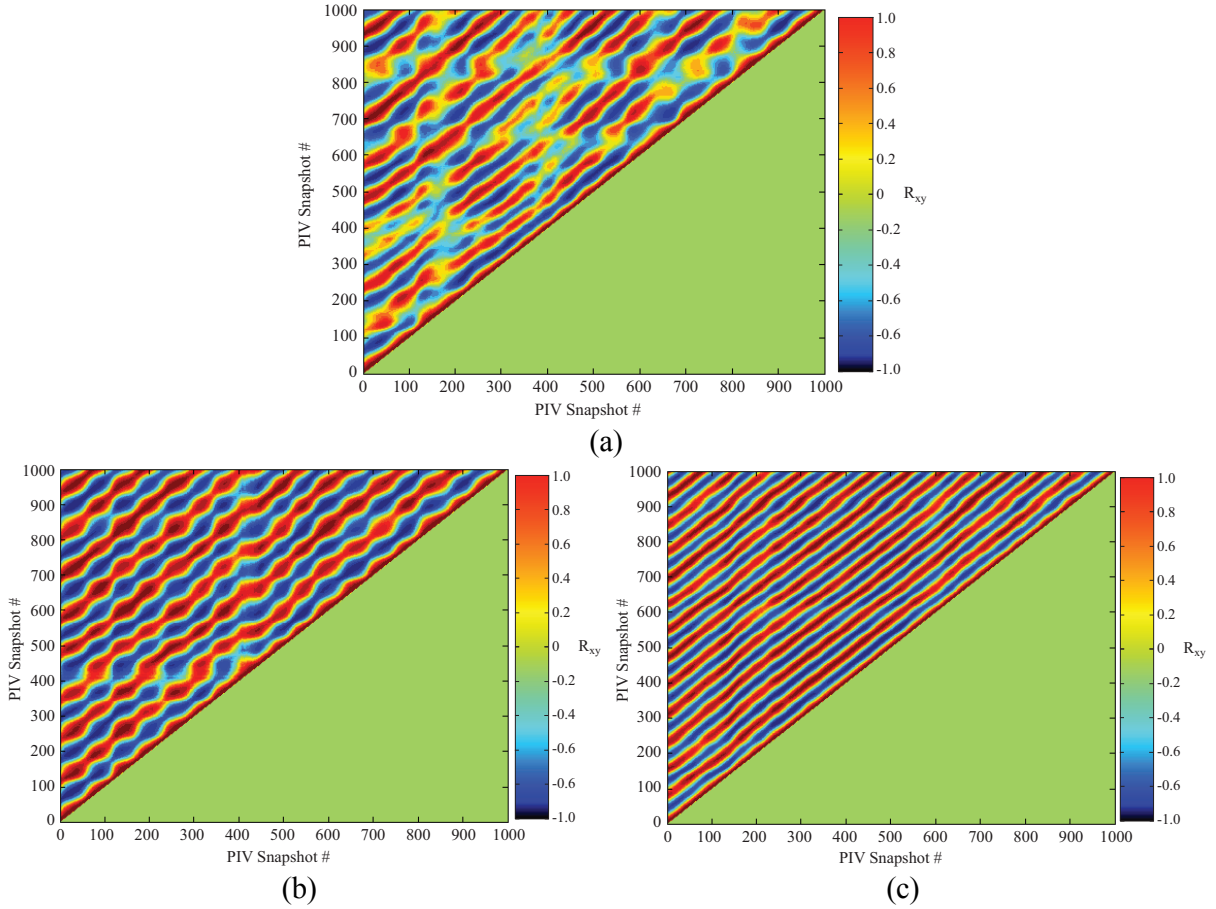

Figure 6.14 Two-dimensional correlation maps of the velocity field of select regions of a dual step cylinder wake at D/d = 2, L/D = 1, and Re_D = 2100: (a) region defined by a solid black line in the dual step cylinder wake , (b) region defined by a white dashed line in the small cylinder wake, and (c) region defined by a white dashed line in the large cylinder wake. Approximately 135 snapshots covers one large cylinder vortex shedding cycle, and 85 snapshots covers one small cylinder vortex shedding cycle.

cylinder wakes (Figure 6.13c-f). This can be viewed as well in two-dimensional correlation maps (Figure 6.14a-c). These 2D correlation maps reveal spatiotemporal information about the regularity of the flow field. As shown in Figure 6.14b-c, when only the small or large cylinder wakes are considered in the correlation analysis, there is a strong regularity in the flow field. On the other hand, when the entire template is considered (Figure 6.14a), the distinct interruptions in the periodicity and strength of the correlation coefficient value match with the vortex dislocation period.

Since the wake vortex dynamics is linked to the dislocation frequency, the shortest time interval on which the vortex interactions between the large and small cylinder vortices is expected to match is the dislocation period. A correlation coefficient threshold of $R_{xy} \geq 0.75$ is used to select the 'matching' flow fields. An adaptive algorithm is also used to ensure that only peaks in the correlation coefficient occurring on the same interval as the vortex dislocation period are selected. Note that in cases where several consecutive correlation coefficient measurements are greater than the specified threshold (e.g., PIV snapshot #690-696 in Figure 6.14a), only the field with the highest correlation coefficient is selected.

6.2.1 Implementation of the pattern-recognition approach

The selected template (Figure 6.12) is correlated with vertical plane measurements in each of the eighteen acquired data sets. On the average, between fifteen and twenty 'matching' vertical plane fields are found in a given data set containing 5456 fields. The corresponding 'matching' horizontal planar fields are averaged. As a result, eighteen averaged horizontal (x-y) planar fields which correspond to the template field are obtained. The averaged horizontal planar fields are then combined via cubic spline interpolation to obtain a three-dimensional reconstruction of the wake topology corresponding to the selected template. This process is applied to forty vertical plane templates spanning approximately three large cylinder vortex shedding cycles, which allows reconstruction of three-dimensional wake vortex dynamics. Figure 6.15 shows selected images from the sequence which illustrate the wake development. In particular, strong vortex connections form between large and small cylinder vortices when they are shed in phase (e.g., Figure 6.15a-b). On the next large cylinder shedding cycle, the vortices begin to move out of phase due to the difference in their shedding frequencies. The small cylinder vortices tilt back and stretch in order to maintain connections with their counterparts in the large cylinder wake (Figure 6.15c-d). Eventually, as the phase misalignment approaches 2π radians, i.e., the dislocation period, the small cylinder vortices lose their connections with the large cylinder vortices (Figure 6.15e-f), and develop half-loop vortex connections with adjacent small cylinder vortices instead (Figure 6.15f). The observed features of the vorticity topology

are in agreement with previous flow visualization results presented in Chapter 4 as well as sketches of the proposed vortex dynamics in the HFS regime.

6.3 A comparison of three-dimensional reconstruction methods

The two three-dimensional reconstruction methods are compared qualitatively in Figure 6.16 using three-dimensional reconstructions of the spanwise vorticity field. The images represent a sequence selected such that the first image features nearly perfect physical alignment between large and small cylinder vortices, with subsequent images being constructed over a single large cylinder vortex

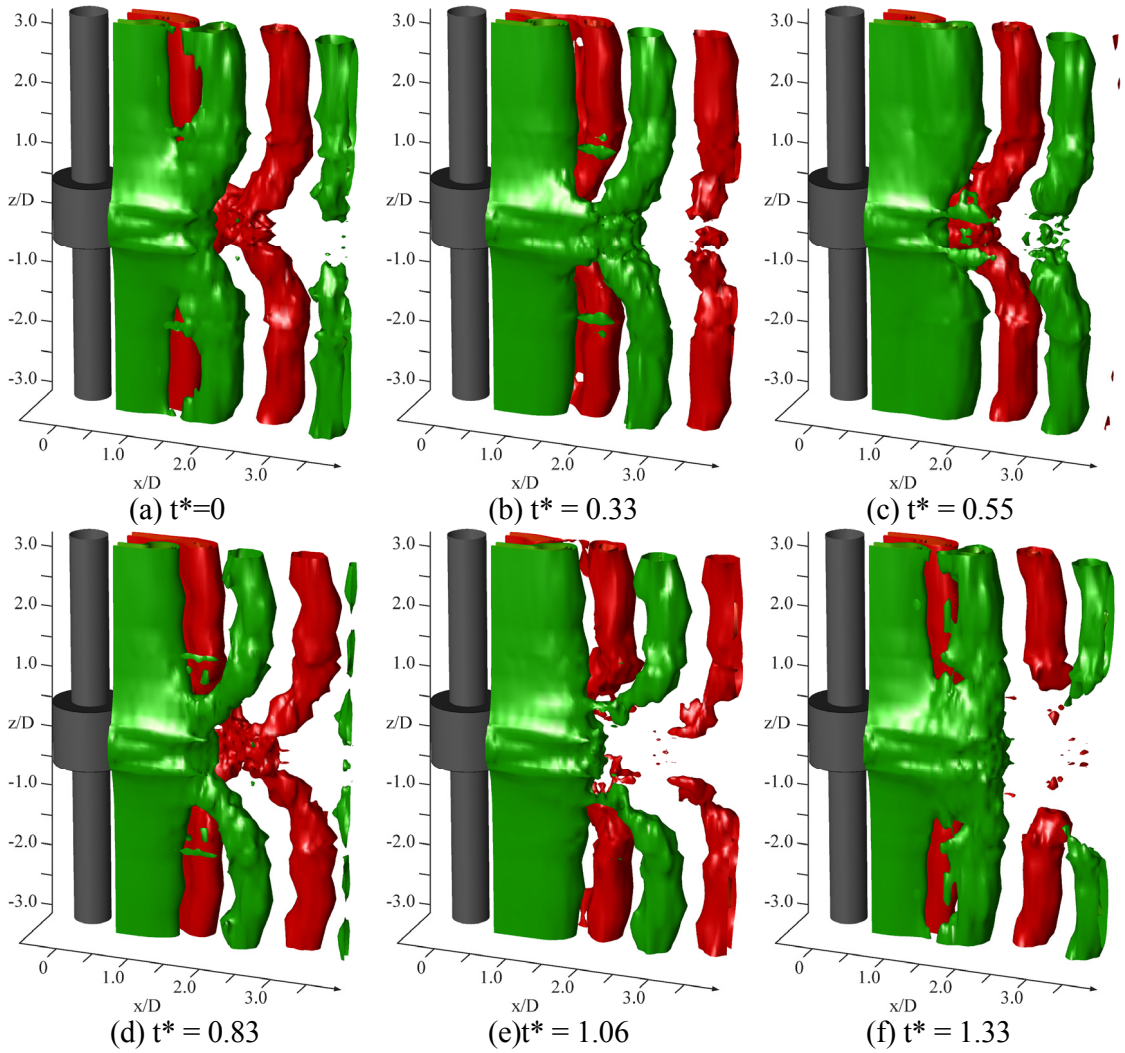

(a) t*=0 (b) t* = 0.33 (c) t* = 0.55

(d) t* = 0.83 (e)t* = 1.06 (f) t* = 1.33

Figure 6.15 A sequence of three-dimensional reconstructions of the vorticity field visualized through spanwise vorticity isosurfaces. t* is the number of large cylinder vortex shedding cycles.

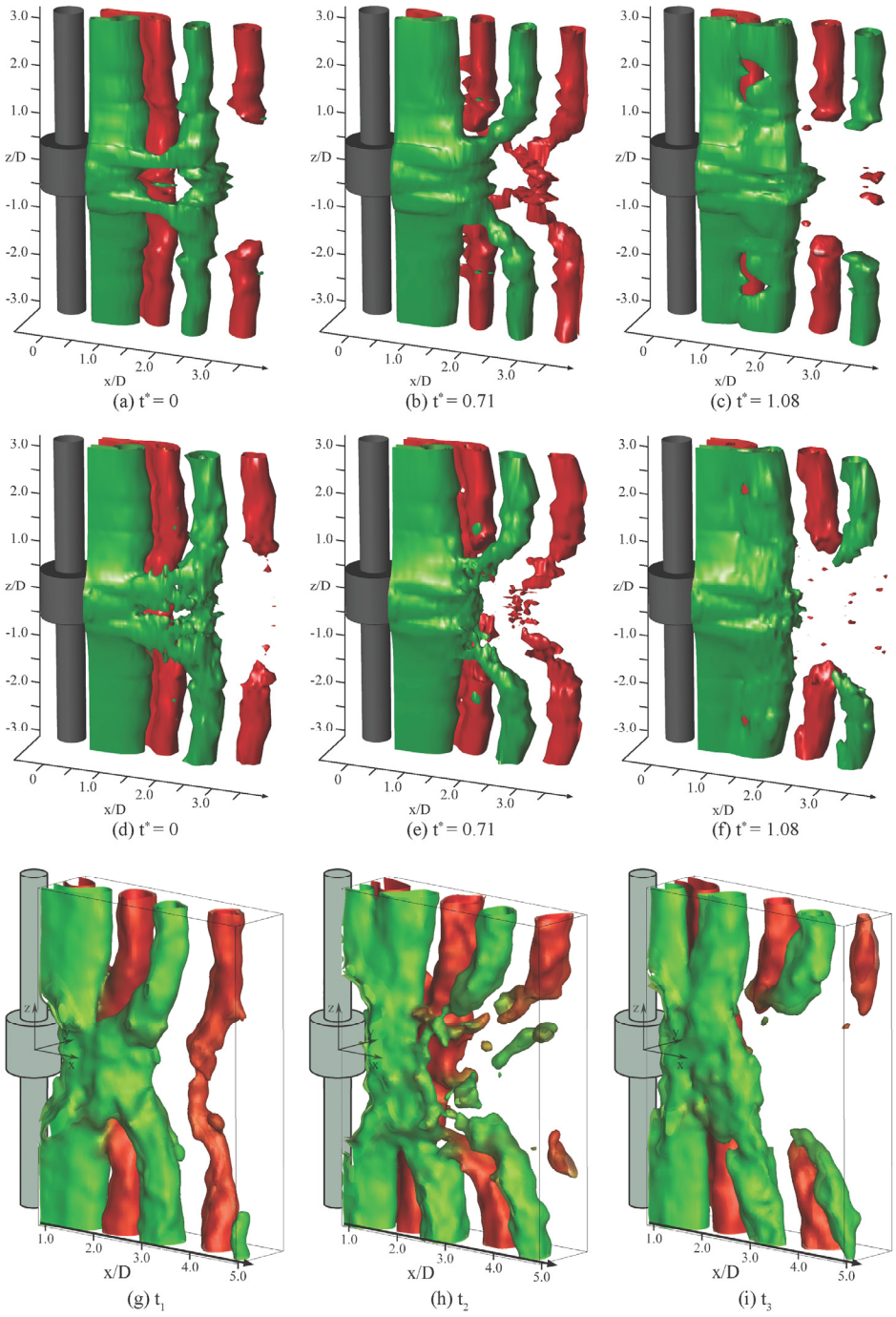

Figure 6.16 Three-dimensional reconstructions of the vorticity field in the wake of a dual step cylinder for L/D = 1, D/d = 2, and Re_D = 2100. (a)-(c) reconstructions using a POD-based conditional phase-averaging methodology, (d)-(f) reconstructions using a pattern recognition based conditional averaging methodology, (g)-(i) tomographic PIV reconstructions. t* is the number of large cylinder vortex shedding cycles.

shedding cycle. Also shown in Figure 6.16g-i are tomographic PIV results. For adequate comparison with the three-dimensional reconstructions, a reduced order model of the tomographic PIV results is shown (see Chapter 5 for further details). The tomographic PIV results are obtained with the same model at the same Reynolds number. Moreover, the reduced order model is representative of the dominant coherent structures in the wake, which is of primary interest in this study. Figures 6.16a,d and g show an instantaneous snapshot of the vorticity field when small and large cylinder vortices are aligned at formation. In this case, for $x/D < 3$, vortex cores connect across the large and small cylinder wakes. As the shedding cycle progresses, the difference in vortex shedding frequencies leads to the small and large cylinder vortices moving out of phase at formation, as shown in Figure 6.16b,e and h. The reconstructed vorticity fields show that small cylinder vortices maintain their connection with large cylinder vortices through the stretching and tilting of the vortex filaments. When the relative phase alignment between large and small cylinder vortices becomes too great, two consecutive small cylinder vortices are expected to form half-loop vortex connections (Figure 6.16c,f and i). The tomographic PIV results (Figure 6.16g-i) depict strong half-loop connections in both small cylinder wakes, which confirms that these connections do indeed form between consecutive small cylinder vortices (Figure 6.16i). Comparing the POD-based reconstruction and pattern recognition results, the pattern recognition reconstruction (Figure 6.16f) appears to resolve the half-loop connection better than the POD-based reconstruction (Figure 6.16c). In both cases, however, the majority of the half-loop connection cannot be reconstructed due to the fact that the streamwise vorticity component is not resolved in the flow field.

It is important to note that the implementation of the two developed methods of three-dimensional reconstruction can be improved. For the POD-based method, the error in the conditionally phase-averaged planar fields is minimized by decreasing the size of the phase angle bins (minimizes smearing) and increasing the number of fields contained within each bin (minimizes random error). Since these two parameters are inversely related, improvements are generally made by obtaining larger samples of data. For the pattern recognition based method, the error in the conditionally averaged planar fields is minimized by increasing the value of the correlation coefficient threshold (minimizes

smearing) and increasing the number of 'matching fields' (minimizes random error). Similar to the parameters influencing the quality of the POD-based reconstructions, these two parameters are inversely related, and larger samples of data are required.

The three-dimensional reconstructions shown in Figure 6.14 can also be evaluated and compared quantitatively. One approach is based on a measure of the average residual error in the total circulation of individual planar fields for a given conditional set of planar data (Appendix E, Equation E.2). This represents the average degree of deviation between the circulation of planar instantaneous and conditionally averaged vorticity fields. The average residual error in total circulation was computed for all x-y planar data using both three-dimensional reconstruction methods and the results are presented in Table 6.1. As shown in the table, the average residual error is about 45% for both methods, and is only marginally higher than that found for a uniform circular cylinder (Table 6.1). In comparison, randomly selected fields with no conditional averaging procedure have an average residual error in total circulation of over 300% (Table 5.1).

The second approach to quantitatively evaluate the three-dimensional reconstruction methods is to compute the average correlation coefficient between planar (x-y) vorticity fields that have been conditionally binned. The average correlation coefficient between the averaged field and all instantaneous fields contained within a bin is computed as follows:

$$\boldsymbol{R_i} = \frac{\boldsymbol{cov}(\boldsymbol{\omega^a}, \boldsymbol{\omega^i})}{\boldsymbol{\sigma_a \sigma_i}} \tag{6.1}$$

$$\boldsymbol{\overline{R}} = \frac{\sum_{\boldsymbol{i=1}}^{\boldsymbol{N}} \boldsymbol{R_i}}{\boldsymbol{N}} \tag{6.2}$$

where R_i is the correlation coefficient between the conditionally averaged vorticity field, ω^a, and the instantaneous vorticity field, ω^i. $\bar{R}$ is the averaged correlation coefficient based on N instantaneous planar vorticity fields within a given conditional bin. This measure represents the degree of correlation-based similarity between planar instantaneous and conditionally averaged vorticity fields. Equation 5.2 is used on all conditionally binned data for all 18 horizontal planar fields for each of the two methods of three-dimensional reconstruction. The results are presented in Figure 6.17 and show that

Table 6.1 Average residual error of the total circulation through all planar data sets for both methods of three-dimensional reconstruction.

	POD, ε (%)	Pattern Recognition, ε (%)
Uniform Cylinder	34 to 39 (Appendix E)	-
Dual Step Cylinder	45.3	45.6
Random selection of planar fields	310	

the average correlation coefficient exceeds 0.6 across all z/D locations. On the average, the pattern recognition conditional binning technique outperforms the POD-based conditional binning methodology (Figure 6.17).

6.4 Conclusion

In this Chapter, a novel multi-plane PIV setup was implemented to develop and validate two methodologies of reconstructing the dominant three-dimensional vortex dynamics in the wake of a dual step cylinder for L/D = 1, D/d = 2, and Re_D = 2100.

Technique #1: A POD-based conditional phase-averaging approach involving the analysis of 2D PIV measurements in x-y and x-z planes. The temporal coefficients associated with a POD analysis of each

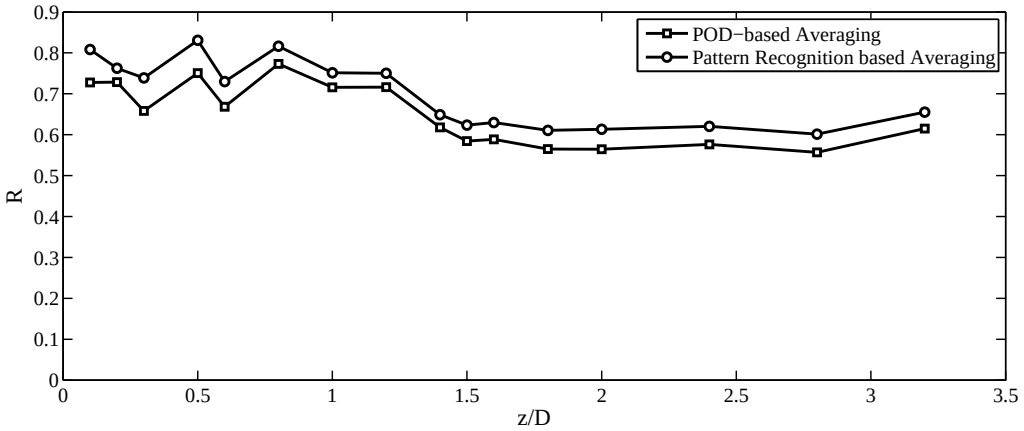

Figure 6.17 The average correlation coefficient between conditionally binned planar data in each horizontal plane.

horizontal plane are used to obtain the phase variation of the dominant coherent structures and conditionally phase-average the flow field. An analysis of the vertical plane is used to determine the average relative phase-alignment between the planes.

Technique #2: A pattern recognition based conditional-averaging approach involving the analysis of 2D PIV measurements in x-y and x-z planes obtained simultaneously. A correlation analysis of a vertical plane velocity field template is used to find 'matching' planar fields in a given data set. The corresponding horizontal x-y planar fields are averaged for all horizontal planes. The three-dimensional flow field corresponding to the velocity field template is reconstructed through a cubic spline interpolation between the horizontal planes.

Both of the techniques successfully reconstruct the dominant vortical structures and their interactions. A qualitative and quantitative comparison of the two reconstruction methods was carried out. Three-dimensional reconstructions of the flow development were compared for the same relative phase alignment between the large and small cylinder vortices. The results indicate that the half-loop vortex connections occurring periodically between consecutive small cylinder vortices are resolved better with the pattern recognition technique. To quantitatively evaluate the quality of the reconstructions, the degree of correlation-based similarity, and degree of deviation in circulation between planar instantaneous and conditionally averaged vorticity fields was estimated. The results also suggest that the pattern recognition technique reconstructs the three-dimensional wake topology with greater accuracy.

Both methods have advantages and disadvantages depending on the availability of equipment and data processing tools. The POD-based conditional averaging technique can be implemented using a single camera PIV system with independently measured horizontal and vertical planar data sets. Reconstructing wake vortex dynamics relies on artificially advancing the phase of the coherent structures based on knowledge of their vortex shedding frequencies. The pattern recognition based technique requires two cameras simultaneously acquiring PIV data in one vertical and one horizontal plane. Analysis of wake vortex dynamics is carried out by reconstructing a sequence of three-dimensional flow fields over several vortex shedding cycles.

Chapter 7

Conclusions

A comprehensive parametric experimental study of a dual step cylinder in cross flow was completed for $1050 \leq Re_D \leq 5000$,$1.33 \leq D/d \leq 4.0$, and $0.2 \leq L/D \leq 17$. In addition, two experimental methods are developed for reconstructing the three-dimensional wake vortex dynamics of a dual step cylinder using 2D PIV measurements in multiple closely spaced planes.

7.1 A dual step cylinder in cross-flow

The study was focused on investigating the effects of dual step cylinder geometry (D/d and L/D) and Reynolds number (Re_D) on wake development and structural loading in turbulent flows. Experimental measurements in the University of Waterloo Water Flume Facility were completed with two-dimensional Particle Image Velocimetry (PIV), Laser Doppler Velocimetry, and a multi-component force balance. In addition, flow visualization was carried out using hydrogen bubble technique, and surface visualization was carried out using a new technique developed for surface visualization in water. Through an analysis of the qualitative and quantitative measurements, six distinct flow regimes were identified based on observed changes in the flow development downstream of the large cylinder. A two-dimensional map of flow regimes was proposed which describes the D/d and L/D ranges where changes in flow development occur.

A tomographic PIV study of the flow development over dual step cylinders was completed in an open jet wind tunnel at TU Delft. The results confirm the presence of the six identified flow regimes, and support the descriptions of the flow regimes and associated two-dimensional map. The tomographic PIV results are also used to validate the two techniques developed for reconstructing the three-dimensional wake topology of a dual step cylinder.

The essential characteristics of the identified regimes can be described as follows:

CS – Cellular Vortex shedding regime

This regime occurs for L/D ≥ 13-20. Multiple vortex shedding cells are detectable downstream of the large cylinder, with the coherence and strength of the vortex shedding resembling those typical for shedding from a uniform circular cylinder of diameter D. The vortex shedding frequency of each of the cells is slightly lower than that found for uniform circular cylinders. This is attributed to earlier boundary layer separation occurring on the large cylinder. Due to the difference in shedding frequency between the three cells, the vortex filaments move in and out of phase, resulting in periodic vortex dislocations which are similar to those observed in the wake of a single step cylinder. Vortex dislocations also occur between the vortices shed in the small and large cylinder wakes. While structural loading characteristics for this flow regime were not evaluated experimentally, they are expected to be similar to those found for the LFS regime.

LFS – Low frequency vortex shedding regime

Transition to the LFS regime from the CS regime occurs when the low frequency end cells found for the CS regime merge into a single cell. This occurs for about L/D < 13-20. The coherence and strength of the vortex shedding in the wake of the large cylinder is similar to that found for the CS regime. The shedding frequency is up to 10% lower than that found for a uniform cylinder of diameter D. This is attributed boundary layer separation along the large cylinder span which is speculated to occur earlier than that found for the CS regime. The wake vortex dynamics involves periodic vortex dislocations occurring between the vortices shed from the large and small cylinders as they move in and out of phase. The structural loading characteristics for the LFS regime show that the mean drag on the large cylinder greater than that found for a uniform cylinder of diameter d with the same length. For fluctuating forces, the RMS lift on the dual step cylinder model is about 10% smaller than that found for a uniform cylinder of diameter d. This is attributed to the presence of the large cylinder, which disrupts the coherence of the shedding from the small cylinders along the span. The degree of RMS lift reduction is speculated to depend on the lengths of the small diameter cylinders, as well as the L/D and D/d of the dual step cylinder.

IS – Irregular vortex shedding regime

The IS regime occurs for larger diameter ratios ($D/d > 1.5$) and a wide range of aspect ratios, $1 < L/D \leq 7$. The coherence, strength, and frequency of vortex shedding from the large cylinder are reduced substantially when compared to that of a uniform cylinder of diameter D. In the IS regime, the separation point on the large cylinder advances upstream when compared to the LFS regime. This results in a wider and longer vortex formation region when compared to a uniform cylinder as well as cylinders in the LFS regime, and explains the observed reduction in vortex shedding frequency. On the average, there is minimal interaction between vortices shed from the small and large diameter cylinders. Large cylinder vortices deform substantially as they are shed into the wake into hairpin-like vortical structures whose 'legs' attain a streamwise orientation and connect to subsequently shed large cylinder vortices. Small cylinder vortices form a continuous band of half-loop connections and some weak connections to large cylinder vortices. Transverse Kelvin-Helmholtz (K-H) instability vortices intermittently form downstream of each of the stepwise discontinuities for a small range of D/d and L/D within the IS regime for $Re_D \geq 2100$. In addition, spanwise K-H rollers form within the large cylinder separated shear layers for similar D/d, L/D, and Re_D. The mean drag in this regime varies substantially with D/d and L/D. At the smallest D/d and L/D pertaining to the IS regime, the mean drag on the large cylinder is comparable to that found for a uniform cylinder of diameter d with the same length. At higher D/d and L/D values, the mean drag increases proportionally with the planform area of the large cylinder. Fluctuating forces on the dual step cylinder are reduced by up to 60% in the IS regime when compared to a uniform small diameter cylinder, and occurs at the highest D/d and L/D values investigated within the IS regime.

HFS – High frequency vortex shedding regime

The HFS regime occurs for a narrow range of aspect ratios and diameter ratios, between the LFS, IS, and NS flow regimes. Coherent vortex shedding occurs from the large cylinder at a frequency that is up to 30% higher than the shedding frequency of a uniform circular cylinder of diameter D. In contrast with previous flow regimes which show an upstream advancement of the separation point on the large cylinder with decreasing D/d and L/D, in this regime, boundary layer separation on the large cylinder

becomes delayed. This leads to a reduction in the size of the vortex formation length and is responsible for the observed increase in vortex shedding frequency. The increased shedding frequency results in a smaller difference in the shedding frequency of large and small cylinder vortices when compared to other flow regimes at the same D/d. As a result, vortex dislocations take place over several large cylinder vortex shedding cycles. The mean drag on the large cylinder is up to 20% larger than the drag force on a uniform cylinder of diameter d with the same length. Fluctuating lift on the dual step cylinder is about 15% smaller than that found for a uniform cylinder of diameter d.

AIS – Asymmetric, irregular vortex shedding regime

The AIS regime occurs for a narrow range of large cylinder aspect ratios (L/D ~ 0.5), and diameter ratios (D/d ≥ 2.67). In this regime, vortex shedding occurs from one side of the large cylinder, with the opposite shear layer remaining relatively steady. The vortices shed have reduced coherence and strength compared to those shed from a uniform cylinder of diameter D. The one-sided vortex shedding results in an asymmetry in the flow development that is not observed for any other flow regime. The mean drag on the large cylinder is up to double that found for a uniform small diameter cylinder of the same length. Fluctuating lift on the dual step cylinder is about 30% smaller than that found for a uniform cylinder of diameter d. It is speculated that a non-zero mean lift force is generated on the large cylinder due to the asymmetry in the flow development.

NS – No vortex shedding regime

At very low aspect ratios, the vortex shedding from the large cylinder ceases completely. This occurs due to a downstream shift in the separation angle on the large cylinder. The vortices shed from the small diameter cylinders interact through complex vortex connections across the wake of the large cylinder. In particular, vortex filaments connect across the large cylinder wake, but their convective velocity is reduced due to the presence of the large cylinder. As a result, these filaments distort and stretch, eventually leading to a vortex dislocation manifested by half-loop connections between consecutive small cylinder vortices. Mean drag on the large cylinder in this regime is approximately the same as that found for a uniform small diameter cylinder at D/d = 2, but is slightly larger for all

other D/d investigated. The fluctuating lift is approximately the same as that found for a uniform small diameter cylinder for all D/d investigated.

Note, the Reynolds number has been found to have an effect on dual step cylinder wake development. While the results suggest that each of the identified flow regimes persist for all Reynolds numbers investigated, the specific D/d and L/D boundaries of the regimes change with Re_D. For example, at D/d = 1.6 and L/D = 2, an intermittent switching between the IS and HFS flow regimes occurs for Re_D = 2000. However, at higher Reynolds number, tomographic PIV measurements show IS regime wake characteristics for this model geometry. More subtle changes in flow development characteristics also occur within each flow regime with Reynolds number. For example, shear layer instability vortices intermittently form within the large cylinder separated shear layers for $Re_D \geq 2100$, but are not observed at lower Reynolds numbers. This is similar to the changes in flow development reported for a uniform cylinder wake, where shear layer vortices have been observed for Reynolds numbers above about 2000 [125]. Thus, with increasing Reynolds number, shear layer instability vortices are speculated to manifest in all flow regimes. In general, characteristics of uniform cylinder flow development which are strongly dependent on Reynolds number are expected to persist for dual step cylinder flow development as well.

7.2 Reconstructing three-dimensional flow topology from 2D time-resolved PIV measurements

Two experimental methods are developed in this thesis for reconstructing the three-dimensional wake vortex dynamics of a dual step cylinder for L/D = 1, D/d = 2, and Re_D = 2100. The methods are designed to handle the presence of more than one dominant frequency in the flow field. The first approach is a POD-based methodology applied to time-resolved planar velocity measurements in multiple closely-spaced two-dimensional horizontal (x-y) planes as well as independent measurement in a single orthogonal vertical (x-z) plane. Each of the horizontal planes is conditionally phase-averaged using POD. The vertical plane is configured to determine the average phase variation of the vortex cores along the span in order to align each of the horizontal planes. The flow is reconstructed

three-dimensionally for different phase alignments of the dominant vortical structures in the large and small cylinder wakes.

The second method is a pattern recognition based conditional averaging approach which uses PIV measurements in horizontal and vertical planes acquired simultaneously. The horizontal plane is moved to multiple closely spaced locations along the span of the model while the vertical plane remains stationary. A cross-correlation analysis of a single instantaneous vertical PIV field with all other instantaneous fields measured in the same plane is used to identify matching fields in each data set. Since each matching vertical PIV field has a corresponding horizontal PIV field, all of the corresponding horizontal PIV fields within the data set are averaged. This process is carried out for all horizontal plane locations. Each conditionally averaged horizontal PIV field is stitched together in three-dimensions to reconstruct the three-dimensional flow field pertaining to the selected instantaneous vertical plane flow field.

Both of the methods are shown to successfully reconstruct salient features of the wake vortex dynamics. A qualitative and quantitative comparison of the two reconstruction methods was carried out. A qualitative comparison of three-dimensional reconstructions obtained with both methods indicates that the pattern recognition technique resolves half-loop vortex connections occurring between consecutive small cylinder vortices with greater accuracy. To quantitatively evaluate the quality of the reconstructions, the degree of correlation-based similarity, and degree of deviation in circulation between planar instantaneous and conditionally averaged horizontal planar vorticity fields was estimated. The results suggest that higher quality reconstructions are generated using pattern recognition.

Both methods have advantages and disadvantages depending on the availability of equipment and data processing tools. The POD-based conditional averaging technique can be implemented using a single camera PIV system with independently measured horizontal and vertical planar data sets. Reconstructing wake vortex dynamics relies on artificially advancing the phase of the coherent structures based on knowledge of their vortex shedding frequencies. The pattern recognition based technique requires two cameras simultaneously acquiring PIV data in one vertical and one horizontal

plane. Analysis of wake vortex dynamics is carried out by reconstructing a sequence of three-dimensional flow fields over several vortex shedding cycles.

Chapter 8

Recommendations

Based on the outcomes of the present thesis, there are several recommendations for further research on dual step cylinders in cross flow, as well as in the general area of using planar PIV for investigating three-dimensional wake characteristics of bluff bodies.

1. This thesis presents the first comprehensive study of the flow development and structural loading on dual step cylinders. Further research is required to identify the effects of Reynolds number on wake topology and structural loading, since the present experimental work is limited to a Reynolds number range of $1050 \leq Re_D \leq 5000$.

2. Six distinct flow regimes were identified based on changes in large cylinder wake topology for a dual step cylinder. However, additional flow regimes may exist at higher diameter ratios and Reynolds numbers than those studied in the present work. Investigations should be carried out at lower and higher D/d in order to approach the limiting D/d cases of a cylinder with free ends ($D/d = \infty$), and a uniform circular cylinder ($D/d = 1$).

3. The present data show that the dual step cylinder geometry has potential to be used as a unidirectional surface modification for the passive control of vortex shedding from circular cylinders. On large aspect ratio structures, multi-step cylinders could be used to mitigate vortex induced vibrations by reducing the spanwise coherence of shed vortices. Moreover, the investigation on multi-step cylinder geometries carried out by Nakamura and Igarashi [17] suggests that a dual step cylinder can also be used for reducing drag. Further research is required to assess the benefits of using dual step or multi-step cylinders for drag reduction and/or suppression of VIV.

4. In order to assess the quality of the developed three-dimensional reconstruction methods developed in this thesis, it is recommended that additional evaluation of the techniques is

carried out. This can be completed by performing numerical simulations. Data from the numerical studies can be used to emulate the acquisition of PIV data and directly compare the reconstruction methods with the three-dimensional flow field data.

5. Once the three-dimensional reconstruction techniques have been evaluated in detail in (4), the techniques can be used to reconstruct the three-dimensional wake topology associated with each of the identified dual step cylinder flow regimes, and also investigate other complex bluff body geometries.

6. The experimental setup used for acquiring multi-plane PIV data in orthogonal planes (Chapter 5) can be improved. Since the two laser sheets intersect, a high intensity band of light is imaged by each of the high speed cameras. This narrow band must be masked during the PIV data analysis. It may be possible to avoid this by modifying the experimental setup as follows. The beam splitting optics can be replaced with an oscillating mirror, which deflects the beam between the horizontal and vertical planes in an alternating fashion. While this implies that the particle images in each plane are obtained at separate instances in time, it will not adversely affect the interpretation of the results as long as the time between successive images is short relative to the timescales of the flow.

Bibliography

[1] Lie, H., and Kaasen, K. E., 2006, "Modal analysis of measurements from a large-scale VIV model test of a riser in linearly sheared flow," J. Fluids Struct., **22**(4), pp. 557–575.

[2] Matsumoto, M., Shiraishi, N., and Shirato, H., 1992, "Rain-wind induced vibration of cabels and cable-stayed bridges," J. Wind Eng. Ind. Aerodyn., **41-44**, pp. 2011–2022.

[3] Wirsching, B. P. H., and Asce, M., 1984, "Fatigue reliability for offshore structures," J. Struct. Eng., **110**, pp. 2340–2356.

[4] Blake, W. K., 2012, Mechanics of Flow-Induced Sound and Vibration V2: Complex Flow-Structure Interactions, Elsevier.

[5] Bernitsas, M. M., Raghavan, K., Ben-Simon, Y., and Garcia, E. M., 2008, "VIVACE (Vortex Induced Vibration Aquatic Clean Energy): A New Concept in Generation of Clean and Renewable Energy From Fluid Flow," J. Offshore Mech. Arct. Eng., **130**(4), p. 41101.

[6] Stephen, N. G., 2006, "On energy harvesting from ambient vibration," J. Sound Vib., **293**(1–2), pp. 409–425.

[7] Barrero-Gil, A., Alonso, G., and Sanz-Andres, A., 2010, "Energy harvesting from transverse galloping," J. Sound Vib., **329**(14), pp. 2873–2883.

[8] Allen, J. J., and Smits, A. J., 2001, "Energy harvesting eel," J. Fluids Struct., **15**(3–4), pp. 629–640.

[9] Zdravkovich, M. M., 1981, "Review and classification of various aerodynamic and hydrodynamic means for suppressing vortex shedding," J. Wind Eng. Ind. Aerodyn., **7**(2), pp. 145–189.

[10] Griffin, O. M., and Ramberg, S. E., 1982, "Some Recent Studies of Vortex Shedding With Application to Marine Tubulars and Risers," J. Energy Resour. Technol., **104**(1), pp. 2–13.

[11] Owen, J. C., Bearman, P. W., and Sszewczyk, A. A., 2001, "Passive control of VIV with drag reduction," J. Fluids Struct., **15**(3–4), pp. 597–605.

[12] Choi, H., Jeon, W.-P., and Kim, J., 2008, "Control of Flow Over a Bluff Body," Annu. Rev. Fluid Mech., **40**(1), pp. 113–139.

[13] Achenbach, E., 1971, "Influence of surface roughness on the cross flow around a circular cylinder," J. Fluid Mech., **46**, pp. 321–335.

[14] Yildirim, I., Rindt, C. C. M., and Steenhoven, A. A., 2010, "Vortex dynamics in a wire-disturbed cylinder wake," Phys. Fluids, **22**(9), p. 094101.

[15] Bearman, P. W., 1965, "Investigation of the flow behind a two dimensional model with a blunt trailing edge and fitted with splitter plates," J. Fluid Mech., **21**, pp. 241–255.

[16] Williamson, C. H. K., 1992, "The natural and forced formation of spot-like ' vortex dislocations ' in the transition of a wake," J. Fluid Mech., **243**, pp. 393–441.

[17] Nakamura, H., and Igarashi, T., 2008, "Omnidirectional reductions in drag and fluctuating forces for a circular cylinder by attaching rings," J. Wind Eng. Ind. Aerodyn., **96**(6-7), pp. 887–899.

[18] Zdravkovich, M. M., Flaherty, a. J., Pahle, M. G., and Skelhorne, I. a., 1998, "Some aerodynamic aspects of coin-like cylinders," J. Fluid Mech., **360**, pp. 73–84.

[19] Morton, C., and Yarusevych, S., 2010, "Vortex shedding in the wake of a step cylinder," Phys. Fluids, **22**(8), p. 083602.

[20] Zdravkovich, M. M., Brand, V. P., Mathew, G., and Weston, A., 1989, "Flow past short circular cylinders with two free ends," J. Fluid Mech., **203**, pp. 557–575.

[21] Arroyo, M. P., and Hinsch, K. D., 2008, "Recent Developments of PIV towards 3D Measurements," Top. Appl. Phys., **112**, pp. 127–154.

[22] Perrin, R., Cid, E., Cazin, S., Sevrain, a., Braza, M., Moradei, F., and Harran, G., 2006, "Phase-averaged measurements of the turbulence properties in the near wake of a circular cylinder at high Reynolds number by 2C-PIV and 3C-PIV," Exp. Fluids, **42**(1), pp. 93–109.

[23] Sung, J., and Yoo, J. Y., 2001, "Three-dimensional phase averaging of time-resolved PIV measurement data," Meas. Sci. Technol., **12**, pp. 655–662.

[24] Berkooz, G., Holmes, P., and Lumley, J. L., 1993, "The proper orthogonal decomposition in the analysis of turbulent flows," Annu. Rev. Fluid Mech., **25**, pp. 539–575.

[25] Perrin, R., Braza, M., Cid, E., Cazin, S., Barthet, a., Sevrain, a., Mockett, C., and Thiele, F., 2007, "Obtaining phase averaged turbulence properties in the near wake of a circular cylinder at high Reynolds number using POD," Exp. Fluids, **43**(2-3), pp. 341–355.

[26] Oudheusden, B. W. van, Scarano, F., Hinsberg, N. P. van, and Watt, D. W., 2005, "Phase-resolved characterization of vortex shedding in the near wake of a square-section cylinder at incidence," Exp. Fluids, **39**, pp. 86–98.

[27] Scarano, F., Benocci, C., and Riethmuller, M. L., 1999, "Pattern recognition analysis of the turbulent flow past a backward facing step," Phys. Fluids, **11**(12), pp. 3808–3818.

[28] Giralt, F., and Ferré, J. A., 1993, "Structure and flow patterns in turbulent wakes," Phys. Fluids A, **5**(7), pp. 1783–1789.

[29] Ferre, J. A., and Giralt, F., 1989, "Pattern-recognition analysis of the velocity field in plane turbulent wakes," J. Fluid Mech., **198**, pp. 27–64.

[30] Williamson, C. H. K., 1996, "Vortex dynamics in the cylinder wake," Annu. Rev. Fluid Mech., **28**, pp. 477–539.

[31] Lienhard, J. H., 1966, Synopsis of Lift, Drag, and Vortex Frequency Data for Rigid Circular Cylinders.

[32] Oertel Jr., H., 1990, "Wakes behind blunt bodies," Annu. Rev. Fluid Mech., **22**, pp. 539–562.

[33] Norberg, C., 2003, "Fluctuating lift on a circular cylinder: review and new measurements," J. Fluids Struct., **17**, pp. 57–96.

[34] Mair, W. A., and Stansby, P. K., 1975, "Vortex wakes of bluff cylinders in shear flow," J. Appl. Math., **28**, pp. 519–540.

[35] Stansby, P., 1974, "The effects of end plates on the base pressure coefficient of a circular cylinder," Aeronaut. J., **87**, pp. 36–37.

[36] Eisenlohr, H., and Eckelmann, H., 1989, "Vortex splitting and its consequence in the vortex street wake of cylinders at low Reynolds number," Phys. Fluids A, **1**, pp. 189–192.

[37] Hammache, M., and Gharib, M., 1989, "A novel method to promote parallel vortex shedding in the wake of circular cylinders," Phys. Fluids A, **1**, pp. 1611–1614.

[38] Hammache, M., and Gharib, M., 1991, "An experimental study of the parallel and oblique vortex shedding from circular cylinders," J. Fluid Mech., **232**, pp. 567–590.

[39] Fox, T. A., and West, G. S., 1990, "On the use of endplates with circular cylinders," Exp. Fluids, **9**, pp. 237–239.

[40] Williamson, C. H. K., 1989, "Oblique and parallel modes of vortex shedding in the wake of a circular cylinder at low Reynolds numbers," J. Fluid Mech., **206**, p. 579.

[41] Gerich, D., and Eckelmann, H., 1982, "Influence of endplates and free ends on the shedding frequency of circular cylinders," J. Fluid Mech., **122**, pp. 109–121.

[42] Norberg, C., 1994, "An experimental investigation of the flow around a circular cylinder: influence of aspect ratio," J. Fluid Mech., **258**, pp. 287–316.

[43] Zdravkovich, M. M., 2003, Flow Around Circular Cylinders: Volume II: Applications, Oxford University Press.

[44] Gerrard, J. H., 1978, "The wakes of cylindrical bluff bodies at low Reynolds number," Philos. Trans. R. Soc. London. Ser. A, Math. Phys. Sci., **288**(1354), pp. 351–382.

[45] Dunn, W., and Tavoularis, S., 2006, "Experimental studies of vortices shed from cylinders with a step-change in diameter," J. Fluid Mech., **555**, p. 409.

[46] Simpson, R. L., 2001, "Junction Flows," Annu. Rev. Fluid Mech., **33**, pp. 415–443.

[47] Krajnović, S., 2011, "Flow around a tall finite cylinder explored by large eddy simulation," J. Fluid Mech., **676**, pp. 294–317.

[48] Sattari, P., Bourgeois, J. a., and Martinuzzi, R. J., 2011, "On the vortex dynamics in the wake of a finite surface-mounted square cylinder," Exp. Fluids, **52**(5), pp. 1149–1167.

[49] Bourgeois, J. a., Sattari, P., and Martinuzzi, R. J., 2011, "Alternating half-loop shedding in the turbulent wake of a finite surface-mounted square cylinder with a thin boundary layer," Phys. Fluids, **23**(9), p. 095101.

[50] Farivar, D., 1981, "Turbulent uniform flow over cylinders of finite length," AIAA J., **19**, pp. 275–281.

[51] Ayoub, A., and Karamecheti, K., 1982, "An experiment on the flow past a finite circular cylinder at high subcritical and supercritical Reynolds numbers," J. Fluid Mech., **118**, pp. 1–26.

[52] Okamoto, T., and Yagita, M., 1973, "The experimental investigation on the flow past a circular cylinder of finite length placed normal to the plane surface in a uniform stream," Bull. Japan Soc. Mech. Eng., **16**(95), pp. 805–814.

[53] Sumner, D., Heseltine, J. L., and Dansereau, O. J. P., 2004, "Wake structure of a finite circular cylinder of small aspect ratio," Exp. Fluids, **37**(5), pp. 720–730.

[54] Rostamy, N., Sumner, D., Bergstrom, D. J., and Bugg, J. D., 2012, "Local flow field of a surface-mounted finite circular cylinder," J. Fluids Struct., **34**, pp. 105–122.

[55] Fox, T. A., and West, G. S., 1993, "Fluid Induced Loading of Cantilevered Circular Cylinders in a low-turbulence uniform flow. Part 2: Fluctuating Loads on a Cantilever of Aspect Ratio 30," J. Fluids Struct., **7**, pp. 15–28.

[56] Afgan, I., Moulinec, C., Prosser, R., and Laurence, D., 2007, "Large eddy simulation of turbulent flow for wall mounted cantilever cylinders of aspect ratio 6 and 10," Int. J. Heat Fluid Flow, **28**(4), pp. 561–574.

[57] Sumner, D., Dansereau, O. J. P., and Heseltine, J. L., 2004, "Vortex shedding from a finite circular cylinder of small aspect ratio," Canadian Society of Mechanical Engineers Congress, pp. 1–9.

[58] Adaramola, M. S., Akinlade, O. G., Sumner, D., Bergstrom, D. J., and Schenstead, a. J., 2006, "Turbulent wake of a finite circular cylinder of small aspect ratio," J. Fluids Struct., **22**(6-7), pp. 919–928.

[59] Pattenden, R. J., Turnock, S. R., and Zhang, X., 2005, "Measurements of the flow over a low-aspect-ratio cylinder mounted on a ground plane," Exp. Fluids, **39**, pp. 10–21.

[60] Fox, T. A., and Apelt, C. J., 1993, "Fluid induced loading of cantilevered circular cylinders in a low-turbulence uniform flow. Part 3: Fluctuating loads with aspect ratios 4 to 25," J. Fluids Struct., **7**, pp. 375–386.

[61] Rostamy, N., Sumner, D., Bergstrom, D. J., and Bugg, J. D., 2012, "Local flow field of a surface-mounted finite circular cylinder," J. Fluids Struct., **34**, pp. 105–122.

[62] Bourgeois, J. A., 2012, "Three-dimensional topology and dynamical modelling of vortex shedding from finite surface mounted bluff bodies," University of Calgary.

[63] Fr, J., "Large – Eddy Simulation of the Flow around the Free End of a Circular Cylinder," pp. 1–12.

[64] Roh, S. C., and Park, S. O., 2003, "Vortical flow over the free end surface of a finite circular cylinder mounted on a flat plate," Exp. Fluids, **49**, pp. 79–100.

[65] Afgan, I., Moulinec, C., Prosser, R., and Laurence, D., 2007, "Large eddy simulation of turbulent flow for wall mounted cantilever cylinders of aspect ratio 6 and 10," Int. J. Heat Fluid Flow, **28**, pp. 561–574.

[66] Jochen Fröhlich, W. R., 2004, "LES of the flow around a circular cylinder of finite height," Int. J. Heat Fluid Flow, **25**, pp. 537–548.

[67] Fox, T. A., and West, G. S., 1993, "Fluid Induced Loading of Cantilevered Circular Cylinders in a low-turbulence uniform flow. Part 1: Mean Loading with Aspect Ratios in the Range 4 to 30," J. Fluids Struct., **7**, pp. 1–14.

[68] Wieselsberger, C., 1921, "New data on the law of hydro and aerodynamic resistance," Phys. Zeitschrift, **22**, pp. 321–328.

[69] Inoue, O., and Sakuragi, A., 2008, "Vortex shedding from a circular cylinder of finite length at low Reynolds numbers," Phys. Fluids, **20**(3), p. 033601.

[70] Lewis, C. G., and Gharib, M., 1991, "An exploration of the wake three dimensionalities caused by a local discontinuity in cylinder diameter," Phys. Fluids, **A**(4 (1)), pp. 104–117.

[71] Ko, N. W. M., Leung, W. L., and Au, H., 1982, "Flow behind two coaxial circular cylinders," J. Fluids Eng., **104**, pp. 223–227.

[72] Ko, N. W. M., and Chan, a. S. K., 1992, "Wakes behind circular cylinders with stepwise change of diameter," Exp. Therm. Fluid Sci., **5**(2), pp. 182–187.

[73] Morton, C., and Yarusevych, S., 2014, "Vortex Dynamics in the Turbulent Wake of a Single Step Cylinder," J. Fluids Eng., **136**(3), p. 031205.

[74] Norberg, C., 1992, "An experimental study of the flow around cylinders joined with a step in the diameter," 11th Australasian Fluid Mechanics Conference, Hobart, Austrailia, pp. 507–510.

[75] Yagita, M., Kojima, Y., and Matsuzaki, K., 1984, "On vortex shedding from circular cylinder with step," Bull. Japan Soc. Mech. Eng., **27**, pp. 426–431.

[76] Chua, L. P., Liu, C. Y., and Chan, W. K., 1998, "Measurements of a step cylinder," Int. Commun. Heat Mass Transf., **25**(2), pp. 205–215.

[77] Morton, C., and Yarusevych, S., 2012, "An experimental investigation of flow past a dual step cylinder," Exp. Fluids, **52**(1), pp. 69–83.

[78] Morton, C., 2010, "Experimental and numerical investigations of the flow development over cylinders with stepwise discontinuities in diameter," University of Waterloo.

[79] Green, M. a., Rowley, C. W., and Smits, A. J., 2011, "The unsteady three-dimensional wake produced by a trapezoidal pitching panel," J. Fluid Mech., **685**, pp. 117–145.

[80] Bourgeois, J. a., Noack, B. R., and Martinuzzi, R. J., 2013, "Generalized phase average with applications to sensor-based flow estimation of the wall-mounted square cylinder wake," J. Fluid Mech., **736**, pp. 316–350.

[81] Oberleithner, K., Sieber, M., Nayeri, C. N., Paschereit, C. O., Petz, C., Hege, H.-C., Noack, B. R., and Wygnanski, I., 2011, "Three-dimensional coherent structures in a swirling jet undergoing vortex breakdown: stability analysis and empirical mode construction," J. Fluid Mech., **679**, pp. 383–414.

[82] Morton, C., and Yarusevych, S., 2014, "On vortex shedding from low aspect ratio dual step cylinders," J. Fluids Struct., **44**(0), pp. 251–269.

[83] Hussain, A. K. M. ., 1986, “Coherent structures and turbulence,” J. Fluid Mech., **173**, pp. 303–356.

[84] Ghaemi, S., and Scarano, F., 2011, “Counter-hairpin vortices in the turbulent wake of a sharp trailing edge,” J. Fluid Mech., **689**, pp. 317–356.

[85] Elsinga, G. E., Poelma, C., Schröder, a., Geisler, R., Scarano, F., and Westerweel, J., 2012, “Tracking of vortices in a turbulent boundary layer,” J. Fluid Mech., **697**, pp. 273–295.

[86] Kopp, G. A., Ferre, J. A., and Giralt, F., 1997, “The use of pattern recognition and Proper Orthogonal Decomposition in identifying structure of fully developed free turbulence,” J. Fluids Eng., **119**, pp. 289–296.

[87] Merzkirch, W., 1987, Techniques of Flow Visualization.

[88] Kazi, S. N., Duffy, G. G., and Chen, X. D., 2010, “Mineral scale formation and mitigation on metals and a polymeric heat exchanger surface,” Appl. Therm. Eng., **30**(14-15), pp. 2236–2242.

[89] Tavoularis, S., 2005, Measurement in fluid mechanics, Cambridge University Press.

[90] Adrian, R. J., and Yao, C. S., 1987, “Power spectra of fluid velocities measured by laser Doppler velocimetry,” Exp. Fluids, **5**, pp. 17–28.

[91] Willert, C. E., and Gharib, M., 1991, “Digital particle image velocimetry,” Exp. Fluids, **10**, pp. 181–193.

[92] Westerweel, J., 1997, “Fundamentals of digital particle image velocimetry,” Meas. Sci. Technol., **8**(12), pp. 1379–1392.

[93] Scarano, F., and Riethmuller, M. L., 2000, “Advances in iterative multigrid PIV image processing,” Exp. Fluids, **29**(1), pp. S051–S060.

[94] Raffel, M., Willert, C. E., Wereley, S. T., and Kompenhans, J., 2007, Particle Image Velocimetry, Springer-Verlag.

[95] Keane, R. D., and Adrian, R. J., 1992, “Theory of cross-correlation of PIV images,” Appl. Sci. Res., **49**, pp. 191–215.

[96] Westerweel, J., and Scarano, F., 2005, “Universal outlier detection for PIV data,” Exp. Fluids, **39**, pp. 1096–1100.

[97] Scarano, F., 2013, “Tomographic PIV: principles and practice,” Meas. Sci. Technol., **24**(1), p. 012001.

[98] Elsinga, G. E., Scarano, F., Wieneke, B., and Oudheusden, B. W., 2006, "Tomographic particle image velocimetry," Exp. Fluids, **41**(6), pp. 933–947.

[99] Wieneke, B., 2008, "Volume self-calibration for 3D particle image velocimetry," Exp. Fluids, **45**(4), pp. 549–556.

[100] Herman, G. T., and Lent, A., 1976, "Iterative reconstruction algorithms," Comput. Biol. Med., **6**(4), pp. 273–294.

[101] Scarano, F., and Poelma, C., 2009, "Three-dimensional vorticity patterns of cylinder wakes," Exp. Fluids, **47**(1), pp. 69–83.

[102] Lumley, J. L., 1967, "The structure of inhomogeneous turbulent flows," In Atmospheric Turbulence and Radio Wave Propagation, A.M. Takarski, and V.I. Yaglom, eds., Moscow: Nauka, pp. 166–178.

[103] Hussain, A. K. M. ., and Reynolds, W. C., 1970, "The mechanics of an organized wave in turbulent shear flow," J. Fluid Mech., **41**(2), pp. 241–258.

[104] Hussain, A. K. M. ., 1983, "Coherent structures - reality and myth," Phys. Fluids, **26**(10), pp. 2816–2850.

[105] Noack, B. R., Afanasiev, K., Morzynski, M., Tadmor, G., and Thiele, F., 2003, "A hierarchy of low-dimensional models for the transient and post-transient cylinder wake," J. Fluid Mech., **497**, pp. 335–363.

[106] Tadmor, G., Lehmann, O., Noack, B. R., Cordier, I., Delville, J., Bonnet, J. P., and Morzynski, M., 2011, "Reduced-order models for closed loop wake control," Philos. Trans. R. Soc. London. Ser. A, Math. Phys. Sci., **369**, pp. 1513–1524.

[107] Noack, B. R., Schlegel, M., Morzynski, M., and Tadmor, G., 2010, "System reduction strategy for Galerkin models in fluid flows," Int. J. Numer. Methods Fluids, **63**, pp. 231–248.

[108] Roache, P. J., 1998, Verification and validation in computational science and engineering, Hermosa Publishers, Albuquerque, New Mexico.

[109] Sirovich, L., 1987, "Turbulence and the dynamics of coherent structures," Q. Appl. Math., **45**, pp. 561–590.

[110] Aubry, N., 1991, "On the Hidden Beauty of the Proper Orthogonal Decomposition," (900265), pp. 339–352.

[111] Loeve, M., 1955, Probability Theory, New York: Van Nostrand.

[112] Lumley, J. L., 1972, Stochastic tools in turbulence, New York: Academic Press.

[113] Ma, X., Karamanos, G.-S., and Karniadakis, G. E., 2000, "Dynamics and low-dimensionality of a turbulent near wake," J. Fluid Mech., **410**, pp. 29–65.

[114] Williamson, C. H. K., 1996, "Three-dimensional wake transition," J. Fluid Mech., **328**, pp. 345–407.

[115] Thompson, M. C., and Hourigan, K., 2005, "The shear-layer instability of a circular cylinder wake," Phys. Fluids, **17**(2), p. 021702.

[116] Siegel, S. G., Seidel, J., Fagley, C., Luchtenburg, D. M., Cohen, K., and Mclaughlin, T., 2008, Low-dimensional modelling of a transient cylinder wake using double proper orthogonal decomposition.

[117] Kourentis, L., and Konstantinidis, E., 2011, "Uncovering large-scale coherent structures in natural and forced turbulent wakes by combining PIV, POD, and FTLE," Exp. Fluids, **52**(3), pp. 749–763.

[118] Shi, L. L., Liu, Y. Z., and Wan, J. J., 2010, "Influence of wall proximity on characteristics of wake behind a square cylinder: PIV measurements and POD analysis," Exp. Therm. Fluid Sci., **34**(1), pp. 28–36.

[119] Berger, E. Wille, R., 1972, "Periodic flow phenomena," Annu. Rev. Fluid Mech., **4**, pp. 313–340.

[120] Sakamoto, H., and Arie, M., 1983, "Vortex shedding from a rectangular prism and a circular cylinder placed vertically in a turbulent boundary layer," J. Fluid Mech., **126**, pp. 142–165.

[121] Timme, V. A., 1957, "Uber die Geschwindigkeitsverteilung in Wirbeln," Band, **XXV**, pp. 205–225.

[122] Davies, M. E., 1976, "A comparison of the wake structure of a stationary and oscillating bluff body using a conditional averaging technique," J. Fluid Mech., **75**, pp. 209–231.

[123] Jang, Y. Il, and Lee, S. J., 2010, "POD analysis on the sphere wake at a subcritical Reynolds number," J. Vis., **13**(4), pp. 311–318.

[124] Pan, C., Wang, H., and Wang, J., 2013, "Phase identification of quasi-periodic flow measured by particle image velocimetry with a low sampling rate," Meas. Sci. Technol., **24**(5), p. 055305.

[125] Prasad, A., and Williamson, C. H. K., 1997, "The instability of the shear layer separating from a bluff body," J. Fluid Mech., **333**, pp. 375–402.

[126] Clayton, B. R., and Massey, B. S., 1967, "Flow visualization in water: a review of techniques," J. Sci. Instrum., **44**(1), pp. 2–11.

[127] Smith, C. R., Seal, C. V., Praisner, T. J., and Sabatino, D. R., 2000, "Hydrogen Bubble Visualization," Flow Visualization: Techniques and Examples, A.J. Smits & T.T. Lim, eds., Imperial College Press, London, pp. 27–42.

[128] Schraub, F. A., Kline, S. J., Henry, J., Jr., P. W. R., and Littlell, A., 1965, "Use of hydrogen bubbles for quantitative determination of time-dependent velocity fields in low speed water flows," J. Basic Eng.

[129] Wu, J., Sheridan, J., Hourigan, K., and Soria, J., 1996, "Shear layer vortices and longitudinal vortices in the near wake of a circular cylinder," Exp. Therm. Fluid Sci., **12**(2), pp. 169–174.

[130] Kappler, M., Rodi, W., Szepessy, S., and Badran, O., 2005, "Experiments on the flow past long circular cylinders in a shear flow," Exp. Fluids, **38**(3), pp. 269–284.

[131] Lamb, H., 1945, Hydrodynamics, Dover Publications, New York.

[132] Baker, C. J., 1980, "The turbulent horseshoe vortex," J. Wind Eng. Ind. Aerodyn., **6**, pp. 9–23.

[133] Langston, L. S., and Boyle, M. T., 1982, "A new surface-streamline flow visualization technique," J. Fluid Mech., **125**, pp. 53–57.

[134] Van Oudheusden, B. W., Nebbeling, C., and Bannink, W. J., 1996, "Topological interpretation of the surface flow visualization of conical viscous/inviscid interactions," J. Fluid Mech., **316**, pp. 115–137.

[135] Corke, T., Matlis, E., Schuele, C. Y., Wilkincon, S., Owens, L., and Balakumar, P., 2010, "Control of stationary cross-flow modes using patterned roughness at Mach 3.5," Seventh IUTAM Symposium on Laminar-Turbulent Transition, IUTAM Bookseries 18, pp. 123–128.

[136] Lu, F. K., 2010, "Surface oil flow visualization," Eur. Phys. J. Spec. Top., **182**(1), pp. 51–63.

[137] Kirk, D. W., and Ledas, A. E., 1982, "Precipitate formation during sea water electrolysis," Int. J. Hydrogen Energy, **7**(12), pp. 925–932.

[138] Guha, A., 2008, "Transport and Deposition of Particles in Turbulent and Laminar Flow," Annu. Rev. Fluid Mech., **40**(1), pp. 311–341.

[139] Haugen, N. E. L., and Kragset, S., 2010, "Particle impaction on a circular cylinder in crossflow as function of Stokes and Reynolds numbers," J. Fluid Mech., **661**, pp. 239–261.

[140] Kleinstreuer, C., and Feng, Y., 2013, "Computational analysis of non-spherical particle transport and deposition in shear flow with application to lung aerosol dynamics - a review," J. Biomech. Eng., **135**(021008).

[141] Jenner, G. A., Longerich, H. ., Jackson, S. E., and Fryer, B. J., 1990, "ICP-MS - A powerful tool for high-precision trace element analysis in Earth sciences: Evidence from analysis of selected U.S.G.S. reference samples," Chem. Geol., **83**(1-2), pp. 133–148.

[142] Williamson, C. H. K., and Govardhan, H., 2004, "Vortex-induced vibrations," Annu. Rev. Fluid Mech., **36**, pp. 413–455.

[143] Relf, E. F., 1914, Discussion of the Results of Measurements of the Resistance of Wires, with Some Additional Tests on the Resistance of Wires of Small Diameter, Reports and Memoranda No. 102, British A.C.A.

[144] Wieselsberger, C., 1922, New data on the laws of fluid resistance.

[145] Barth, T., and Jesperson, D., 1989, "The design and application of upwind schemes on unstructured meshes," 27th Aerospace Sciences Meeting, Reno, Nevada.

[146] Grundmann, R., and Posdziech, O., 2001, "Numerical Simulation of the Flow Around an Infinitely Long Circular Cylinder in the Transition Regime," Theor. Comput. Fluid Dyn., **15**(2), pp. 121–141.

[147] Mittal, S., 2001, "Computation of three-dimensional flows past circular cylinder of low aspect ratio," Phys. Fluids, **13**, pp. 177–191.

[148] Henderson, R. D., 1995, "Details of the drag curve near the onset of vortex shedding," Phys. Fluids, **7**(9), pp. 2102–2104.

[149] Persillon, H., and Braza, M., 1998, "Physical analysis of the transition to turbulence in the wake of a circular cylinder by three-dimensional Navier-Stokes simulation," J. Fluid Mech., **365**, pp. 23–88.

[150] Huang, Z., Narasimhamurthy, V. D., and Andersson, H. I., 2010, "Oblique and cellular vortex shedding behind a circular cylinder in a bidirectional shear flow," Phys. Fluids, **22**(114105).

[151] Rastogi, P. K., 2000, "Photomechanics," Top. Appl. Phys., **77**, pp. 373–412.

[152] Benedict, L. H., and Gould, R. D., 1996, "Towards better uncertainty estimates for turbulence statistics," Exp. Fluids, **22**, pp. 129–136.

[153] Doorne, C. W. . Van, and Westerweel, J., 2007, "Measurement of laminar, transitional and turbulent pipe flow using stereoscopic-PIV," Exp. Fluids, **42**(2), pp. 259–279.

[154] Adrian, R. J., 1991, "Particle-imaging techniques for experimental fluid mechanics," Annu. Rev. Fluid Mech., **23**(1), pp. 261–304.

[155] Yoon, J.-H., and Lee, S.-J., 2002, "Direct comparison of 2D PIV and stereoscopic PIV measurements," Meas. Sci. Technol., **13**(10), pp. 1631–1642.

[156] Thom, A., 1929, A.R.C., Reports and Memoranda No. 1194, British A.C.A.

[157] Lam, K., Wang, F. H., and So, R. M. C., 2004, "Three-dimensional nature of vortices in the near wake of a wavy cylinder," J. Fluids Struct., **19**(6), pp. 815–833.

[158] Hu, J. C., and Zhou, Y., 2009, "Aerodynamic characteristics of Asymmetric bluff bodies," J. Fluids Eng., **131**(1), p. 011206.

[159] Szepessy, S., and Bearman, P. W., 1992, "Aspect ratio and end plate effects on vortex shedding from a circular cylinder," J. Fluid Mech., **234**, pp. 191–217.

[160] West, G. S., and Apelt, C. J., 1993, "Measurements of fluctuating pressures and forces on a circular cylinder in the Reynolds number range 10^4 to 2.5x10^5," J. Fluids Struct., **7**, pp. 227–244.

[161] Apelt, G. S., and West, C. J., 1997, "Fluctuating lift and drag forces on finite lengths of a circular cylinder in the subcritical Reynolds number range," J. Fluids Struct., **11**, pp. 135–158.

[162] Bouak, F., and Lemay, J., 1998, "Passive control of the aerodynamic forces acting on a circular cylinder," Exp. Therm. Fluid Sci., **16**, pp. 112–121.

[163] Moeller, M. J., and Leehey, P., 1984, "Unsteady forces on a cylinder in cross flow at subcritical Reynolds numbers. In: Paidoussis, M.P. Griffin, O.M., Sevik, M. (Eds.)," ASME Symp. Flow-Induced Vib., **1**(ASME, New York), pp. 57–71.

[164] Leehey, P., and Hanson, C. E., 1971, "Aeolian tones associated with resonated vibration," J. Sound Vib., **13**, pp. 465–483.

[165] Wu, M.-H., Wen, C.-Y., Yen, R.-H., Weng, M.-C., and Wang, an-B., 2004, "Experimental and numerical study of the separation angle for flow around a circular cylinder at low Reynolds number," J. Fluid Mech., **515**, pp. 233–260.

[166] Cao, S., Ozono, S., Tamura, Y., Ge, Y., and Kikugawa, H., 2010, "Numerical simulation of Reynolds number effects on velocity shear flow around a circular cylinder," J. Fluids Struct., **26**, pp. 685–702.

[167] Wissink, J. G., and Rodi, W., 2008, "Numerical study of the near wake of a circular cylinder," Int. J. Heat Fluid Flow, **29**, pp. 1060–1070.

[168] Parnaudeau, P., Carlier, J., Heitz, D., and Lamballais, E., 2008, "Experimental and numerical studies of the flow over a circular cylinder at Reynolds number 3900," Phys. Fluids, **20**(8), p. 085101.

[169] Ballengee, D. W., and Chen, C. F., 1969, "Experimental determination of the separation point of flow around a circular cylinder," Flow, its Meas. Control Sci. Ind. - Part I, pp. 419–431.

[170] Stucke, P., and Taipel, I., 1991, "Separation of flow around a circular cylinder at moderate Re-numbers," Separated Flows Jets Int. Union Theor. Appl. Math., pp. 751–74.

[171] Bokaian, A., and Geoola, F., 1984, "Wake-induced galloping of two interfering circular cylinders," J. Fluid Mech., **146**, pp. 383–415.

Appendix A
Hydrogen bubble flow and surface visualization

Hydrogen Bubble Flow Visualization

Among various visualization methods suitable for water flows, the hydrogen bubble technique is one of the most common [126,127]. It involves generating hydrogen bubbles on a thin metal wire via electrolysis. When sufficiently small, the hydrogen bubbles have negligible buoyancy and hence serve as reliable flow tracers [128]. In order to provide adequate contrast with the background, illumination of these tracers is usually completed using a light sheet [129,130]. However, the planar illumination provides insight primarily into flow patterns in a localized plane, which limits the utility of such a technique in three-dimensional flows.

When performing wake visualizations with the hydrogen bubble technique, the buoyancy of hydrogen bubbles must be minimized. The terminal rising velocity of the bubbles, U_t, can be computed analytically [131]:

$$\boldsymbol{U_t = \frac{g l^2 (\rho - \rho_h)}{18 \mu}} \qquad \text{(A-1)}$$

where l is the bubble diameter, ρ is the density of water, and ρ_h is the density of hydrogen. Hence, reducing the bubble diameter decreases its rising velocity. This can be achieved by controlling the diameter of the cathode wire and the voltage applied, while ensuring that the produced bubbles can be adequately imaged. In the present study, hydrogen bubbles were generated on a thin, 0.085mm diameter stainless steel wire via electrolysis by applying a DC voltage of about ten to twenty volts. A cylindrical aluminum rod acting as the upper support for the uniform and dual step cylinder models served as the anode in the hydrogen bubble circuit. The models were insulated from the circuit through plastic threaded-rod connections. While producing adequate flow visualization, the generated bubbles had a sufficiently small rising velocity (less than 5% of free stream velocity) to ensure insignificant displacement due to buoyancy within the wake region of interest. The hydrogen bubble wire was

positioned less than 0.7D upstream of the model and offset slightly from the model axis to visualize vortices on one side of the wake for both the uniform and dual-step cylinder models. The Reynolds number based on the wire diameter was less than ten, so that no shedding of vortices occurred in the wire wake, minimizing adverse effects from the wire on the flow development around the model. In addition, to minimize flow disturbances due to wire supports, the wire was mounted on a rigid probe that extended upstream of the cylinder model at an angle of approximately forty-five degrees.

To improve the quality of the visualizations, a laser volume illumination of the hydrogen bubbles was achieved using a two-watt continuous wave Spectra-Physics laser. The laser source passed through two consecutive cylindrical lenses in order to generate a conical illumination volume (see Chapter 3, Figure 3.2 for details). Image recording was carried out using a Photron SA4 camera outfitted with a 50mm focal length Nikon lens operating at 100 Hz, which is more than twenty-five times the highest frequency of interest for the models investigated.

Surface Visualization

Surface visualization is a specific branch of flow visualization that is used for interpreting the flow development near walls based on surface marker patterns produced by the wall shear stress. It is often used to identify boundary layer separation, transition, and reattachment on various geometries [64,132–136]. In contrast to methods used for visualizing patterns within water flows, virtually all known surface visualization techniques are designed to be performed with air (or gas) as the fluid medium, and, to the best knowledge of the author, comparable visualization tools are not yet available for experiments in water.

Surface visualization using hydrogen bubble technique was achieved as follows. When hydrogen bubbles are produced on a wire-based cathode, the electro-chemical reactions involve the formation of insoluble metal hydroxides and salts, e.g., magnesium hydroxide and calcium carbonate [137]. The deposition off these materials on the wire is responsible for the well-documented degradation of hydrogen bubble system performance with time [87]. The removal of deposits from the wire can be achieved by periodically reversing the polarity on the wire or operating it on a duty cycle. With the wire placed sufficiently close to the model surface, the mineral particles, whose density is larger than

that of water, occasionally impact on the surface of the model, leaving behind a white residue which acts as a surface visualization agent. Note that, in the present experiments, the hydrogen bubble wire is positioned slightly off from the centerline of the model, thus producing more substantial surface residue on the lower half of the cylinder in Figure A.1. Moreover, while the surface deposition takes place, flow visualizations of the wake region can be performed. The residue can be easily cleaned from the surface after the experiments using a polishing agent, and the models can then be re-used.

An important consideration for the described surface visualization is the ability of the mineral particles to adequately follow the fluid motion near the surface. Figure A.1 illustrates surface patterns in the vicinity of the stagnation point and around the surface of a uniform circular cylinder at Re_D = 2100. The images show impact sites near the stagnation point resulting from what is commonly referred to as inertial impaction [138]. Impaction occurs in a region of about ±5 degrees surrounding the stagnation point ($\theta = 0^{\circ}$), while for larger angles, well-defined white streaks of residue can be seen (Figure A.1). Evaluating the approximate size of impact sites and the width of the streaks (Figure A.2) and time-resolved visualization of particles near the surface (Figure A.3), the diameters of the particles forming on the hydrogen wire and their fragments forming after impacting the model are estimated to be less than about 0.15 mm and 0.05 mm, respectively. The results depicted in Figure A.2 also show that the streaks are getting thinner as they develop downstream, suggesting that the particle fragments lose a significant portion of their mass as they travel along the surface. Based on the estimated size of the fragments, the Reynolds number (Re_P) based on fragments diameter is $Re_P < 1$ within the cylinder boundary layer. Therefore, the dynamics of the fragments can be approximated using the Stokes drag law. Considering only fluid mechanics forces, the particle relaxation time (τ) is given by

$$\tau = \frac{\rho_p d_p^2}{18\mu} \tag{A-2}$$

where ρ_p is the particle density, d_p is the particle diameter, and μ is the kinematic viscosity of water [139]. The corresponding Stokes number is $Stk = \tau U_{ref}/d_p$, where U_{ref} is the reference velocity. In the

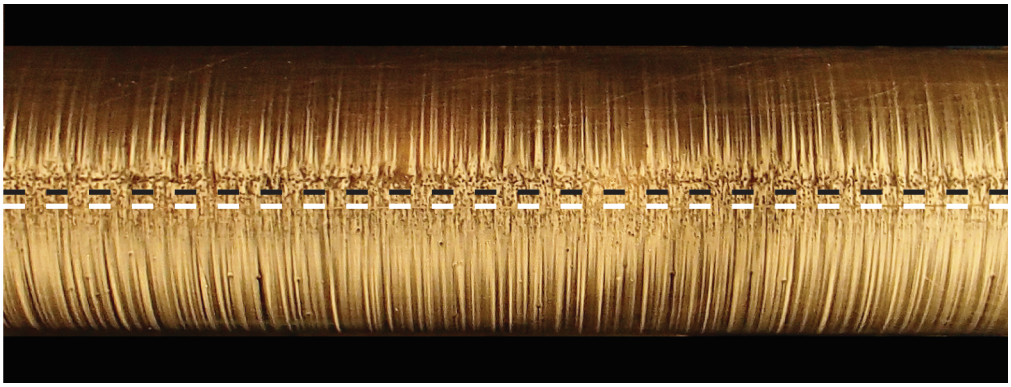

Figure A.1 Surface visualization of the stagnation point of a uniform cylinder at Re_D = 2100. A black dashed line identifies the approximate location of the cylinder stagnation point while a white dashed line marks the location of the hydrogen bubble wire, which is slightly offset from the stagnation location.

present investigation, $Stk << 0.1$ within the boundary layer, so that particle fragments are expected to closely follow streamlines [139]. However, characterizing particle dynamics in contact with a solid boundary is complicated, as it depends, among other factors, on van der Waals forces, electrostatic forces, surface material and characteristics, local velocity profile, particle shape, etc. [139]. For weak attractive forces between the particle and the model surface, particle lift-off may occur prior to flow separation. On the other hand, relatively strong attractive forces result in the deviation between the particle trajectories and local fluid streamlines. The modelling of such particle dynamics in practical applications is presently not feasible without major simplifications [140]. In this study, an experimental approach was utilized to describe mineral particle dynamics in a uniform cylinder boundary layer using a high speed Photron SA4 camera. The frame rate and exposure time of the camera was set to ensure that only particles moving close to the surface at velocities below approximately 15% of the free stream flow speed would remain in focus, while particles and hydrogen bubbles moving in the outer region and free stream would appear as streaks. A pair of images shown in Figure A.2a and Figure A.2b illustrates the motion and deposition of particles at the model surface while the hydrogen bubble system is activated. In the images, larger particles deposited on the model surface can be seen near the stagnation point ($\theta \approx 0^{\circ}$) and in some other areas (Figure A.2a and Figure A.2b). Smaller particle fragments are moving close to the model surface, as illustrated in Figure A.2c. Figure A.2c presents an overlay of small regions identified by rectangles in Figure A.2a and Figure A.2b. Selected particle positions corresponding to images in Figure A.2a and Figure A.2b are marked

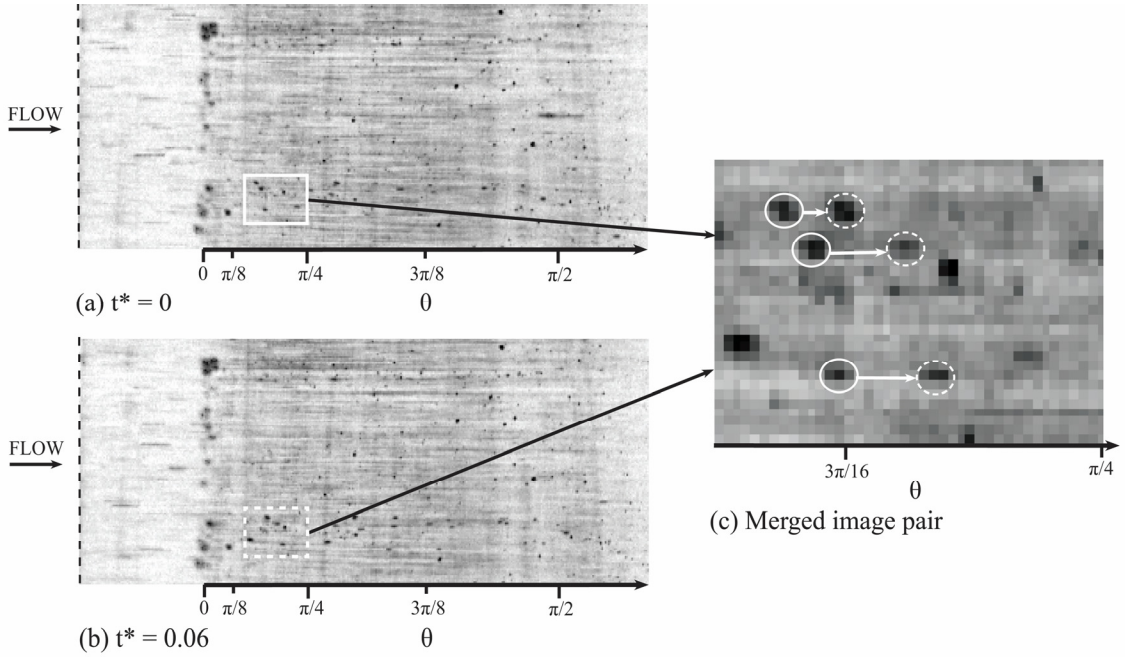

Figure A.2 Surface visualization of mineral particles within a uniform cylinder boundary layer at Re_D = 2100. t* is the number of vortex shedding periods, and the dashed vertical line in (a) and (b) identifies the location of the hydrogen bubble wire. White arrows in (c) represent the particle paths within the boundary layer beween (a) and (b). To improve clarity, the images show negatives of the raw particle images.

by solid and dashed circles, respectively, with particle displacements illustrated by arrows. The obtained particle displacements correspond to velocities between 5% and 10% of the free stream velocity, which confirms that the observed sediment particles are moving in the near wall region. It was also verified that, when the hydrogen bubble system was deactivated, concentrations of particles moving within the boundary layer decreased substantially. Thus, the results confirm that the surface visualization is achieved due to surface deposition of sediment particles produced on the wire.

Since the process of surface visualization proposed in the present investigation is relatively time consuming, it is of interest to enhance the rate of mineral deposition on the model surface. Among other experiment-specific parameters, such as model geometry, flow field characteristics, the time required to achieve adequate surface visualization is governed by the material of the model, the amount of deposits released into the flow from the wire, and the proximity of the wire to the model surface.

Table A.1 Metal concentrations in the water supply. Metals with less than 1mg/L concentration are not included. Uncertainty in the concentration estimates is ±0.5 mg/L.

Metal	Concentration (mg/L)
Calcium	87.5
Magnesium	23.9
Sodium	15.0
Silicon	4.8
Potassium	1.7

Based on the investigation of mineral scale formation on metal surfaces by Kazi et al. [88], aluminum was selected as the model material due to its high capacity to accumulate precipitates compared to other common metals and alloys, which was confirmed by comparing results on aluminum and stainless steel models. Moreover, it was determined that the aluminum models should be polished before visualization experiments since the formation of an aluminum oxide layer (alumina) on the model surface adversely affects surface deposition.

The rate of mineral formation on the wire is dependent on the rate of hydrogen production and the concentration of dissolved minerals in water. The former is controlled by the applied voltage and should be at the maximum value which produces acceptable flow visualization, while the latter can vary substantially between experimental facilities. In the present study, an unaltered municipal water supply was used for the experiments. The concentration of minerals in the water was evaluated using Inductively Coupled Plasma Mass Spectrometry (ICP-MS) [141] and the results are summarized in Table A.1. The results suggest that the majority of the deposits on the model surface consist of calcium and magnesium hydroxide, compounds known to form during electrolysis of salt water [137]. Thus, increasing the mineral concentration can help increase the rate of mineral formation. The release of deposits from the wire can be achieved by periodically reversing the polarity on the wire or operating it on a duty cycle. The latter approach, with a 50% duty cycle, was used in this study.

For surface visualization, the wire should be placed in close proximity upstream of the model, aligned in the plane of stagnation point when possible. For example, the results in Figure A.1 were

obtained with a wire placed 0.2D (< 5mm) upstream of the stagnation point. Placing the wire 0.4D (10mm) upstream of stagnation point reduces the rate of surface deposition on the model by more than 50%. Based on experimental evaluation, the recommended amount of precipitate required per unit area for adequate surface visualization is approximately 0.5 mg/cm^2, which could be achieved after about three to five hours of operation in the present study.

Surface visualization images obtained with hydrogen bubble technique are shown in Figure A.3 for uniform circular cylinders at Re_D = 1050 and 2100. As was discussed earlier, the frontal view of the models suggests that particles impact the surface in the stagnation region, producing white streaks around the fore portion of the cylinder. The rotated view images in Figure A.3c and Figure A.3d shows that the streaks end abruptly on the surface, marking the location of boundary layer separation by a distinct line along the cylinder span. The separation angle is estimated to be $\theta_{sep} = 89^\circ \pm 1^\circ$ for Re_D = 2100 (Figure A.3c), and $\theta_{sep} = 92^\circ \pm 1^\circ$ for Re_D = 2100 (Figure A.3d). These results are compared with data from previous experimental and numerical studies in Figure A.4. It can be seen that the estimates obtained in the present investigation agree well with data from previous studies. This confirms that particulates adequately follow the fluid motion near the boundary.

To investigate the ability of the new technique to visualize wake development and surface flow patterns on more complex geometries, tests were conducted on a dual-step cylinder at L/D = 0.5, D/d = 2, and Re_D = 2100. The surface pattern seen on the large cylinder near the stagnation point (Figure A.5) resembles that seen on the uniform cylinder models (Figure A.3a and Figure A.3b). However, there is substantially more precipitate on the large cylinder surface, which is located closer to the hydrogen bubble wire (see Chapter 3, Figure 3.2), and the size of the particle impact sites near the stagnation point of the small diameter cylinder is substantially larger while their number is smaller than in Figure A.1. This is due to the fact that the distance between the hydrogen bubble wire and the small cylinder is larger than that in the experiment shown in Figure A.1(1.4D vs 0.7D), which illustrates the significance of the wire proximity to the model on the rate of deposition. As the distance of the wire to the model is increased, only larger particle fragments that are less prone to follow fluid flow being deflected around the stagnation line will have an inertial impaction on the model surface. Focusing on the large cylinder, it can be seen from Figure A.5b that boundary layer separation is

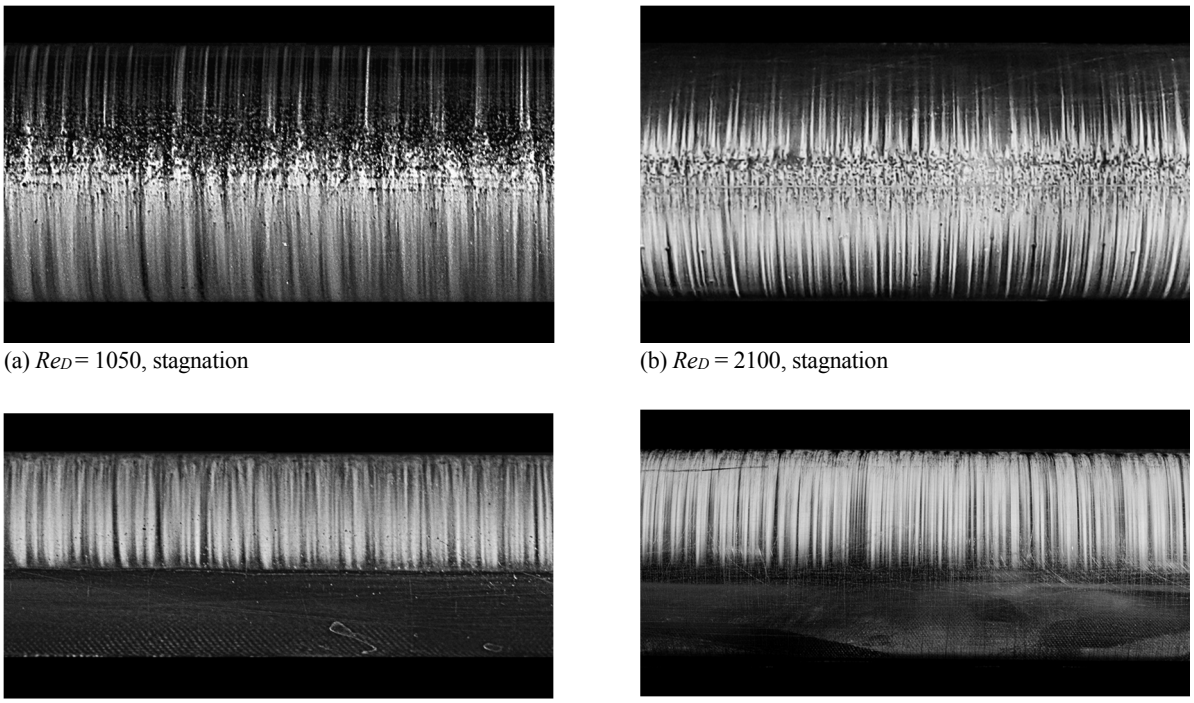

(a) Re_D = 1050, stagnation

(b) Re_D = 2100, stagnation

(c) Re_D = 1050, separation line

(d) Re_D = 2100, separation line

Figure A.3 Hydrogen bubble surface visualization for a uniform cylinder at Re_D = 1050 and Re_D = 2100.

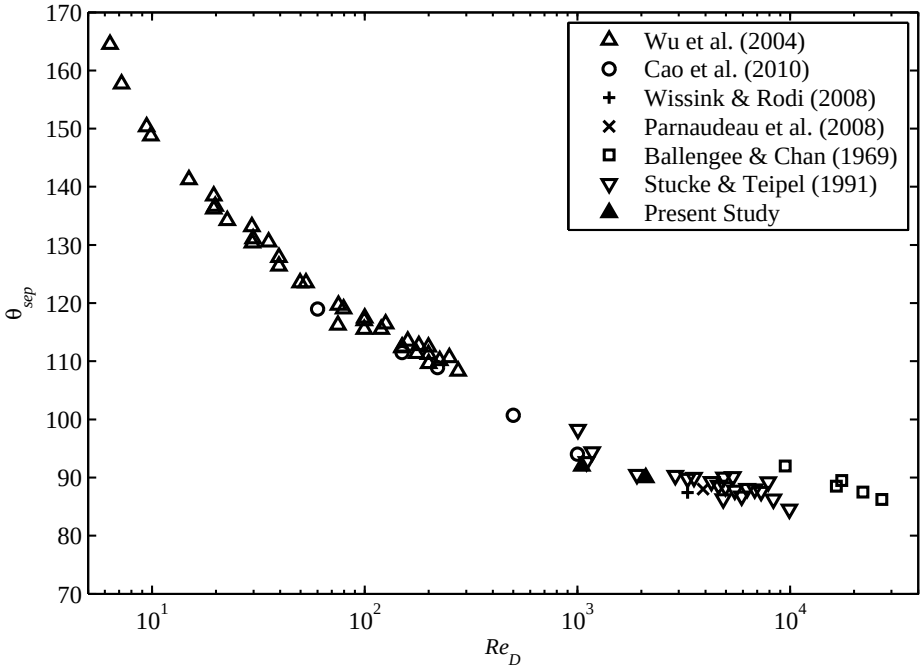

Figure A.4 Effect of Reynolds number on separation angle for a circular cylinder [165–170].

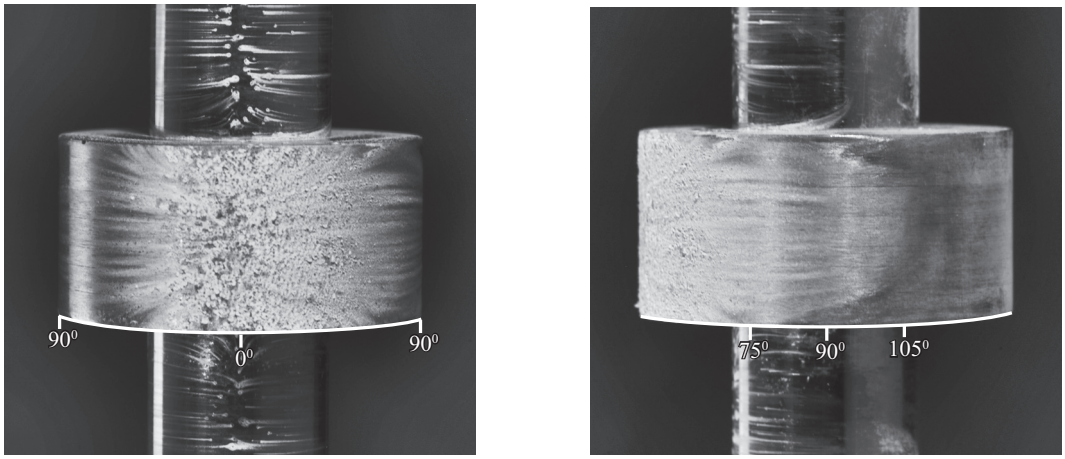

(a) (b)

Figure A.5 Hydrogen bubble surface visaulization on a dual-step cylinder for $Re_D = 2100$, $D/d = 2$, and $L/D = 0.5$.

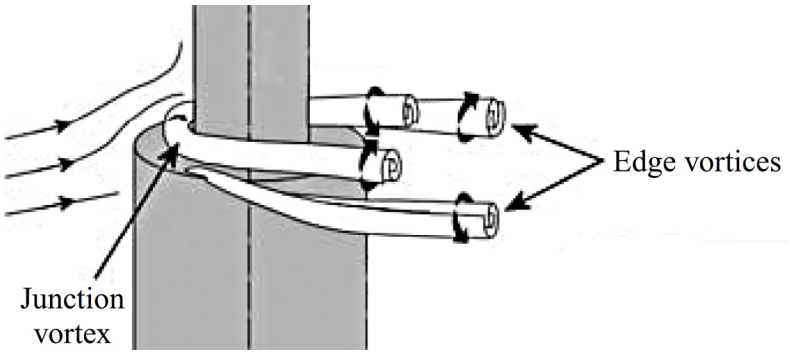

Figure A.6 Streamwise vortices generated at the stepwise discontinuity of a single step cylinder (Dunn & Tavoularis, 2006).

delayed substantially, with $\theta_{sep} \approx 105^{\circ}$ at the mid-span of the large cylinder and decreasing towards the edges.

Dunn & Tavoularis (2006) have shown that at the junction of a single step cylinder, a pair of edge vortices as well as a junction vortex form on the step surface, as illustrated in Figure A.6. Since their experiments were performed for the diameter ratio matching that in the present study ($D/d = 2$) and in the same intermediate Re_D range (~1000), the same topology is expected at the junction of the dual step cylinder in the present investigation. Indeed, surface visualization at the step junction presented in Figure A.7 shows distinct footprints of a junction vortex which wraps around the base of the small

(a) (b)

Figure A.7 Hydrogen bubble surface visaulization on the step junction of a dual-step cylinder for $Re_D = 2100$, $D/d = 2$ and $L/D = 0.5$.

cylinder, and two counter-rotating edge vortices, bounded by the junction vortex and the edges of the large cylinder. The edge vortices roll off the large cylinder within $75^\circ < \theta < 90^\circ$ (Figure A.7b), and the resulting induced velocity likely contributes to the spanwise variation of the separation angle seen in Figure A.5b. The surface patterns in Figure A.7 closely resemble those reported in surface visualizations of various junction flows [46] and accurately reflect the expected topology from [45].This illustrates the ability of the proposed technique to adequately capture changes in local near surface streamline curvature, which is of particular importance in investigations involving vortical structures forming near solid boundaries.

Appendix B
2D PIV Calibration

Calibration of the PIV system for different measurement planes was performed using a custom manufactured target shown in Figure B.1. Images of the calibration target at different distances from the camera lens were processed in DaVis Software to identify the pixel size relative to the known distance between markings on the calibration target (Figure B.1). A calibration curve in Figure B.2 was created by joining the calibration values corresponding to different distances from the camera lens using a fourth order polynomial curve fit, which closely follows the calibration data.

The calibration results are subject to the combined uncertainty due to image analysis, target positioning, and curve fitting. In order to estimate the uncertainty introduced by the image analysis, five images were acquired and analyzed, with the target remaining at a fixed position for all

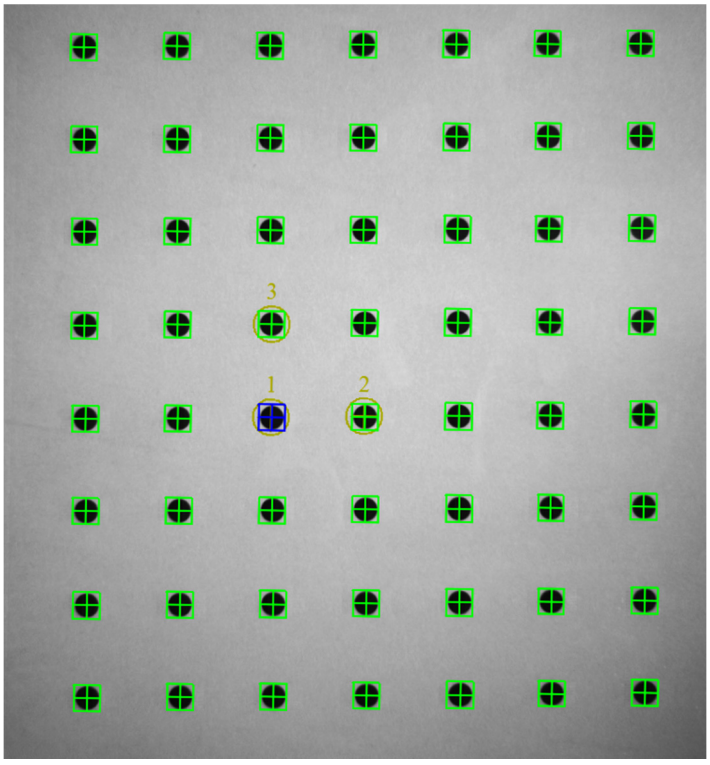

Figure B.1 Custom manufactured target used for calibration of the PIV system. The small black circles spaced evenly on the target are approximately 5 mm in diameter. The search algorithm in LaVision Davis 8 software plots green squares around each black circle represent the successful identification of the circular target points.

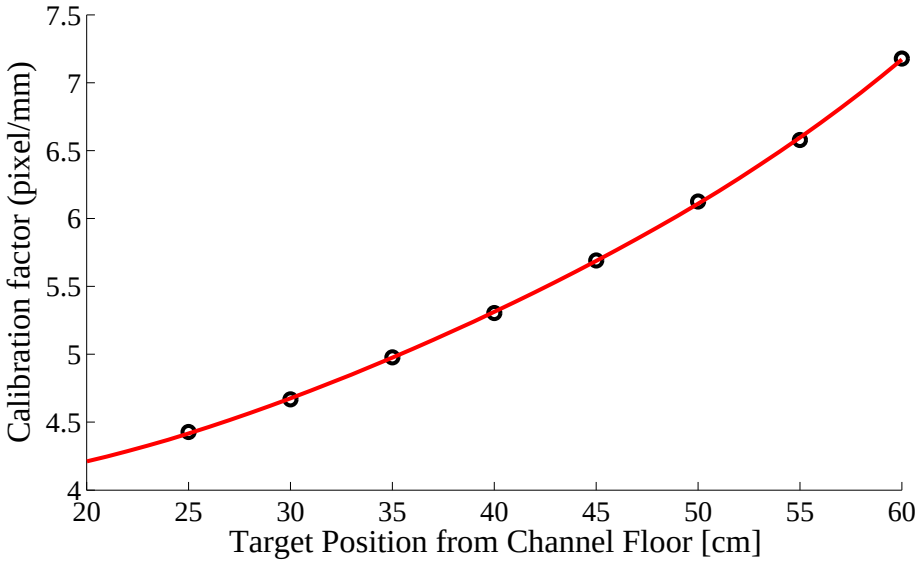

Figure B.2 PIV calibration curve and raw calibration data. The red line represents a fourth order polynomial fit. Black circles show the experimentally determined calibration values. The target position range corresponds to the position and length of the models placed in the flow, i.e., between 20 cm and 60cm.

measurements. Based on these results, the software calibration error was estimated to be approximately 0.18 %. In order to quantify target positioning error, five calibrations were performed with the target being moved and repositioned to approximately the same location (to within 1mm). With 95% confidence, the calibration uncertainty due to target positioning is estimated to be approximately 0.5%. Finally, the uncertainty in the polynomial curve fit was estimated by computing the standard deviation of the nine experimentally determined calibration values shown in Fig. C.2 with the polynomial curve function taken as the true value. With 95% confidence, the curve fitting error is less than 0.45%. The total uncertainty in the reported calibration, calculated based on a root-sum-square combination of the error in the polynomial fit an error in target positioning and software image processing is about 0.7%.

Appendix C
Calibration and Validation of Force Balance Measurements

Calibration

Calibration of the force balance system was completed for each model investigated. For brevity, the calibration procedure for one model is shown. First, a set of precise calibration weights with mass 1g to 8g (in 1g increments) are used to apply a known force to the center-span location (z/D = 0) of a uniform cylinder model of diameter d, as illustrated in Figure C.1. The weights have a measured mass uncertainty of less than ±0.001g (< 0.1%). The weights are held using thin monofilament line carefully placed around a small, 3mm diameter roller bearing (Figure C.1). Sixty second samples of drag and lift data are recorded at a data acquisition rate of 200Hz for each of the calibration weights in the static position shown in Figure C.1. Once data is acquired with the weights oriented in the drag direction,

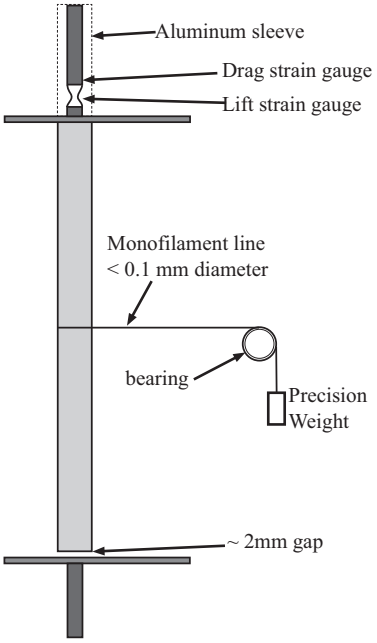

Figure C.1 Sketch of force balance calibration setup.

the process was repeated for the lift direction. An example pair of calibration curves for a uniform circular cylinder at $Re_D = 2100$ is illustrated in Figure C.2a, with the corresponding residual error in the linear fit shown in Figure C.2b. Since the expected mean drag values for all uniform and dual step cylinder models lie in the range of 1.5g to 4.0g, a measure of the error introduced in the calibration can be estimated based on the magnitude of the residual error. For a maximum residual error magnitude of about 0.006 V (Figure C.2b), and an output voltage of 0.25 V (corresponding to a 1.5g drag force in Figure C.2a), the error associated with the calibration is 2.4%. For larger drag forces, the error in the calibration is proportionally smaller.

Following the static calibration procedure performed under ambient air conditions, buoyancy effects on the submerged models are identified through a careful measurement of the static lift and drag force on the models while they are submerged in quiescent water. In order to perform this measurement, the water flume exit is closed temporarily and the entire channel is filled with water to a level matching that used in the experiments (~80cm water depth). Five minute samples of drag and lift force data are obtained once the water settled to quiescent conditions. The magnitude of the buoyancy forces act as an offset value in the calibration curves in Figure C.2a, while the slope of the calibration curve remains constant. The buoyancy forces varied between the different models investigated and were approximately one order of magnitude larger than the residual error

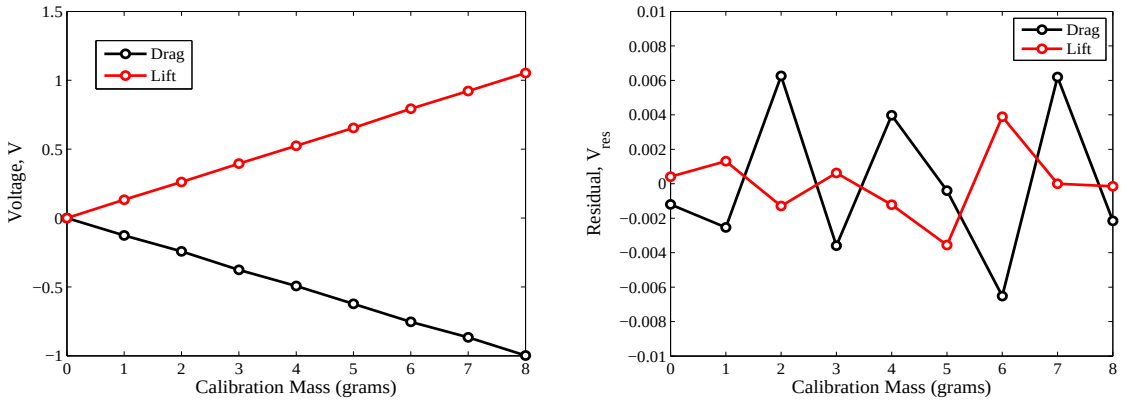

(a) (b)

Figure C.2 Force balance calibration data: (a) calibration curve for a uniform circular cylinder at $Re_D = 2100$, (b) residual error in the corresponding linear curve fit to the data points in (a).

(Figure C.2b). The uncertainty in the buoyancy offset value was estimated for each model using five repeated buoyancy offset measurements. Based on these repeated measurements, the random error associated with the estimation of buoyancy forces is estimated to be less than 10% of its measured value, with 95% confidence. Prior to in-flow measurements, quiescent conditions were tested over a period of two hours in order to identify the extent of any drift in the force measurements. Less than 2% drift was identified to occur over this time span, and over 90% of the observed drift occurred over the first forty-five minutes of testing. Hence, for all testing, models were left submerged for over 45 minutes in order to mitigate effects of drift on the strain gauge output. Thus, the apparent error due to strain gauge drift is less than 0.2%. Once experimental measurements were completed on the uniform circular cylinder model of diameter d, measurements on dual step cylinders immediately followed.

The measurements took place over several days of testing. Therefore, the uncertainty in the day-to-day flow conditions must be incorporated (Appendix I). The total uncertainty in the reported mean drag force, estimated following the recommendations in Roache [108] for combining the effects of independent error source values, is ±5%. The RMS lift forces on dual step cylinder models are an order of magnitude smaller than the mean drag forces. Based on the range of RMS lift forces measured in the experiments, the uncertainty in RMS lift force is between ±25% and ±66%, depending on the model.

Model vibrations

It is important to characterise the natural vibration frequency of each model investigated, so as to ensure that it is outside of the range of excitation based on the vortex shedding frequency [142]. Several measurements of the impulse response of the models and surrounding force balance support components were carried out while the models were submerged under quiescent conditions. Figure C.3a presents the resulting amplitude spectrum of the measured lift force fluctuations on a uniform circular cylinder for two conditions: the impulse response on the model and the impulse response on the water flume wall. The results show two strong peaks in each spectra, one centered on approximately 6 Hz, and another centered on approximately 14 Hz. Based on the changes in the amplitude of the peaks in the spectra, it can be inferred that the natural frequency of the

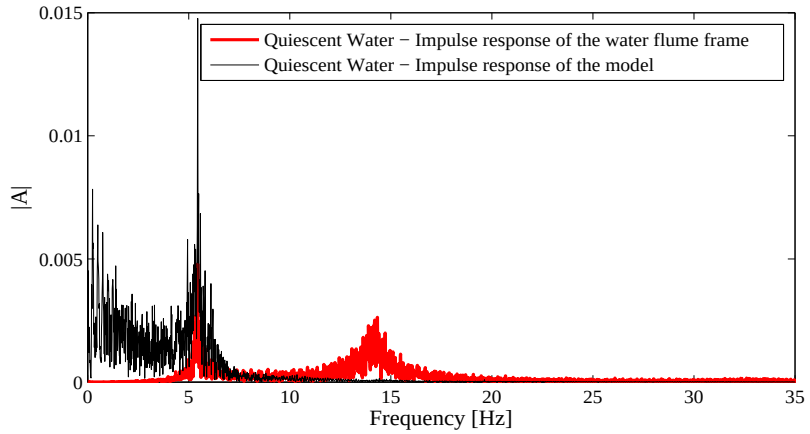

(a)

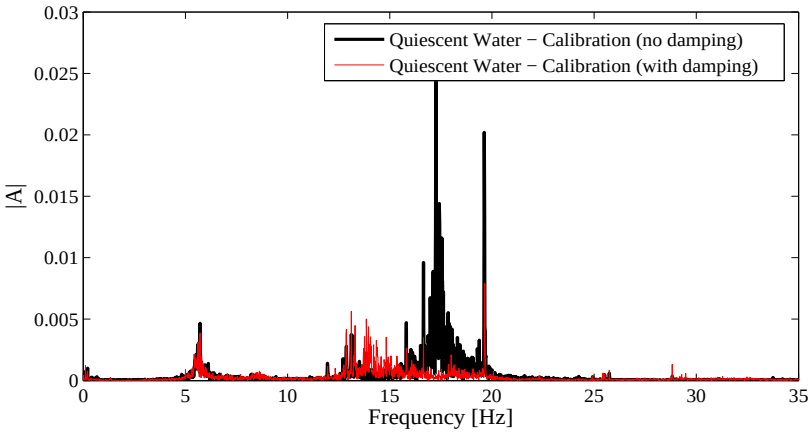

(b)

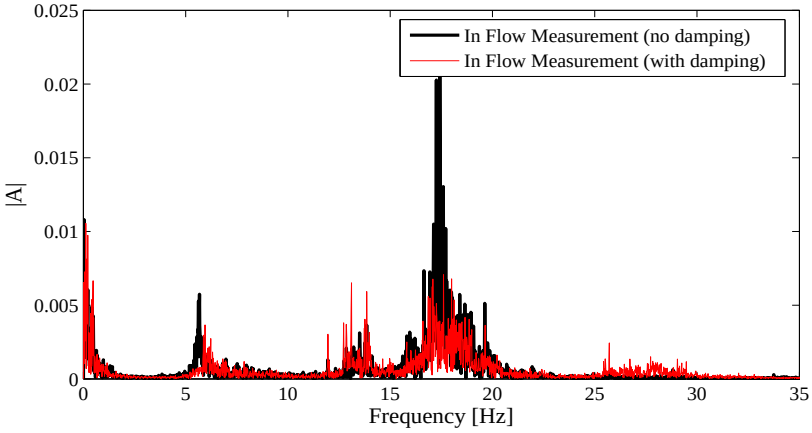

Figure C.3 Spectrum of force fluctuations in the lift direction under various test conditions: (a) Impulse response for identifying model natural frequency, (b) buoyancy calibration with and without rubber damping pads, (c) in flow measurement with and without rubber damping pads.

cantilevered model is approximately 6 Hz for a cylinder of diameter D = 25.4 mm, and the natural frequency of the water flume frame supporting the model is approximately 14 Hz. These frequencies are outside the range of excitation[142], and therefore vortex induced vibrations of the model are not expected to occur. Similar impulse response measurements were carried out for all models investigated to ensure no vortex induced vibrations of the models would occur during the experiments.

The force balance is mounted directly to the frame of the water flume, and is subjected to ambient vibrations originating from the operation of the flumes hydraulic pump. The presence of these vibrations is detectable in the strain gauge measurements which are amplified significantly, as shown in Figure C.3b. Evidently, the vibrations transmitted through the water flume walls and force balance frame are stronger than the flow induced forces on the model itself. In an effort to dampen these unwanted vibrations, rubber padding was added to several joints in the frame assembly. Following the testing of several different damping pad arrangements, one was selected as the best possible arrangement for all uniform cylinder and dual step cylinder models. The results are illustrated in Figure C.3b and C.3c for a uniform circular cylinder, and show that the strength of vibrations can be reduced so that they are on the same order of magnitude as the measured in-flow lift forces (Figure C.3c).

Although the damping improves the energy distribution in the amplitude spectra (Figure C.3), there still remains a significant high frequency noise in the raw lift and drag signals. Therefore, an ideal low pass filter was applied to all data by performing a Fourier decomposition of the raw data and reconstructing the signals for frequencies up to 4 Hz, as shown in Figure C.4 for a uniform circular cylinder at $Re_D = 2100$. Note that, the frequencies of interest in the flow field are in the range of 0.25 Hz to 2.5 Hz, which is well below the specified cut-off frequency of 4 Hz.

Validation of drag and lift force measurements on uniform circular cylinders

The drag coefficient and sectional lift coefficient on uniform circular cylinders investigated in the present study is presented in Figure C.5. Also shown in the figures are a compilation of experimental results from experimental studies conducted over the last century. Surprisingly, there is a limited amount of experimental data available on the drag coefficient of uniform circular cylinders in the

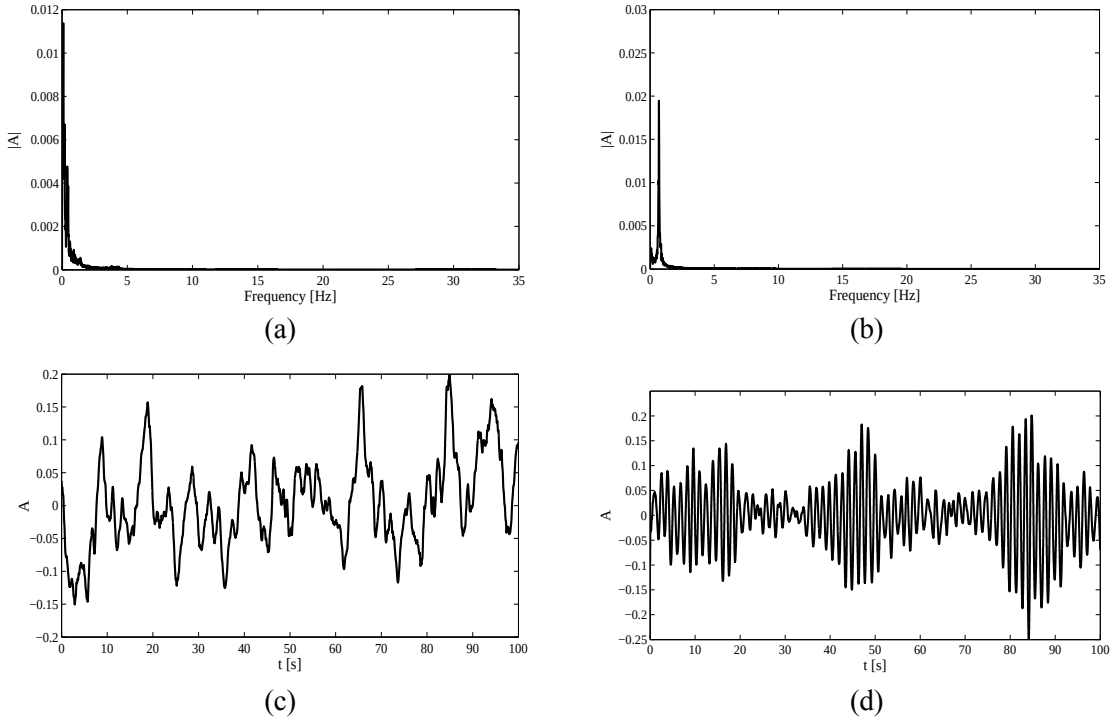

Figure C.4 Filtered force data for a uniform circular cylinder at $Re_D = 2100$: (a) Filtered drag spectrum, (b) filtered lift spectrum, (c) filtered drag fluctuations, (d) filtered lift fluctuations.

Reynolds number range investigated in the present work. Nevertheless, the results are in good agreement with the experimental measurements of Relf [143], and Weiselburger [144], with a decrease in drag coefficient occurring with increasing Reynolds number in the range of $Re_D = 500 – 1600$, and a local minimum in the drag coefficient occurring approximately $Re_D = 1600$.

The estimated sectional RMS lift coefficients in the present study were obtained using the total RMS lift measurements on each uniform circular cylinder model, scaled based on the estimated spanwise correlation length provided by Norberg [33]. The results in the present study are significantly lower than those obtained by Norberg [33]. This can be explained by the overall uncertainty in the lift RMS measurements as well as the uncertainty in the estimated spanwise correlation length, which will change depending on the flow conditions in a given experimental facility [33].

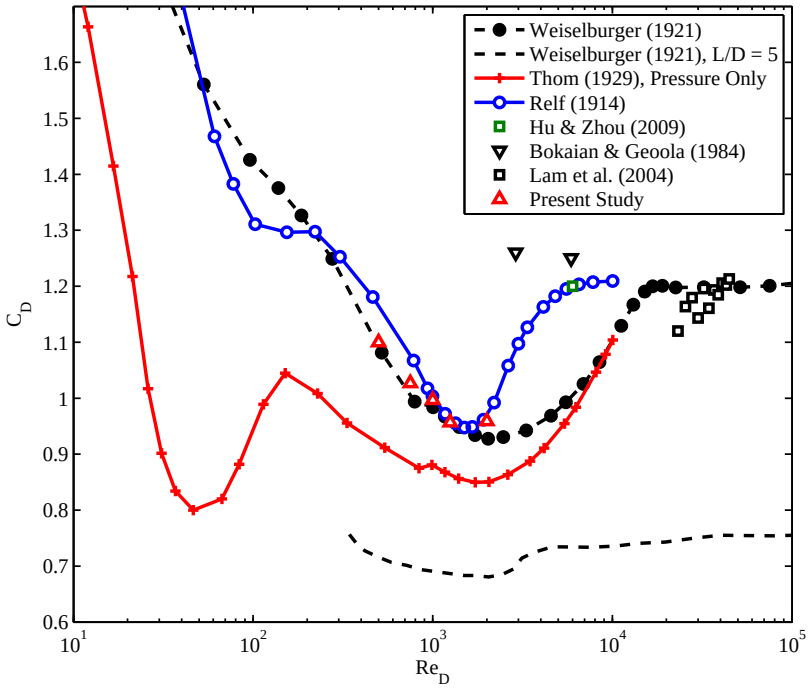

(a)

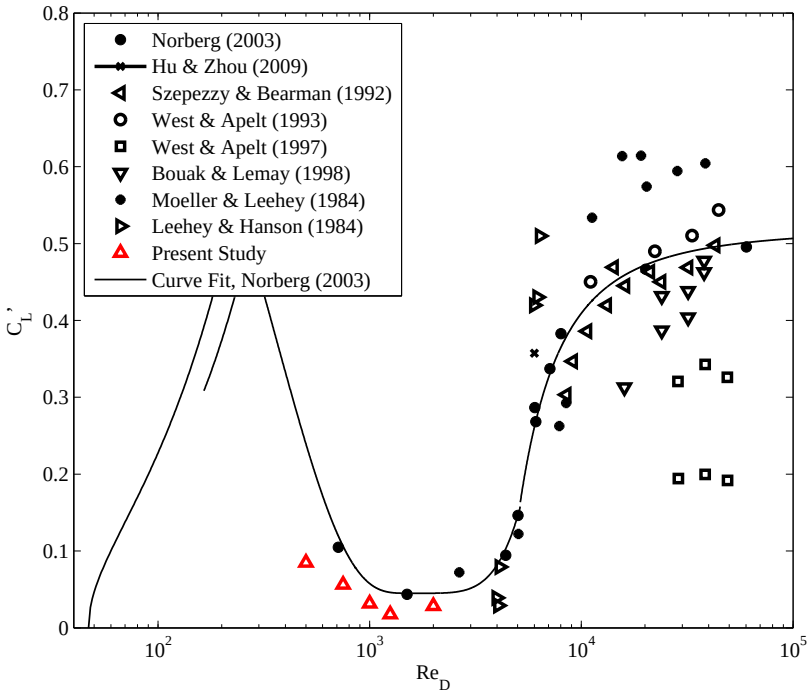

(b)

Figure C.5 Structural loading on uniform circular cylinders: (a) Drag coefficient vs Reynolds number [143,144,156–158,171], (b) Sectional lift coefficient vs Reynolds number [33,158–164].

Appendix D
Flow development past uniform and single step cylinders

Flow development over uniform and single step cylinders

Representative flow visualization images of the wake of a uniform cylinder and a single step cylinder are shown in Figure D.1a and Figure D.1b, respectively. In each image, hydrogen bubbles mark spanwise vortices in the wake. Figure D.1a depicts three vortex shedding cells that form in the wake of a uniform cylinder, identified with curled braces in the figure. Two cells form near the cylinder ends, referred to as end cells (E-cells). These cells extend up to 5D from the cylinder ends and are

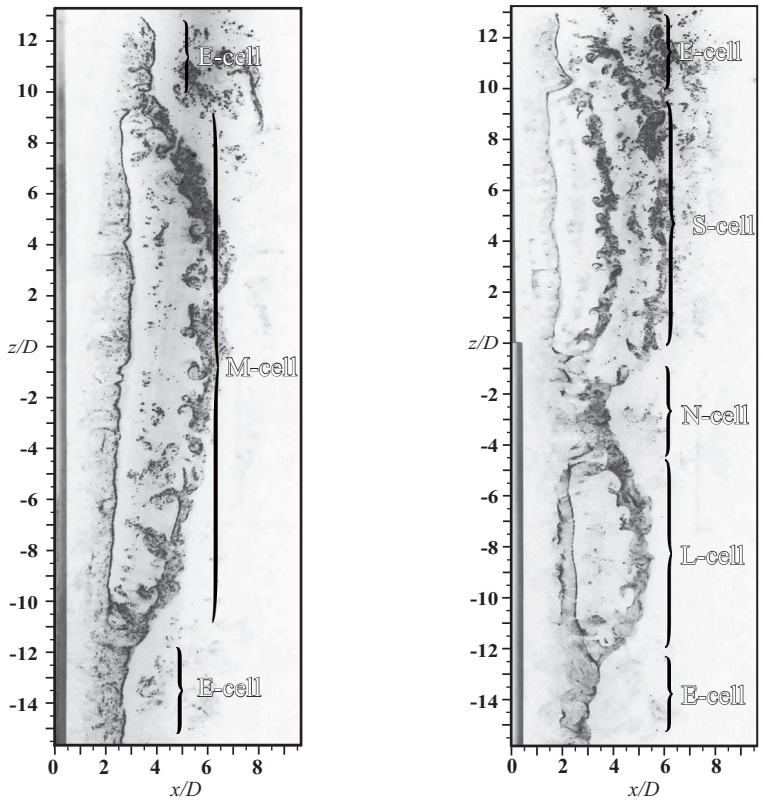

Figure D.1 Hydrogen bubble flow visualization in the wakes of cylindrical geometries: (a) uniform cylinder, (b) single step cylinder. Curled braces are used to identify the approximate extent of the vortex shedding cells.

characterized by a lower vortex shedding frequency compared to that of the main cell (M-cell), positioned away from the boundaries. Analysis of flow visualization video records revealed that the main cell sheds vortices nearly parallel to the cylinder axis, but may also develop an oblique shedding pattern that is induced by the presence of the end cells, similar to that observed by [40] for uniform cylinders in the laminar shedding regime. The frequency of vortex shedding in the main cell, estimated based on analysis of flow visualization video records, matches that expected for an infinite uniform cylinder at the corresponding Reynolds number [33]. For a single step cylinder (Figure D.1b), five distinct vortex cells can be identified in the wake. Two end cells develop within about five local diameters from the cylinder ends, similar to those found for a uniform cylinder. Away from the ends, the variation in shedding frequency due to the change in diameter leads to the formation of three vortex shedding cells in the step cylinder wake. The three cells are labeled in Figure D.1b following the terminology introduced by Dunn & Tavoularis [45]. The S-cell forms downstream of the small diameter cylinder and is characterized by a distinct vortex shedding frequency f_S. The L-cell and N-cell form downstream of the large diameter cylinder and shed vortices at frequencies f_L and f_N, respectively. Analysis of flow visualization video records showed that the N-cell and L-cell have comparable shedding frequencies, with that of the N-cell being slightly lower, while the S-cell frequency is approximately double that of the L-cell. The observed topology of the step cylinder wake is similar to that reported by Dunn & Tavoularis [45] and Lewis & Gharib [70] for single step cylinders with a diameter ratio of two in the laminar shedding regime. It should be noted that since the development of end cells is not the main focus of the present study, only the wake development away from the end regions will be discussed henceforth.

Sequences of flow visualization images were used to investigate temporal changes in the wake development. Figure D.2 presents hydrogen bubble flow visualization images illustrating the N-cell dynamics and vortex interactions at the cell boundaries. Figure D.2a shows nearly parallel vortex shedding in the wake of the large and small cylinders, so that the existence of two distinct cells in the wake of the large cylinder is not immediately apparent because they are aligned in phase. Over time, vortices in the large cylinder wake begin inclining towards the step discontinuity (Figure D.2b),

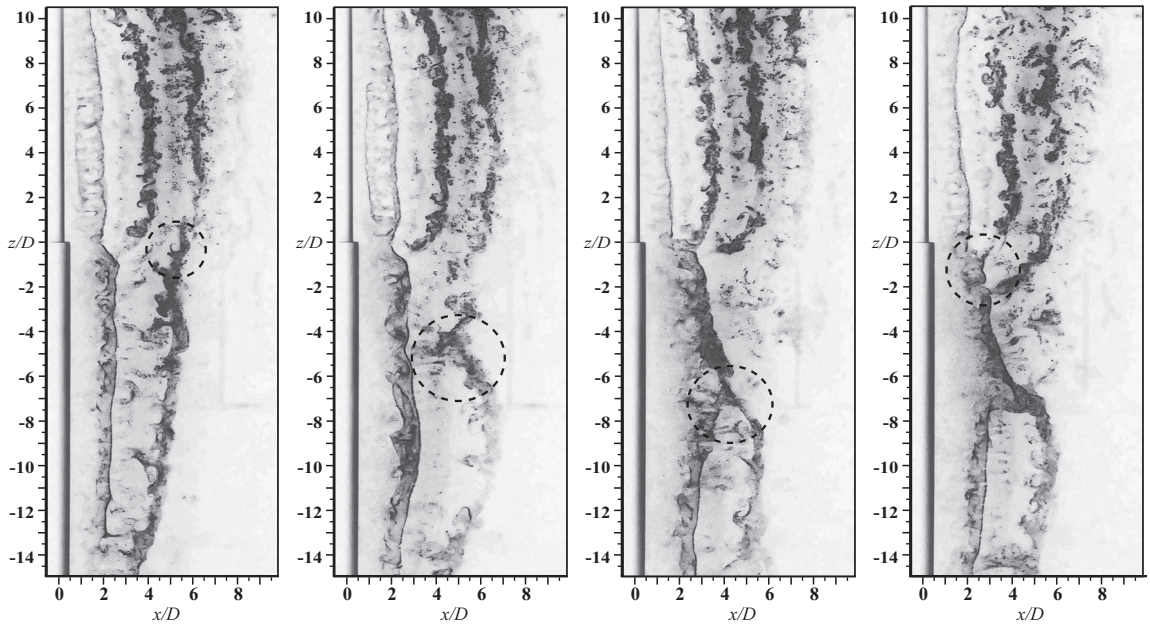

(a) t*=0 (b) t*=24 (c) t*=42 (d) t*=56

Figure D.2 A sequence of hydrogen bubble flow visualization images depicting N-cell development. t* is the number of small cylinder vortex shedding periods. Dashed circles identify some vortex interactions occurring in the wake.

indicating that the convective velocity of vortices in this region is reduced. The presence of such a region in the large cylinder wake is likely responsible for the formation of a lower frequency vortex shedding cell, i.e., the N-cell. In Figure D.2b, the N-cell's extent appears limited to a distance of approximately 6D from the stepwise discontinuity. Due to the difference in frequency between the N-cell and the adjacent L-cell, N-cell vortices gradually move out of phase with L-cell vortices (Figure D.2b-d) and eventually re-align (Figure D.2a), thus completing a full 2π phase shift. The observed 2π phase variation between the N-cell and L-cell is referred to as the N-cell cycle. Such a cyclic variation in the extent of the N-cell agrees qualitatively with that observed by Dunn & Tavoularis [45] and Morton & Yarusevych [19] in the laminar shedding regime. Analysis of flow visualization video records revealed significant temporal variations in the duration of N-cell cycles, which will be discussed in more detail later.

Figure D.2 also illustrates complex vortex interactions occurring at the boundaries between the identified vortex cells. At the boundary between the N-cell and S-cell, S-cell vortices often form direct vortex connections with N-cell vortices, as can be seen within the circled regions in Figure D.2a and

Figure D.2d. Although it is not easy to identify in Figure D.2, analysis of video records showed that two consecutive S-cell vortices can also form half-loop connections. At the boundary between the N-cell and L-cell, N-cell vortices form direct vortex connections with L-cell vortices, with one such connection marked in Figure D.2b. The vortex interactions at the N-L and N-S cell boundaries are described by the vortex dislocation phenomenon described by Williamson [16]. Specifically, the difference in vortex shedding frequency of adjacent cells causes them to move in and out of phase in a continuous fashion, leading to an array of vortex interactions involving vortex splitting, half-loop vortex connections, and direct vortex connections. Within the circled region in Figure D.2c the N-cell vortices begin to split into multiple filaments in the near wake and form connections between consecutive L-cell vortices of the same sense.

Figure D.3 depicts vortex interactions at the boundary between the S-cell and N-cell. Evidently, due to the difference in diameters, more than one S-cell vortex is shed for each N-cell vortex, with the ratio given approximately by *D/d*, i.e., a factor of two in this study. Figure D.3a-b show two S-cell vortices on one side of the wake (S1 & S3) connecting to the forming N-cell vortex (N1) of the same

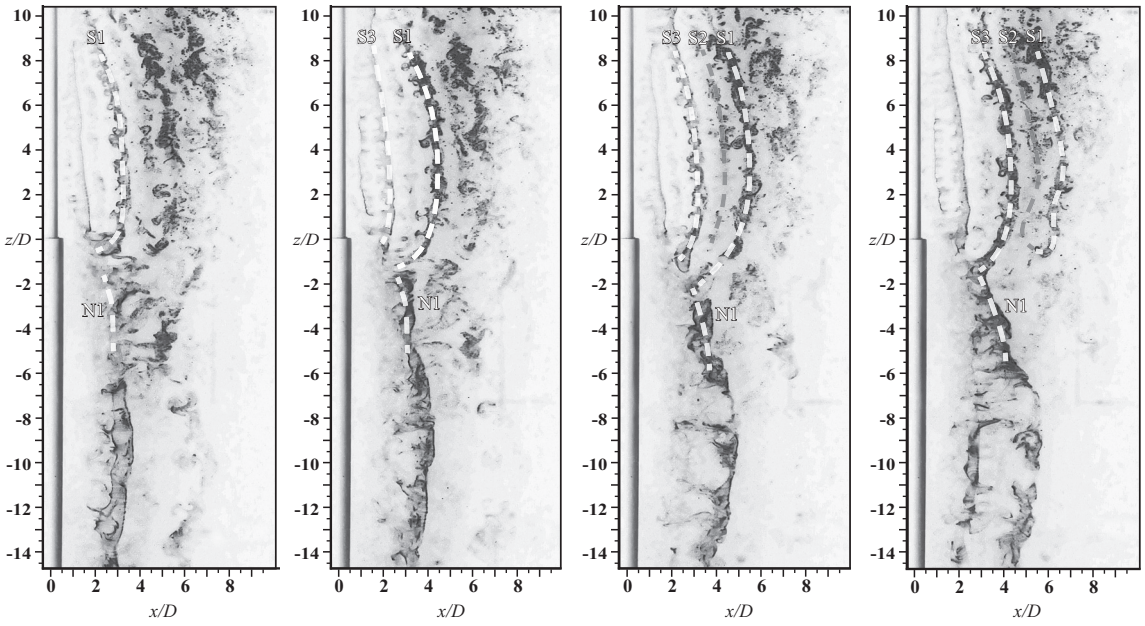

(a) t*=0 (b) t*=0.45 (c)t*=0.90 (d)t*=1.35

Figure D.3 Hydrogen bubble visualization of a half-loop vortex connection in the S-cell. t* is the number of S-cell vortex shedding periods.

sign. As it sheds, vortex S1 deforms significantly to maintain the connection with the N-cell (Figure D.3a-b). Depending on the relative phase between the S-cell and N-cell vortices, some S-cell vortices can no longer maintain connection with the N-cell. This is seen is Figure D.3c-d, where highly stretched vortex filament S1 breaks away from N1 and instead connects to small cylinder vortex S2 shed on the opposite side of the wake, forming a half loop. Such half-loop vortex connections and direct cross boundary connections between the S-cell and N-cell occurred frequently in the flow visualization video records, resembling the topology visualized numerically in Morton & Yarusevych [19] for $D/d = 2$ at $Re_D = 150$ and 300.

At the boundary between the L-cell and N-cell, direct vortex connections and vortex splitting can occur as the two cells progressively move out of phase (Figure D.2). Figure D.4 illustrates the splitting of N-cell vortices at this cell boundary via an image sequence. In Figure D.4a, vortex N1 is shed out of phase with L1. Under such a condition, vortex N1 splits into two filaments connecting to the two adjacent L-cell vortices of the same sign, namely, L1 and L3 in Figure D.4b and Figure D.4c.

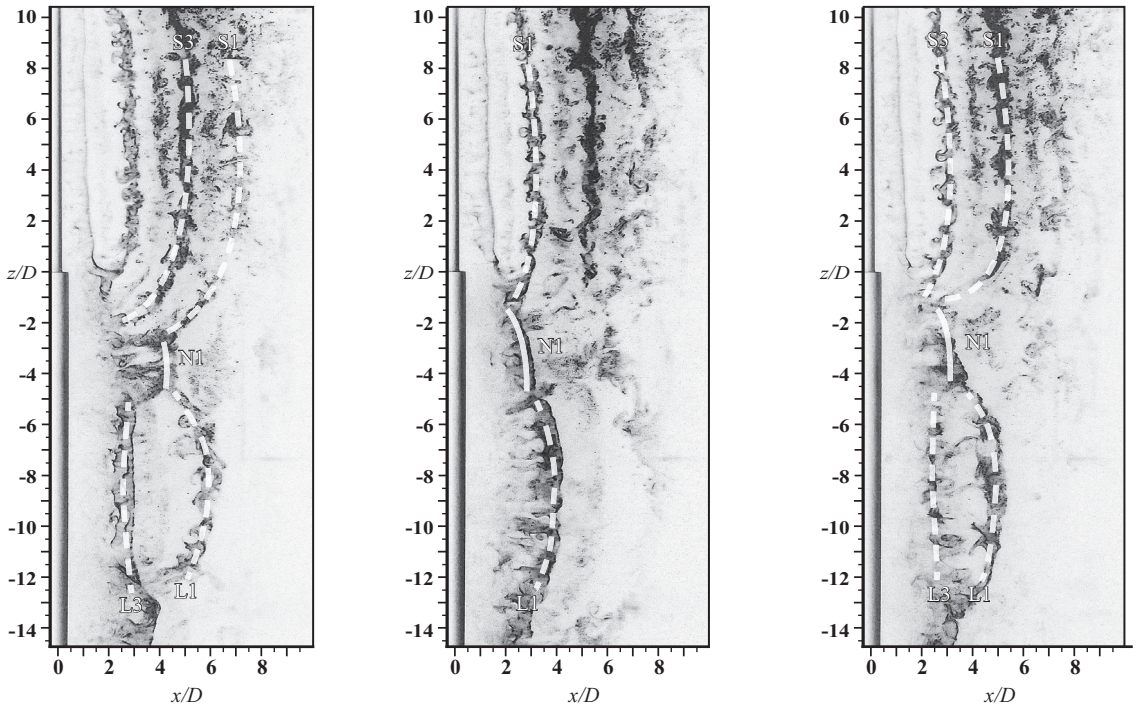

(a)t*=0 (b) t*=0.40 (c)t*=0.78

Figure D.4 Hydrogen bubble visualization of vortex splitting in the N-cell. t* is the number of S-cell vortex shedding periods.

Analysis of velocity measurements in the step cylinder wake

The flow visualization results show that three distinct vortex shedding cells develop in the turbulent wake of a single step cylinder at $Re_D = 1050$ and D/d = 2. The results provide insight into vortex interactions occurring at the cell boundaries. In this section, a quantitative analysis of wake characteristics is presented.

Spectral analysis of velocity measurements was used to determine the vortex shedding frequency and investigate its variation along the cylinder span. The obtained streamwise velocity spectra are presented in Figure D.5. The results show three well-defined regions characterized by distinct shedding frequencies, associated with the S-cell, N-cell, and L-cell. Note that the variation in the dominant energy content within each vortex shedding cell is largely attributed to substantial temporal

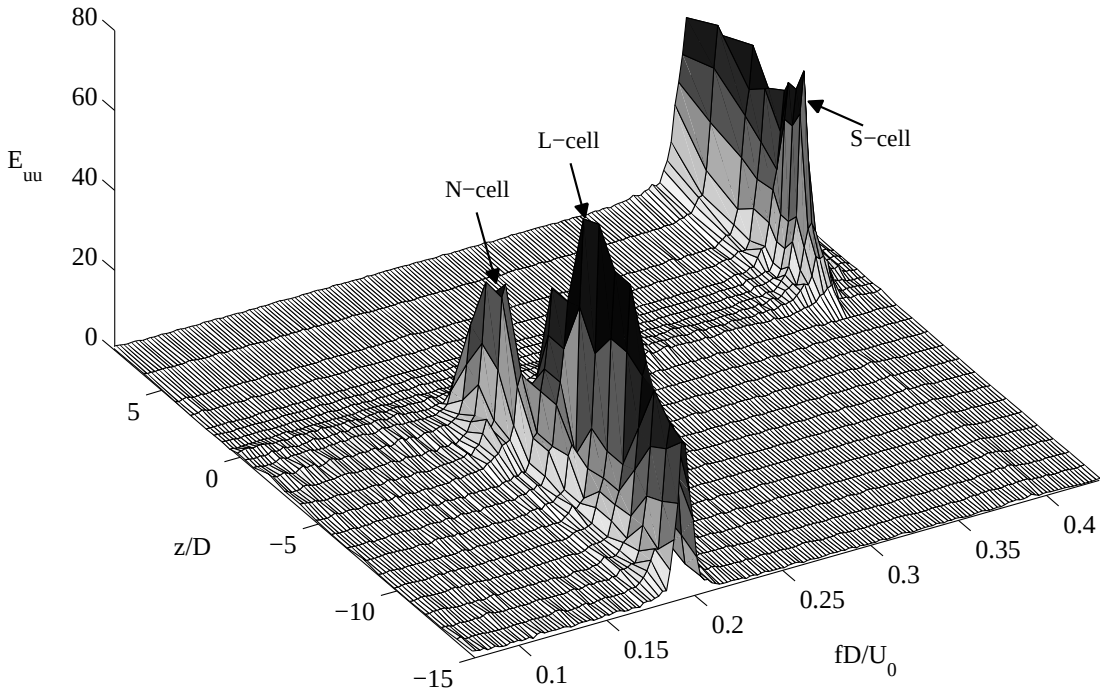

Figure D.5 Streamwise velocity spectra in the wake of a single step cylinder. Arroes indicate the peaks in the spectra corresponding to the S-cell, N-cell, and L-cell vortex shedding frequencies. Velocity measurements were acquired at $x/D = 5$, and $y/D = 0.75$.

fluctuations in the cell boundary locations. Within each vortex shedding cell, each velocity spectrum exhibits a single peak associated with the vortex shedding frequency of each cell, while at cell boundaries, two dominant peaks can be seen and are associated with the vortex shedding frequencies of the adjacent cells.

Based on the spectra shown in Figure D.5, the most dominant frequency was determined for each spanwise plane, and the results are presented in Figure D.6. These data serve to characterize average locations of cell boundaries, marked by a change in dominant frequency, as well as the average shedding frequency of each cell, marked by solid lines in Figure D.6. The results show that the S-cell extends down to $z/D \approx -0.5$, and has a dimensionless shedding frequency of $f_S D/U_\infty \approx 0.396$. In the large cylinder wake, N-cell vortex shedding at $f_N D/U_\infty \approx 0.189$ is dominant within $-5.0 \leq z/D \leq -0.5$, while L-cell shedding occurs for $z/D < -5.0$ at $f_L D/U_\infty \approx 0.198$.

As mentioned earlier, analysis of flow visualization results showed that N-cell development

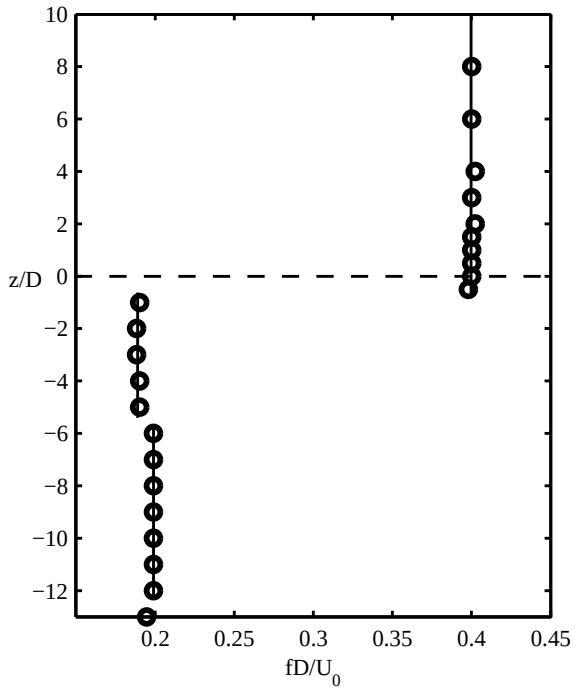

Figure D.6 Variation in the dominant shedding frequency along the span of a single step cylinder. Note, the uncertainty in the dimensionless frequency estimates is accommodated by the size of the data symbols.

exhibits a cyclic behavior, with the attendant fluctuation in the extent of the N-cell. Dunn & Tavoularis [45] speculate that the N-cell development is linked to the presence of downwash over the step. Morton & Yarusevych [19] confirmed that, for $Re_D = 150$ and 300, the downwash flow was cyclic, and correlated to the N-cell development. In the present study, spanwise velocity measurements confirmed the presence of a downwash of about 7% of the free stream speed. A spectrum of the spanwise velocity fluctuations revealed that the energy content of the downwash velocity fluctuations was centered on $fD/U_0 \approx 0.009$. This frequency matches the difference in the measured N-cell and L-cell shedding frequencies, $(f_L\text{-}f_N)D/U_\infty = 0.009$. The results agree with Morton & Yarusevych [19] and Dunn & Tavoularis [45], who found that the frequency of N-cell cycles in the laminar shedding regime approximately matches the beat frequency between the L-cell and N-cell. Evidently, the link between downwash fluctuations and the N-cell cycle persists in the turbulent shedding regime.

A review of flow visualization video records revealed there are temporal fluctuations in the duration of N-cell cycles. In order to quantify such fluctuations, flow visualization video records capturing over 1500 S-cell vortex shedding periods were analyzed. Figure D.7 shows the resulting histogram of the N-cell cycle durations estimated based on the time elapsed between consecutive phase dislocations occurring at the N-cell and L-cell boundary, which can be detected in hydrogen bubble flow visualizations (e.g., Figure D.2d). A Gaussian fit to the histogram data is shown in Figure D.7 for comparison. The results suggest that the mean duration of the N-cell cycle is about fifty small cylinder shedding periods. This corresponds to a dimensionless N-cell cycle frequency of $f_{LN}D/U_\infty \approx 0.009$, which matches the difference in the L-cell and N-cell vortex shedding frequencies, $(f_L\text{-}f_N)D/U_\infty = 0.009$. Dunn & Tavoularis [45] observed interruptions in N-cell shedding occurring prior to the start of each N-cell cycle but did not quantify them. Present results suggest that the perceived interruptions may be attributed to the variation in the duration of consecutive N-cell cycles. On the other hand, the numerical simulations conducted by Morton & Yarusevych [19], designed to match the experimental conditions in Dunn & Tavoularis [45], found no interruptions in N-cell shedding and no variations in N-cell cycle duration. It is speculated that the experimentally observed variability in the duration of N-cell cycles is attributed to variations in the shedding frequencies in the large cylinder wake, which would not be present in numerical simulations at a low Reynolds number. Indeed, random fluctuations

in the L-cell and N-cell shedding frequencies on the order of 1% would produce a standard deviation in the N-cell cycle duration of $\sigma_{t^*} \approx 12$, matching that of the Gaussian fit in Figure D.7. Such fluctuations in the vortex shedding frequency can occur in many experimental facilities due to changes in test section environment and may be expected in the turbulent shedding regime.

Further investigation of the temporal variation in vortex shedding was completed through spectrogram analysis of the wake velocity measurements. Figure D.8 shows spectrograms illustrating temporal variations in the dominant frequency in the S-cell (Figure D.8a), N-cell and S-cell boundary (Figure D.8b), N-cell (Figure D.8c), N-cell and L-cell boundary (Figure D.8d), and L-cell (Figure D.8e). As expected, spectrograms of the velocity measurements in the S-cell and L-cell (Figure D.8a and Figure D.8e) show small but distinct fluctuations in amplitude and frequency. More substantial fluctuations are detected at cell boundaries and within the N-cell (Figure D.8b-d), where temporal fluctuations in the cell boundary locations and dislocations occur. At the boundary between the N-cell

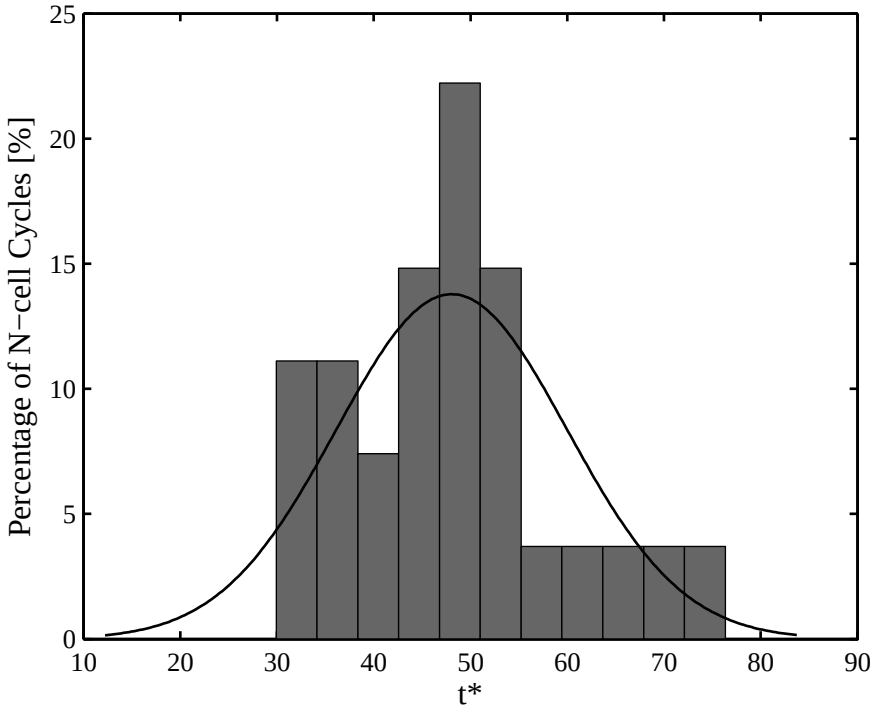

Figure D.7 Histogram for the duration of the N-cell cycle. The solid line represents a Gaussian fit to the histogram data. t* is the number of small cylinder vortex shedding periods.

and S-cell, Figure D.8b shows a substantial spread of the energy content across a range of frequencies. Dominant frequency-centred activity in this region is associated with the passage of N-cell vortices and highly distorted S-cell vortex filaments connecting to N-cell vortices. At the N-L cell boundary (Figure D.8d), the dominant frequency in the spectrogram fluctuates between that of the N-cell and L-cell. Moreover, notable modulations in both amplitude and frequency occur at this cell boundary, e.g., at $t^* \approx$ *10, 40, 70, 100, 170, 225* and *250*. The temporal separation of these events approximately corresponds to the duration of N-cell cycles (Figure D.7) and, thus, is attributed to the passage of phase dislocations between the N-cell and L-cell, which occur at the N-cell cycle frequency $(f_L - f_N)$.

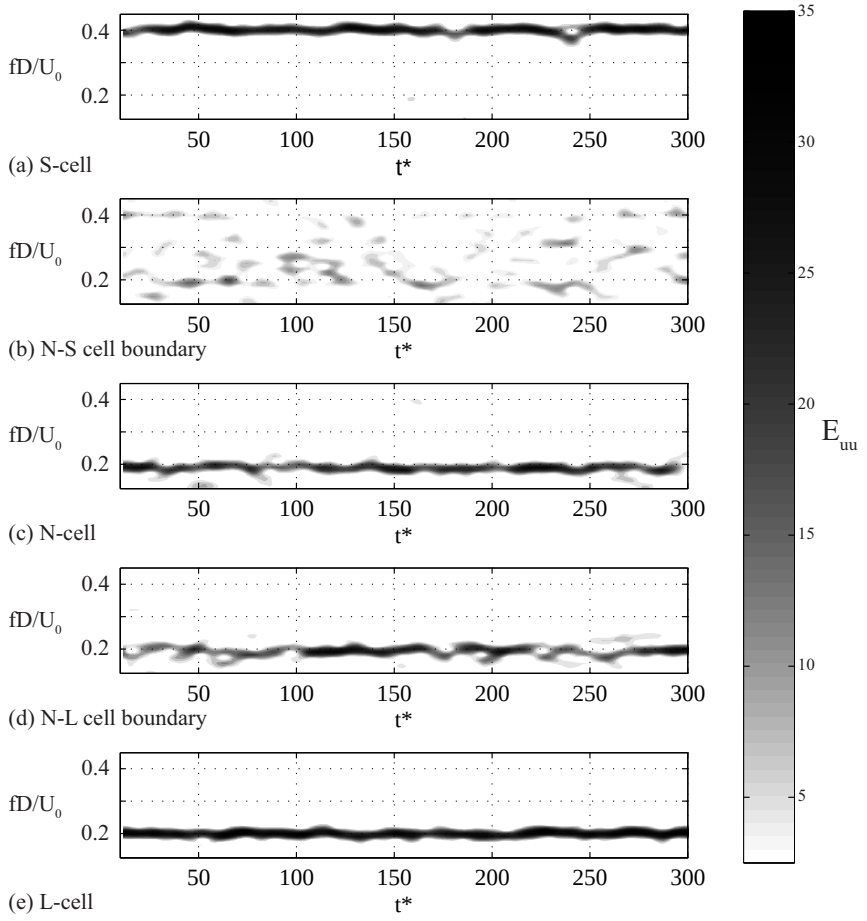

Figure D.8 Spectrograms illustrating temporal variations in the dominant frequency and energy content in the wake of a single step cylinder: (a) z/D = 4, (b) z/D = -1, (c) z/D = -3, (d) z/D = -5, and (e) z/D = -10. Spectrograms are normalized by the variance of the corresponding velocity signal. t* is the number of S-cell vortex shedding periods.

A model of vortex dynamics in the single step cylinder wake

Vortex shedding frequency estimates for the S-cell, N-cell, and L-cell (Figure D.6) as well as extensive flow visualizations (Figure D.1-Figure D.4) were used to construct a simplified model of the wake vortex dynamics. The nature of vortex interactions between the main cells in the step cylinder wake is expected to depend primarily on: (i) the circulation of vortices within each cell and its decay, (ii) the frequency of each cell, and (iii) three-dimensional effects due to the presence of the step discontinuity.

Berger & Wille [119] suggest that, for a uniform circular cylinder, circulation of vortices (Γ) is inversely proportional to the frequency of vortex shedding (f) and proportional to the square of the free stream velocity (U_0). This is described by the following equation:

$$\Gamma = \frac{\Lambda U_0^2}{f} \tag{D-1}$$

where Λ is a dimensionless parameter. Dunn & Tavoularis [45] applied this concept in deducing the vortex connections between the N-cell, L-cell, and S-cell for a single step cylinder under laminar shedding conditions. In the present work, however, the wake is turbulent, hence, significant variations in the circulation of vortices are expected within each cell. Timme [121] and Davies [122] have shown that the maximum cycle to cycle variation in circulation of turbulent vortices is ±40% for a uniform circular cylinder. Thus, variability in vortex connections is expected and was observed in the present study. Here, Equation (D-1) is used to estimate average relative circulations of vortices in the three main cells.

Figure D.9 shows a simplified model of vortex connections in the wake of a step cylinder for $Re_D = 1050$, and $D/d = 2$. This model depicts wake topology for an average N-cell cycle. As the phase shift between the N-cell and L-cell increases, the N-cell expands, with N-cell vortices trailing their L-cell counterparts. At the N-S cell boundary, S-cell and N-cell vortices interact. Equation (D-1) suggests that, on the average, the strength of S-cell vortices is approximately half that of vortices in the N-cell. Thus, to conserve circulation, each N-cell vortex must split into at least two filaments at the N-S cell boundary as confirmed by flow visualization results in Figure D.4. In the presence of periodically occurring half-loop connections between pairs of S-cell vortices, one of the N-cell filaments connects

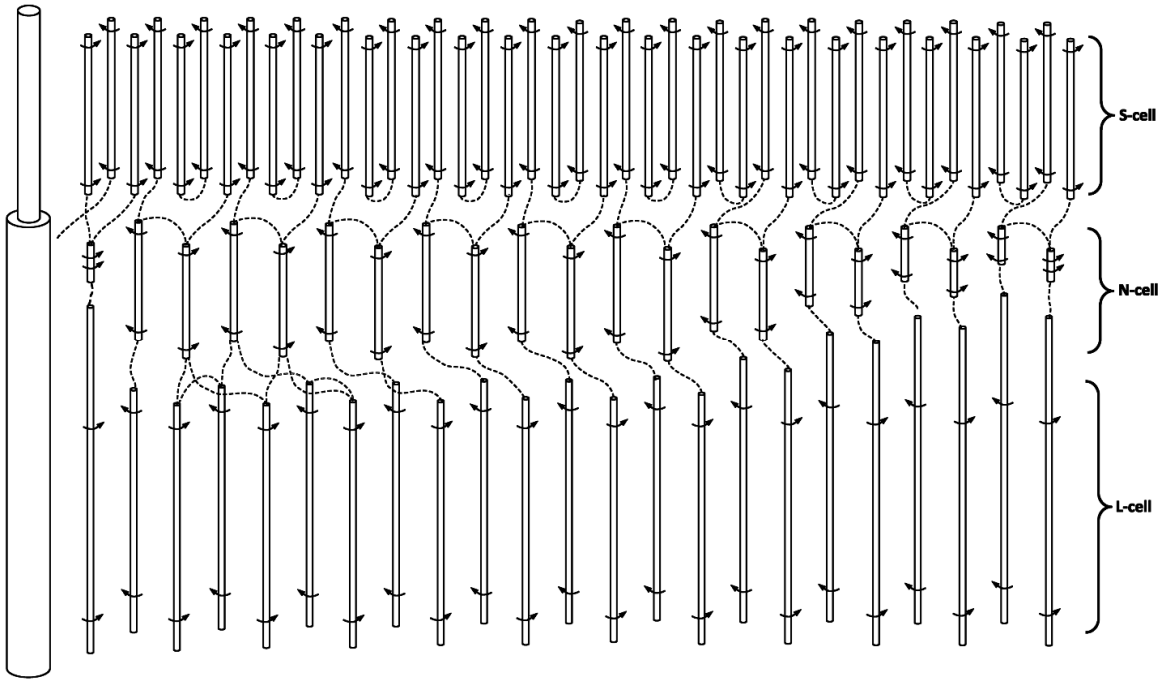

Figure D.9 A simplified sketch of vortex interactions occurring in the wake of a single step cylinder for Re_D = 1050, and D/d = 2. Dashed lines show vortex connections occurring between main vortex filaments.

to an S-cell vortex and the other forms a half-loop with an adjacent N-cell vortex, resulting in the pattern shown in Figure D.9.

At the N-L cell boundary, N-cell vortices form direct connections with L-cell vortices during most of the N-cell cycle (Figure D.9). However, as the phase lag between the two cells becomes significant, a series of vortex dislocations occurs. Specifically, as shown by flow visualization, N-cell vortices begin to split and connect with consecutive vortices in the L-cell of the same sign, which is similar to vortex dislocations observed by Williamson [16] in the wake of a uniform circular cylinder. Since, on the average, N-cell and L-cell vortices have comparable strength (D-1), this requires consecutive L-cell vortices connecting with one N-cell vortex to form half-loop connections in order to conserve circulation (Figure D.9). The dislocations persist for a few cycles, until the N-cell and L-cell realign in phase, marking the beginning of the next N-cell cycle.

The dominant vortex interactions depicted in Figure D.9 are in agreement with the results of Dunn & Tavoularis [45] and Morton & Yarusevych [19] pertaining to the laminar shedding regime. However,

the expected cycle to cycle variation in circulation as well as the temporal changes in shedding frequencies will undoubtedly influence the nature and periodicity of vortex interactions at both cell boundaries. For example, intermittency was observed in the formation of half-loop connections between S-cell vortices at the N-S cell boundary. Although it could not be confirmed definitively, this may occur if two consecutive S-cell vortices of the same sign connect with a single N-cell vortex. From a vortex dynamics perspective, such dual connections between the S-cell and N-cell would appear in pairs, and only for a specific phase alignment between S-cell and N-cell vortices. In addition, at both the N-L and N-S cell boundaries, other weaker vortex connections likely exist, particularly during the main dislocations between the N-cell and L-cell.

Conclusions

The flow development over a single step cylinder was investigated experimentally for $Re_D = 1050$ and $D/d = 2$. Hydrogen bubble flow visualization was utilized to investigate three-dimensional vortex dynamics in the step cylinder wake. Additionally, velocity measurements were used to estimate spatial and temporal changes in the vortex shedding frequency.

The results show that turbulent vortex shedding from a step cylinder occurs in three distinct cells along the cylinder span. For the parameters investigated, vortex shedding occurs from the small cylinder in a single cell, the S-cell, at $f_S D/U_0 \approx 0.398$. Two vortex shedding cells develop in the wake of the large cylinder: the N-cell forms within about 5D of the step discontinuity and sheds vortices from the large cylinder at $f_N D/U_0 \approx 0.189$, while L-cell vortex shedding occurs at $f_L D/U_0 \approx 0.198$. The spanwise extent of the N-cell fluctuates at a frequency corresponding to the beat frequency between the N-cell and L-cell, $(f_L - f_N)D/U_0 \approx 0.009$, and is referred to as the N-cell cycle. While the main elements of the wake topology are similar to those found in the laminar shedding regime [19,45,70], significant variations in the duration of N-cell cycles and intermittency in the attendant vortex interactions is observed in the turbulent shedding regime. The observed fluctuations in N-cell cycle duration are attributed to temporal variations in the frequency of the N-cell and L-cell, which is inherent to turbulent wake development.

Due to the difference in vortex shedding frequencies of the three cells, complex vortex interactions occur at cell boundaries as vortices move in and out of phase. Contrasting with earlier observations in the laminar shedding regime, significant cycle-to-cycle variations in circulation of shed vortices produce strong intermittency in vortex interactions taking place between the main cells. A simplified model for the salient elements of vortex dynamics in the turbulent wake is constructed for an average N-cell cycle on the basis of flow visualization and velocity measurements. At the boundary between the S-cell and N-cell, N-cell vortices form direct vortex connections with S-cell vortices. Since the circulation of N-cell vortices is higher than that of the S-cell vortices, all N-cell vortices split and form connections with adjacent N-cell vortices in order to conserve the circulation. S-cell vortices that do not connect to N-cell vortices form half-loop connections with adjacent S-cell vortices shed on the opposite side of the wake. At the N-L cell boundary, N-cell vortices and L-cell vortices, which have comparable strength, form direct vortex connections for the majority of the N-cell cycle. However, when the phase lag between the two cells becomes significant, a series of vortex dislocations occurs, marking the end of the N-cell cycle. This is manifested by N-cell vortices splitting into at least two vortex filaments and connecting with two L-cell vortices which also split and form half-loop connections.

Appendix E
Laminar vortex shedding from uniform and dual step cylinders

Numerical Methodology

The flow over uniform cylinders and dual step cylinders has been investigated numerically using the finite volume code, ANSYS CFX 13.0. The numerical studies are completed in order to emulate the acquisition of experimental data with LDV and PIV, and develop data processing strategies which can then be applied to actual experimental data. While the investigations are performed at Reynolds numbers pertaining to the laminar vortex shedding regime, they provide insight into intricate vortex interactions between main spanwise vortex cells, which are expected to be qualitatively similar to those observed at higher Reynolds numbers.

Simulations were carried out on a custom built workstation equipped with two Intel Xeon E5520 processors and 24GB of RAM. The pressure-velocity coupling within ANSYS CFX is handled by the Rhie-Chow interpolation scheme. For spatial discretization, a second order high resolution scheme is employed [145]. A fixed time step was selected based on the results of preliminary studies on uniform circular cylinders and the Courant Freidrich Lewis (CFL) criterion, CFL<1. The continuity and momentum equations are solved using a laminar flow model for all simulations. A velocity profile is specified at the inlet boundary, and a constant (zero) pressure is applied at the outlet of the domain. All other domain boundaries have free-slip conditions while a no-slip condition is applied at the model surface(s).

Planar Computational Mesh

Mesh independence and domain size independence studies were completed for two-dimensional simulations of the flow development over uniform circular cylinders at Re_D = 50, 75, 100, 150, and 200. These Reynolds numbers were selected based on the range of flow conditions encountered in the uniform and dual step cylinder simulations being considered in this investigation. A diagram of the

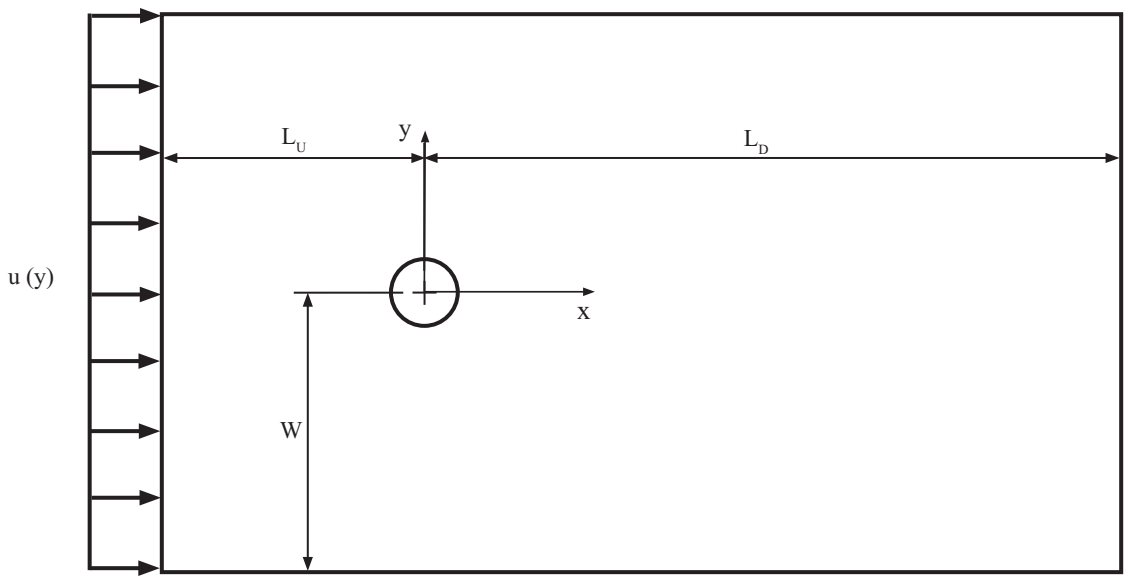

Figure E.1 General diagram of the computational domain.

computational domain is shown in Figure E.1. Figure E.2 shows an O-Grid computational mesh generated with ICEM software. This type of grid was employed in all simulations. Each of the mesh variables under consideration, M1, M2, M3, and M4 (Figure E.2), corresponds to an element length or width, depending on the direction indicated by the arrows in the figure: (i) M1 – mesh spacing at the inlet of the domain, (ii) M2 – mesh spacing in the near wake of the cylinder, (iii) M3 – mesh spacing governing the number of mesh elements around the cylinder circumference, and (iv) M4 – radial mesh spacing at the cylinder surface. All the mesh and domain configurations investigated are shown in Table E.1. It should be noted that the same mesh relaxation factor of 1.1 is applied to spacing M2 and M4. This matches the relation used by Inoue & Sakuragi [69] for the numerical modeling of flow past a cylinder with two free ends.

A baseline mesh and domain configuration (case A3 in Table E.1) was generated first based on the configurations used in previous numerical studies (e.g., [146,147]). Configurations A1 through A4 (Table E.1) were generated from the baseline case A3 (highlighted in red in the table) by adjusting the mesh size by a constant multiplicative factor. Mesh configurations A5 through A9 are used to determine the effect of domain size while keeping the mesh configuration matching that of A3. In

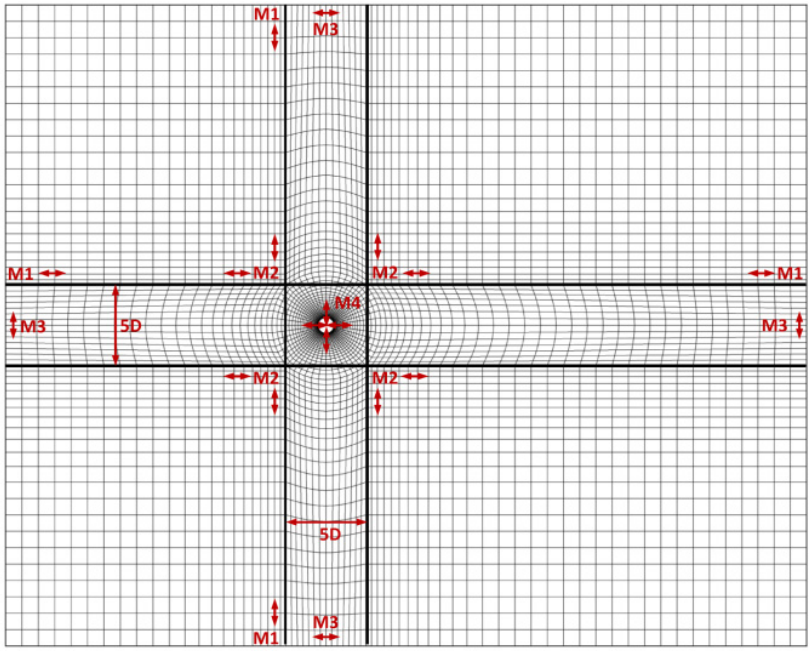

Figure E.2 General two-dimensional diagram of the computational mesh.

Table E.1, any mesh size or domain size deviation from configuration A3 (baseline) is in bold text. The Strouhal number (St) and drag coefficient (C_D) results for Re_D = 100 & 150 are also shown for comparison. The mesh configuration and domain size were deemed acceptable if both St and C_D were within 1% of their converged values based on the rate of convergence estimation employed by Roache [108]. From comparing the results shown in the Table E.1 for Re_D = 100 & 150, configuration A8 was selected as the planar mesh and domain size for three-dimensional computations at $Re_D \leq 150$. For higher Reynolds numbers, i.e., $Re_D > 150$, the results of Morton & Yarusevych [19] are used to determine appropriate mesh parameters, which correspond to configuration A10 in Table E.1. A comparison of the numerical results obtained using the selected mesh configurations with both experimental and numerical results of other researchers is shown in Figure E.3a and Figure E.3b. The present numerical results are in excellent agreement with two-dimensional simulations performed by Henderson [148] and three-dimensional simulations performed by Grundmann [146] (Figure E.3). The Strouhal number estimates match that obtained experimentally by Williamson [16] to within the uncertainty in St (Figure E.3). The drag coefficient estimates show more scatter, and are attributable

Table E.1 Domain and mesh parameters investigated on a uniform cylinder.

		Configuration									
		A1	A2	A3 baseline	A4	A5	A6	A7	A8	A9	A10
Lu/D		20	20	20	20	**10**	**15**	20	20	20	20
W/D		20	20	20	20	20	20	**10**	**15**	20	**15**
Ld/D		30	30	30	30	30	30	30	30	**15**	30
M1/D		**1.111**	**0.667**	**0.400**	**0.240**	0.400	0.400	0.400	0.400	0.400	**0.240**
M2/D		**0.347**	**0.208**	**0.125**	**0.075**	0.125	0.125	0.125	0.125	0.125	**0.075**
M3/D		**0.174**	**0.104**	**0.063**	**0.038**	0.063	0.063	0.063	0.063	0.063	**0.038**
M4/D		**0.111**	**0.067**	**0.040**	**0.024**	0.040	0.040	0.040	0.040	0.040	**0.024**
Re_D		100, 150	100, 150	50, 75, 100, 150, 200	100, 150	100	100	100	100	100	100, 150
Re_D 100	St	0.146	0.158	0.164	0.164	0.166	0.164	0.166	0.164	0.164	0.164
	C_D	1.271	1.313	1.335	1.332	1.354	1.343	1.359	1.331	1.322	1.331
Re_D 150	St	0.164	0.176	0.181	0.184	-	-	-	-	-	0.184
	C_D	1.262	1.304	1.316	1.319	-	-	-	-	-	1.317

to domain size and computational mesh differences for the numerical results of Persillion and Braza [149].

Three-dimensional computational mesh

From the results presented in Table E.1, either configuration A8 or A10 was extended into three-dimensions to construct the three-dimensional mesh. In the spanwise direction, mesh spacing was selected to be 0.1D for $Re_D \leq 150$, and 0.075D for $Re_D > 150$ based on the three-dimensional numerical simulations completed by Morton & Yarusevych [19].

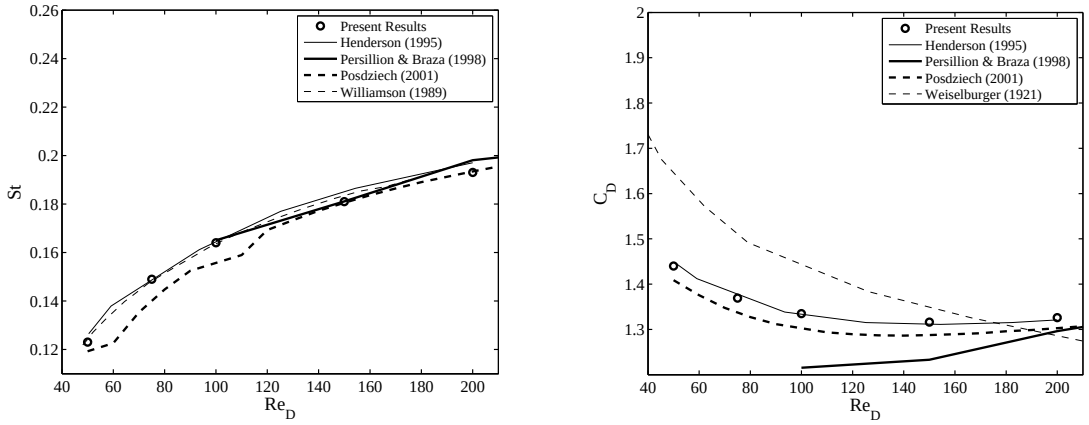

Figure E.3 Strouhal number and drag coefficient results for a two-dimensional uniform circular cylinder in comparison with experiments and other numerical studies [40,146,148,149].

Three-dimensional simulations on uniform circular cylinders in cross-flow

The computational domain and mesh used for three-dimensional numerical simulations on the cross flow over a uniform circular cylinder is shown in Figure E.4, with the extent and placement of the domain boundaries specified in the figure. The orientation of the coordinate system used for data presentation is depicted in Figure E.4, and its origin is located on the cylinder axis at the mid-span of the domain. The depth of the domain is extended to 10D in order to minimize the effects of the top and bottom free-slip wall boundary conditions, and is the same as that employed by Mittal [147]. Two Reynolds numbers were investigated, one corresponding to $Re_D = 100$, and the other at $Re_D = 300$. All numerical data presented were obtained following the onset of a quasi-steady vortex shedding in the wake of the cylinder. The acquired numerical data contained over twenty-five vortex shedding cycles for $Re_D = 100$, while a smaller data set of eight vortex shedding cycles was acquired for $Re_D = 300$. The results for these numerical simulations are presented in Appendix F.

Three dimensional simulations on dual step cylinders in cross-flow

Simulations on dual step cylinders were performed for $Re_D = 150$ & 180, D/d = 1.5 & 2, and L/D = 0.2, 0.25, 0.5, & 1.0. The computational domain used for the dual step cylinder numerical simulations

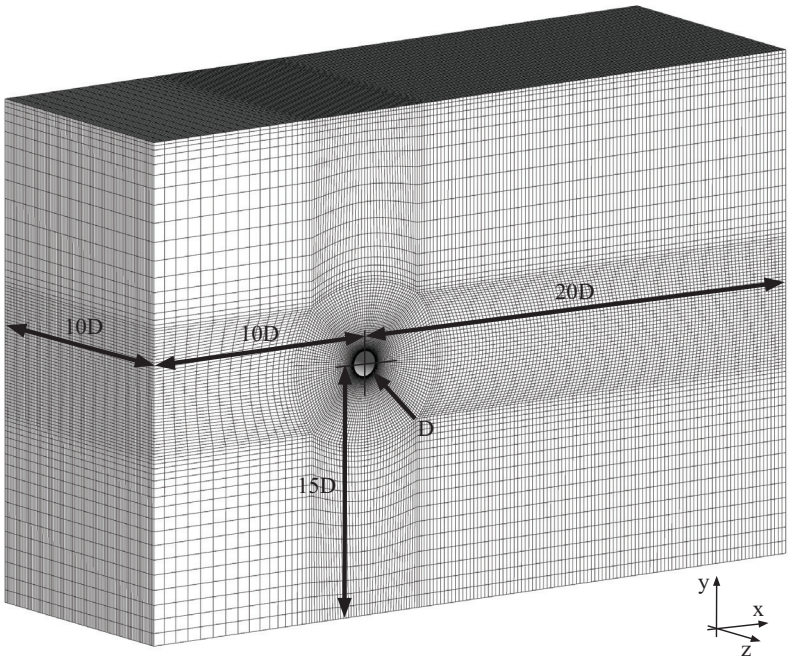

Figure E.4 Computational domain used for uniform cylinder simulations.

is shown in Figure E.5, with the extent and placement of the domain boundaries specified in the figure. The orientation of the coordinate system used for data presentation is depicted in the figure and its origin is located on the cylinder axis at the mid-span of the large cylinder. Near the stepwise discontinuities in diameter, the mesh density is increased to resolve boundary layer development on the flat ends of the large cylinder. This is achieved by following the methodology employed by Morton & Yaruseyvch [19], and is similar to that used by Persillon & Braza [149] and Mittal [147] for modeling the flow over a uniform circular cylinder. Specifically, spanwise mesh spacing and gradual relaxation away from the step is matched to those used in the radial direction near the cylinder surfaces (see mesh spacing M4 in Table E.1 for the precise values).

The spanwise extent of the domain for a dual step cylinder is governed by the extent of the small cylinders attached above and below the larger cylinder. Morton & Yarusevych [19] showed that the flow development for a single step cylinder is reproduced with a small cylinder aspect ratio of 5d. Numerical simulations were completed on a dual step cylinder for $Re_D = 150$, $D/d = 2$, and $L/D = 0.2$ for three different small cylinder aspect ratios: (i) 5d, (ii) 10d, and (iii) 20d. An analysis of the wake

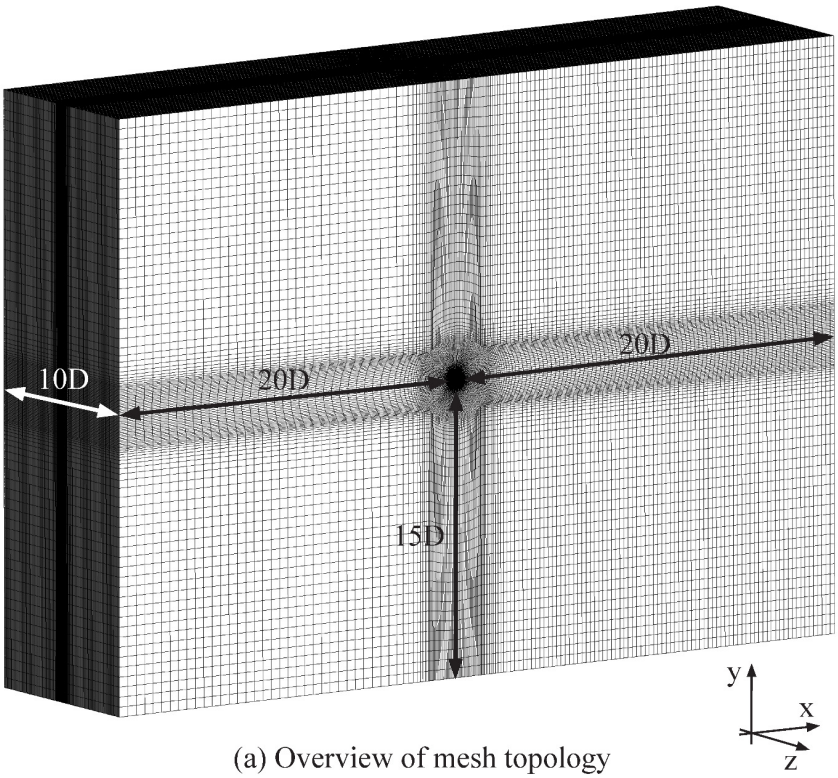

(a) Overview of mesh topology

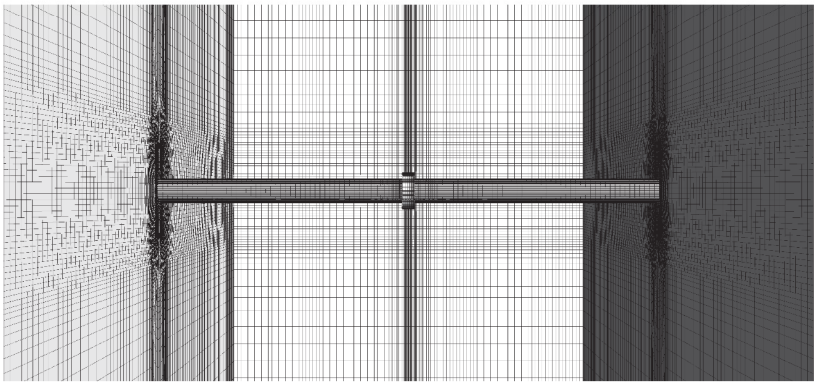

(b) Perspective view of model

Figure E.5 Computational domain used for dual step cylinder simulations at L/D = 0.5, D/d = 1.5, and Re_D = 150.

development showed that, downstream of the cylinder model, the wake topology is virtually identical for a small cylinder aspect ratio of 10d and 20d. Hence, the depth of the domain was selected so that each of the small cylinder regions occupy 10d, with the large cylinder of variable aspect ratio positioned at the mid-span of the domain between these small cylinder regions. All numerical data

presented were obtained following the onset of a quasi-steady vortex shedding in the wake. The results the numerical study are presented in the following sections, and a detailed investigation of the results for one dual step cylinder model (L/D = 0.5, D/d = 2, and Re_D = 150) are presented in Appendix G.

Numerical Data Analysis

Data is extracted from the numerical simulations to emulate the acquisition of planar velocity measurements through PIV. This is carried out by exporting data from the numerical simulation in prescribed planes, and interpolating the data from the original curvilinear grid (e.g., Figure E.4) into rectangular coordinates which are then averaged within simulated interrogations windows. The resulting planar velocity data is designed to match in spatial resolution with the experimentally acquired PIV measurements.

Velocity measurements are extracted from the numerical simulations to perform spectral analysis. Unless specified otherwise, the duration of velocity signals used for spectral analysis contained more than twenty vortex shedding cycles and provided a frequency resolution of ± 0.005 fD/U_∞, adequate to detect small changes in the shedding frequency.

Results

The numerical results are first compared with experimental findings of Williamson [16]. Figure E.6 shows a Q-criterion visualization of the wake vortex shedding for Re_D = 180, D/d = 1.5, and L/D = 0.25. A flow visualization image from Williamson [16], obtained at approximately the same instant in the vortex shedding cycle for the same flow conditions and geometry is shown in Figure E.6. Vortices are labeled in the figure in order to facilitate a comparison of the results. It can be seen that the overall flow topology is in good agreement, namely, the number of shed S and L vortices is the same (Figure E.6), and the position of these vortices in the wake is well matched. Vortex interactions between the S-cell and L-cell are also quite similar. In the near wake, cross boundary vortex connections, inclination of S-cell vortices, and vortex splitting occurs regularly (e.g., vortices S6, S7, and L4 illustrate such vortex interactions in Figure E.6a and Figure E.6b).

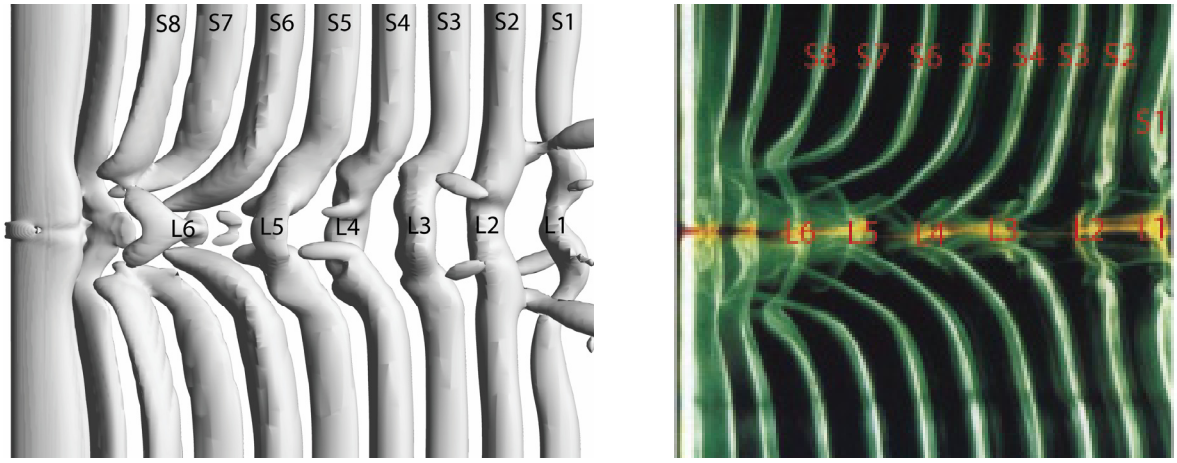

(a) (b)

Figure E.6 Vortex shedding in the wake of a dual step cylinder for $Re_D = 180$, L/D = 0.25, D/d = 1.5: (a) Isosurfaces of $Q \approx 7x10^{-4}$ (b) flow visualization image adapted from Williamson [16].

Due to the different vortex shedding frequencies, the vortices in the small cylinder wakes move in and out of phase with the vortex filaments in the large cylinder wake. During each 2π phase variation between large and small cylinder wake vortices, a vortex dislocations occurs [16]. The vortex dislocation frequency can be estimated from the number of S and L vortices involved in a 2π phase variation. Based on the results presented in Figure E.6, approximately 6 L-cell vortices are shed for every 8 S-cell vortices, giving the ratio of the L-cell and S-cell shedding frequencies $f_L/f_S \approx 6/8 = 0.75$.

Spectral analysis of velocity measurements was used to quantify the dominant frequency in the large and small cylinder wakes. Based on the numerical results pertaining to Figure E.6, the dimensionless shedding frequency in the small cylinder wakes is $f_S D/U \approx 0.170$, the large cylinder wake is $f_L D/U \approx 0.125$, and the dislocation frequency is $f_D D/U \approx 0.0045$. These values are in excellent agreement with quantitative measurements reported by Williamson [16]. In addition, the ratio of the shedding frequencies, f_L/f_S, matches that estimated from a count of the vortices in the wake region in Figure E.6.

Effect of geometric parameters on the dominant frequencies in the dual step cylinder wake

The effect of geometrical parameters (L/D and D/d) and the Reynolds number on the vortex dynamics in the large cylinder wake was investigated. Although the effect of D/d and Re_D on the flow development over dual step cylinders has been studied by Williamson [16], simulations for different

Table E.2 Comparison of simulation results with Williamson [16] for different Re_D and D/d. The presented results are for L/D = 0.5.

			Re_D					
			150			180		
			f_SD/U_∞	f_LD/U_∞	f_DD/U_∞	f_SD/U_∞	f_LD/U_∞	f_DD/U_∞
Simulation Results	*D/d*	1.5	-	-	-	0.167	0.123	0.043
		2.0	0.143	0.095	0.047	0.153	0.105	0.047
Williamson (1992)	*D/d*	1.5	-	-	-	0.169	0.125	0.044
		2.0	0.145	0.097	0.048	0.155	0.106	0.048

D/d and Re_D were completed for validation of the present numerical results. The results are shown in in Table E.2, where the vortex shedding frequency in the small cylinder wake, vortex shedding frequency in the large cylinder wake, and frequency of vortex dislocations are shown. In agreement with Williamson [16], the numerical results in Table E.2 show that the frequency of the L-cell increases and the frequency of vortex dislocations decreases with decreasing D/d. The Reynolds number appears to have an insignificant effect on the frequency of vortex dislocations (Table E.2). However, the results of Williamson [16], obtained for a wider range of Reynolds numbers, indicate that the dislocation frequency follows a trend similar to that observed for a uniform circular cylinder.

Figure E.7 shows the variation of L-cell frequency and vortex dislocation frequency with L/D for Re_D = 150 and D/d = 2. The results of Williamson [16] corresponding to L/D = 0.25 are shown for

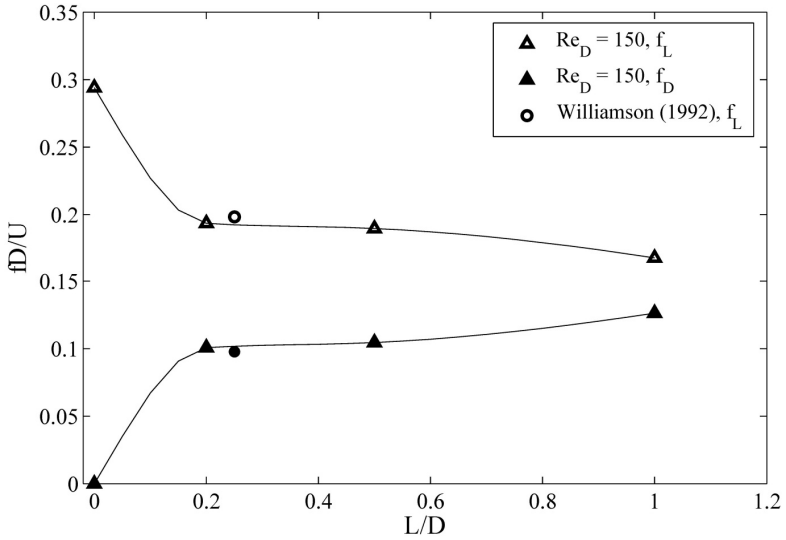

Figure E.7 Variation of the L-cell frequency and dislocation frequency with L/D.

comparison. The numerical results show that the L-cell frequency decreases and the dislocation frequency increases with increasing L/D. This agrees with the experimental results obtained in the present investigation (Chapter 4) at much higher Reynolds numbers.

Appendix F
Extracting three-dimensional coherent structures from time-resolved planar PIV measurements in the wakes of circular cylinders

The aim of this combined experimental-numerical study, is to use traditional phase-averaging methodologies in order to reconstruct the three-dimensional wake characteristics of circular cylinders immersed in a shear flow. For the numerical simulations, details of the numerical solver, computational domain, and boundary conditions are described in Appendix E. At the inlet of the domain, a shear flow profile is $(u, v, w) = (U_\infty + 0.01U_\infty\, z/D\,, 0,0)$ is applied, with the free stream velocities investigated corresponding to a Reynolds number of 100 and 300. For the experiments, the free stream speed corresponds to a Reynolds number of 2100, and the velocity gradient in the test section is approximately 5%.

Oblique vortex shedding in the wake of a uniform circular cylinder

Figure F.1a and Figure F.1b illustrate the instantaneous wake topology of a circular cylinder in a uniform shear flow for Re_D = 100 and 300, respectively. In the images, isosurfaces of spanwise vorticity (dark gray) visualize obliquely shed spanwise vortices. For Re_D = 300 (Figure F.1b), smaller-scale structures are visualized by isosurfaces of streamwise vorticity (lighter gray). The formation of these structures and their average spanwise wavelength agree with previous investigations [30].

The following LDV and PIV measurements were extracted from the numerical simulation: (i) Measurement of a reference wake velocity signal with an LDV probe was simulated by exporting the streamwise velocity component, *U*, from a fixed location downstream of the cylinder, (*x/D*, *y/D*, *z/D*) = (5, 0.75, 3), for each time step, (ii) The acquisition of time-resolved, two-dimensional PIV data was simulated by exporting *u* and *v* wake velocity data from five planes corresponding to *z/D* = -1.0, -1.5, -2.0, -2.5, and -3.0, as shown with dashed lines in Figure F.1. For each plane, the velocity data were extracted so that the resolution roughly matched that of experimentally acquired PIV

measurements which will be discussed in detail in the following sections. The numerical data were interpolated from the original curvilinear grid into rectangular coordinates and averaged within simulated interrogation windows. Thus, from each of the two numerical simulations, the data extracted for analysis imitated the simultaneous experimental acquisition of a reference LDV signal at a fixed location and PIV data in five distinct planes.

Note that, due to the imposed boundary conditions, vortex filaments are deformed slightly near the top and bottom boundaries of the computational domain; however, this effect is confined to a narrow region and does not affect vortex filaments away from the boundaries where the measurement planes are located. In the simulations for $Re_D = 100$, the angle of shedding remained approximately constant (Figure F.1a). In contrast, for $Re_D = 300$, small variations in the shedding angle occurred from cycle to cycle due to spanwise deformations of vortex filaments (Figure F.1b). Also, larger variations in the shedding angle, on the order of 30˚, occurred in the flow. Although such substantial variations may be attributed to the relatively short cylinder aspect ratio employed in the simulations, they serve to emulate comparable variations in the shedding angle observed in the experiment.

The aim of the analysis of numerical and experimental results is to reconstruct the dominant three-dimensional coherent structures in the wake region for $-3.0 \leq z/D \leq -1.0$ using the five sets of planar velocity data and the single point velocity reference signal. The following two phase-averaging methods are considered in the present work. The 'LDV-based' method relies solely on the reference LDV signal to phase average the PIV data in each plane, and reconstruct the three-dimensional flow topology. The 'POD-based' method uses a local reference signal obtained for each local PIV plane via POD analysis, and the LDV reference signal. The local reference signal is used to phase average planar velocity data, and the LDV reference is used to estimate the phase variation between the measurement planes.

In the LDV-based method, for a given PIV plane, post processing of the LDV signal was used to estimate the phase of vortex shedding. Specifically, all reference signals were reconstructed using one hundred Fourier modes pertaining to a frequency-band of $0.2f_s$ centered at the vortex shedding frequency (f_s). A Hilbert transform was performed on the reconstructed signals to determine the phase

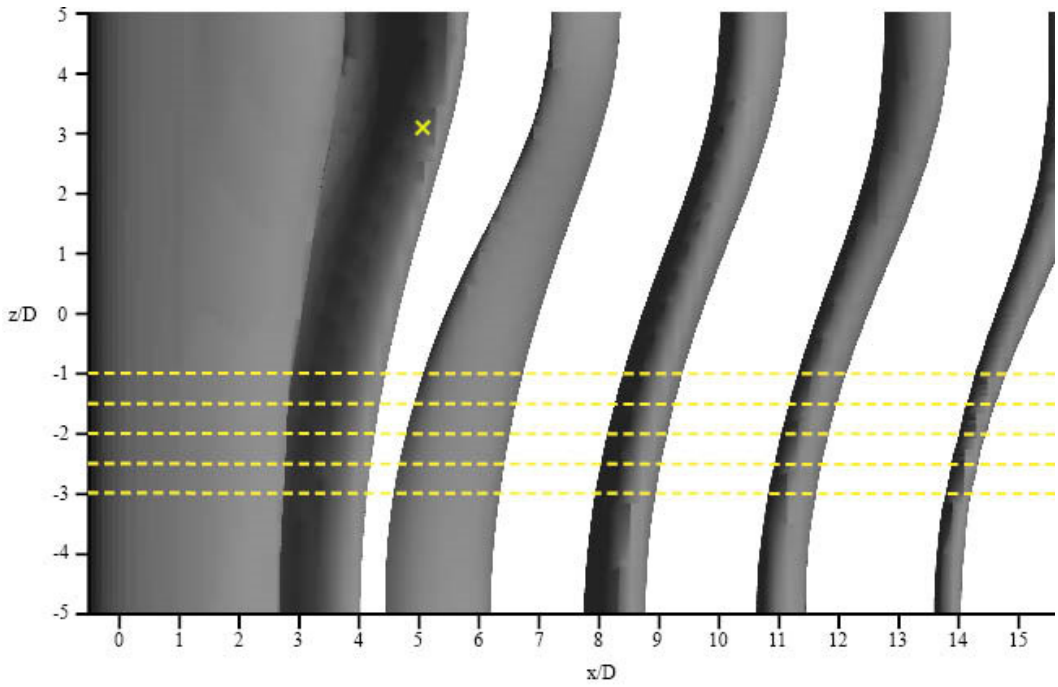

(a) $Re_D = 100$

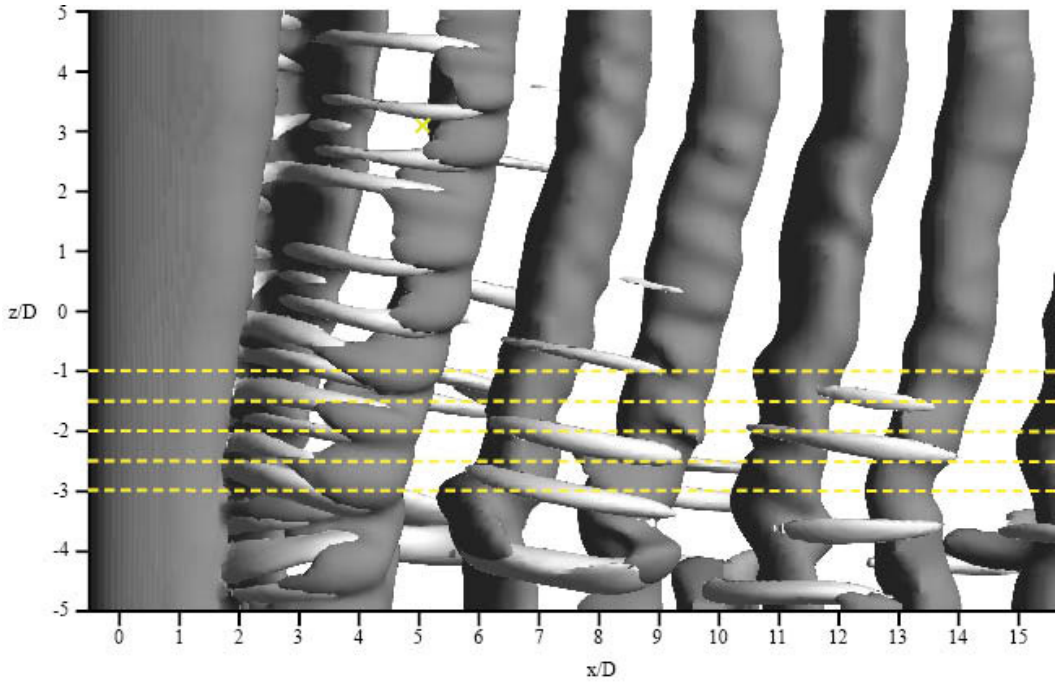

(b) $Re_D = 300$

Figure F.1 Oblique vortex shedding in the wake of a circular cylinder: (a) $Re_D = 100$ and (b) $Re_D = 300$. Dashed horizontal lines identify the planes where data acquisition via PIV is simulated, and 'x' identifies the location where data acquisition via LDV is simulated.

angle. Similar signal processing methodologies have been used for obtaining a phase reference in turbulent flows with hot-wire and surface pressure measurements (e.g., [25,48]). Using the phase reference, PIV snapshots in each plane are assigned a distinct phase angle and sorted. Twenty four phase angle bins are used, with a bin width of five degrees and a bin separation of fifteen degrees. Note that PIV snapshots associated with phase angles outside of the selected bins are not used in the analysis. Within each bin, PIV data are averaged to give a phase- averaged representation of vortex shedding in a given plane. Then, the phase-averaged planar fields are meshed using a cubic spline interpolation in order to reconstruct the three-dimensional phase-averaged wake topology.

In the POD-based method, a local phase reference signal is obtain in each plane from POD analysis of the planar velocity data [22,26], following the methodology presented in Chapter 3.3. It must be stressed that, inherent to the energy-based phase decomposition, a given phase angle corresponds to the same instant in the shedding cycle across all planes. Thus, in order to resolve any possible phase variations across the span, such as that expected in the selected test case of a cylinder in shear flow, an external reference signal is required. Here, the relative phase shift between the planar fields is obtained by comparing the LDV reference signal to the local temporal coefficient reference signal. The mean difference in the phase angle between these two reference signals is used to adjust the phase of planar PIV data. Once all five planes have been adjusted, the planes are meshed using a cubic spline interpolation in order to reconstruct the three-dimensional phase-averaged wake topology.

The simulated PIV measurements were phase-averaged using the LDV-based and POD-based techniques, as outlined above. Phase-averaged flow images corresponding to $\theta = 0^{\circ}$ are shown in Figure F.2a-b and Figure F.3a-b for $Re_D = 100$ and 300, respectively. Representative instantaneous spanwise vorticity isosurfaces from the corresponding phase bin are shown in Figure F.2c and Figure F.3c for comparison. It can be seen that the phase-averaged results obtained with the two techniques successfully capture the oblique nature of the shedding for both Reynolds numbers. For $Re_D = 100$ (Figure F.2), the two techniques produce equivalent results, with minor differences between the phase-averaged and instantaneous vorticity fields attributed primarily to the discrete size of the phase angle bins. For $Re_D = 300$ (Figure F.3), the spanwise deformations of the vortex cores, induced by the streamwise vortices (Figure F.3c) are, as expected, smoothed in the phase-averaged reconstructions.

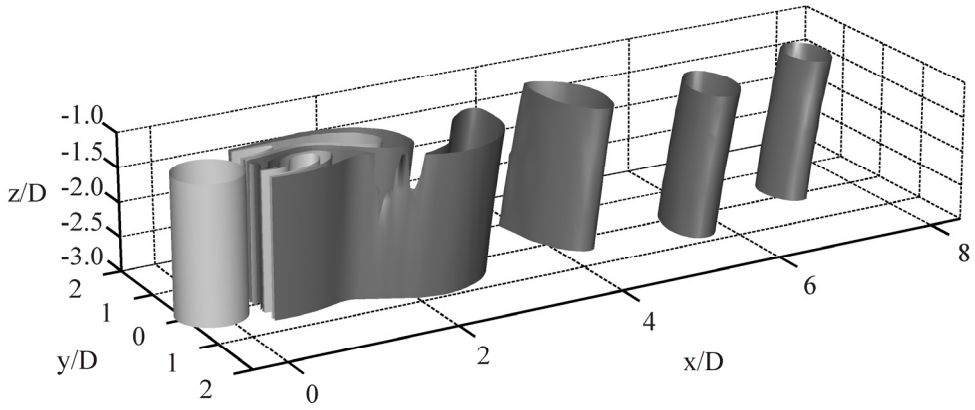

(a) LDV-based

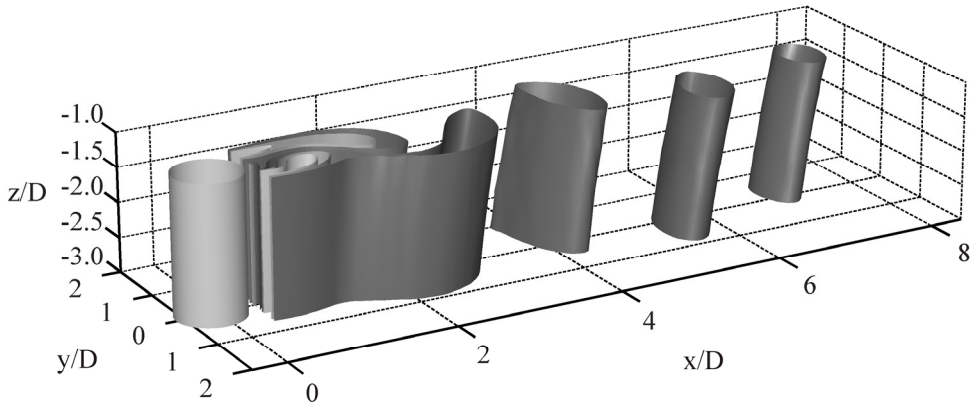

(b) POD-based

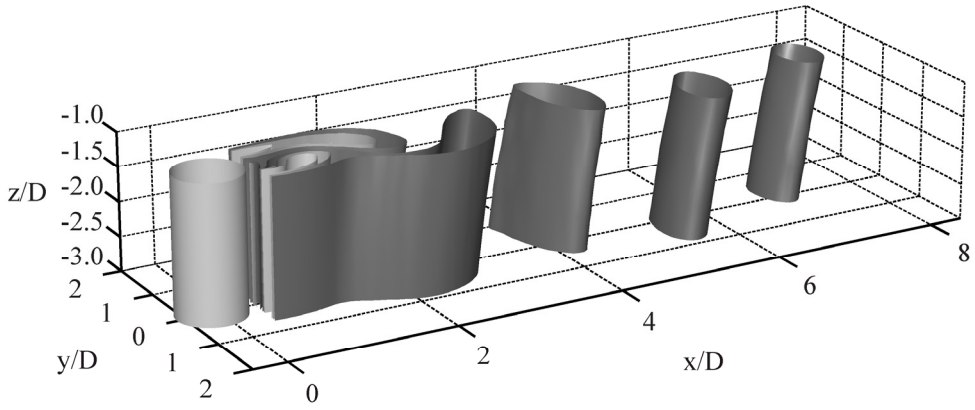

(c) Instantaneous flow

Figure F.2 Isosurfaces of spanwise vorticity constructed from five PIV planes at $Re_D = 100$ for $\theta = 0^\circ$: (a) phase-averaged results for LDV-based technique, (b) phase-averaged results for POD-based technique, and (c) instantaneous flow.

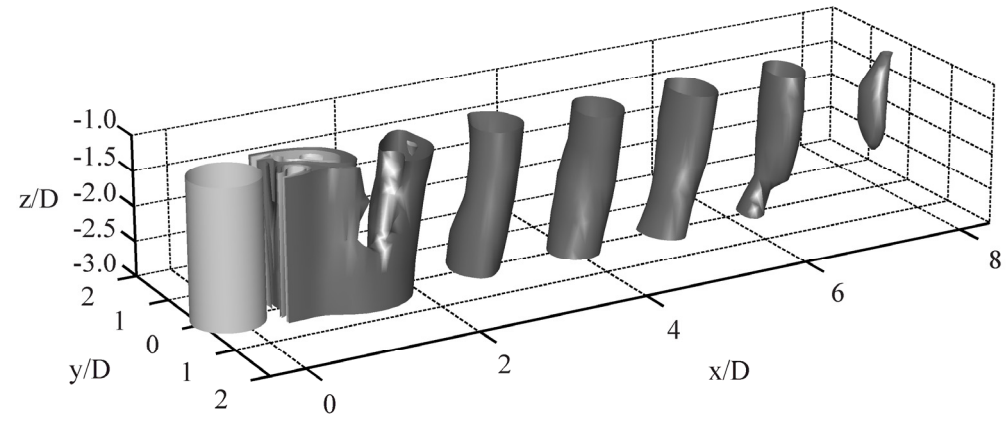

(a) LDV-based

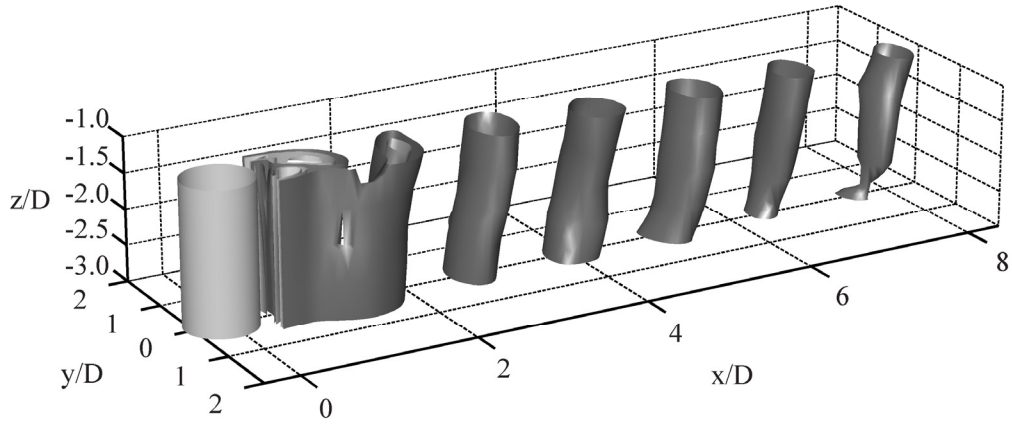

(b) POD-based

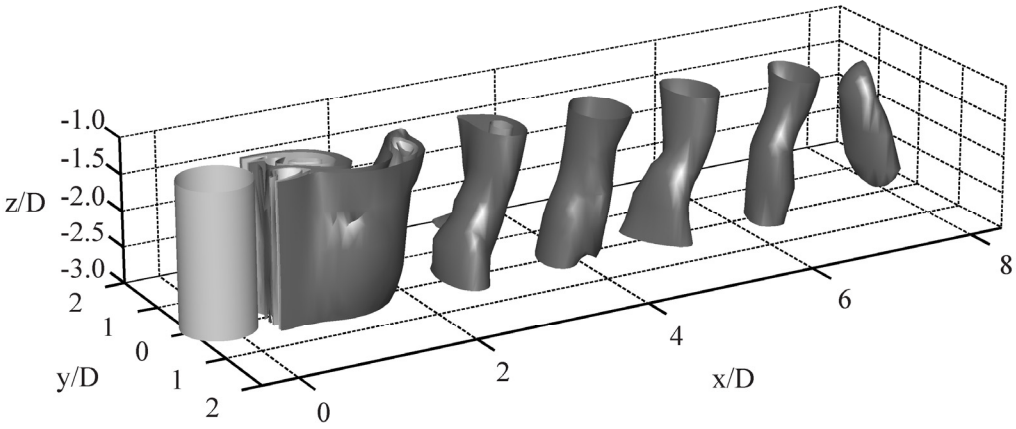

(c) Instantaneous flow

Figure F.3 Isosurfaces of spanwise vorticity constructed from five PIV planes at $Re_D = 300$ and $\theta = 0^\circ$: (a) phase-averaged results for LDV-based technique, (b) phase-averaged results for POD-based technique, and (c) instantaneous flow.

Also, the LDV-based results appear to have a higher rate of vorticity decay compared to both POD-based phase-averaged and instantaneous results for this Reynolds number.

In order to assess the two phase averaging methods, the variation between instantaneous fields and phase-averaged results within each phase bin was analyzed. First, the phase-averaged vorticity field for a given bin is subtracted from each of the instantaneous vorticity fields in that bin. The circulation of each of the resulting residual vorticity fields, Γ, is then computed as follows:

$$\Gamma = \iint_A (\omega - \hat{\omega}) dA \tag{F-1}$$

where ω is the spanwise vorticity of an instantaneous velocity field, $\hat{\omega}$ is the phase-averaged vorticity for the corresponding phase angle bin, A is the area of the measurement plane. The normalized standard deviation of the residual circulations, ε, is then computed for each bin using Equation (F-3).

$$\boldsymbol{\varepsilon = \frac{1}{\hat{\Gamma}} \sqrt{\frac{1}{(N-1)} \sum_{i=1}^{N} (\Gamma_i - \bar{\Gamma})^2} \times 100\%} \tag{F-2}$$

where $\hat{\Gamma}$ is the circulation of the phase-averaged vorticity field, $\bar{\Gamma}$ is the average circulation of all residuals, and N is the total number of fields in the corresponding phase angle bin. The results of this analysis are illustrated in Table F.1 for each planar location at $\theta = 0^{\circ}$. For $Re_D = 100$, both techniques are associated with a comparably low deviation between the corresponding instantaneous and phase-averaged flow fields. For $Re_D = 300$, the discrepancy becomes more substantial, as there are more significant cycle-to-cycle variations between the instantaneous fields. Nevertheless, the POD-based method shows a considerable improvement over the LDV-based method.

The observed improvement in the phase-averaged reconstructions using the POD-based technique at $Re_D = 300$ is attributed to two factors affecting the accuracy of phase estimation. As shown by Perrin et al. [22], phase-jitter effects caused by the use of an external reference signal in turbulent flows are virtually eliminated in phase averaging with POD techniques, which is done independently in each measurement plane here. Second, there is an adverse effect due to cycle-to-cycle variations in

the phase angle along the cylinder span. Figure F.4 shows a plot of the absolute difference between the phase angle obtained from the LDV reference signal (θ_{LDV}) and that computed form the POD temporal coefficient signal (θ_{POD}) for Re_D = 100 (Figure F.4a) and Re_D = 300 (Figure F.4b). The phase difference is defined as follows for a given plane:

$$\Delta\boldsymbol{\theta} = |\boldsymbol{\theta_{LDV}} - \boldsymbol{\theta_{POD}}| \tag{F-3}$$

As shown in Figure F.4a, $\Delta\theta$ fluctuates within ±2.5˚ at every z/D location for Re_D = 100. The difference in mean $\Delta\theta$ values between two planes relates to the average angle of vortex shedding in the corresponding spanwise region. In contrast to the case of Re_D = 100, significant temporal changes in $\Delta\theta$ occur for Re_D = 300 (Figure F.4b), reflecting substantial cycle-to-cycle changes in the orientation of vortex filaments. Under such conditions, the LDV-based technique will accumulate errors by placing some instantaneous velocity fields into incorrect phase bins across the cylinder span. This is mitigated in the POD-based technique by the relative phase adjustment performed for each measurement plane based on the time-averaged phase difference in $\Delta\theta$ for this plane, leading to the improved phase estimation reflected in Table F.1.

The ability to estimate the relative phase difference between two adjacent measurement planes in the POD-based technique provides added insight into the flow development. In particular, it allows estimating the average physical angle of vortex filaments (α) between the two planes. Using the convective velocity of the wake vortices (U_c) and the local Strouhal number ($St = f_s D/U_0$), the streamwise spacing between consecutive wake vortices, L, can be computed as follows.

$$\boldsymbol{L} = \frac{\boldsymbol{U_c}}{\boldsymbol{f_s}} = \frac{\boldsymbol{U_c \cdot D}}{\boldsymbol{U_0 \cdot St}} \tag{F-4}$$

Given the spacing between adjacent PIV planes, Δz, the physical angle of the vortex shedding given by:

$$\boldsymbol{\alpha} = \boldsymbol{atan}\left[\frac{\boldsymbol{2\pi\Delta z}}{(\overline{\boldsymbol{\Delta\theta_1}} - \overline{\boldsymbol{\Delta\theta_2}})\boldsymbol{L}}\right] \tag{F-5}$$

where $\overline{\Delta\theta_1}$ and $\overline{\Delta\theta_2}$ are the time-averaged phase differences for the two selected PIV planes. Estimates of the vortex shedding angle were found to be in agreement with instantaneous flow visualization images (e.g., Figure F.1).

Oblique vortex shedding in the wake of a uniform circular cylinder at $Re_D = 2100$

The flow past a uniform cylinder in a uniform shear flow is depicted in Figure F.5 with a sequence of hydrogen bubble flow visualization images. Also shown in Figure F.5a are the approximate locations of the PIV measurement planes (marked by dashed lines) and the LDV measurement volume (marked by an 'x'). In the image sequence, the hydrogen bubbles trace the vortex cores and illustrate that vortex shedding occurs at an angle relative to the cylinder axis, similar to that seen for Re_D = 100 and 300. Analysis of flow visualization video records revealed that there are substantial temporal variations in the angle of vortex shedding due to the occurrence of vortex dislocations in the wake.

TR-PIV measurements were first performed in a single horizontal plane at z/D = 0 (Figure 3.4) for Re_D = 1050 and 2100. For the uniform cylinder model at Re_D = 2100, additional sets of measurements was also performed whereby the horizontal plane was traversed to five evenly spaced spanwise locations in the range $-2.0 \leq z/D \leq 0$. During these planar measurements, LDV measurements were acquired simultaneously at a fixed location in the wake located at ($\Delta x/D$, $\Delta y/D$, $\Delta z/D$) = (5, 0.75, 3), as depicted in the figure.

Table F.1 Relative variation between instantaneous and phase-averaged vorticity fields for Re_D = 100 and Re_D = 300 at $\theta = 0^\circ$.

	ε (%)			
	LDV-based Phase Averaging		**POD-based Phase Averaging**	
z/D	**Re_D = 100**	**Re_D = 300**	**Re_D = 100**	**Re_D = 300**
-1	2.9	17.4	2.0	10.0
-1.5	2.6	18.2	2.1	10.5
-2	1.9	16.3	1.9	9.6
-2.5	2.9	16.9	1.8	9.8
-3	1.8	17.7	1.8	10.1

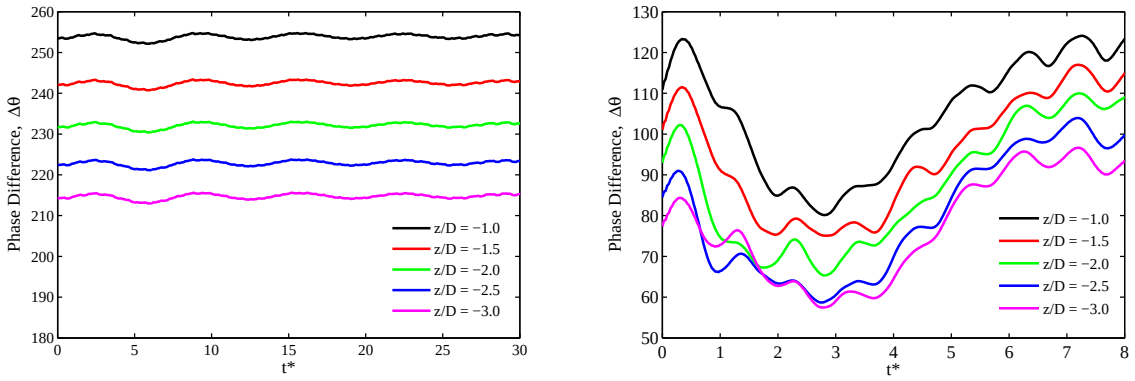

(a) $Re_D = 100$ (b) $Re_D = 300$

Figure F.4 Phase angle difference between the LDV reference signal and POD temporal coefficient signal at each z/D location. t^* is the number of vortex shedding periods.

Phase-averaged flow reconstructions for $\theta = 0^\circ$ are shown in Figure F.6. While both techniques are able to capture the oblique nature of the shedding in the vortex formation region, the POD-based technique (Figure F.6b) provides an improved reconstruction of the shed vortical structures in the near wake. Utilizing the same analysis performed for the numerical results, the degree of relative deviation

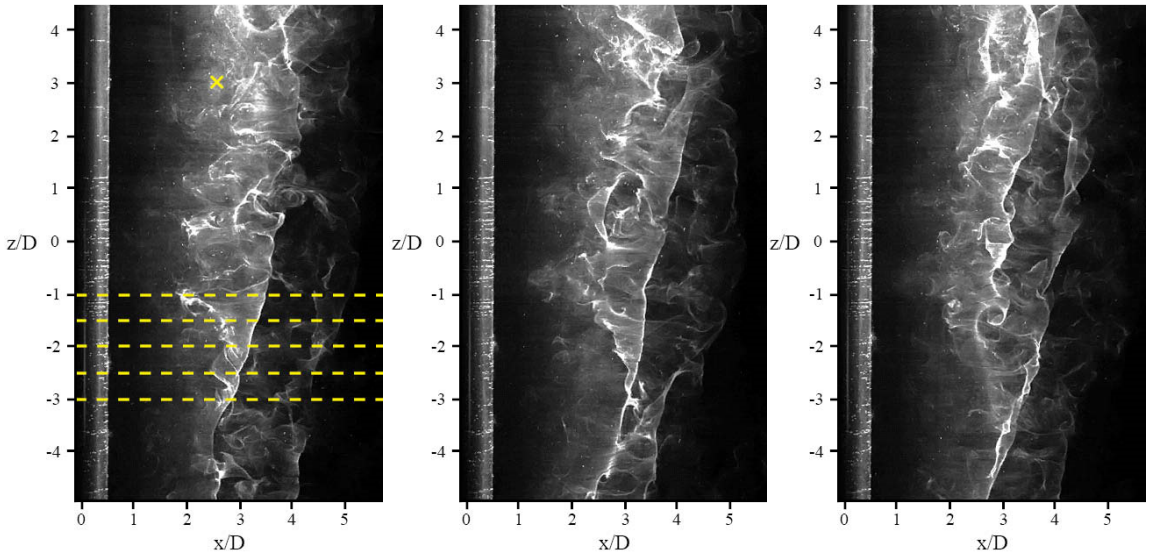

(a) $t^* = 0$ (b) $t^* = 0.9$ (c) $t^* = 1.1$

Figure F.5 Hydrogen bubble flow visualization in the wake of a uniform circular cylinder at $Re_D = 2100$. t^* is the number of vortex shedding periods

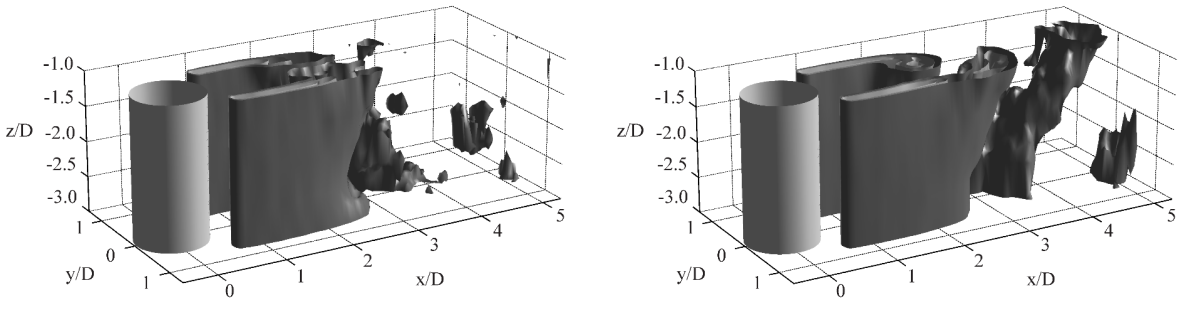

Figure F.6 Phase averaged isosurfaces of spanwise vorticity constructed from meshing five PIV planes in the wake of a uniform circular cylinder at $Re_D = 2100$: (a) LDV-based technique, (b) POD-based technique.

between planar instantaneous and phase-averaged flow fields was assessed for each phase bin. The results are illustrated in Table F.2 for $\theta = 0^\circ$. The data suggest that the POD-based technique leads to a significantly lower deviation compared to the LDV-based method, which is attributed to the improved phase estimation. Moreover, for the LDV-based results, the deviation increases substantially as the spanwise distance between the LDV measurement volume and the PIV plane increases. As a consequence, the LDV method leads to a less accurate reconstruction of the wake topology (Figure F.6). Comparing the results in Table F.1 and Table F.2, it can be seen that both techniques are associated with significantly higher deviations between instantaneous and phase averaged results for $Re_D = 2100$. This is attributed primarily to the following three factors: (i) substantial cycle-to-cycle variations in the strengths of vortices shed from the cylinder in the turbulent shedding regime [122]; (ii) additional temporal variations in the vorticity fields due to the passage of vortex dislocations, associated with vortex splitting and out of plane deformations of vortex filaments [150]; (iii) inherent experimental uncertainties in both PIV and LDV measurements, which are amplified in the computations of vorticity fields. On the other hand, these factors lead to more severe phase-jitter effects and cycle-to-cycle variations in the phase angle at each plane. As the POD-based technique is less susceptible to these adverse effects, more significant differences are observed between the results obtained with the two phase averaging techniques for $Re_D = 2100$ than for the lower Reynolds numbers (cf., Table F.1 and Table F.2).

As discussed earlier, the superior performance of the POD-based technique is due to the improved phase estimation for each measurement plane. Figure F.7 shows a representative temporal variation of

Table F.2 Relative variation between instantaneous and phase-averaged vorticity fields for $Re_D = 2100$ at $\theta = 0^\circ$.

	ε (%)	
z/D	LDV-based Phase Averaging	POD-based Phase Averaging
-1	55.9	38.1
-1.5	64.7	38.8
-2	86.1	36.7
-2.5	129.2	35.9
-3	192.1	34.0

the difference in phase angle between the LDV and POD-based reference signals at z/D = -1.0. Compared to the numerical results, there are more substantial fluctuations in the phase difference, and they occur on shorter time scales, i.e., every few vortex shedding cycles. Agreeing with flow visualization results, the observed fluctuations in $\Delta\theta$ reflect cycle-to-cycle changes in the angle of vortex shedding filaments. Since the relative phase difference between the planar PIV measurements is adjusted using the time average of $\Delta\theta$, it is important to ensure that a sufficiently long sample of data is acquired to adequately calculate this parameter. Figure F.7 shows a plot of the cumulative average of $\Delta\theta$ for all z/D planes investigated. The results indicate that, for the conditions investigated here, over 50 vortex shedding cycles must be captured in order to properly estimate the average difference in phase and average shedding angle.

The results in Figure F.7 suggest that, for planes separated by large spanwise distances, e.g., larger than the distance between planes at z/D = -1.0 and -3.0 in Figure F.7b, it is possible for the mean phase difference to exceed 2π radians. For a mean phase difference greater than 2π, e.g., $\Delta\theta \approx 2\pi + \pi/4$, the phase can be incorrectly interpreted as $\Delta\theta \approx \pi/4$. To avoid this problem, the spanwise spacing between adjacent PIV planes must be kept sufficiently small. If the phase variation along the span is roughly known, Equation (F-5) can be re-arranged to obtain the minimum required spacing between two PIV planes, Δz.

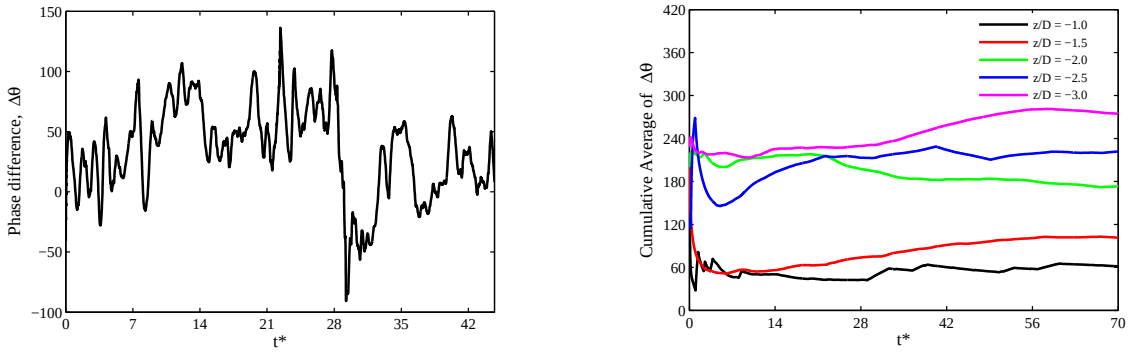

(a) (b)

Figure F.7 Phase angle difference between the LDV reference signal and POD temporal coefficient signal: (a) at z/D = -1.0, (b) cumulative average for all z/D planes.

Discussion

A new POD-based phase averaging technique has been proposed for extracting dominant three-dimensional wake characteristics based on time-resolved two-dimensional PIV measurements. The technique relies on extracting the phase signal in each measurement plane from the Proper Orthogonal Decomposition (POD) of planar PIV data. The relative phase between planar phase-averaged fields is established using a reference LDV signal. The method has been compared with a classical phase averaging approach that uses a reference wake velocity signal measured at a fixed location with Laser Doppler Velocimetry (LDV). The two techniques have been evaluated using the results of numerical simulations and experiments on the flow past a circular cylinder immersed in a uniform shear flow at Re_D = 100, 300, and 2100.

The results show that both techniques are able to reconstruct the oblique vortex shedding patterns equally well in the laminar cylinder wake at Re_D = 100. However, when spatial and temporal variations appear in the flow field at higher Re_D, the POD-based approach is shown to produce superior results. This is attributed to the ability of the POD-based method to mitigate adverse effects of phase jitter and cycle-to-cycle variation in shedding angle, leading to improved estimation of the phase. The experimental results also reveal that, for adequate estimation of the relative angle between the adjacent PIV planes, a relatively large number of samples is required.

Appendix G
A POD-Analysis of planar velocity measurements in dual step cylinder wakes

A numerical study on the flow development past a dual step cylinder was completed to extend on the techniques of phase-averaging and three-dimensional reconstruction developed in Appendix F. The goal of the study is to emulate the extraction of planar PIV data in multiple closely spaced planes, and use a POD analysis of the PIV data to extract the phase variation of the dominant vortical structures in the small and large cylinder wakes. The numerical study was completed for Re_D = 150, D/d = 2, and L/D = 0.5. Details of the numerical setup are described and a validation of the numerical results are presented in Appendix E with a comparison to the experimental results of Williamson [16]. Overall, the simulations captured over 40 small cylinder vortex shedding cycles. Flow field data was captured at a rate of four times the small cylinder vortex shedding frequency.

Overview of the flow development

Figure G.1 shows a sequence of images illustrating the wake development. The results in Figure G.1 depict vortical structures shed from the small diameter cylinders connecting across the large cylinder wake, for example, small cylinder vortices connect across the large cylinder wake for x/D < 11 in Figure G.1a, and also show consecutive small cylinder vortices forming half-loop connections as part of a vortex dislocation, for example, x/D =4-7 in Figure G.1d. The present numerical results agree well with the flow visualizations performed by Williamson [16]. Williamson [16] proposed a model of vortex dynamics in the dual step cylinder wake based on the relative strengths of the vortices shed from the large and small cylinders and their corresponding shedding frequencies. Based on this model, it is speculated that the wake vortex dynamics can be predicted based on an analysis reference signals pertaining the small cylinder

vortex shedding, the large cylinder vortex shedding, and the corresponding vortex dislocation frequency.

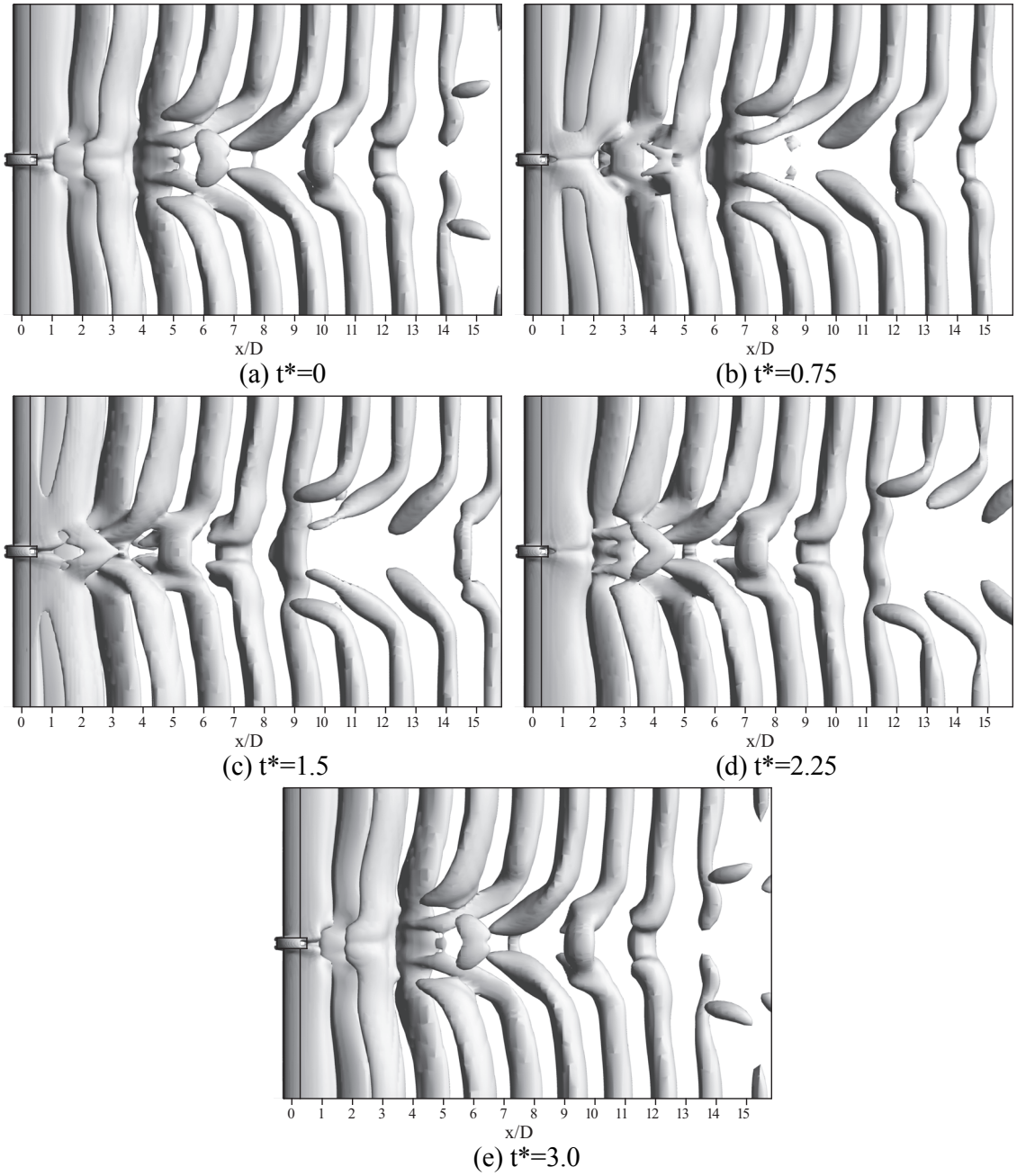

Figure G.1 Vortex shedding in the wake of a dual step cylinder. Vortices are visualized using isosurfaces of Q = 0.025. t* is the number of small cylinder shedding cycles.

PIV data extraction and POD analysis

PIV measurements were extracted from the numerical results in order to perform a POD analysis. The aim of the POD analysis is to obtain phase reference signals for the phase variation of the dominant coherent structures in the wake. The following planar measurements were extracted from the simulation: (i) the acquisition of time-resolved, two-dimensional PIV data in the x-z plane was simulated by exporting *u* and *w* wake velocity data at y/D = 0.5 (Figure G.2), (ii) the acquisition of time-resolved, two-dimensional PIV data in x-y planes was simulated by exporting *u* and *v* wake velocity data for discrete planes in the range $-3.0 \leq z/D \leq 0$. For each plane, velocity data were extracted so that the spatial resolution of velocity vectors matched that of experimentally acquired PIV measurements, with a vector pitch of about 0.06D (see Chapter 3 for details). The data were interpolated from the original curvilinear grid into rectangular coordinates and averaged within simulated interrogation windows. Thus, from the numerical simulations, the data extracted for analysis imitated the simultaneous experimental acquisition of planar PIV in a single x-z plane and multiple x-y planes.

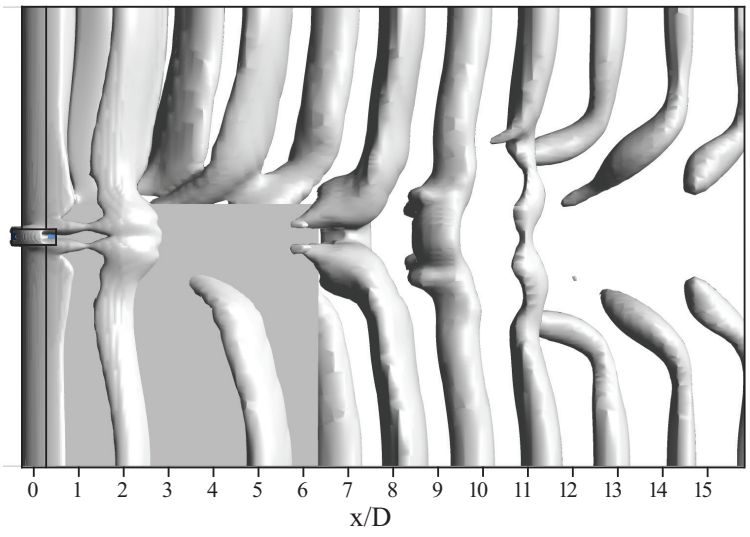

Figure G.2 Planar region used for emulating PIV measurements in the x-z planes. Vortices are visualized using isosurfaces of Q = 0.025.

Figure G.2 also shows an instantaneous snapshot of the vortex topology using Q-criterion isosurfaces, illustrating that the selected x-z plane extends beyond the vortex formation region in both the large and small cylinder wakes. POD analysis was performed on the velocity data obtained from the x-z plane shown in Figure G.2, and the results are shown in Figure G.3 to Figure G.5. Figure G.3 shows the distribution of energy content across the POD modes. For the first six modes, the energy is distributed into pairs of nearly equal energy content (Figure G.3a), and the cumulative energy content of these modes is over 95% of the overall energy content (Figure G.3b). The results in Figure G.4 and Figure G.5 show the first six spatial eigenfunctions and corresponding temporal coefficients. Three mode pairs are formed[1] with the first two and third and fourth modes forming pairs which contain fluctuations at both the large and small cylinder shedding frequencies (Figure G.5). The fifth and sixth modes form a pair containing wake energy fluctuations that occur at the vortex dislocation frequency (Figure G.5). The coherent structure associated with the vortex dislocation frequency (Figure G.4c and Figure G.4d) is a large scale structure with a long wavelength, indicating that this mode is associated with a low frequency

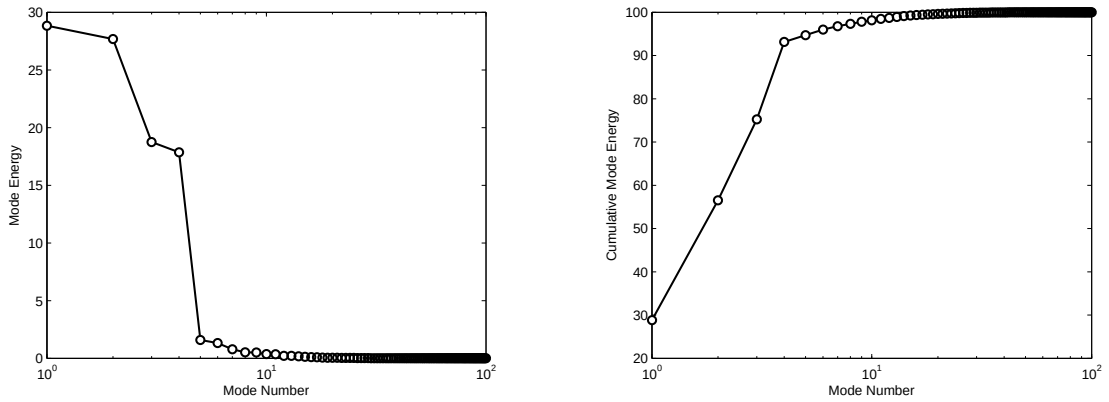

(a) (b)

Figure G.3 Distribution of wake energy content: (a) mode energy distribution, (b) cumulative mode energy distribution.

[1] A mode pair exists if the two temporal coefficient signals match when phase-shifted by $\pi/2$ radians, and the corresponding spatial modes match with a spatial shift of one half the wavelength of the spatially periodic coherent structure.

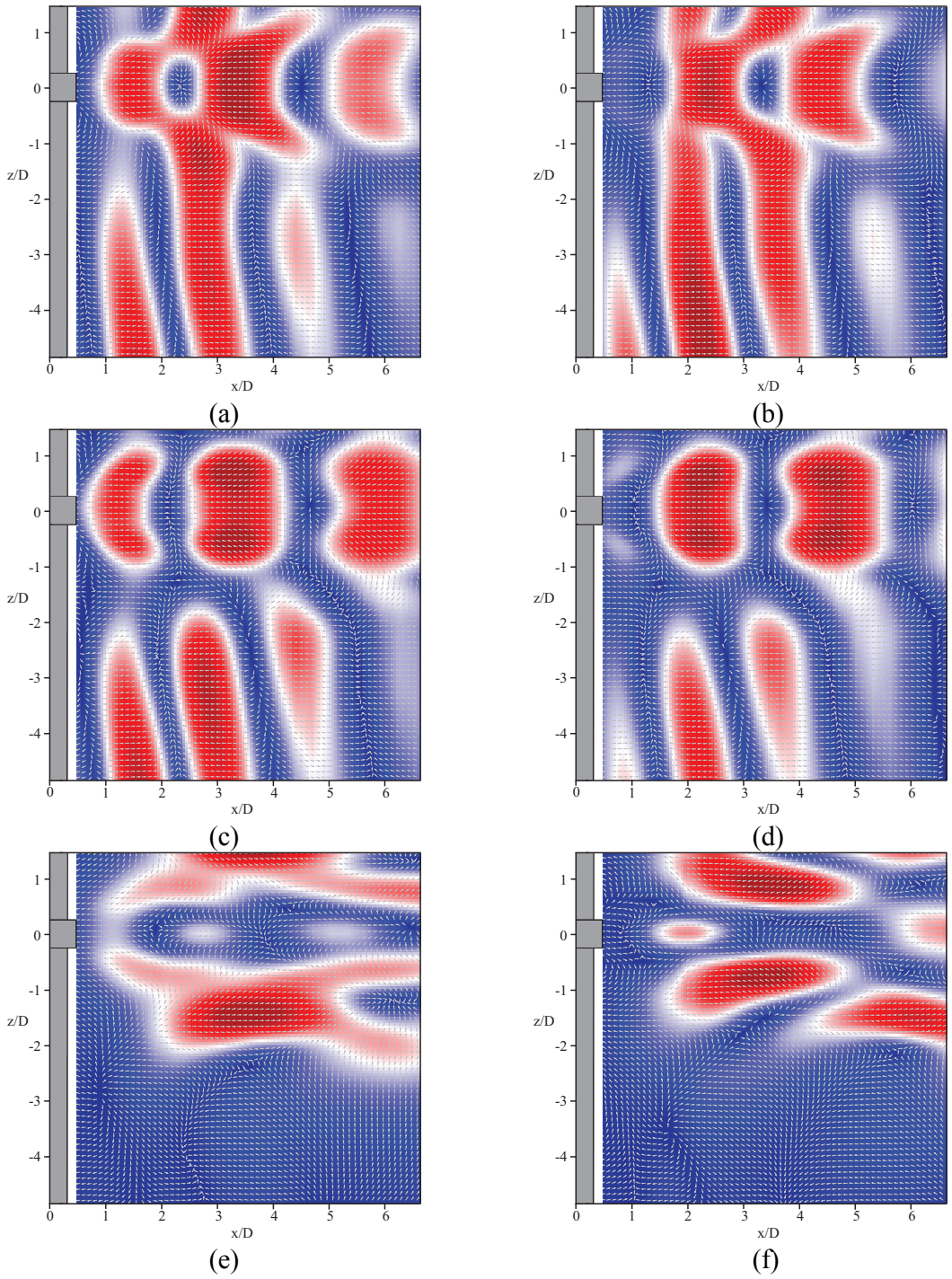

Figure G.4 Spatial eigenfunctions obtained from POD of the x-z planar velocity data extracted from numerical simulation results.

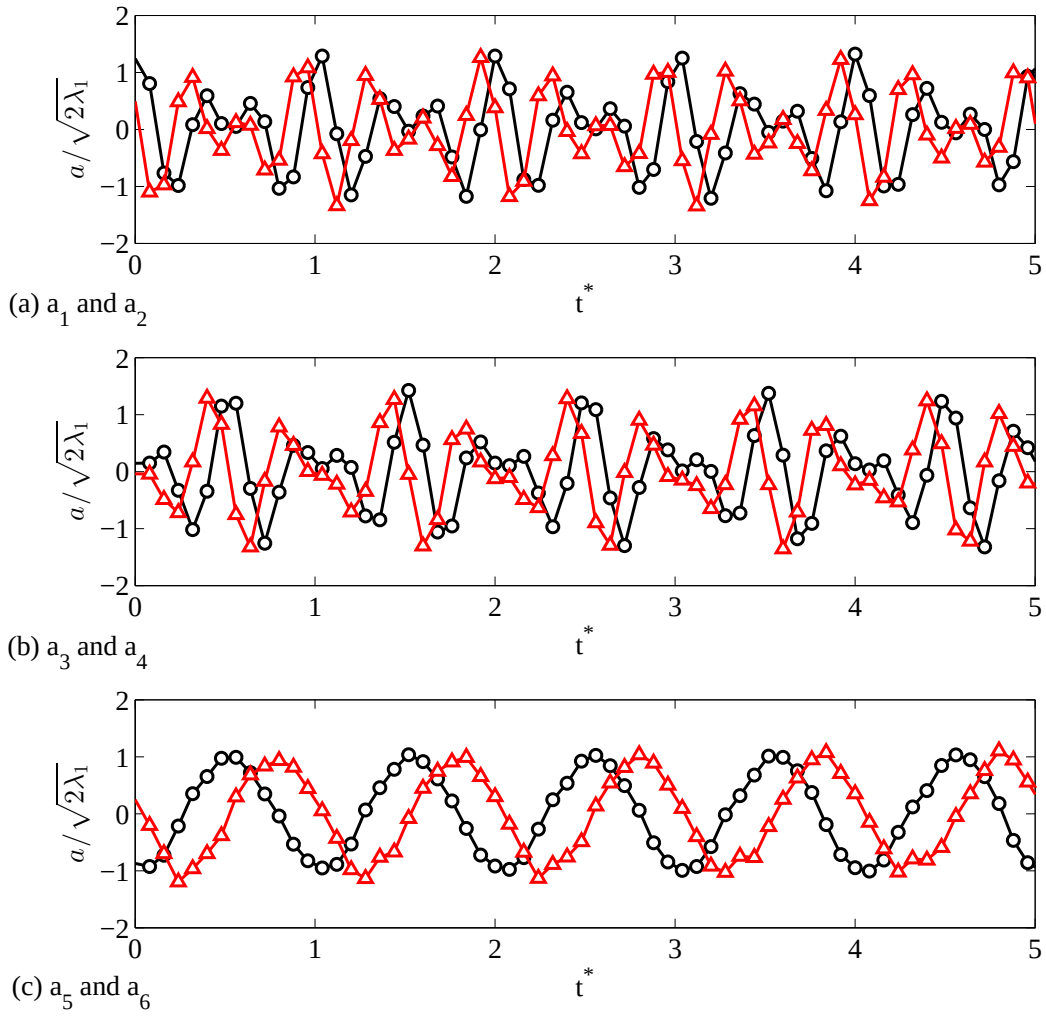

Figure G.5 Temporal coefficient signals obtained from POD analysis of the x-z plane. t* is the number of vortex dislocations.

modulation in the wake energy content due to changes in vortex dynamics as vortices in the large and small cylinder wakes move in and out of phase. Any of the first six temporal coefficients can be used as reference signals for phase-averaging. Since temporal coefficients 5 and 6 contain energy fluctuations at the vortex dislocation frequency, it is of interest to use these signals to investigate changes in vortex dynamics between consecutive vortex dislocations. (Figure G.5). Similar to the work of van Oudheusden et al. [26] and Perrin et al. [25], a cross plot of the

normalized temporal coefficients is used to extract the phase variation of the coherent structures that are characterized by a the vortex dislocation frequency. Figure G.6 presents a cross-plot of the normalized fifth and sixth temporal coefficients. The variation in phase is estimated from the inverse tangent of the normalized temporal coefficient ratio, similar to equation 3.14. Each data point in Figure G.6 has a corresponding instantaneous planar velocity field. There is a notable scatter in the data which is attributable to slight variations in the amplitude of the temporal coefficients associated with the vortex dislocation frequency. The presence of these variations points to the possibility that the vorticity dynamics involved in consecutive vortex dislocations is not the same. To investigate this, three-dimensional flow field snapshots falling in a narrow phase angle band depicted in Figure G.6 are compared in Figure G.7. Of the three flow field snapshots falling within the narrow phase angle band, two are visibly quite similar (Figure G.7a and

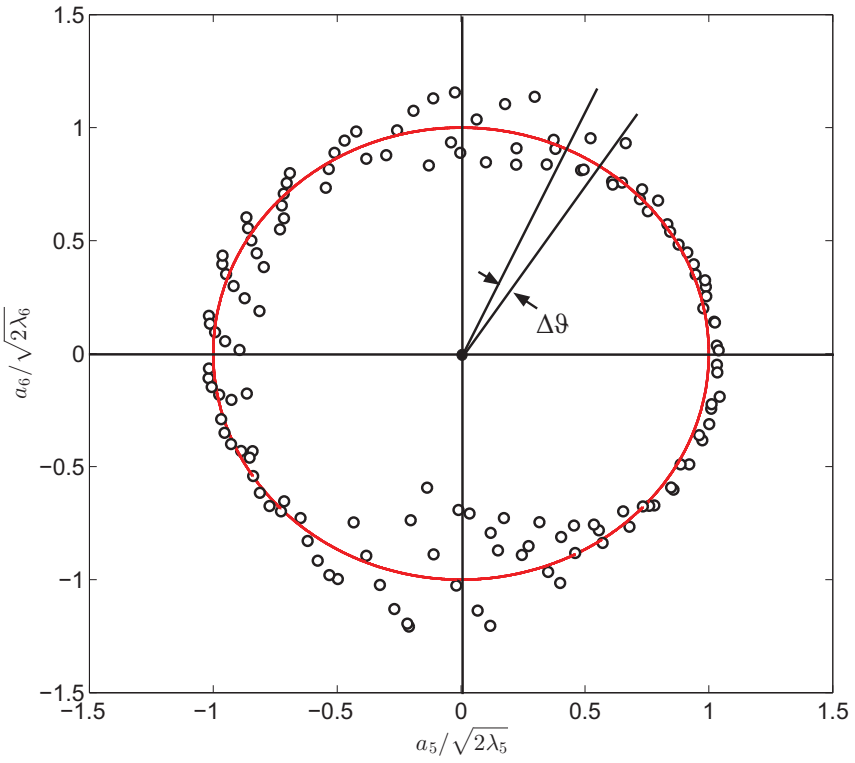

Figure G.6 Cross-plot of temporal coefficients a_5 and a_6. A unit circle is drawn with a red dashed line for illustrative purposes.

Figure G.7b), while the third (Figure G.7c) shows distinct differences in vortex connectivity downstream of the large cylinder. Of the corresponding data points in the cross plot in Figure G.6, the two which are closest together (overlapping) correspond to the three-dimensional flow fields which are nearly a perfect match (Figure G.7a and Figure G.7b). Evidently, for this dual step cylinder geometry, the wake vortex dynamics involved in each vortex dislocation is not consistent. It is important to note that the presence of vortex dislocations only requires that vortices in two adjacent cells move in and out of phase. This places no restrictions on the resulting vortex dynamics since the start and end points of a vortex dislocation cycle here are defined by global fluctuations in the kinetic energy of the entire wake.

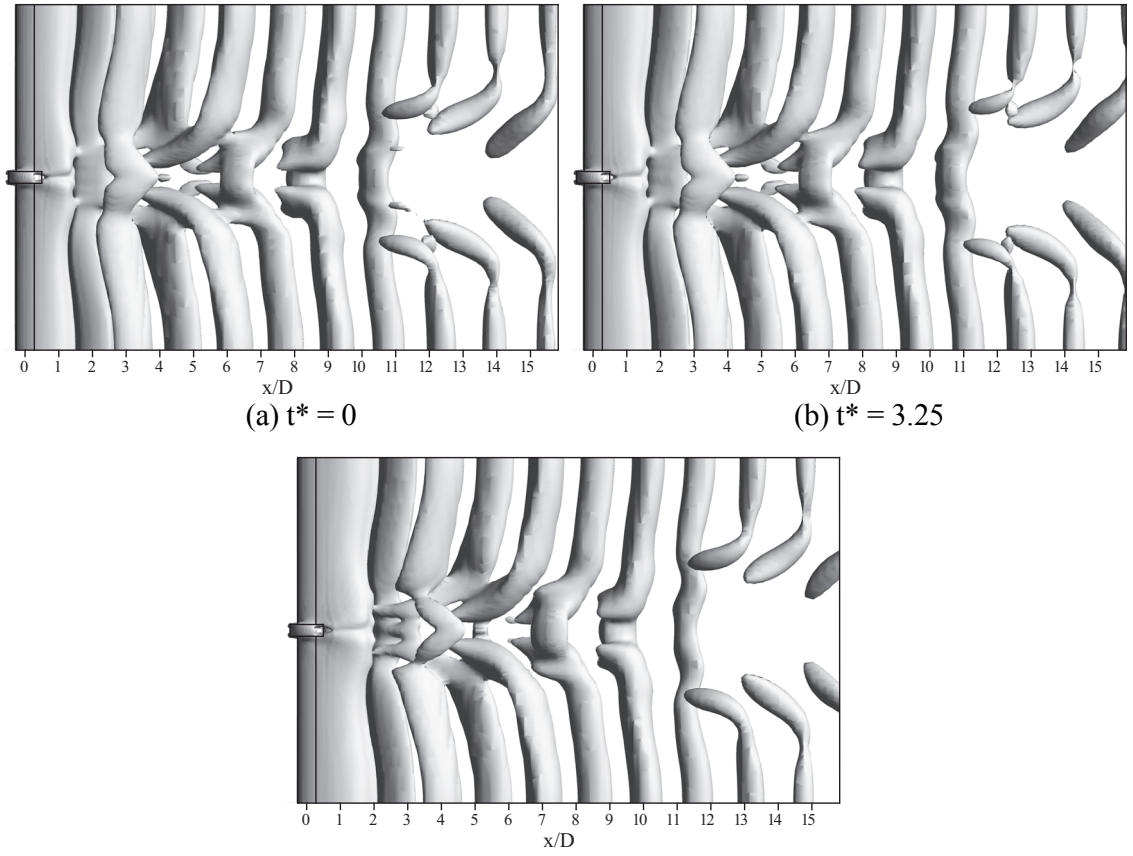

(a) t* = 0

(b) t* = 3.25

(c) t* = 23

Figure G.7 Instantaneous snapshots of the three-dimensional wake development of a dual step cylinder corresponding to the same phase in the vortex dislocation cycle.

A POD analysis of the horizontal plane measurements was carried out in order to extract the phase-variation of the vortices in individual planes. For brevity, a subset of the data analysed through POD is presented in Figure G.8 to Figure G.10. Figure G.8 presents the distribution of wake energy content for planar measurements at three selected spanwise locations in the wake of a dual step cylinder. In the small cylinder wake and large cylinder wake, the first two modes contain over 90% of the overall wake energy content and represent the coherent structures (vortex shedding) from the small cylinder (Figure G.8 and Figure G.9e-f) and large cylinder (Figure G.8 and Figure G.9a-b). In between these regions, where vortex interactions occur, the energy content of the first two modes is reduced (Figure G.8), and the spatial modes depict a coherent structure that is different than the spatial modes found in the large and small cylinder wakes (Figure G.9c-d). The corresponding temporal coefficients pertaining to the interaction region (Figure G.10) are comprised of two frequencies, indicating that the dominant coherent structures within this region are an interaction of large cylinder and small cylinder wake structures.

The results suggest that the wake of a dual step cylinder can be divided into three spanwise regions: (i) Large cylinder vortex shedding region, (ii) small cylinder vortex shedding region, and (iii) vortex interaction region. In regions (i) and (ii), the planar wake topology can be completely

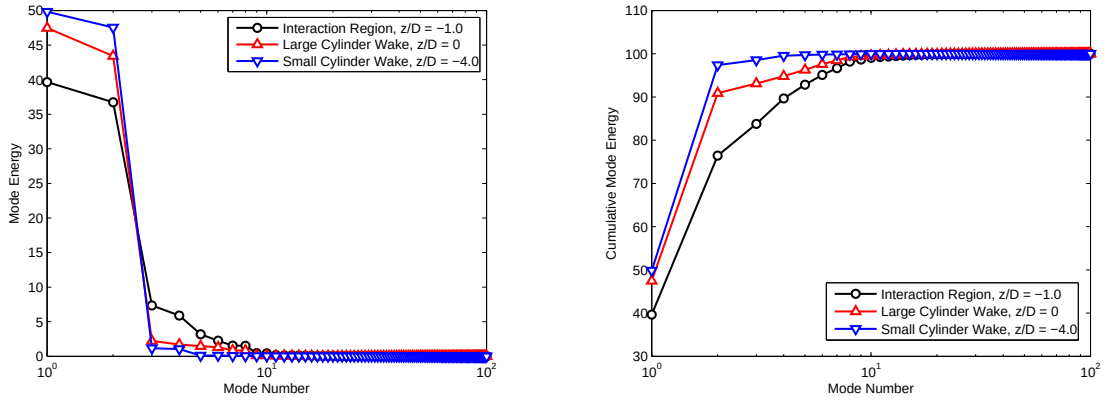

(a) (b)

Figure G.8 Distribution of wake energy content: (a) mode energy distribution, (b) cumulative mode energy distribution.

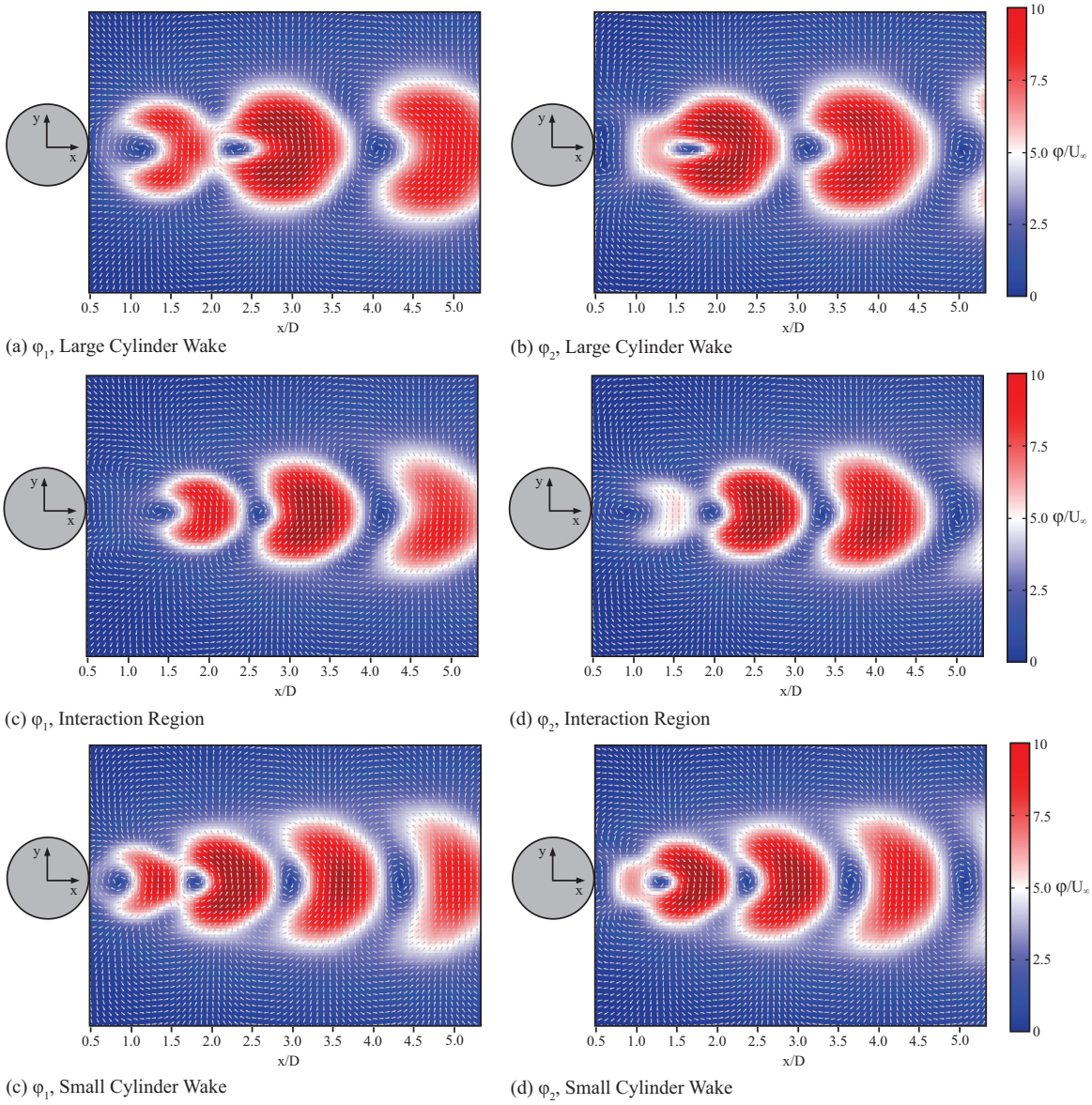

(a) φ_1, Large Cylinder Wake

(b) φ_2, Large Cylinder Wake

(c) φ_1, Interaction Region

(d) φ_2, Interaction Region

(c) φ_1, Small Cylinder Wake

(d) φ_2, Small Cylinder Wake

Figure G.9 Spatial modes within the: (a)-(b) large cylinder wake, (c)-(d) interaction region, and (e)-(f) small cylinder wake.

characterised by a single frequency, namely, the vortex shedding frequency in that region. In the vortex interaction region on the other hand, the planar wake topology is defined by both the large and the small cylinder vortex shedding frequencies due to the fact that vortices of different frequency interact in this region. In order to extract the phase-variation of the dominant vortical structures in regions (i) and (ii), a traditional approach can be used, that is, a cross plot of the

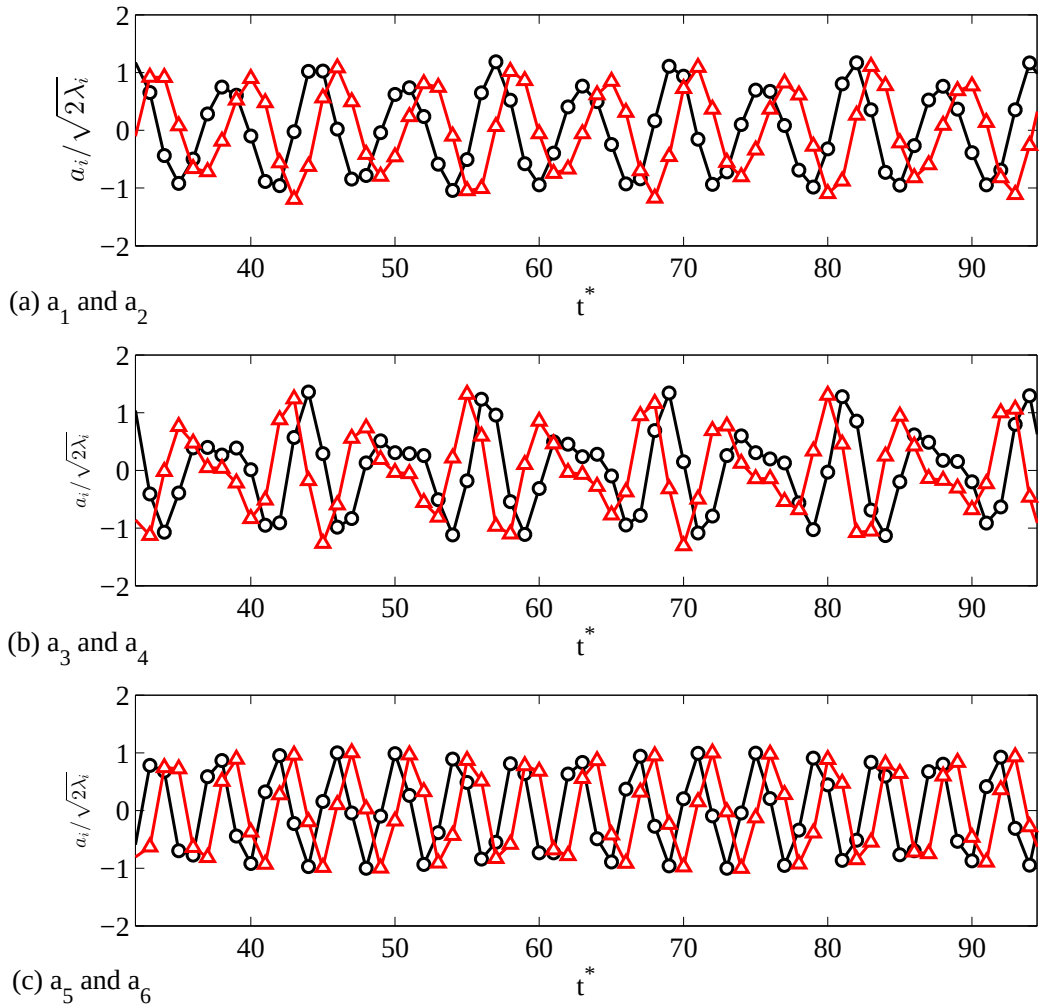

Figure G.10 Temporal coefficient signals within (a) Large cylinder wake, (b) Interaction region, and (c) small cylinder wake.

temporal coefficients (a_1 and a_2) can be used to obtain the phase variation of the dominant vortical structures. On the other hand, in the interaction region, it is proposed that band-pass filter be used to extract the energy fluctuations associated with each of the two dominant wake frequencies. In this way, the phase variation of the coherent structures in the interaction region can also be obtained.

Discussion

The flow development for a low aspect ratio dual step cylinder was investigated numerically for Re_D = 180, D/d = 1.5, and L/D = 0.5. Experimentally obtained PIV measurements in the dual step cylinder wake were emulated by exporting data in discrete x-y and x-z planes. A POD analysis of the vertical planes revealed that the wake vortex dynamics is related to the frequency of vortex dislocations, but the vortex dynamics can vary slightly between subsequent dislocations.

A POD analysis of the horizontal planes show that within the large and small cylinder wakes away from the step discontinuity in diameter, the wake topology is dominated by vortex shedding at a single frequency. Analysis of the temporal coefficients obtained from the POD can be used to extract the phase variation of the dominant structures. In the region near the step discontinuities, vortex interactions give rise to dominant coherent structures comprised of two frequencies. Thus, the wake topology within this region depends on both of these frequencies. It is speculated that filtering of the temporal coefficient data can be used to decompose the temporal coefficient signals in this region into their individual frequency components. The frequency decomposition allows for characterisation of the coherent structures by the phase variation of two signals, one pertaining to the large cylinder vortex shedding frequency, and another pertaining to the small cylinder vortex shedding frequency.

Appendix H
Tomographic PIV measurements in the wakes of dual step cylinders

The important features of the three-dimensional wake topology of a dual step cylinder are described in the main body of the thesis in Chapter 5. This appendix presents a larger compilation of the experimental data acquired. Specifically, this appendix presents mean wake topology and instantaneous wake topology images for a larger set of the models investigated. Following this, the three-dimensional structure of the spatial eigenfunctions obtained from the POD is presented. The focus is on presenting data which supports the discussions contained in Chapter 5. For a more detailed interpretation of the results, the reader is referred to the discussions contained within Chapter 5.

Mean velocity field

The mean velocity field results are depicted in Figure H.1 for a Reynolds number of 2000. The flow regime corresponding to each geometry can be easily identified from the mean flow field by comparing with the results presented in Chapter 5.

Instantaneous flow fields

Instantaneous flow fields were visualized using Q-criterion isosurfaces. In Chapter 5, a reduced order model of the wake was used in order to obtain a clearer picture of the dominant vortical structures in the wake. Figures H.3 to Figure H.6 depict the instantaneous snapshots of the three-dimensional flow field pertaining to the reduced order model results presented in Chapter 5. The images serve to illustrate the complexity of the vortical structures and their interactions in the wake for each regime.

POD Analysis

A POD analysis was performed in order to investigate the dominant coherent structures in each flow regime. The distribution of mode energy across all models investigated is presented in Chapter 5, and here, the three-dimensional structure of the corresponding spatial eigenfunctions (modes) is presented

using Q-criterion isosurfaces (Figure H.6 to Figure H.9). In each of the flow regimes, six of the first eight POD modes capture the structure of the wake vortex shedding. However, as noted in Chapter 5, the modes do not form distinct pairs, indicating that for each model there is substantial complexity in the nature of the dominant vortex interactions. While the majority of modes eight through sixteen also contain spatially periodic features, they are not presented in this section since the main focus is on the primary vortical structures. In the NS, HFS, and LFS flow regimes, the coherent structures are vortices in the small and large cylinder wakes which are shown to interact through direct vortex connections, vortex splitting, and half-loop connections. The coherent structures associated with each spatial mode depict the structure of such vortex interactions between large and small cylinder wake vortices (Figure H.7 to H.9). However, in the IS regime, the large and small cylinder wake vortices only form weak connections, and as a result, the spatial eigenfunctions become isolated based on the flow development downstream of each cylinder (Figure H.10).

The effect of Reynolds number on the spatial modes is illustrated in Figure H.11 and H.12 for L/D = 2 and D/d = 1.6. At lower Reynolds numbers, the spatial modes more closely resemble those found for the HFS regime in Figure H.7, and at higher Reynolds numbers, the wake development changes, leading to spatial modes resembling those observed in the IS regime in Figure H.8. Note that the spatial modes for all other geometries were invariant to changes in Reynolds number.

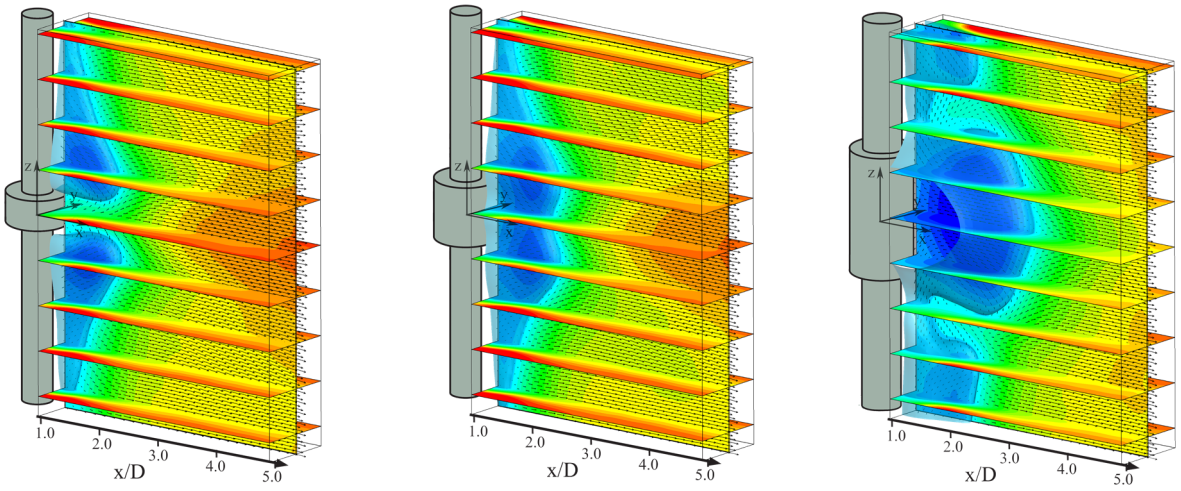

(a) L/D = 0.5, D/d = 2 (b) L/D = 1, D/d = 2 (c) L/D = 2, D/d = 1.6

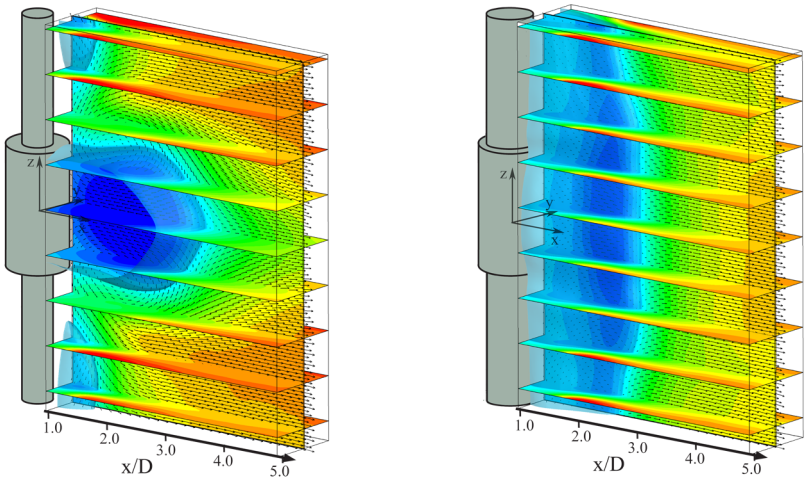

(d) L/D = 2, D/d = 2 (e) L/D = 2, D/d = 1.33

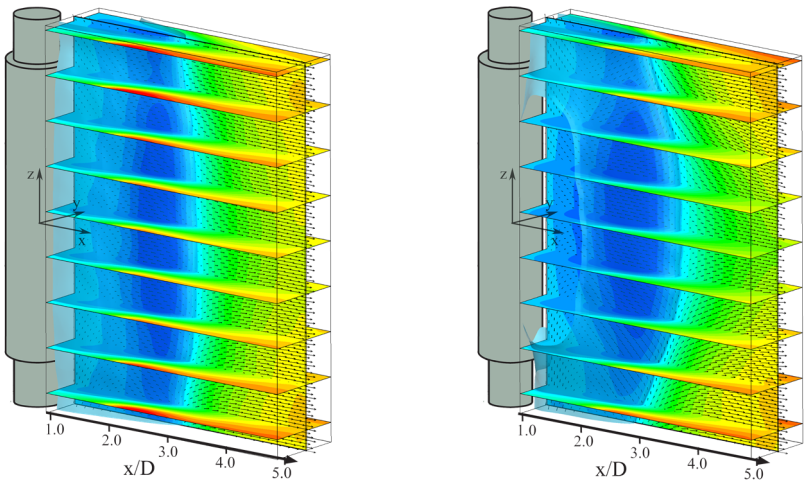

(f) L/D = 5, D/d = 1.6 (g) L/D =5, D/d = 1.6

Figure H.1 Mean velocity field in the wake of a dual step cylinder at $Re_D = 2000$.

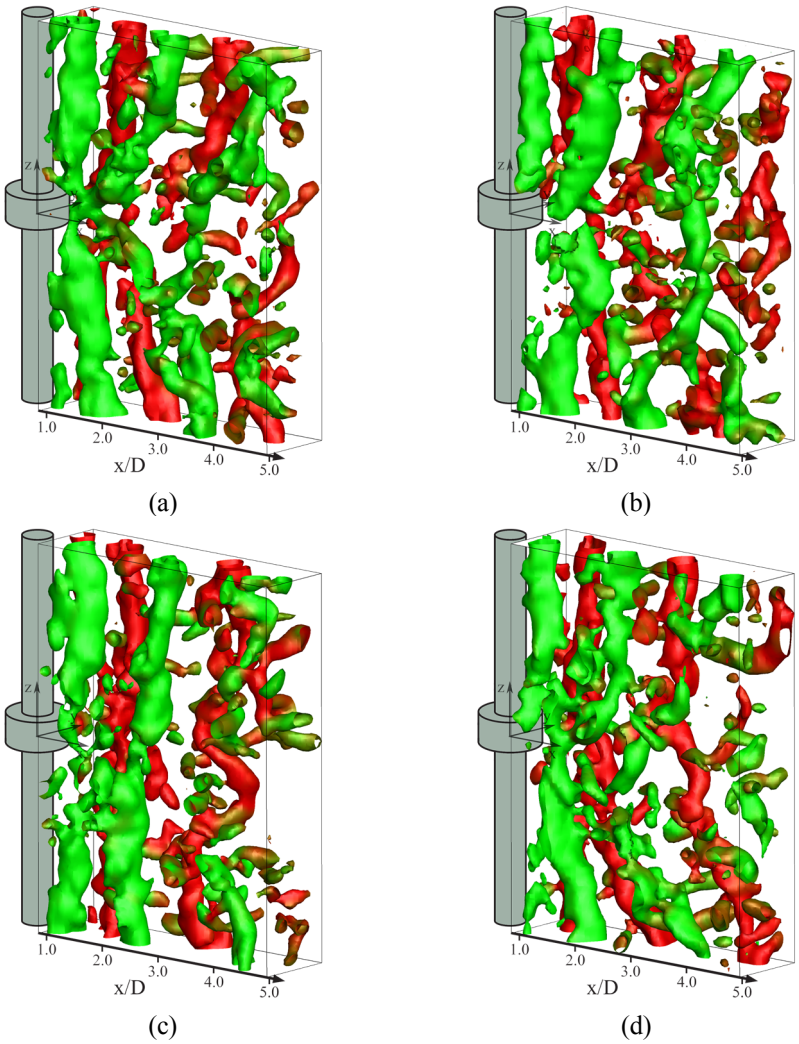

Figure H.2 Vortex shedding in the wake of a dual step cylinder in the NS flow regime at L/D = 0.5, D/d = 2, and Re_D = 2000.

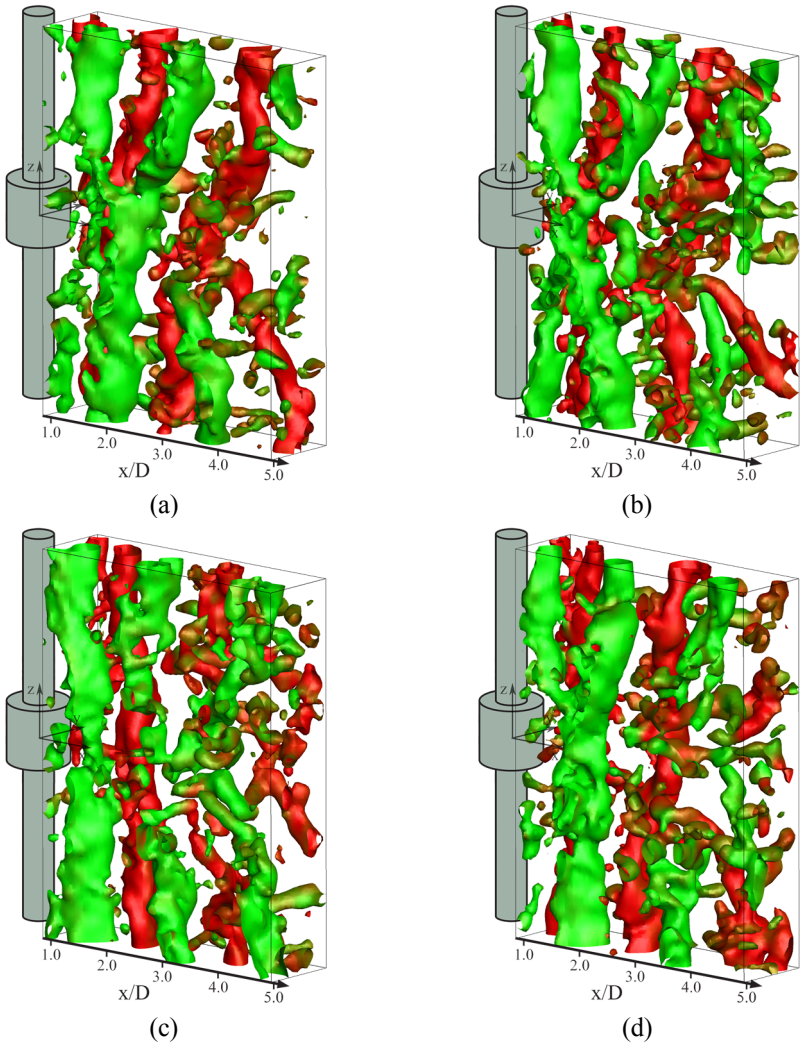

Figure H.3 Vortex shedding in the wake of a dual step cylinder in the HFS flow regime at L/D = 1, D/d = 2, and Re_D = 2000.

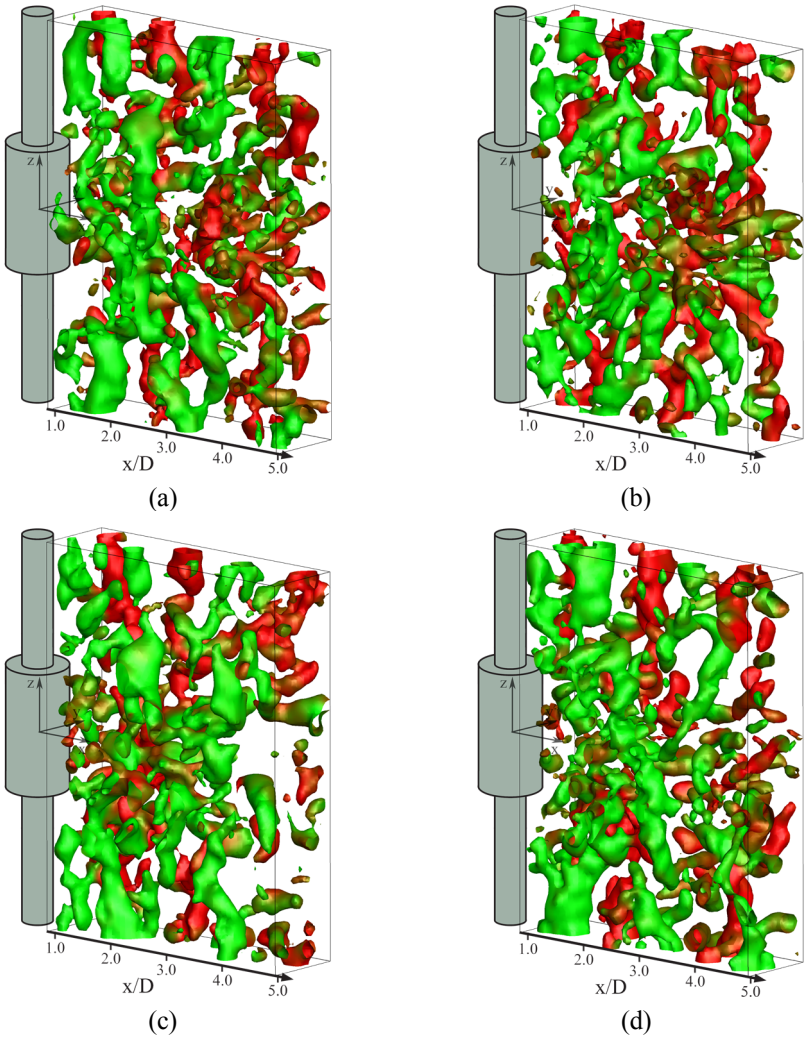

Figure H.4 Vortex shedding in the wake of a dual step cylinder in the IS flow regime at L/D = 2, D/d = 2, and Re_D = 2000.

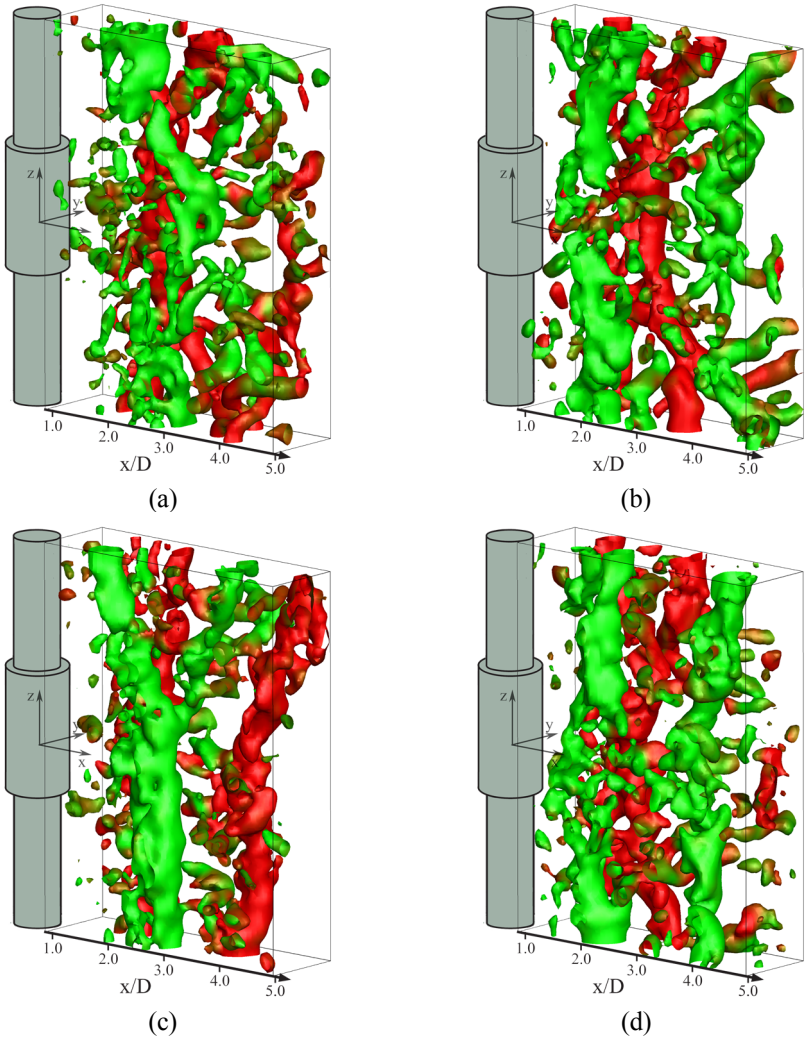

Figure H.5 Vortex shedding in the wake of a dual step cylinder in the LFS flow regime at L/D = 2, D/d = 1.33, and Re_D = 2000.

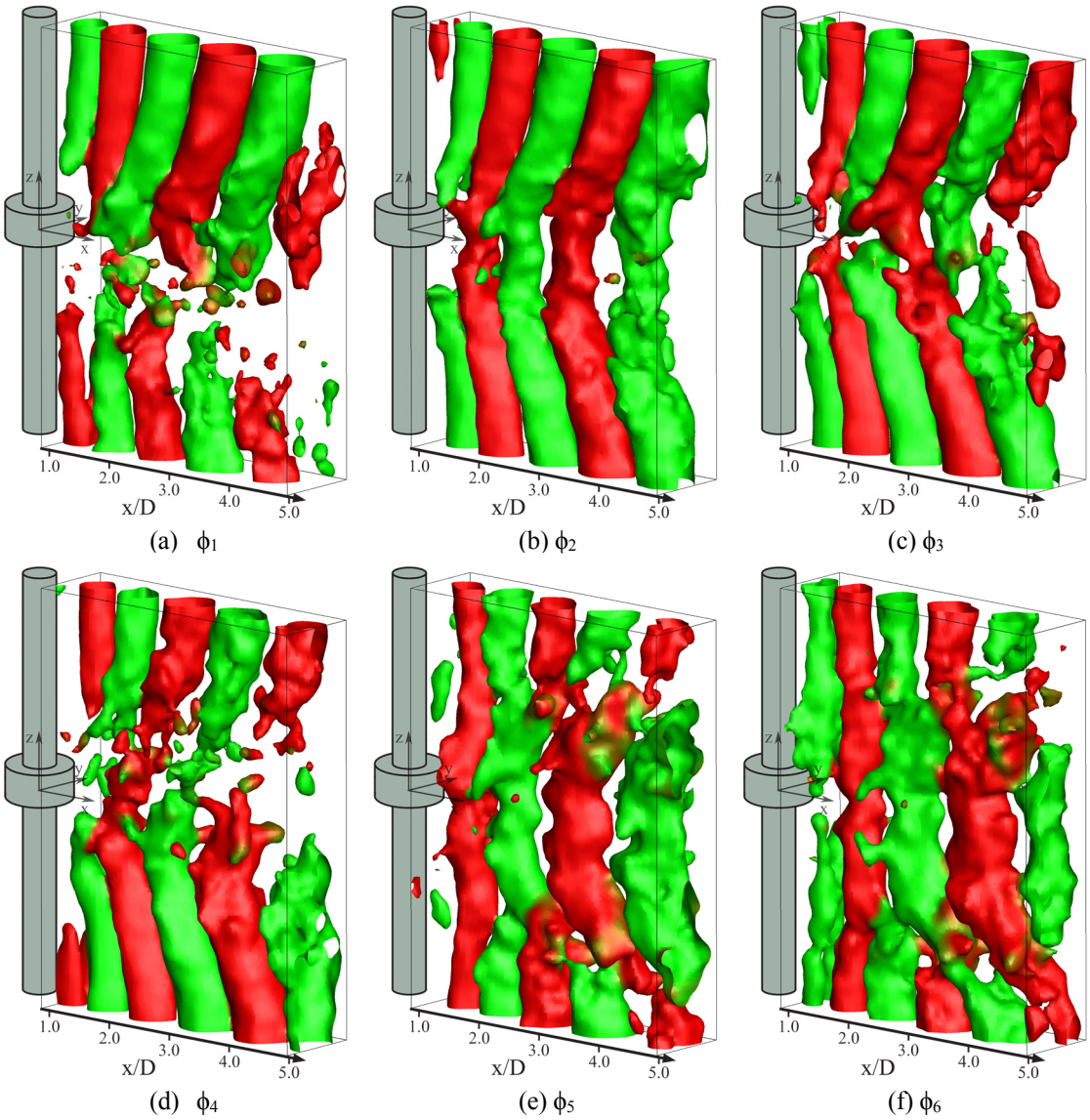

(a) ϕ_1 (b) ϕ_2 (c) ϕ_3

(d) ϕ_4 (e) ϕ_5 (f) ϕ_6

Figure H.6 Spatial eigenfunctions pertaining to the NS regime at L/D = 0.5, D/d = 2, and Re_D = 2000.

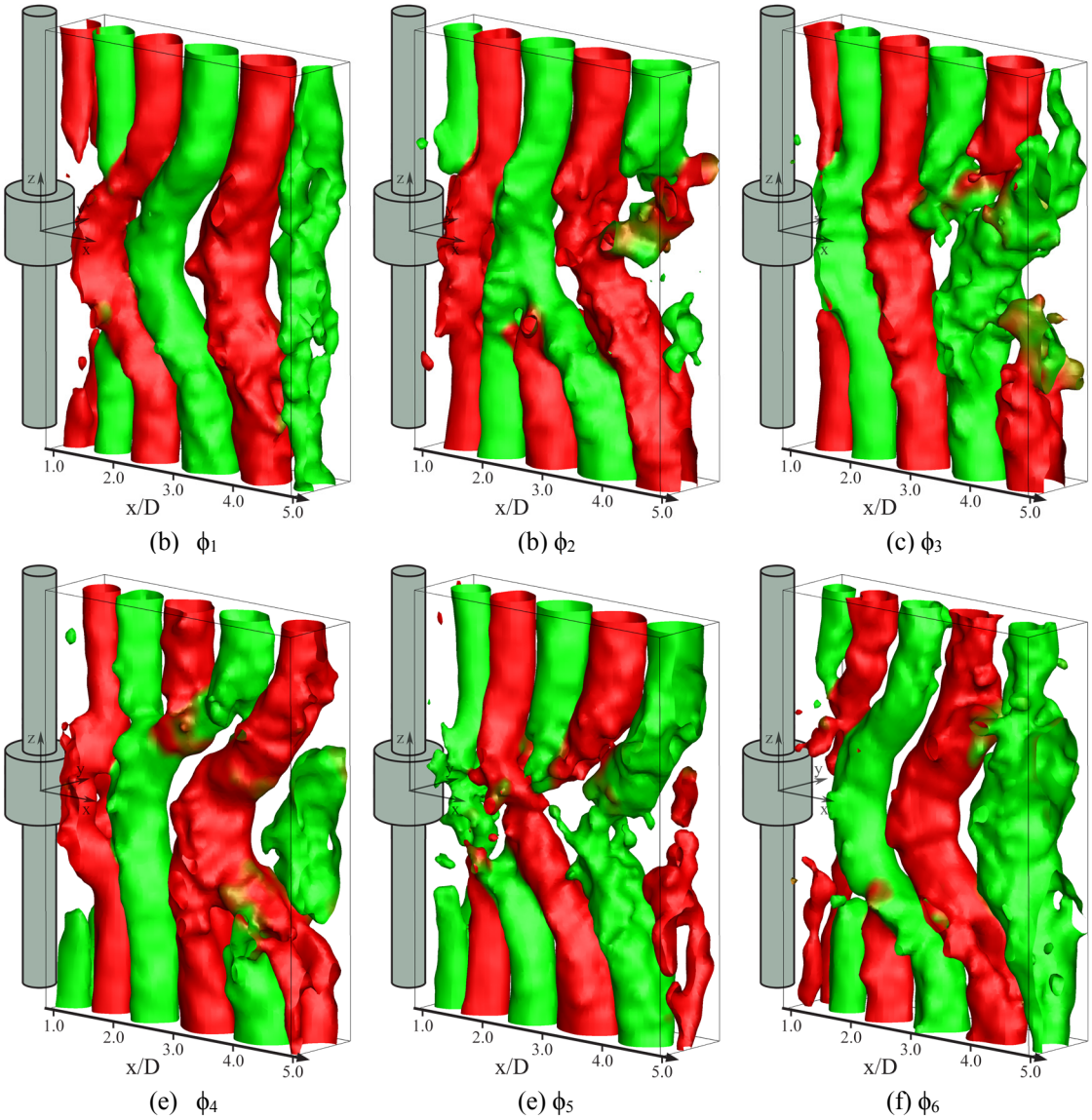

(b) ϕ_1 (b) ϕ_2 (c) ϕ_3

(e) ϕ_4 (e) ϕ_5 (f) ϕ_6

Figure H.7 Spatial eigenfunctions pertaining to the HFS regime at L/D = 1, D/d = 2, and Re_D = 2000.

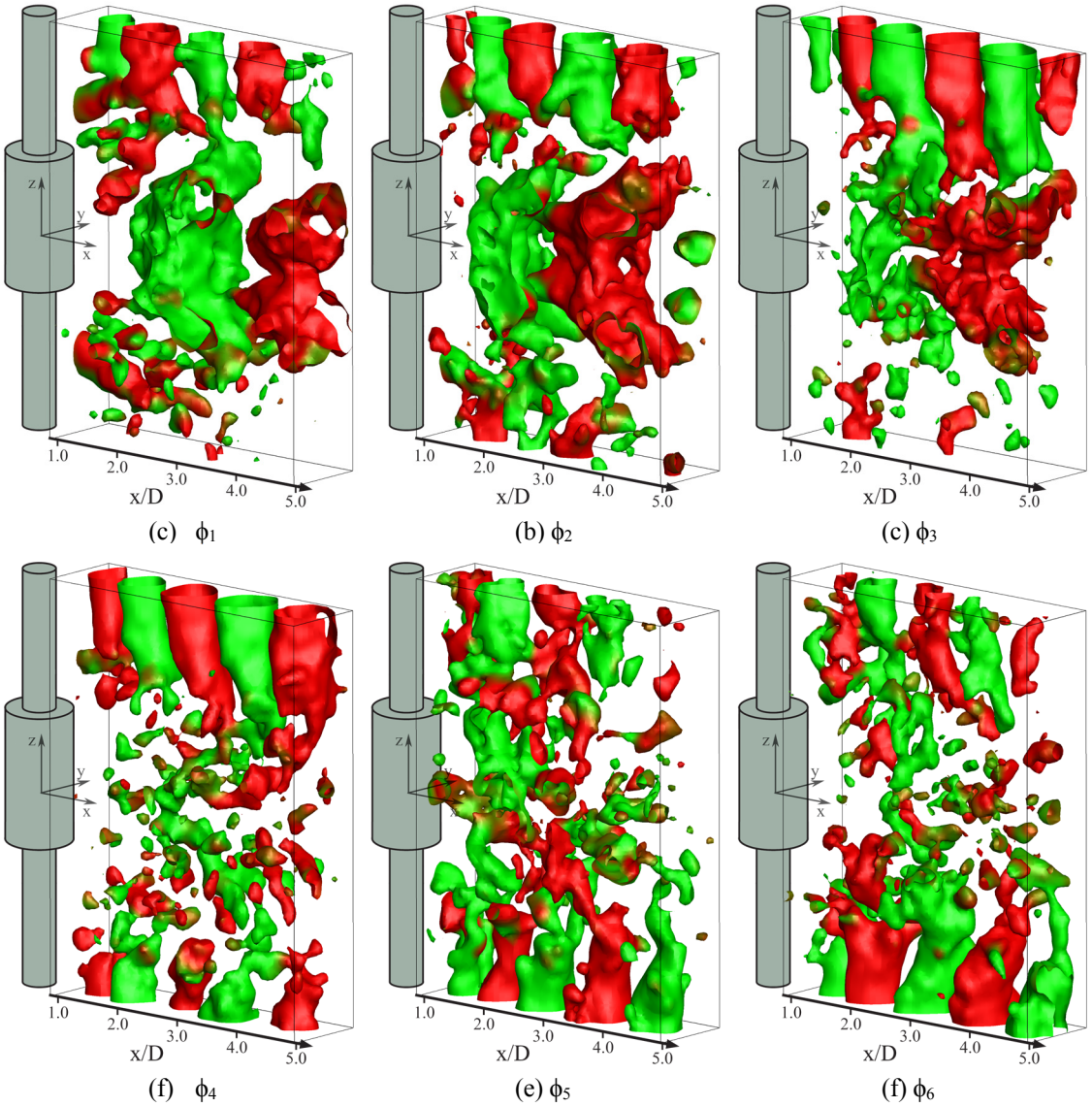

(c) ϕ_1 (b) ϕ_2 (c) ϕ_3

(f) ϕ_4 (e) ϕ_5 (f) ϕ_6

Figure H.8 Spatial eigenfunctions pertaining to the IS regime at L/D = 2, D/d = 2, and Re_D = 2000.

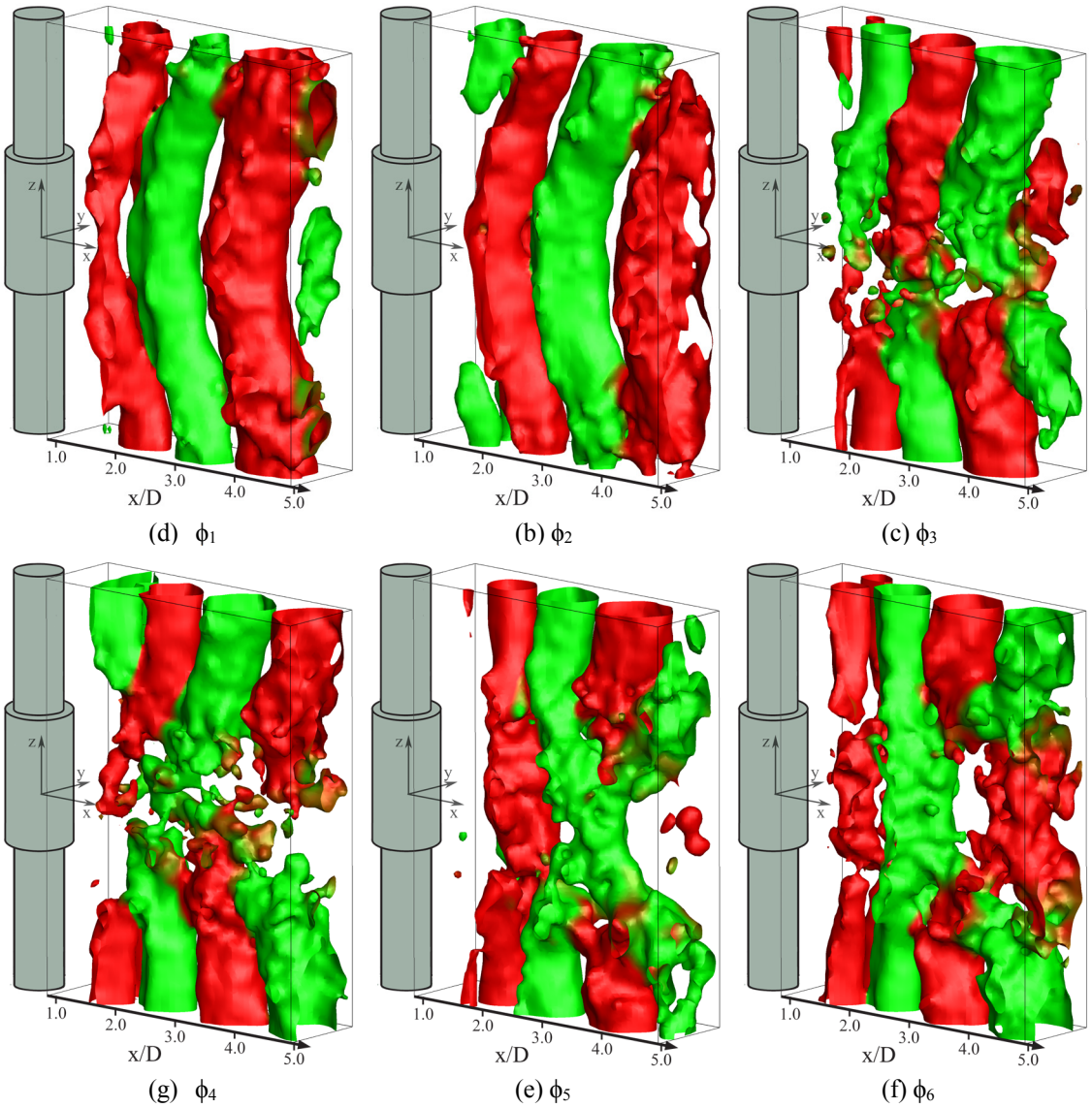

(d) ϕ_1 (b) ϕ_2 (c) ϕ_3

(g) ϕ_4 (e) ϕ_5 (f) ϕ_6

Figure H.9 Spatial eigenfunctions pertaining to the LFS regime at L/D = 2, D/d = 1.33, and Re_D = 2000.

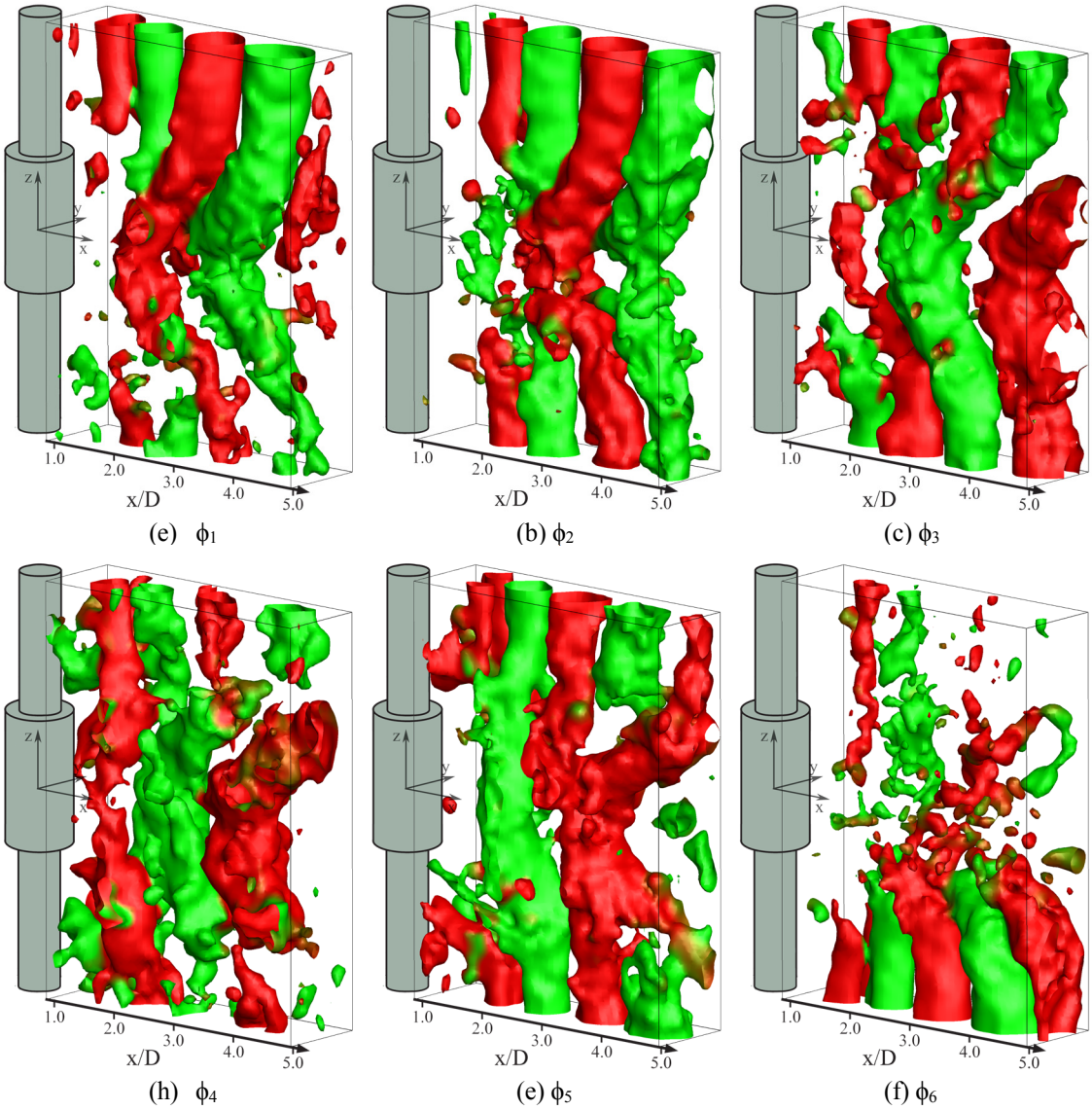

(e) ϕ_1 (b) ϕ_2 (c) ϕ_3

(h) ϕ_4 (e) ϕ_5 (f) ϕ_6

Figure H.10 Spatial eigenfunctions pertaining to the HFS-IS transition regime at L/D = 2, D/d = 1.6, and Re_D = 2000.

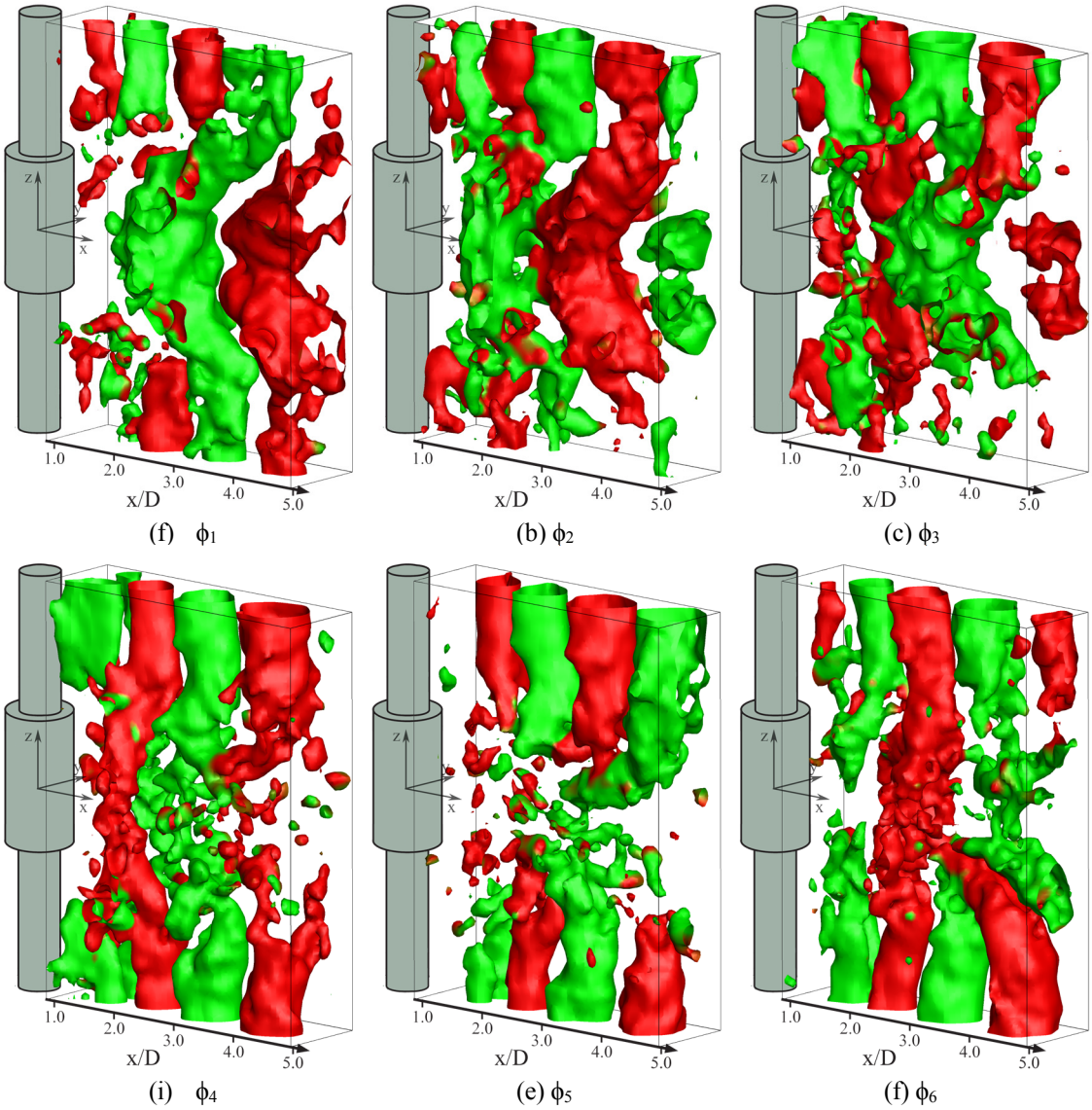

(f) ϕ_1 (b) ϕ_2 (c) ϕ_3

(i) ϕ_4 (e) ϕ_5 (f) ϕ_6

Figure H.11 Spatial eigenfunctions pertaining to the HFS-IS transition regime at L/D = 2, D/d = 1.6, and Re_D = 5000.

Appendix I
Uncertainty Analysis

Experimental uncertainty estimates for the LDV and PIV measurement techniques used in the present study are discussed in this section.

Experimental Uncertainty in LDV Measurements

For the LDV measurements, the total uncertainty associated with all known fixed error sources is estimated to be 4.0% in the wake and 0.45% in the free stream.

Velocity bias error is the most significant source of error in the LDV measurements. It arises from the random data acquisition rate inherent in LDV since higher speed particles cross the measurement volume more frequently than slower ones. The magnitude of this bias in the mean velocity measurements can be estimated using the following equation [89]:

$$\frac{U}{U_T} \approx 1 + \frac{\left(\overline{u'}\right)^2}{(U_T)^2} \qquad \text{(I-1)}$$

where u' is the true RMS of the velocity, U_T is the true mean velocity, and U is the mean velocity measured with LDV. For the experiments conducted in this investigation, all velocity data are re-sampled at a constant frequency, which reduces the bias in the velocity measurements [90]. In Morton [78], velocity measurements were analyzed using re-sampled data. An estimate of the bias error in the free stream flow was found to be negligible, and the bias error in the cylinder wake was at most 4.0%. These values are representative of the bias error in the current experiments.

Other factors which influence the accuracy of LDV measurements include the alignment of each laser beam, the variation in laser power being supplied to each beam, and the alignment of the laser probe for receiving Doppler signals [89]. These sources of error are minimized through carefully controlled alignment procedures and power optimization. Random errors in the LDV measurement may be introduced through variations in the seeding particle shape and size [89,151]. These errors may influence the measured RMS velocity and are not expected to significantly alter the mean velocity[89].

Repeatability: An estimate the random error introduced by the experimental facility and changes in experimental conditions was completed with repeated experiments on consecutive testing days. It was found that variation in the average free stream velocity was less than 0.4%. For wake velocity measurements, this small variation can be neglected since it is an order of magnitude lower than the bias error.

Statistical precision error: The statistical precision error in the velocity measurement is estimated following recommendations in Benedict and Gould [152]. The statistical precision error in the free stream velocity measurements is less than 0.2%, with 95% confidence. For wake velocity measurements, error is less than 0.5%, with 95% confidence. For all LDV measurements completed in the free stream flow, this confidence level was always maintained.

The total uncertainty in the reported mean velocity, calculated based on a root-sum-square combination of all fixed and variable error sources, is about 4.0% in the wake and 0.45% in the free stream.

Error sources in PIV Measurements

This section describes all known error sources in the PIV measurements. The uncertainty in free stream and wake measurements is estimated by comparing PIV measurements in the wake and free stream with measurements obtained in the same locations using LDV. For PIV measurements in the free stream, the uncertainty is estimated to be approximately 2% and in the wake, the uncertainty is approximately 5%.

Sources of uncertainty in PIV measurements originate from calibration (Appendix B), image acquisition, and image processing [94]. Important aspects of the image acquisition include: particle seeding density, camera focus and aperture, alignment of the laser and camera system, laser sheet properties, and image acquisition rate. For image processing, considerations include the uncertainty introduced through interrogation window selection, the cross-correlation and corresponding displacement vector computation, the validation protocol for the raw data, and the replacement of incorrect or erroneous data [94]. The outmost care was taken to minimize the abovementioned error sources, and a brief description for each is given below:

Camera field of view: The cameras used for PIV experiments were mounted either above the water flume, or at the side of the water flume, as described in Chapter 3. In both cases, the resolution in the image plane is approximately the same, at 0.2 pixels/mm. This resolution is used as an aid for selection of an appropriate interrogation window size. It should be noted that for multi-plane PIV measurements, the resolution varies between 0.18 pixels/mm and 0.21 pixels/mm, depending on the location of the image plane.

Camera focus and aperture: The cameras were manually focused on the image plane in the flow, and the camera aperture was adjusted to a value of f# = 5.6 to ensure that the depth of focus in the field of view encompassed the thickness of the laser sheet. This allows for small in-plane displacements of particles to remain in focus. One of the most important aspects of the camera focus and aperture settings is the 'pixel locking' effect. This occurs when the particle-image diameter falls below two pixels, which results in the particle image displacement being biased towards integer pixel values. Unfortunately, for the PIV setup used in the water flume, 'pixel-locking' occurs at all f# aperture settings. Therefore, the cameras are slightly defocused with an aperture of f#=5.6 so that the average particle image diameter is between 3 and 4 pixels, as per the recommendations in Raffel et al. [94].

Interrogation window size and image acquisition rate: Results of Adrian [153] and Willert & Gharib [91] suggest that the velocity gradient within an interrogation window should ideally be less than half the particle image diameter from the top of the interrogation window to the bottom. In the present study, 16x16 pixels interrogation windows were selected in order to maximize vector resolution in the flow, and minimize errors due to velocity gradients being present within interrogation windows. Relative to the large cylinder diameter of D = 25.4 mm, 16 pixels corresponds to approximately 3.2 mm or 0.126D. In near-wall regions, velocity gradients are stronger than the maximum recommended values recommended by Adrian [153] and Willert & Gharib [91]. This does not substantially alter the interpretation of the results since the main focus is in the wake region, where velocity gradients are substantially smaller. In addition to velocity gradient effects, it is also important that the displacement of particles does not exceed the interrogation window size. Given that the image acquisition rate is 100 Hz, this corresponds to an average free stream displacement of approximately 4 pixels, or ¼ of the interrogation window.

Laser sheet: The laser sheet thickness must be sufficient to ensure that particles do not move out of plane between consecutive particle images. In general, it is recommended that out of plane motion be between consecutive particle images be less than 25% of the laser sheet thickness to minimize pixel displacement errors and erroneous vector generation due to particle losses through the laser sheet [154]. In the present experiments, out of plane velocities were calculated to be a maximum of 15% of the free stream velocity. Based on the image acquisition rate of 100 Hz, a free stream velocity of about 85 mm/s, and the measured laser sheet thickness of 2 mm, this results in particles travelling in-plane less than 10% of the laser sheet thickness between consecutive images. The 2 mm sheet is the smallest laser sheet thickness possible using the LaVision PIV system optics. It should be noted the laser sheet thickness will increase image acquisition noise, decreasing the signal-to-noise ratio in the cross-correlation analysis [153].

Particle seeding density: Recommendations in Adrian [154] and Willert & Gharib [91] suggest that the number of particles in each interrogation window should be at least 10. This particle density achieves the smallest RMS fluctuation in the pixel displacements based on locating the correlation peak in a 32x32 pixel interrogation window [91]. In the present work, 16x16 pixels interrogation windows are required, with the average number of particles in each interrogation window being approximately 10. Under these conditions, the RMS fluctuation in the pixel displacement has been shown to be about double that found for 32x32 window [91]. These random displacement fluctuations correspond to velocity fluctuations at less than 1% of the free stream velocity.

Particle Displacements and correlation method: Recommendations in Adrian [153] indicate that particle displacements should be approximately ¼ of the interrogation window size to minimize the RMS fluctuation in particle displacement for single pass direct correlation. Based on the image acquisition rate of 100 Hz, final interrogation window size of 16x16 pixels, and free stream flow speed of 85 mm/s, this corresponds to about 4 pixels displacement, matching the recommendations in Adrian [153]. The use of iterative, multi-grid correlation methods [93] reduce the RMS fluctuation in particle displacement and allows for larger particle displacements. In the present study, an iterative, multi-grid correlation method is employed, starting with 32x32 pixel interrogation windows with 50% overlap, and ending with 16x16 pixel interrogation windows with a 75% overlap. The intermediate

interrogation window sizes and overlap were selected based on trial and error approach to minimize the number of erroneous vectors present in the final interrogation window pass.

Detection and replacement of erroneous vectors: Erroneous vectors were detected and replaced by employing the universal outlier detection technique [96]. For all experiments, less than 0.5% of vectors were regarded as erroneous and replaced.

Overall RMS pixel displacement error: By following all of the listed recommendations for performing planar PIV measurements, particle displacement errors when using a single pass cross-correlation approach typically reported to be on the order of 0.1 pixels [91,93–95,154]. However, by applying iterative multi-grid approaches like those used in the present study [93], the particle displacement errors can be reduced [93]. As a worst case scenario estimate of the particle displacement error in the present study, 0.1 pixels corresponds to approximately 2.4% of the free stream velocity. This value is stated for reference only. The next section presents a quantitative analysis of free stream and wake velocity measurements used to estimate the uncertainty in the PIV measurements.

Indirect estimate of the PIV uncertainty

Due to the multitude of the error sources, there is no generally accepted procedure for estimating experimental uncertainty in PIV [92,94]. In order to make an estimate of the total uncertainty in PIV measurements used for the present investigation, the known random and fixed errors are quantified, the repeatability of measurements is carefully quantified, and the measurement error is estimated through comparison with available LDV data.

When using a single camera for obtaining particle images, error in the velocity measurement is introduced because the spanwise (w) velocity component is not resolved, i.e., out of plane movement of particles cannot be detected with a single camera. In the present experiments, the spanwise velocity component is estimated to be less than 15% of the free stream velocity for wake measurements, which is estimated to introduce an uncertainty in the measured wake velocity of less than 1.2% [155]. The random error introduced by the experimental facility and changes in experimental conditions is the same as that found with LDV measurements, i.e., approximately 0.4%. The calibration uncertainty is about 0.7% (Appendix B). In order to estimate the measurement errors, LDV and PIV measurements

acquired in the free stream flow and the wake of a uniform circular cylinder are compared. For this comparison, PIV and LDV measurements were acquired at approximately the same location in the free stream and in the wake. Care was taken to ensure the environmental conditions, facility conditions and experimental setup was identical for all tests.

For free stream velocity measurements with LDV, the mean velocity is 85.9 mm/s at (x/D, y/D, z/D) = (5, 0.75, 0) with an uncertainty of 0.45%. Repeated measurements with PIV were completed in the free stream at the same location in order to establish an estimate of the free stream velocity. The PIV measurements yielded a mean free stream velocity of 87.3 mm/s with uncertainty of at least 0.8% being attributed to the calibration and random error due to changes in facility conditions. In order for the PIV measurement error bounds to overlap with the LDV measurement estimate, the uncertainty in the PIV measurement is likely about 2%.

For wake velocity measurements with LDV, the mean velocity at (x/D, y/D, z/D) = (5, 0.75, 0) is approximately 79.1 mm/s with an uncertainty of 4%. The PIV measurements yielded a mean velocity at the same location in the wake of 81.6 mm/s. Using the same approach as that shown for the free stream measurements, the uncertainty in the PIV measurement in the wake is likely about 5%.

Strouhal number and Reynolds number

The uncertainty in the velocity measurement has a direct impact on the estimated Strouhal number and Reynolds number. The Reynolds numbers and Strouhal numbers are reported based on the mean free-stream velocity at approximately (x/D,y/D,z/D) = (5,0.75,0). There are a few additional sources of uncertainty which may impact these flow parameters but do not influence the velocity measurement uncertainty.

From the floor of the water flume to the water surface, there is a gradual increase in velocity with z. Thus, there is a change in the local Reynolds number and Strouhal number due to the gradient in the velocity with z. From the data presented in Morton [78], this equates to a change along the model span of ±1.5%.

The experimental testing conducted as part of this thesis took place over the period of four years of water flume operation. During that time, the naturally occurring fluctuations in the temperature of

the reservoir water place an uncertainty of ±0.75% in the Reynolds number. More importantly, there are notable changes in the free stream velocity over the four years of operation. While the uniformity of the flow remained approximately unchanged, the mean velocity of the free stream decreased by approximately 3.5%. This is attributed to the buildup of insoluble deposits on the turbulence reducing stainless steel screens. This introduces an uncertainty in the reported Reynolds number of 3.5%. Since the decrease in velocity over time was closely monitored, any of the reported Strouhal number results have been normalized by the free stream velocity acquired during the time of the data acquisition. The total uncertainty in the Reynolds number and Strouhal number is ±2.5% and ±2.0%, respectively.

Numerical Uncertainty

An estimate of the uncertainty in the numerical results was completed through mesh independence studies, temporal independence studies, and direct comparison with experimental results. The uniform circular cylinder geometry was used as a test case. Based on Roache [108], the bias error associated with the selected mesh, domain, and time step size was estimated to be less than 1%. The bias error associated with the employed numerical model is estimated by comparing the numerical and experimental results in for the matching Reynolds number. The discrepancy in the reported drag coefficient is less than 4% and in the reported Strouhal number is less than 2%. This includes the error associated with the mesh and time step size, since a direct comparison is being made with the experimental values.

A statistical precision error is introduced in the numerical results due to the frequency resolution in the computed velocity spectra. In particular, for a dimensionless shedding frequency of about $fD/U_\infty = 0.2$ and a frequency resolution of $\Delta fD/U_\infty \approx \pm 0.005$, the precision error in the reported Strouhal number values is ±2.3%. This error inherently contributes to the differences in the numerical and experimental values of St. Therefore, the total uncertainty in the numerical results is estimated to be about 4% for the drag coefficient and 2.3% for the Strouhal number.